Nanoscale Mechanical and Electrical Properties of Low-Dimensional Structures

Marta San Juan Mucientes

Thesis submitted for the degree of Doctor of Philosophy

Department of Physics
Lancaster University
Lancaster, UK

December 2020

Abstract

In this thesis, we mainly study the mechanical, electrical and electromechanical properties of low-dimensional structures of advanced materials, in particular two-dimensional (2D) materials and compound semiconductor (CS) structures and devices. Given the scarcity of methods for direct nano-mapping of physical properties of complex three-dimensional (3D) multilayer CS and 2D materials heterostructures, we adapted and developed suitable optical methods and functional scanning probe microscopies (SPM) approaches based in atomic force microscopy (AFM). These allowed us to successfully investigate the behaviour of one- and two-dimensional (1D and 2D) free oscillating structures, such as AFM cantilevers, tuning forks (TF), Si_3N_4 membranes and graphene drums using the optical laser Doppler vibrometry (LDV) and dynamic AFM modes, finding governing relations of the dynamic behaviour in real-life systems and comparing these with modelling. In addition to the existing ultrasonic SPM, such as force modulation and ultrasonic force microscopy (FMM and UFM), we developed a new method called modulation ultrasonic force microscopy (M-UFM), which allows for nonlinear local excitation and the probing of membrane vibrations. Furthermore, we probe mechanical, electrical and thermal properties of supported layers and heterostructures of diverse transition metal dichalcogenides (TMDCs) and franckeite, understanding their intrinsic surface and subsurface nanostructure. In the final part of this thesis, we explored the feasibility of combining nano-sectioning via Beam Exit Cross-sectional Polishing (BEXP) and the material sensitive SPM analysis for the investigation of defects in CS structures, such as multiple quantum wells (MQW) and nanowires (NWs), and 2D material heterostructures. We applied this methodology to investigate the propagation of material defects, such as antiphase domains in CS, and their effects on the morphology, nanomechanics and electric properties in MQW structures, and to directly observe reverse piezoelectric domains inside individual GaN NWs.

Declaration

This thesis is my original work and has not been submitted in whole or in part for a degree at this or any other university. Nor does it contain, to the best of my knowledge and belief, any material published or written by another person, except as acknowledged in the text.

"Si algo es difícil y duro de hacer, entonces no merece la pena hacerlo."

Homer J. Simpson

Acknowledgements

It has been a great journey for me to study in, Lancaster University, a triple top ten university and International University of the Year 2020, through the past four years. During this period of time, I enjoyed loads of great support and help from so many people, whom I would like to express my sincere gratitude in here.

First and foremost, I would like to thank my supervisor Prof Oleg Kolosov, for giving me the opportunity to start a scientific career, as well as for the continuous guidance and support over the whole PhD. I must also acknowledge Yuri Pashkin for the co-supervision during the PhD. I would also like to extend my gratitude to the rest of the Lancaster Nanoscale Characterization group: Alex, Angelo, Ben, Eli, James, Leo, Sam, Sophie and Xintai for promoting a very inspiring and pleasant work environment. I must acknowledge Alex, for the transference of the BEXP nano-sectioning skills, which have made a big impact on the results of this thesis. I also want to thank Angelo for the endless complain sessions in the office, Ben for the constructive comments in the drum paper, Eli for disappearing during two years, James for not letting me go into the train in Salzburg, Leo for being an awesome flatmate, Sam for keeping active the Isolab Iso, Sophie for bringing some fun to the group and Xintai for the excellent advice in the menu selection at the Aroma Chef.

I must acknowledge all our collaborators, from Lancaster ULT group, from Wisconsin University and CSHub partners: University College London, Sheffield, Cardiff and Manchester Universities, for providing very interesting results and samples. Also, I must thank Leo and Andy for the hard work in the CSHub project.

I would also like to thank all the professional and support staff of Lancaster Physics Department. In particular, diolch i Steve Holden am y gwersi Saesneg a Chymraeg, ac am y gefnogaeth dechnegol a phersonol. I would like to thank all the people from the electrical workshop: Stephen, Lucy, Ashley and John, for the delicate work repairing the lab gadgets and the support in the development of novel instrumentation; to all the members of the mechanical workshop: Phelton, Reece, James, Graham and Ian, making a great job and dealing with the rush, and to the coolest technicians: Alan and Martin from the cryogenics workshop, thanks for the never-ending help and fun. I must also thank the safety, health and wellbeing guru, Shonah, for always guaranteeing safe working conditions. Also to Rob and Rupert, for the infinite help and patience dealing with the mysterious IT issues. I also need to acknowledge Deborah and Grainne for the limitless help in the administrative tasks and support; Vicky,

Helen and Lynn for making possible all the purchases, ensuring positive values in my personal bank account and for the enjoyable chats in the breakout room.

I must acknowledge the Revenge group for the scientific and life stimulating mentoring. I need to thank Kunal for smoothly highlighting my defects and English mistakes, also for being an unbeatable circuit fellow and a great 4:30 *bananaja* buddy. I also must thank Ramón and Elena for adopting me as their daughter, for the incredible walks in the Lake District always finishing with a well-deserved pint (in each of the pubs) and the incommensurable support. Thanks also to Charalambos for showing me what are the really important things in life, and summarising the key points for the PhD-life survival: *"filtra y focusa*". *Ευλόγησον πάτερ*! I would like to thank Jean for teaching me something/anything/everything/nothing and for keeping the boss free to answer my stupid questions. Also, thanks to Deneva (Denise and Eva) for providing the background music in the office and sharing your craziness. A special thought goes to Eli, for the great support during the writing up period mixed with the Covid-19 lockdown. Ohio pava! I really appreciate 每首雷鬼曲，每首啤酒和意甲比賽，這都讓我不放棄 during this hard time.

I need to acknowledge James and Charlotte for helping with the English grammar, teaching me smashing expressions, which make my vocabulary cracking, and letting me know that I should make and not do friends.

Then, I have to acknowledge the Sports Centre of Lancaster University for the (un)conditional support offered due to my meniscus injury during a Body Blitz session.

I must also thank my Spanish friends, Irene and Sofia, for visiting and bringing me some joy; and *Las Locas por el Verdejo*, for your particular support.

Finally, I would like to thank my family, my grandparents and particularly my parents, Asun and Felipe, whose support has been unquestionable not only throughout my PhD but at all times. Also, a special thought goes to my brothers, Jesús and Rubén, for the encouragement provided during my whole life, *por tutatis!*

Contents

Contents ... 6
List of publications ... 9
List of acronyms ... 12
List of figures ... 13
1. Introduction ... 21
2. Literature review ... 25
2.1. Introduction ... 25
2.2. Physical properties and structure of solid state materials ... 26
2.3. Bulk semiconductors and insulators ... 34
2.3.1. Group IV – Silicon and silicon compounds. ... 34
2.3.2. III-V Compound Semiconductors ... 35
2.4. Two-dimensional materials ... 38
2.4.1. Graphene ... 38
2.4.2. Transition Metal Dichalcogenides ... 39
2.5. Nanoscale measurements methodology ... 42
2.5.1. Scanning probe microscopy ... 42
2.5.2. Nano-mechanical measurements in SPM. ... 44
2.5.3. Electrical measurements in SPM. ... 48
2.6. Optical characterisation methods ... 53
2.6.1. Interferometric methods: laser Doppler vibrometry ... 53
2.6.2. Raman spectroscopy and photoluminescence ... 55
2.7. 3D Sectioning and sample preparation for SPM ... 56
2.8. Micro and nanoscale MEMS and NEMS ... 57
2.8.1. Mechanical resonators ... 57
2.8.2. Beams and tuning forks – fundamental principles ... 58
2.8.3. Membranes ... 60
2.8.4. 2D materials drums ... 60
2.9. Summary. ... 61
3. Target materials and sample preparation ... 62
3.1. 2D materials – exfoliation, lifting and transfer ... 62
3.1.1. Graphene flakes ... 62
3.1.2. Multilayer structures of transition metal dichalcogenides ... 65
3.2. Semiconductor nanostructures ... 67
3.2.1. III-V materials – growth ... 67
3.2.2. Heterostructures – MQW, QD and VCSEL ... 68
3.2.3. III-nitrides - GaN nanowires ... 70

3.3. MEMS devices - mechanical resonators 73
3.3.1. Silicon nitride membranes 73
3.3.2. Tuning forks and cantilevers 74
3.4. Sample preparation 77
3.4.1. Beam exit cross-sectional polishing (BEXP) 77
3.4.2. Nanowires processing with spin-on glass (SOG) 79
3.5. Fabrication of graphene nanodrums on patterned Si substrates 81
3.6. Summary 82
4. Nanoscale physical property measurements – methods development 83
4.1. Introduction 83
4.2. AFM as a platform for nanoscale properties mapping 83
4.3. SPM - Electrical measurements 84
4.3.1. Kelvin probe force microscopy 84
4.3.2. Dielectric electrostatic force microscopy 87
4.4. Nanomechanical measurements 88
4.4.1. Ultrasonic excitation 88
4.4.2. Force modulation microscopy and contact resonance AFM 90
4.4.3. Ultrasonic force microscopy and waveguide-UFM 90
4.4.4. Heterodyne force microscopy 91
4.4.5. Modulation ultrasonic force microscopy 91
4.4.6. Piezoelectric properties measurements – piezoelectric force microscopy 93
4.5. Optical methods 96
4.5.1. Laser Doppler vibrometry 96
4.5.2. Raman spectroscopy and photoluminescence 97
4.6. Summary 98
5. Free oscillating structures MEMS/NEMS 99
5.1. AFM cantilevers: analytical model and optical characterization 100
5.1.1. AFM cantilever modelling 100
5.1.2. Optical characterization of AFM cantilevers 100
5.2. Tuning forks 103
5.2.1. Quartz tuning forks 103
5.2.2. Lithium niobate tuning forks 109
5.3. Silicon nitride membranes 114
5.4. Graphene nanodrums 121
5.4.1. Experimental measurements. 121
5.4.2. Analytical modelling for the cantilever behaviour in a FLG drum 125
5.5. Summary 133
6. Supported Layered Structures 134

6.1. Synthetic structures – introduction 134

6.1.1. Nanomechanical probing of subsurface defects in synthetic layered vertical heterostructures 135

6.1.2. 3D nanomechanical mapping of synthetic WS_2 heterostructures 139

6.1.3. 3D dielectric mapping of vertical WS_2 heterostructures 142

6.2. Synthetic lateral heterostructures of MoS_2 and WS_2 143

6.3. Natural occurring heterostructures 150

6.3.1. Franckeite 150

6.4. Summary 152

7. 3D structures of Compound Semiconductors 153

7.1. Introduction 153

7.2. III-V multiple quantum wells nanostructures on Si 155

7.2.1. Study of the 3D morphology and nanomechanical properties of DFL with and without the presence of APD 156

7.2.2. Comparison of contact potential distribution in MQW structures with and without the presence of APD 160

7.3. Charges transfer in complex structures for light-emitting applications – VCSEL 161

7.4. Metamorphic III-Nitride nanowires on Si 165

7.4.1. Nanomechanical mapping of GaN nanowires 166

7.4.2. Surface potential study at the substrate-NW interface 168

7.4.3. PFM mapping of polarity reversal in individual NWs 170

7.4.4. Understanding of the electrostatic contribution in the PFM response 174

7.5. Summary 176

8. Achievements and perspectives 177

8.1. Key achievements of this thesis 177

8.2. Perspectives 179

References 181

Annexe I 187

Annexe II 189

List of publications

Peer-review papers

- *Nanoscale Thermal Transport in 2D Nanostructures from Cryogenic to Room Temperature*, Evangeli, C., Spiece, J., Sangtarash, S., Molina-Mendoza, A.J., Mucientes, M., Mueller, T., Lambert, C., Sadeghi, H., Kolosov, O. 1/10/2019 In: Advanced Electronic Materials. 5, 10, 10 p.
- *Multimode Probing of Superfluid ^{4}He by Tuning Forks,* Guthrie, A., Haley, R., Jennings, A., Kafanov, S., Kolosov, O., Mucientes, M., Noble, M., Pashkin, Y., Pickett, G., Tsepelin, V., Zmeev, D., Efimov, V. 13/09/2019 In: Applied Physics Letters. 115, 11, 4 p.
- *Mapping nanoscale dynamic properties of suspended and supported multi-layer graphene membranes via contact resonance and ultrasonic scanning probe microscopies,* Mucientes, M., McNair, R., Peasey. A., Shao, S., Wengraf, J., Lulla, K., Robinson, B., Kolosov, O. 17/07/2020 In: Nanotechnology. 31, 41, 415702 p.

Papers submitted

- *Nanoparticles-Assisted Deposition of Solution-Processed Yttria Stabilized Zirconia Gate Dielectrics for Metal-Oxide-Based Thin Film Transistors,* Antoniou, G., Halcovitch, N.R., Mucientes, M., Milne, W.I., Kolosov, O., Adamopoulos, G. (Under review, in ACS Applied Materials & Interfaces)

Papers in preparation

- *Exploration of internal reversal piezoelectric domains in individual GaN nanowires,* Mucientes, M., Forcieri, L., Lulla, K., Bernardo Gavito, R., Robson, A.J., Jarvis, S., Wang, T., Gong, Y., Kolosov, O. (Nano Letters, in preparation).
- *Tailoring Optical and Electrical Properties in Monolayer of MoS_2 Using Non-Covalent Bonded Interspacer Self-Assembled Monolayer of Fullerene,* Lamantia, A., Wang, X., Fong, J., Mucientes, M., Forcieri, L., Jarvis, S., Young, R.J., Kolosov, O., Robinson, B.J. (In preparation).

This work has also been presented at the following scientific conferences and workshops:

Lead presenter:

- *Beam Exit Cross-Sectional Polishing (BEXP) and Functional SPM - New Approach for 3D Mapping of Physical Properties of Nanostructures*, Oral presentation in 2019 MRS Fall Meeting & Exhibit, Boston, MA, US. Best student talk award.
- *Nanomechanical and Nanoelectrical Mappings of Buried Defects in Lateral and Vertical Van der Waals Heterostructures,* Poster presentation in 2019 MRS Fall Meeting & Exhibit, Boston, MA, US.
- *Multiphysics 3D Study of Compound Semiconductor Nano-structures via Scanning Probes,* Oral and poster presentations in Microscopy Microscience Conference 2019, Manchester, UK.
- *Visualisation of Subsurface Defects in Van-der-Waals Heterostructures via 3D SPM Mapping,* Poster presentation in Microscopy Microscience Conference 2019, Manchester, UK.
- *Multiphysics 3D Study of CS Nano-structures via SPM,* Oral presentation in 9th Early Stage Researchers Workshop in Nanoscience - Imdea Nanociencia, Madrid, Spain.
- *Comparison of Local Dynamic Response of MEMS Nanostructures Using Ultrasonic Force Microscopy and Laser Doppler Vibrometry,* Poster presentation in 2018 MRS Spring Meeting & Exhibit, Phoenix, AZ, US. Best Poster Award.
- *Nanomechanical Visualisation of Subsurface Defects in WS_2/WSe_2 CVD Flakes via Ultrasonic Force Microscopies*, Poster presentation in 2018 MRS Spring Meeting & Exhibit, Phoenix, AZ, US. Best Poster Award.
- *Mapping Heat Transport in Van der Waals Nanostructures via Cryogenic Scanning Thermal Microscopy,* Poster presentation in 2018 MRS Spring Meeting & Exhibit, Phoenix, AZ, US.
- *Nanoscale Mapping of Graphene Membranes Nanomechanics via Contact Resonance AFM*, Poster presentation in Graphene Study Winter 2018, Graphene Flagship, Obergurgl, Austria.
- *Mapping Vibrational Modes of Si_3N_4 Membrane - Ultrasonic Force Microscopies vs Laser Doppler Vibrometry,* Poster presentation in Christmas Conference 2017, Lancaster University, UK. Best Poster Award.
- *Imaging Subsurface Defects in WS_2/WSe_2 CVD Flakes via Ultrasonic Force Microscopies,* Poster presentation in Surface Science Day 2017, University of Liverpool, Liverpool, UK.

- *Subsurface Imaging of Stacking Faults and Dislocations in WS_2 CVD Grown Flakes via Ultrasonic and Heterodyne Force Microscopy,* Poster presentation in Bruker SPM Conference and User Meeting 2017, University of Leeds, UK.
- *Mapping of Vibrational Modes of Nanoscale Membranes via Scanning Probe Microscopy,* Poster presentation in Microscopy Microscience Conference 2017, Manchester, UK.

Contributing author:

- *New high electromechanical coupling $LiNbO_3$ fully shielded tuning fork sensor for multi-environment non-contact AFM*, *Kolosov, O., Mucientes, M., Forcieri, L. & Jarvis, S., The 22nd International Conference on Non-contact Atomic Force Microscopy, Regensburg, Germany.
- *Nanoscale 3D potential mapping in buried semiconductor nanostructures using sideband Kelvin Force Probe Microscopy,* *Kolosov, O., Mucientes, M., Forcieri, L. & Jarvis, S., The 22nd International Conference on Non-contact Atomic Force Microscopy, Regensburg, Germany.
- *Imaging 3D nanostructure of III-V on Si via cross-section SPM: quantum wells and nanowires - defects, polarity, local charges,* *Kolosov, O., Mucientes, M., Forcieri, L., Jurczak, P., Tang, M., Lulla, K., Gong, Y., Jarvis, S., Liu, H. & Wang, T., E-MRS Fall Meeting 2019, Warsaw, Poland.
- *Cross-sectional Nanoscale Resolution Mapping of Potential and Current Distribution in 3D Structure of Vertical Cavity Surface Emitting Laser iii-v Nanostructures*, Mucientes, M., Forcieri, L., Jarvis, S., Eddie, I., Meredith, W., Haji, M., Smowton, P. & *Kolosov, O., Microscopy Microscience Conference 2019, Manchester, UK.

List of acronyms

0D	Zero-dimensional
1D	One-dimensional
2D	Two-dimensional
3D	Three-dimensional
CS	Compound semiconductors
MEMS	Microelectromechanical system
NEMS	Nanoelectromechanical system
TF	Tuning forks
LDV	Laser Doppler vibrometry
TDMC	Transition metal dichalcogenides
SPM	Scanning probe microscopy
AFM	Atomic force microscopy
FMM	Force modulation microscopy
CR-AFM	Contact resonance atomic force microscopy
UFM	Ultrasonic force microscopy
HFM	Heterodyne force microscopy
M-UFM	Modulation ultrasonic force microscopy
KPFM	Kelvin probe force microscopy
PFM	Piezoelectric force microscopy
SThM	Scanning thermal microscopy
BEXP	Beam exit cross-sectional polishing
SEM	Scanning electron microscopy
FIB	Focussed ion beam
TEM	Transmission electron microscopy
SOG	Spin-on-glass
QD	Quantum dots
MQW	Multiple quantum well
NW	Nanowire
VCSEL	Vertical cavity surface emitting laser
APD	Antiphase domains
CVD	Chemical vapour deposition

List of figures

Figure 2.1 Scheme of the different filling of the electronic states in various types of materials at equilibrium. Height is energy while width is the density of available states for a certain energy in the material listed. The shades follows the Fermi-Dirac distribution (dark purple means all states filled, white means no state filled). In metals and semimetals the Fermi level E_F lies inside at least one band. In insulators and semiconductors the Fermi level is inside a band gap; however, in semiconductors the bands are near enough to the Fermi level to be thermally populated with electron or holes. 26

Figure 2.2 Reflection, propagation and transmission of a light beam incident on an optical medium.. 27

Figure 2.3 a) Comparison of material deformation for soft (green) and a stiff (yellow) materials. b) Deformation of a solid under shear strain by a force, *F*. c) Uniform compression of a solid under pressure, *P*. d) Illustrates a unit cube of material with forces acting on it in three dimensions and the stress tensor, σij 30

Figure 2.4 Illustration of the piezoelectricity concept. In piezoelectric crystals, the application of an expansive (pulling) or compressive (compressional) force results in a change of the distribution of dipole moments. This causes a change in the surface charge, which is proportional to the applied force [23]. . 31

Figure 2.5 Schematic diagrams showing an edge dislocation (left) and a screw dislocation (right). The dislocation lines are highlighted with dashed thick black lines. The Burgers vectors are represented by a red and blue arrows, for the edge and the screw dislocations, respectively. 32

Figure 2.6 Scheme of a p-n junction in thermal equilibrium with zero-bias voltage applied, highlighting the area of the depletion region and the neutral regions. Under the scheme of the junction, plots of the charge density, the electric field and the voltage are presented. 36

Figure 2.7 Schemes of hybrid structures with binary CS grown on a Si substrate. The left side scheme presents a normal crystal free of defects. The right side scheme shows the antiphase domains and antiphase boundary produced at the monoatomic step of the Si substrate. 37

Figure 2.8 The carbon allotropes: graphite, graphene, nanotube, fullerene and diamond. Graphene is a monolayer of graphite and a nanotube is a graphene sheet rolled up. 38

Figure 2.9 General scheme of Transition Metal Dichalcogenides (TMDCs) monolayers.[36] 39

Figure 2.10 Calculated band structure of bilayer MoS_2, WS_2 and WSe_2. The bands forming the conduction band minimum and valence band are indicated in orange.[37] 40

Figure 2.11 Force vs distance plot. (https://www.doitpoms.ac.uk/tlplib/afm/tip_surface_interaction.php) 42

Figure 2.12 a) MultiMode SPM. b) Quad photodetector arrangement. [43] 43

Figure 2.13 Scheme of the springs model for the sample cantilever interaction. 44

Figure 2.14 (a) For small ultrasonic amplitudes such as a_0, the normal force averaged in time over one ultrasonic period is equal to the initial value F_1 as the force curve is linear in the first approximation. For the threshold amplitude a_1, the average normal force (averaged over the broken line) has a discontinuity that depends on the adhesion hysteresis. The contact is broken for part of the ultrasonic cycle. (b) Schematic normal deflection response induced by an out-of-plane ultrasonic vibration of the sample.

There is a variation of the normal deflection only for ultrasonic amplitudes higher than the threshold amplitude a_1. At this amplitude value, a discontinuity in normal force and normal deflection occurs (force jump). [55] 46

Figure 2.15 Optical schematic of typical components of a single-point vibrometer (Mach-Zehnder). A laser beam is produced by the LDV is focused on a vibrating surface and reflected from there. The Doppler shift in frequency of the reflected beam is used to find out frequency and amplitude of the vibrating target. [74] 54

Figure 2.16 Preparation of organic solar cells cross sections by (a) FIB milling, (b) cleavage and (c) microtome cutting is depicted (view perpendicular to the exposed cross-section); SEM images of (d) FIB milled, (e) cleaved and (f) microtome cut cross-sections. [75] 56

Figure 2.17 Scheme of the single-end clamped beam. 58

Figure 2.18 Plot of $f k n L = \cos k n L \cosh k n L + 1$, with the numerical solution superposition for $f k n L = 0$. 59

Figure 3.1 Exfoliated graphene transferred onto a Si substrate with top 290 nm SiO_2 layer. Magnification x20. Thin multilayer graphene flakes present pink-like color. Thick flakes are displayed in yellow tones. 62

Figure 3.2 2D materials transfer station. a) Front view of the transfer station, showing the setup with the optical microscope and the micro-positioners. b) Lateral view of the stage with a glass slide, where is placed the tape with 2D materials. In addition, the sample stage and its micro-positioners, which allow the tilt and position control, are also shown. There is a Peltier stage on top of the sample stage, to heat up or cool down the sample, to easy the 2D-materials transfer. 63

Figure 3.3 Controllable growth of "wedding cake" structure and spiral structure of WS_2. (a) Illustration of the CVD experiment setup for TMDCs synthesis. (b) A schematic of nanoplates illustrate the distribution of wedding cake structures and spiral structures in different deposition regions. (c) Trends in the synthesis conditions for forming the wedding cake structures versus the spiral structures. Schematic illustrations of layer-by-layer (LBL) growth mechanism and (e) screw-dislocation-driven (SDD) growth mechanism. [84] 65

Figure 3.4 (a) Schematic illustration of the experimental setup for WS_2-MoS_2 heterostructure growth by water-assisted chemical vapour transport. The MoS_2 precursor was placed upstream of the WS_2 precursor. When MoS_2 precursor was pushed into Zone 2, WS_2 precursor would simultaneously be pushed into Zone 3, which is downstream of the substrate. (b-d) The growth pathways of WS_2 and WS_2-MoS_2 heterostructures via lateral epitaxy leading to three common types of heterostructures. [85] 66

Figure 3.5 Optical images of (a) lateral heterostructure of MoS_2 and WS_2; (b) WS_2 vertical heterostructures. 66

Figure 3.6 Schematic diagram of MQW structure scheme grown on Si substrate with the top layer of uncapped InAs QDs, followed: by 2 nm InGaAs, 50 nm GaAs, 100 nm AlGaAs, 5 periods of GaAs/InGaAs/InAs QDs/ InGaAs, 50 nm GaAs, 100 nm AlGaAs, 300 nm, 2 sets of 5 periods of InAlAs/AlAs separated by 300 nm GaAs, 1000 nm GaAs and 4 periods of GaAs/AlgaAs. 68

Figure 3.7 Scheme of a lateral view of a VCSEL device. 70

Figure 3.8 (a) Crystallography and c-axis orientation for the growth of GaN layers. Grey scheme shows polar growth with c-axis normal to the layer surface; the growth plane is the (00-01). Red and blue schemes show non-polar growth with c-axis parallel to the layer surface; the growth planes are m-plane

(10-10) and a-plane (11-20) respectively. Green, purple and yellow schemes show semi-polar growth with the c-axis incluned with respect to the layer surface; these present the growth planes: (20-11), (10-11) and (11-22), respectively. (b) Wurtzite structure of GaN. [87] 71

Figure 3.9 SEM image of GaN NWs onto Si substrate. 72

Figure 3.10 SEM image of the silicon nitride membrane. (Agar Scientific) 73

Figure 3.11 (a) and (b) SEM images of a 76 kHz, 393 kHz, multimode quartz TF, showing the two tines in detail. (c) $LiNbO_3$ TF scheme, showing the electrodes shape and location in detail. [93] 74

Figure 3.12 Schemes of the top view of the TF with the representation of the electric field in the $LiNbO_3$ TF (a) bare and (b) with Au coating, respectively. 75

Figure 3.13 SEM image of a typical contact mode cantilever from Budget Sensors (ContAl-G 13kHz). 76

Figure 3.14 Images of the EM-TIC020 or EM-TIC 3X. https://www.leica-microsystems.com/products/sample-preparation-for-electron-microscopy/p/leica-em-tic-3x/) 77

Figure 3.15. Parts of the ion source cartridge. Scheme of the three guns with the focused beams onto the sample. (http://smif.pratt.duke.edu/sites/smif.pratt.duke.edu/files/operating/EMTIC3X_16771403_OM_EN_07_17.pdf) (http://www.semat.lab.uminho.pt/Documentos/TIC%203X%20-Ion%20Beam%20Milling.pdf) 78

Figure 3.16 Scheme of the sample mounted on the holder in the mask-beam configuration. Real image of the three beams focused on the sample.. 79

Figure 3.17 Spin-on-glass (SOG) processing. A drop of SOG is deposited using a pipet. Then, the sample is spun to create a uniform thin film. Finally, the sample is baked to remove the solvent and solidify the SOG. 80

Figure 3.18 SEM image of a hole patterned in the SiO_2/Si substrate by photolithography. 81

Figure 4.1 Probe-holder for electric measurements. With BNC cable for the active drive or detection. An additional connection to the ground.. 84

Figure 4.2 General setup for electrostatic SPM measurements. KPFM, D-EFM and SSRM setups are included in the scheme. The electrical excitation applied to the sample is represented by an orange cable, which connect the lock-in output to the sample. This is used all the setups. KPFM and D-EFM setups use the tapping (blue cable) and deflection (red cable) outputs from the breaking box, to trigger the signal and monitoring of the cantilever response, respectively. In addition, KPFM uses the purple cable connecting an auxiliary output of the lock-in, which provides the DC voltage to nullify the tip-sample electrostatic force, to the add input of the driving output. SSRM setup is represented with the green cable, which connects the cantilever (by the electric holder) with the I-V converter scheme.... 86

Figure 4.3 Frequency spectrum from a fast Furier transform (FFT). The central peak (indicated by the yellow arrow) displays the tapping frequency. The red arrows point to the sidebands' peaks of the modulation frequency. 87

Figure 4.4 Scheme of the AFM setup with the additional piezotransducer under the sample for the excitation of ultrasonic vertical vibrations. The ultrasonic excitation applied to the piezotransducer is driven by a wave generator, which is also triggering the lock-in amplifier for the deflection signal monitoring. The lock-in is fed by the cantilever deflection signal, extracted using a breaking box. The outputs of the lock-in are recorded using two of the auxiliary inputs of the AFM controller. 88

Figure 4.5 a) Metal discs (I), ceramic pieces (II) and piezotransducers (III). b) Piezo-stage for ultrasonic excitation – 4 MHz. c) Home-made heterodyne force microscopy (HFM) probe holder with BNC connector. 89

Figure 4.6 Experimental setups of M-UFM. The simplest setup, using the zi-HF2LI is represented with the wires with dashed lines. The setup with the wave generators, the mixer and lock-in are wired with the continuous lines. 92

Figure 4.7 Principle of piezoelectric force microscopy (PFM). a) Electric field aligned parallel to the spontaneous polarisation leads to a lifting of the cantilever due to the d_{33} effect (out-of-plane signal). It causes additional lateral contraction of the ferroelectric via the d_{31} piezoelectric coefficient. b) The antiparallel alignment of the electric field and the spontaneous polarisation leads to a vertical contraction and a horizontal expansion of the ferroelectric. c) and d) Electric field applied orthogonal to the polarisation results in a shear movement due to the d_{15} coefficient. This movement causes a torsional deformation of the cantilever forcing the laser spot to move horizontally (in-plane signal). . 93

Figure 4.8 Schematic Polytec Laser Doppler Vibrometer. 96

Figure 4.9 Laser Doppler vibrometer images a) Setup for OFV-2500 and OFV-2750 controllers. b) Setup of UHF-120. (Polytec, Germany) 97

Figure 5.1 a) Optical image of a force modulation cantilever (Multi75, Budget Sensors) with the point measurements superposed. Magnification x20. b) Schematic of the free resonance (f_1) and the first overtone (f_2) of a cantilever. c) Plot of the displacement of the cantilever in the centre and at the end, while sweeping in frequency the driving of a piezotransducer inserted under the cantilevers. 101

Figure 5.2 LDV displacement maps of a Multi75 cantilever at the fundamental (f_0=84 kHz) and first overtone (f_1=425 kHz) frequencies. Vibrations excited via an externally driven piezotransducer, inserted under the cantilever chip. Colour scale indicate maximum positive desplacement in the out-of-plane direction with dark blue and maximum in the negative direction with dark red. 102

Figure 5.4 a) Schematic of a quart TF side view. The laser spot indicates the place where the LDV laser was focused on the measurements. b) Top view of the TF tine with the velocity vectors of the rotational modes displayed. 106

Figure 5.5 Velocity and current plots as a function of the driving voltage. The linear dependence of both vibrational modes, flexural and torsional, allowed us to establish the calibration for the ULT measurements. 108

Figure 5.6 Electrical response of the flexural and torsional modes. Comparison between the response of the bare TF and the Au-coated ones. 109

Figure 5.7 Plot of the TF displacement vs current. The plot indicates an almost perfect linear dependence. 110

Figure 5.8 A comparison of the resonance curves from the TF response, with and without the tip attached to the end of the TF. The results show the shift in frequency and the significant drop in the amplitude of the response, around two orders of magnitude. 111

Figure 5.9 Experimental setup for the immersed measurements using the MultiMode scanner and the $LiNbO_3$ TF as a piezoelectric probe. 111

Figure 5.10 Electrical response of the $LiNbO_3$ TF in air (red) and water (blue). 112

Figure 5.11 Topography, PID drive voltage and δf maps of an ITO sample made the TF probe method. Images of the top row were made in air and the images of the bottom were made in water. Imaging parameters: TF drive V_{AC}=10mV and phase offset $\varphi=-130^{\circ}$. 113

Figure 5.12 Plot of two resonance peaks of the Si_3N_4 membrane measured via LDV. The peak at 315 kHz correspond with the fundamental mode of the membrane shown in the inset above the peak. The peak at 630 kHz correspond with the second harmonic also shown in the inset above the peak. 115

Figure 5.13 Topography and UFM images of a corner of a Si_3N_4 membrane. The topography image shows neglegible contrast between the suspended and the suported regions of the membrane. Conversely, the UFM image presents clean contrast between the two areas. The dark contrast indicates low UFM response, due to the poor propagation of ultrasounds, and corresponds with the suspended region. 116

Figure 5.14 Comparison of UFM, FMM and M-UFM results for the same area. The dashed lines represent the boundary between the supported and the suspended areas. 117

Figure 5.15 a) Image of 1D scans across the membrane while sweeping frequency, from 280 to 380 kHz using FMM setup. b) Image of M-UFM scans using 330, 340, 350 and 360 kHz at the modulation frequency. 118

Figure 5.16 Schematics of the probing of the cantilever across the membrane. The cantilever behaviour is approximated to a spring attached to a mass point. The membrane dynamics are represented as a lever with a mass point at the free end attached to spring. 118

Figure 5.17 Plot of the resonance frequency as a function of the distance from the edge. The plot of the bottom is the first derivative of the top plot. 120

Figure 5.18 Optical images of the patterned substrate with the transfer of multiple multi-layer graphene (MLG) flakes. 121

Figure 5.19 a) AFM topography. b) UFM. c) and d) CR-AFM amplitude and phase respectively at 30.8 kHz. e) and f) CR-AFM amplitude and phase respectively at 57 kHz. g) and h) CR-AFM amplitude and phase respectively at 66.6 kHz. 122

Figure 5.20 Plot of the CR-AFM response as the function of the position r across the hole (horizontal axis, r) and frequency (vertical axis, f_{dr}) with (a) amplitude A as the function of $A(r,f_{dr})$ and (b) $\phi(r,f_{dr})$ phase profile at driving frequency f_{dr} changing from 50 to 69 kHz in 1 kHz steps. 124

Figure 5.21 Resonant frequencies of the cantilever for the first contact resonance mode (n=1) for the different values of the sample stiffness. 125

Figure 5.22 Two typical boundary conditions for the plate suspended over a circular hole. (a) simply supported edges and (b) clamped edges. 127

Figure 5.23 CR-AFM at 62 kHz, amplitude and phase, respectively. 129

Figure 5.24 (a) Matlab modelling of the amplitude response $A(r,f_{dr})$ of the CR-AFM as the function of the radius from the centre of the plate and the driving frequency f_{dr} for the 50 to 69 kHz frequency range, (b) experimental CR-AFM data of the $A(r,f_{dr})$ response for the same frequency range. (c, d) comparison of the simulated and measured one-dimensional profiles *A(r)* at the frequencies below and above contact resonance frequency for the solid contact. (e) Experimentally measured CR-AFM response in the centre of the MLG plate vs supported graphene, the frequency shift allows for precise determination of the stiffness of the GR membrane. 131

Figure 5.25 One-dimensional scans across the ripples while sweeping frequency from 60 to 68 kHz. 132

Figure 6.1 Triangular islands of WS_2. Magnification x20. (False colour scale) 135

Figure 6.2 Image in a) shows the topography of a WS_2 pyramidal heterostructure over a continuous layer of the same material. Image b) shows the UFM image of the region in a) clearly displaying low stiffness (dark contrast) in the centre of the structure. Image c) and d) are the amplitude and phase of HFM images of the same region, respectively. 136

Figure 6.3 Image a) shows the topography of multiple WS_2 vertical heterostructures where the whole region of the map is fully covered by a continuous layer of the same material. Image b) shows the nanomechanical map made by UFM of the same region shown in a). In images a) and b) the dashed lines are superposed, where the profiles show in the plots c), d) and d) were extracted. Plot c) presents profile #1, where the step in the topography corresponds with the change in contrast. Plot d) shows profile #2 where UFM contrast is produced without apparent topographical feature. Plot e) displays profile #3 where mechanical change is produced with no direct topography link, presenting a possible change in the crystallographic orientation. 138

Figure 6.4 Image a) is a 3D render of the topography with superposed UFM contrast of the sectionioned WS_2 heterostructure. The thickness of the layers with different UFM contrast are also superposed on the map. Image b) shows the UFM image of the sectioned WS_2 vertical heterostructure. The image has superposed the labels, I, II, III, IV and V, which are used to identify the areas with different UFM response. Plot c) and d) present the profiles of the topography and UFM response, respectively, extracted in the same region. 139

Figure 6.5 Plot of the normalised values of Young's Modulus to the Si for the UFM response and the theoretical values inferred from the material Young's Modulus and experimental conditions. 141

Figure 6.6 Images a), b) and c) show the topography, D-EFM amplitude and phase maps, respectively. Plot d) shows the profiles extracted from the images a), b) and c). 142

Figure 6.7 Optical microscope image of the WS_2-MoS_2 lateral heterostructure. Magnification x40. ..143

Figure 6.8 Image a) topography of the rippled area. Image b) shows the of the profile extracted from a) in the area highlighted with the yellow dashed line. In the same plot the simulation of the surface undulation is also superposed. Images c) and d) show the HFM amplitude and phase, respectively. e) shows the plot of the FFT of the profile extracted from a) in the area highlighted with the yellow dashed line. 145

Figure 6.9 a) and b) are the topography and UFM maps of the MoS_2 region of the lateral heterostructure. Plot c) shows the profiles extracted from topography and UFM response in the region displayed with the dashed black lines in images a) and b). Plot d) shows the correlation between the thickness of the layers and the UFM nanomechanical response. 147

Figure 6.10 a) Topography and b) SThM response in the 3rd harmonic maps of the boundary of the structure. c) SThM image in the 1st harmonic response. d) plots of the topography and SThM profiles extracted from the images a) and b) in the area presented with the white dashed line. 148

Figure 6.11 Plot of the RMS response of the SThM measurements in the 1st and 3rd harmonic for the different materials and interfaces. 149

Figure 6.12 Optical image of the franckeite flake and a zoomed-in section of the area with the thinnest region. 150

Figure 6.13 Images a) topography and b) UFM maps of an exfoliated franckeite flake. Several thicknesses can be observed with different mechanical responses. As the franckeite thickness increases, its stiffness increases as well. Images c) and d) show the plots of profiles 1 and 2 respectively, where topography vs UFM response are compared. 151

Figure 7.1 Sketch of the APB formation in the [111] and [110] lattice planes of the GaP zinc-blende structure due to the presence of mono-layer steps on the Si surface. [139] 155

Figure 7.2 Optical images of the BEXP section of the MQW structure sample. 156

Figure 7.3 a) Profile of the topography of the 3D section. Inset: 3D render of the topography overlaid with KPFM response. b) 3D rendering of the topography, displaying the presence and propagation of APD. c) and d) Topography images of the area of the DFL structure, c) in the presence of APD; d) Sample free of APD. 157

Figure 7.4 a) image of the topography of the rippled InAlAs/AlAs superlattice due to the APD. b) UFM image simultaneously recorded with image a). c) shows the profiles extracted from the images a) and b), the crests in the topography correspond with the InAlAs layers, which show lower UFM amplitude; the AlAs layers present the valleys in topography matching with the higher UFM response. d) shows the comparison of the elastic moduli (C_{11}) of GaAs, AlAs and InAs. 159

Figure 7.5 KPFM images of the InAlAs/AlAs superlattices separated by the GaAs layer. a) Image of a sample free of APD; the darkest contrast represents the InAlAs/AlAs superlattice, GaAs is displayed by the medium and light contrast. b) Image of a sample with APD; InAlAs/AlAs layers are shown darker than the GaAs areas. 160

Figure 7.6 Optical image in the dark field of the VCSEL wafer after BEXP sectioning. 161

Figure 7.7 Topography and KPFM images of the VCSEL (A) section in the area of the active region. Profiles of both images plotted in the graph.. 162

Figure 7.8 High magnification of the topography and KPFM images in the active region area. Plot of the profiles highlighting the 3 QW in the active region with the green arrows. (VCSEL A)........................ 163

Figure 7.9 a) Optical image of the section area of the VCSEL A, with magnification x100. b) Raman map of the VCSEL A extracted in the area highlighted with the black square in a). c) Map of PL response of VCSEL A, covering the whole structure from the substrate to the top surface. The fringes in b) are due to the interference phenomena, rather than picking up individual DBR layers................................. 164

Figure 7.10 SEM images of the GaN nanowires. 165

Figure 7.11 a) image of the topography of the substrate-NW boundary (beginning of the growth) of the sectioned area. b) UFM image of the same area as image a). c) and d) are the profiles extracted from images a) and b) in the highlighted regions with the dashed lines. 167

Figure 7.12 Plot of the effective contact stiffness (E^*) whilst increasing the sample stiffness (E_{sample}) for various tip materials; Diamond, GaN, Si and SiO_2. 167

Figure 7.13 a) topography of the NWs forest embedded in SOG and BEXP nanosectioned. b) KPFM map of the same area of image a). c) and d) topography and KPFM images, respectively, of a higher magnification of one of the NWs, sectioned in the initial part of the growth. e) plot of the profiles extracted from images c) and d). f) scheme of the depletion region formed at the interface between the substrate and the NWs.. 169

Figure 7.14 Total polarisation as a function of the angle in the c-plane. List of polar, non-polar and selected semi-polar planes with inclined angles to the c-plane. [151] 170

Figure 7.15 a) Schematic of a unit cell of wurtzite GaN. The lattice parameters are indicated as a and c. Vectors $a1$, $a2$ and c are the bases in the hexagonal coordinates. b) Schematic of Ga-polar and N-polar GaN structures. c) and d) schematics of Ga-polar and N-polar atomic layers stacking with spontaneous polarisation (Pps) indicated in each case. 171

Figure 7.16 Plot of the frequency sweep of the contact flexural and the torsional resonances. 172

Figure 7.17 Amplitude and phase PFM images of the response of the vertical and lateral PFM modalities, respectively. Profiles of the section presented in the images with the dashed line............................173

Figure 7.18 PFM images of an individual nanowire for different potential offsets, +1 V, 0V and -1 V. 174

Figure 7.19 Schematic analysis of the piezoelectric and electrostatic signal contributions. PE – Piezoelectric response. ES – Electrostatic contribution. Plot a) represents the piezoresponse vectors PE_0 (with red arrows), in the cartesian coordinates and in absence of electrostatic contribution (ES_0 = 0). Also, the representation of the phases of the PE vectors are superposed, represented by yellow and green arcs the positive and the negative responses, respectively. Plot b) shows the PE_1 response with positive electrostatic contribution ES_1. [78] 175

Figure 8.1 Optical images of the VCSEL devices after BEXP sectioning. a) shows the 5x magnification of multiple devices, some of them sectioned in the edge of the sample. b) shows 40x magnification of one of the sectioned devices. 180

1. Introduction

Indeed, size matters [1]. Since the famous speech of Richard Feynman, in which he said: “there’s plenty of room at the bottom” in 1959 [2], nanoscience has become a recognised field of research for scientists with the curiosity to explore and exploit multiple phenomena at the nanoscale. The idea of miniaturisation of systems has opened a number of possibilities to solve today’s problems, such as in the fields of health and technology [3, 4]. Small devices like the micro and nano-electromechanical systems (MEMS and NEMS) are present in many devices that we use on a daily basis, like smartphones, tablets and computers. Nevertheless, size reduction is not a straightforward task. The scaling down of devices results in a very challenging and exciting mission for scientists, in particular when new exotic material properties start to appear. Saying that, one cannot forget graphene, a single layer formed of carbon atoms, as the perfect example of a material with interesting emerging properties at the nanoscale. Since 2004, when Geim and Novoselov first revealed the outstanding electrical properties of monolayer graphene [5], which was rewarded in 2010 with the Nobel prize in physics, an extraordinary family of novel nanomaterials, the so-called two-dimensional (2D) materials, have appeared and thrived. Multiple researchers in the field have demonstrated that these materials can be excellent candidates for the fabrication of nanoscale devices and can provide winning solutions for materials from energy storage to electronics [6, 7]. One of the most remarkable characteristics of the 2D material's layers is that they can be easily stacked and combined, forming new material heterostructures with tailored properties. This is a direct consequence of the out-of-plane van der Waals interaction forces that hold the layers together. The flexibility of the design and fabrication of such heterostructures allows for the tuning of material characteristics, satisfying the complex multiparametric requirements for the development of new technologies and applications [8].

Among all the 2D materials, graphene has been the most widely investigated for its electrical conductivity, mechanical, optical or thermal properties. Graphene has been awarded with the title of the “strongest material”, presenting an in-plane Young’s Modulus of approximately 1 TPa [9]; a high optical transparency determined by fundamental constants [10], and an extremely high thermal conductivity [11], between 2000-5000 $Wm^{-1}K^{-1}$. In particular, the outstanding in-plane stiffness of graphene, together with the low mass of the monolayers, make graphene an ideal material for the fabrication of high-frequency (HF) resonating systems.

With all the advantages of graphene, the absence of an electron bandgap limits its suitability for electronic and optoelectronic applications. In order to fill this void, other materials from the 2D family have been extensively studied. The transition metal dichalcogenides (TMDCs), in particular MoS_2, WS_2 and WSe_2 have gained a lot of attention due to their attractive semiconducting properties with direct bandgap in the visible range (~1-2 eV) [12, 13] suggesting them as excellent candidates for optoelectronic applications. Nevertheless, the fabrication and manipulation of such materials is still very challenging. Thus, major improvements are still needed to achieve quality mass-production rates of the already existing semiconductors commonly used in mainstream microelectronics such as silicon (Si) or germanium. In addition to its semiconducting properties, its abundance and a well-debugged manufacturing process, have allowed Si to achieve one of the leading positions in the electronic and optoelectronic markets for the last three decades. However, compound semiconductors offer solutions beyond the capabilities of Si, in particular as light sources for data communications and lighting, and platforms for efficient high-frequency and -power electronics.[14] Furthermore, the variety of compound semiconductor (CS) materials allows for the creation of complex structures with diverse compositions and dimensionality, from zero-dimension (0D), such as quantum dots, to one-dimensional (1D) nanowires and 2D quantum wells, with their three dimensional (3D) bulk counterparts, expanding the possibilities for potential applications. [15] The integration of CS in Si technologies is a tempting solution, providing both the cost-efficiency of Si platform manufacturing and the unique functional capabilities of CS.[16] Nevertheless, the implementation of these material hybrids presents serious challenges, especially for mass-production, including the defects originated at the interfaces of different materials, and their propagation in the bulk of CS heterostructures, the presence of inhomogeneous strain, and the need to match often-incompatible growth conditions of Si and CS materials. To overcome this, innovative investigation methods with the ability to map physical properties with nanoscale resolution across the 3D structure of CS and Si substrate are required. Currently, the most common methodology used to image these nanoscale defects is the Ga focused ion beam cross-sectioning and TEM analysis, which usually provides structural information of very localised areas of the sample. Whilst offering high-resolution information on the morphology, TEM does not provide representative information of local defects across wide areas of the sample. Furthermore, TEM is not capable of measuring mechanical, thermal and electronic properties of the CS structures. To overcome these issues, the already existing microscopy technologies, such as scanning probe microscopies (SPM) and scanning electron microscopy (SEM), have been essential tools to push forward this development process. However, to successfully exploit these advanced

materials, i.e. 2D materials and CS, and extract all their potential, a full understanding of the physical properties at the nanoscale is required, with adequate techniques and matching sample preparation processes.

One of the main goals of this thesis is to explore the feasibility of existing and novel SPM approaches to study diverse microscale and nanoscale structures of advanced materials. This has been used to allow the nanomechanical study of 1D and 2D oscillating structures; the investigation of physical properties in supported structures of 2D materials; and exploration of defects in CS structures. The composition of the thesis and the organisation of the chapters are discussed below:

- Chapter 2 reviews the literature regarding the main concepts behind the topics relevant to this work, namely physical properties of representative materials, nanoscale characterisation methods and micro/nanoelectromechanical systems (MEMS/NEMS) devices.
- Chapters 3 and 4 are dedicated to the materials and the measurement methodology. They contain detailed descriptions of materials, samples and devices studied in the experimental results in chapters 5 through 7; as well as the methods used in the preparation and the nanoscale characterisation of the samples, including newly developed techniques and processing.
- In chapter 5, we develop a theoretical analysis in parallel with the experimental evidence, to report on the study of free resonating structures. The structures analysed include AFM cantilevers and tuning forks that effectively are 1D oscillating systems; followed by Si_3N_4 and graphene drums as 2D vibrating structures. These structures were investigated using laser Doppler vibrometry (LDV) and dynamic AFM modes, including a novel method called modulation ultrasonic force microscopy (M-UFM).
- In chapter 6, through the use of ultrasonic microscopies, such as UFM and HFM, we were able to investigate subsurface defects in vertical heterostructures of transition metal dichalcogenides (TMDCs) based on the variation of the mechanical stiffness. Furthermore, we explore 3D sections of 2D materials' heterostructures, using the beam exit cross-sectional polishing (BEXP) technique, mapping directly the physical properties of the internal structure, using various SPM methods. In addition, we examined the variation of the

mechanical stiffness in lateral heterostructures of TMDCs with formed ripples at the heterostructure interfaces.

- Using concepts and systems developed before, in chapter 7 we review the investigation of material defects in compound semiconductor structures using a combination of BEXP with the functional SPM analysis. The samples studied are layered structures such as multiple quantum wells (MQW) and vertical cavity-surface emitting-lasers (VCSELs). Another part of this chapter is dedicated to the electromechanical characterisation of the internal structure of 1D GaN nanowires. The combined study shows great potential of these methods in advancing the understanding of intrinsic properties of complex CS nanostructures.
- Finally, a summary of main conclusions and suggestions for further work is presented in chapter 8.

2. Literature review

2.1. Introduction

Over the past decades, the field of nanotechnology has been dedicated to the miniaturisation of systems of interest and the understanding of physical phenomena emerging at the nanoscale. The downscaling of devices offers multiple possibilities in the hunt for smaller and more efficient electronic devices. New challenges linked to size reduction, such as electromigration of materials or electron confinement, have motivated the exploration of new materials and structures. For example, since the discovery of graphene, two-dimensional (2D) materials have become promising for the fabrication of electronic and optoelectronic devices, due to their reduced size and the possibility of tuning their properties. In addition, enormous advances have been achieved in the nanotechnology field since the invention of adequate methods for characterisation and nanoscale studies of the physical properties and atomic manipulation, including scanning probe microscopies (SPM).

This chapter outlines the theoretical foundations used to understand and explore the physical properties of materials and the behaviour of diverse micro- and nano-structures at the nanoscale. It has been divided into three parts, starting with the description of materials and their properties, followed by the existing tools for the functional probing of diverse physical phenomena at the nanoscale. The final section explores the background theory essential for the characterisation of micro- and nano-electromechanical systems (MEMS and NEMS) and mechanical resonator systems.

2.2.Physical properties and structure of solid state materials

Quantum mechanics establishes that an isolated atom has discrete energy levels occupied by electrons. However, in a situation where multiple atoms form a solid, the discrete energy levels overlap and spread out, creating bands. In the case of a single crystal, the band structure is made by the valence band, the highest electron-occupied energy band at absolute zero temperature, and by the conduction band, the lowest unoccupied energy band. [17] In between the conduction and valence band is a forbidden region called the "band-gap". The band structure determines the electrical conductivity of solids, being unique for each material. Therefore, solids can be categorised by their electrical conductivity in three groups: conductors, semiconductors and insulators. The conductor group is formed by metals and semimetals; their electronic bands, conduction and valence, are semi-occupied and overlap, letting the charges flow along the materials. When the electronic bands, up to the valence band, are fully occupied and the bandgap between the conduction and the valence band is large enough, the electrons are not able to jump from the valence band to the conduction band by thermal excitation. At this point the solid can be considered as an insulator. These two examples are the extreme conditions, whereas there is an intermediate situation in which the materials are not overlapping between the conduction and valence bands, but the

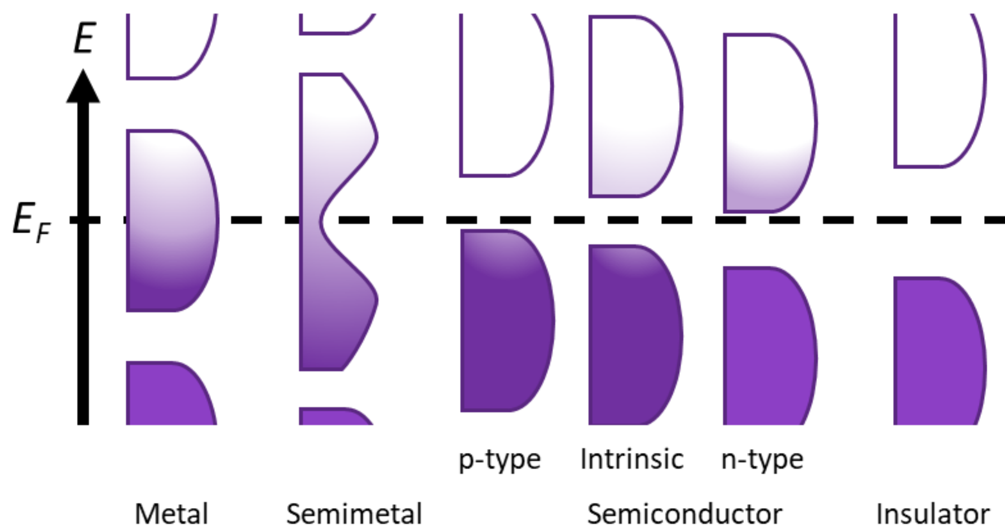

Figure 2.1 Scheme of the different filling of the electronic states in various types of materials at equilibrium. Height is energy while width is the density of available states for a certain energy in the material listed. The shades follows the Fermi-Dirac distribution (dark purple means all states filled, white means no state filled). In metals and semimetals the Fermi level E_F lies inside at least one band. In insulators and semiconductors the Fermi level is inside a band gap; however, in semiconductors the bands are near enough to the Fermi level to be thermally populated with electron or holes.

bandgap is small enough to allow the charges to jump from the valence to the conduction band, and vice versa. These materials are called semiconductors. Owing to the vicinity of the bands, small quantities of energy, such as by thermal excitation or light absorption, are sufficient to allow the charges to change band. The pure semiconductor materials are formed from elements of column IV of the periodic table, such as Silicon (Si) and Germanium (Ge). However, the list of semiconductor materials is not limited to that group, as there are multiple combinations of semiconductors, so-called compound semiconductors (CS), formed by the combination of two or more elements, sometimes with variable quantities of the different species. This group of materials and their numerous applications will be examined in detail in the following sections and chapters.

Semiconductors can be classified into two subgroups in terms of their bandgap type, either direct or indirect bandgap. Direct bandgap semiconductors have the minimal-energy state in the conduction band and the maximal-energy state of the valence band with the same momentum. Whereas, for indirect bandgap semiconductors, the valence band maximum differs in momentum from the conduction band minimum. Hence, in the electron-hole recombination processes of indirect bandgap semiconductors, additional momentum is required to conserve the total momentum.[18] Therefore, in addition to the electrical properties, the band structure of semiconductors also determines their optical properties.

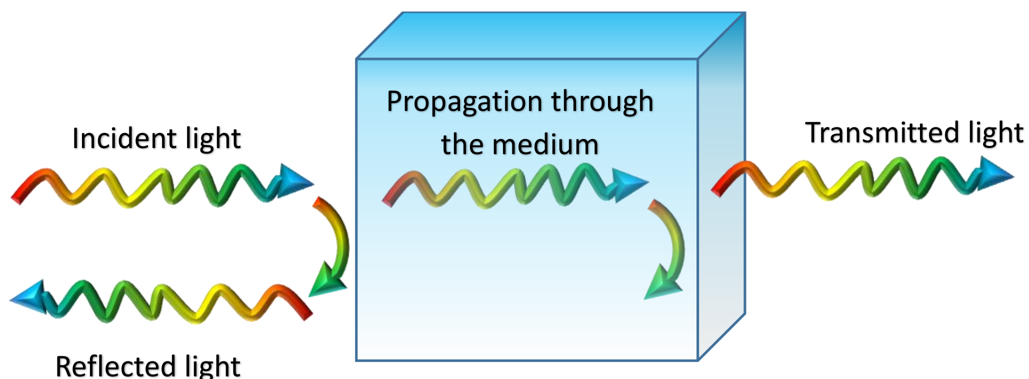

Figure 2.2 Reflection, propagation and transmission of a light beam incident on an optical medium.

The optical properties of a material are determined by the way light interacts with the solid. The wide range of optical phenomena observed in solids can be classified in four categories: reflection, transmission, emission and absorption. Linked to the propagation, other linear optical phenomena which can occur while light propagates through an optical medium are refraction, luminescence and scattering. In particular, the phenomenon used later in this report, luminescence, is the process of spontaneous emission of light by exciting atoms in a

material or substance. [19] Sub-categories of the luminescence are photoluminescence (PL), which is the process in which a molecule or solid absorbs a photon, exciting an electron to a higher electronic state and, upon relaxing to the lower energy state, a second photon is radiated; and electroluminescence (EL), which is a combination of electrical and optical phenomena in which the material emits light in response to the passage of an electric current or a strong electric field.[12] These phenomena are purely dependent on the band structure of the solid.

Of the many physical properties of materials, the mechanical ones are of enormous importance since they regulate the material stability under acting forces. There is a vast list of mechanical properties, but the ones that are directly linked to the thesis topic are stiffness and elasticity. The stiffness can be explained as the ability of a material to resist deformation in response to an applied force and the elasticity is the ability of a solid to resist a distorting influence of stress and to return to its original size and shape when the stress is removed. There are several parameters which characterise the elasticity of a material, such as Young's modulus, the shear modulus and the bulk modulus. The Young's modulus, E, of a material describes the ratio between the stress, σ, (force per unit area) and proportional deformation or strain, ε, (see eq. *1*). Therefore, giving an uniaxial stress to the solid, in other words, applying tensile or compressive forces, the material deformation depends on the material stiffness (see Fig 2.3.a), and

$$E = \frac{\sigma}{\varepsilon}. \qquad (1)$$

The shear modulus G is described as the relationship between shear stress τ_{xy} and the shear strain γ_{xy} by

$$G = \frac{\tau_{xy}}{\gamma_{xy}}. \qquad (2)$$

This modulus is related to the deformation of the solids when bodies suffer antiparallel forces applied in opposite faces, see Fig. 2.3.b.

The bulk modulus is the resistance of a substance to compression, its inverse being the compressibility. Therefore, the analytical expression of the bulk modulus B relates the pressure P with the volume V by

$$B = -V\frac{dP}{dV}. \qquad (3)$$

The first two parameters, E and G, may depend on the orientation of the material. Therefore, tensor representation is required to express the stress-strain relations using the elastic modulus tensor C_{ijkl} or the elastic compliance tensor S_{ijkl} as

$$\sigma_{ij} = C_{ijkl}\varepsilon_{kl} \qquad (4)$$

$$\varepsilon_{ij} = S_{ijkl}\sigma_{kl} \qquad (5)$$

in the linear limit of low-stress values.[20]

Isotropic materials, such as most metals and ceramics, have the same mechanical properties in all directions. On the contrary, mechanically, anisotropic materials work differently, depending on the direction of the applied forces. A clear example of highly anisotropic solids is the group of two-dimensional (2D) materials which are made by atoms that are covalently bonded in the plane, whilst the interlayers are linked via weak van der Waals forces. This difference in the atomic bonding causes enormous differences in the in-plane and out-of-plane mechanical properties. Probably, the best example of a mechanically anisotropic material is graphene, which is one of the strongest and stiffest materials with an in-plane Young's modulus for a monolayer in the absence of defects. At the same time, the few-layer graphene Young's modulus is 36 GPa [9, 21]. Moreover, the weakness of the interlayer interactions allows easy exfoliation and layer sliding under low shear stress, producing lubricant effects. It is necessary to mention that the anisotropy not only affects the mechanical properties, it equally concerns the other physical properties of materials, such as thermal or electrical transport. In addition to the anisotropy, an essential factor in the physical properties of materials is the presence of defects. However, prior to considering the materials' defects, it is convenient to describe the physical property resulting from the electrical and mechanical coupling, namely piezoelectricity.

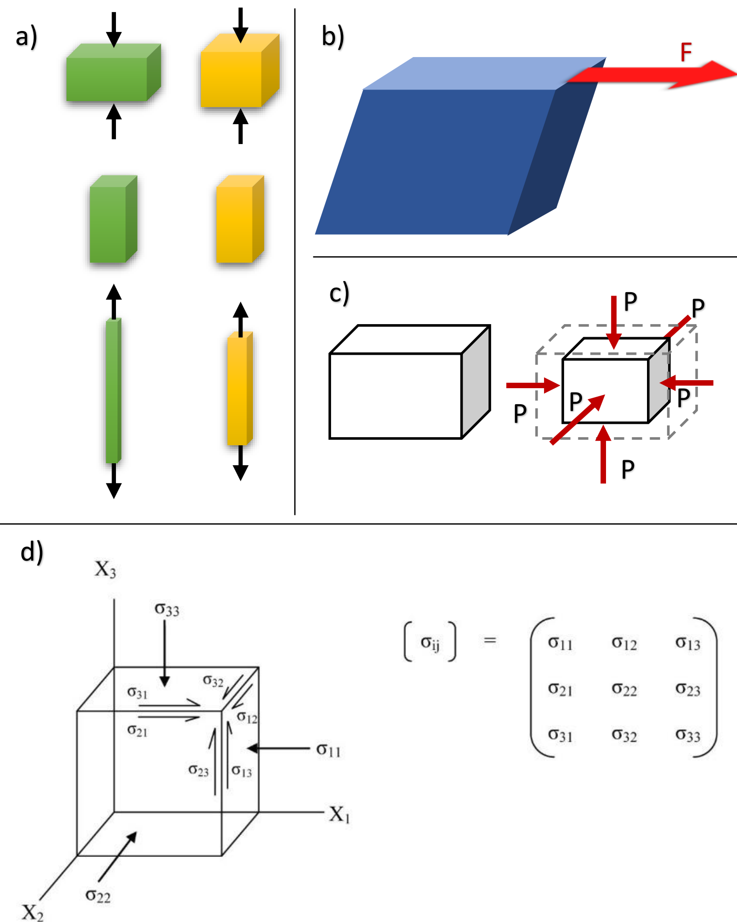

Figure 2.3 a) Comparison of material deformation for soft (green) and a stiff (yellow) materials. b) Deformation of a solid under shear strain by a force, *F.* c) Uniform compression of a solid under pressure, *P*. d) Illustrates a unit cube of material with forces acting on it in three dimensions and the stress tensor, σ_{ij}.

Piezoelectricity describes the ability of materials to develop an electric displacement that is directly proportional to an applied mechanical stress. The piezoelectric effect is a reversible process; it means it is possible to generate an internal mechanical strain from an applied electrical field and vice versa. This property appears in crystals, ceramics and biological matter, such as bones. In crystalline materials, piezoelectricity is limited to certain crystallographic symmetries, with only non-centrosymmetric crystals being piezoelectric. [22]

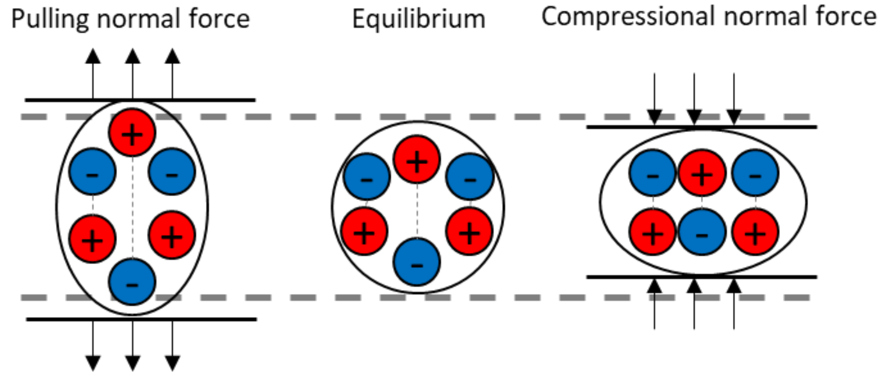

Figure 2.4 Illustration of the piezoelectricity concept. In piezoelectric crystals, the application of an expansive (pulling) or compressive (compressional) force results in a change of the distribution of dipole moments. This causes a change in the surface charge, which is proportional to the applied force [23].

When a piezoelectric crystal is subjected to a mechanical stress (compression, pulling or torsion) the molecular dipole moments re-orient themselves, creating a variation in the surface charge density and, consequently, a voltage difference. Analogously, when the piezoelectric material is exposed to an electric field, the dipoles slightly change their shape, changing the dimensions of the material (see Fig. 2.4).

Under small field conditions, the constitutive relations for piezoelectric materials can be written as

$$D_i = e_{ij}E_j + d_{im}^{d}\sigma_m \quad (6)$$

$$\varepsilon_k = d_{jk}^{c}E_j + S_{km}\sigma_m \quad (7)$$

where D_i is the electric displacement, ε_k is the strain, E_j is the applied electric field and σ_m is the stress. The piezoelectric constants are the dielectric permittivity e_{ij}, S_{km} the elastic compliance, d_{im}^{d} and d_{jk}^{c} are the direct (d) and converse (c) piezoelectric coefficients, respectively.[24]

The last physical properties we would like to describe are related to thermal transport. The thermal properties of solids depend on the ability of a material to transfer heat. Heat transfer is subject to energy transfer and can occur in many mechanisms, such as conduction, convection and radiation processes. In the case of macroscopic solids, heat transfer is attributed to energy conduction through phonons and electrons. Phonons are quantised modes of vibrations and, in the case of insulating or semiconducting crystals, the phonon-transferred heat is transported through the atoms oscillating around the equilibrium position

in the lattice. Nevertheless, the miniaturisation of the systems requires the consideration of other heat transfer mechanisms, due to phonons behaving dissimilarly in the micro- and macro-scale. Diffusive heat transport has to be considered for macroscopic studies, with heat transfer governed by the Fourier equation $\phi = -k\nabla T$, where ϕ is the flux, k is the thermal conductivity and T the temperature. In nanoscale heat transport, the phonons behave as particles and/or waves, involving ballistic propagation, scattering and interference events. Conversely, in metals, the main heat transfer is attributed to electrons instead of phonons. Equal to the rest of the physical properties, thermal phenomena are also highly dependent on the anisotropy of the material and the presence of defects.

Crystalline solids present periodic structure; however, in most cases of real crystals, the structure contains a variety of defects, which determine the physical properties of the materials. These defects can be classified into four groups:

- Point defects, such as interstitials, vacancies and antisites.
- Line defects, described by the variety of dislocations.
- Planar defects, such as grain boundaries, stacking faults and interfaces.
- Volume defects – voids and precipitates.

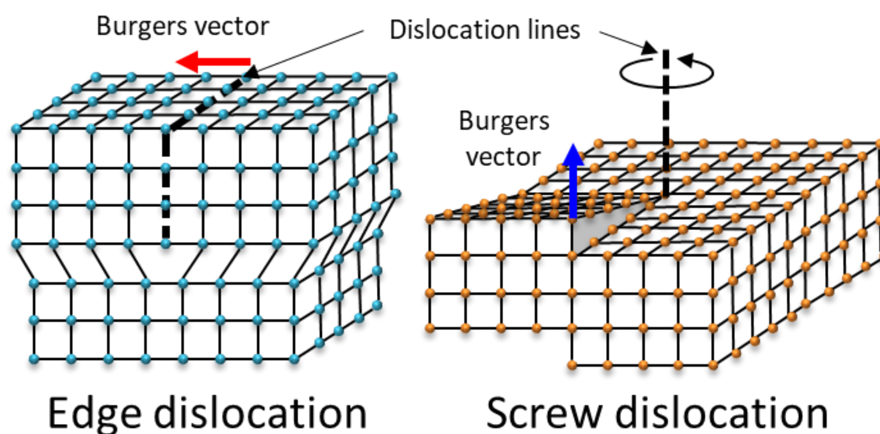

Figure 2.5 Schematic diagrams showing an edge dislocation (left) and a screw dislocation (right). The dislocation lines are highlighted with dashed thick black lines. The Burgers vectors are represented by a red and blue arrows, for the edge and the screw dislocations, respectively.

As was previously mentioned, the modification of the crystalline structure due to the presence of defects defines the properties of the material. This modification can be accidental or voluntary, creating a new research field: defect engineering, in which defect control is essential for the mechanical, electrical, optical and thermal properties of the materials.

For linear defects, there are two major types: edge and screw dislocations. The edge dislocation is formed when an extra plane of atoms is intercalated in the crystal, distorting adjacent planes of atoms. The screw dislocation is formed by the atomic plane following a helical structure around the dislocation line. Schemes of both types of dislocations are presented in Fig. 2.5. The result of the combination of both dislocations, edge and screw, becomes the most typical linear defect in real solids, namely “mixed dislocations”. The distortions of the crystal lattice resulting from the dislocations are denoted by two properties - the dislocation line direction and the Burgers vector. In edge dislocations, the Burgers vector is perpendicular to the line direction, contrary to the screw dislocation in which the direction of the vector is parallel to the line direction. The resulting distortion of the lattice generates a structural stress-field, which is revealed in the physical properties. [25]

2.3. Bulk semiconductors and insulators

As explained in the previous section, the presence of a forbidden energy gap in the band structure is the key characteristic of the electronic configuration of semiconductors and insulators. This section will detail some of the physical properties of materials belonging to the semiconductor and insulator groups.

2.3.1. Group IV – Silicon and silicon compounds.

Silicon is a single element semiconductor material. It is the 14th element in the periodic table. Due to its electronic configuration, the hybridisation of 3s and 3p orbitals in 4 tetrahedral 3sp orbitals is the most stable configuration. This results in a bulk crystal structure formed by covalent bonds between the Si atoms with the characteristic diamond cubic lattice.

Silicon is extensively used by the electronic and photovoltaic industry due to the fact that it is one of the most abundant elements on Earth and can be produced in the monocrystalline silicon boules by Czochralski process. These two factors place Si as a material with reasonable performance for the required applications.

Regarding the physical properties of silicon, we can highlight that, mechanically, it is a reasonably robust semiconductor, when compared with other species and their compounds. Si Young's Modulus is defined by the crystallographic orientation, with E_{001}=129.5 GPa, E_{110}=168 GPa and E_{111}=186 GPa. Its Poisson's ratio is also dependent on the orientation, taking values from ν=0.22 to ν=0.28. [26] However, it is not its mechanical properties which makes silicon very attractive for electronic applications. Silicon has an indirect bandgap in the band structure, which means that a phonon is needed to emit a photon by transfer of the electron from the conduction to the valence band. The bandgap value of intrinsic Si is 1.1 eV at 273 K. To change the electrical properties of Si, its wafers are commonly doped with other elements, such as boron, aluminium, gallium and indium for the p-type doping and by phosphorus, arsenic, antimony, bismuth and lithium for the n-type.

Silicon can also form compounds, such as silicon dioxide (SiO_2), silicon nitride (Si_3N_4) and silicon carbide (SiC), offering completely different properties from the pure material. In the case of silicon dioxide, its physical properties vary considerably with the crystallinity. For example, one of the multiple crystalline forms of silica is the well-known quartz, α-quartz being the most stable configuration at room temperature, consisting of a three-dimensional network built by interconnected SiO_4 tetrahedrons. This material is prized as a piezoelectric material for the fabrication of piezoelectric actuators, such as tuning forks (TF) and quartz crystal

microbalances (QCM). The electromechanical properties of quartz crystals can be characterised by its piezoelectric coefficient: e_{11}=0.151 C m^{-2} and e_{14}=-0.061 C m^{-2}. [27] The nitride compound, Si_3N_4, is used in multiple sectors of the industry, such as the fabrication of engine parts, bearings, high-temperature applications, orthopaedic applications, metal working and cutting tools, electronics, and MEMS/NEMS fabrication of membranes and cantilevers. Similarly to the oxide, the Si_3N_4 can be synthesised in different crystallographic forms and phases, α and β being the easiest forms to make. The Young's Modulus of Si_3N_4 is considerably higher than the pure silicon, varying from 166 – 297 GPa, equally dependent on the crystallographic orientation. Electrically, this material is categorised as an insulator, with a resistivity between 10^8 and 10^{13} Ω m, and its dielectric constant between 9.5 and 10.5. [28] Si_3N_4 is characterised by its low thermal conductivity, with values in the range of 10 – 43 W m^{-1} K^{-1}.

2.3.2. III-V Compound Semiconductors

In the quest for new properties, novel materials and their compounds are investigated to accomplish demanding requirements. The family of compound semiconductors (CS) has demonstrated to offer promising candidates for multiple electronic and optoelectronic applications. These compounds are formed by the combination of elements from groups II and VI or III and V of the periodic table, in the case of the binary CS, or the CS alloys, like ternary, quaternary and quinary, multiple combinations of the groups II-VI and III-V, varying the concentration of the different species to tune the properties. Whilst the CS exhibit superior physical properties to silicon for optoelectronic devices, the complexity of the manufacturing and toxicity of some of these compounds have hindered their implementation in the fabrication of new electronic devices. Nevertheless, recent advances in this industry have made possible their implementation in the fabrication of some devices. The methodologies used in the growth of CS, such as molecular beam epitaxy (MBE) or chemical vapour deposition (CVD), offer precise control in the thickness and purity of the materials, allowing the stacking of multiple layers to create complex device structures.

One of the typical structures formed in the stacking of different layers is the p-n junction, where n-type and p-type semiconductors are in intimate contact. This contact creates an interface between the two sides of the junction, which allows free charge exchange across the boundary. When the p-n junction is being formed, charge diffusion occurs, with electrons diffusing from the n-type to the p-type region, and inversely, holes diffusing from p-type to the n-type region. When equilibrium is attained, the Fermi level of both regions is

constant across the junction. It is necessary to highlight that far away from that interface, the properties of the semiconductors remain the same as in the case of isolated semiconductors. Near to the junction, no mobile carriers exist in the equilibrium, known as "depletion region". Far from the junction, is the quasi-neutral region, where the carrier concentration is equal to the dopant concentration.

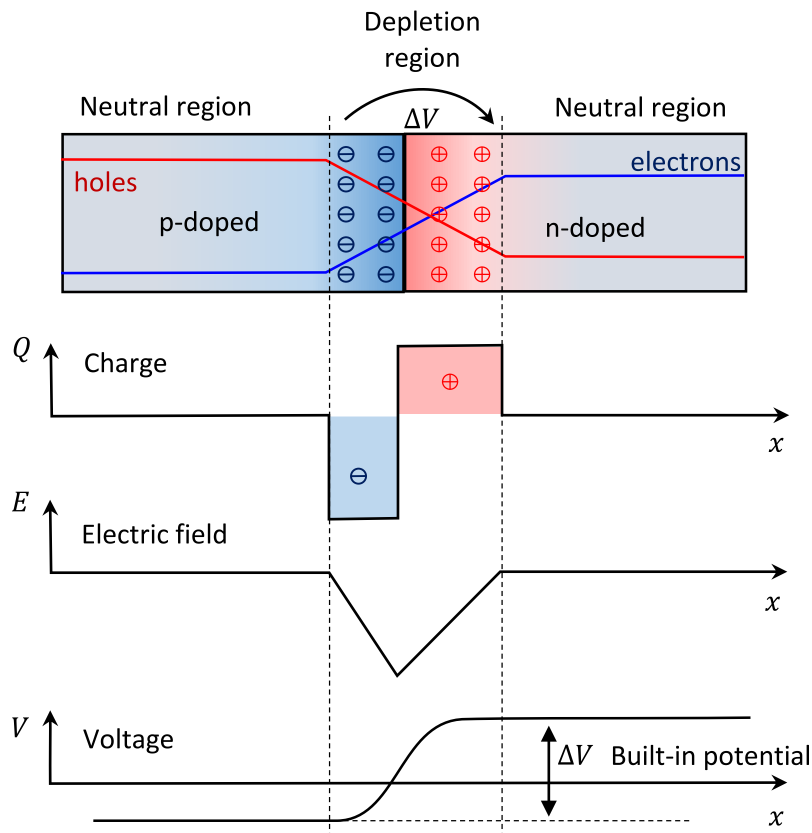

Figure 2.6 Scheme of a p-n junction in thermal equilibrium with zero-bias voltage applied, highlighting the area of the depletion region and the neutral regions. Under the scheme of the junction, plots of the charge density, the electric field and the voltage are presented.

Light emitters, such as light-emitting diodes (LEDs) and lasers, are some of the main applications of III-V compound semiconductors. The integration of III-V on group IV substrates is a possible solution to achieve high-efficiency, low-cost devices using deposition methods for the III-V on Si, Ge or Ge/Si substrates. In the case of the III-V hybrids on Si substrates, the monolithic growth of III-V on Si presents a high density of dislocation due to the lattice mismatch between the Si and the III-V and, therefore, the poor performance of the systems. These hybrid structures are affected by diverse types of defects. One of the major issues produced in these structures is the formation of anti-phase domains (APD), showed schematically in Fig. 2.7. These defects consist of the change in the order of the atoms due to

single atom steps in the substrate or the previous layer that creates a union between the atoms of the same species. Because these unions are not optimal, the material tends to create defects which will propagate producing severe changes in the properties of the materials, such as decreasing the mean free path of the electrons.

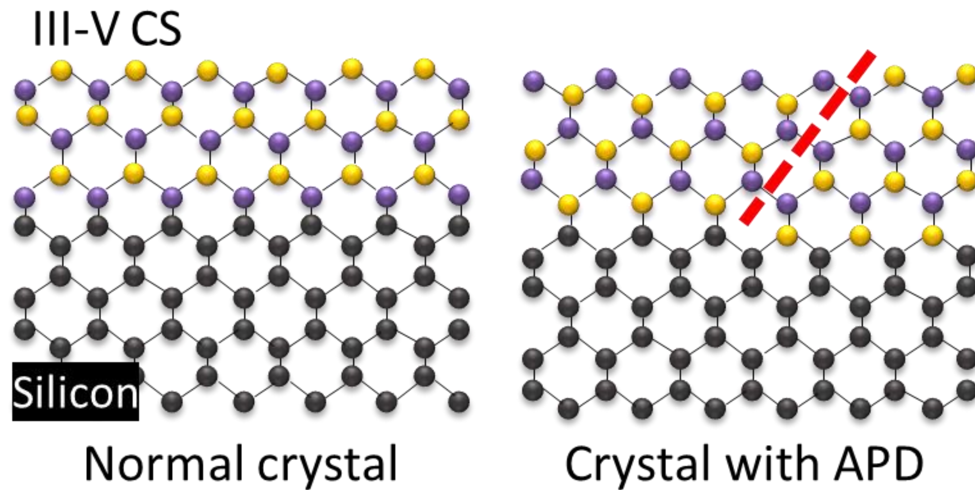

Figure 2.7 Schemes of hybrid structures with binary CS grown on a Si substrate. The left side scheme presents a normal crystal free of defects. The right side scheme shows the antiphase domains and antiphase boundary produced at the monoatomic step of the Si substrate.

Lattice mismatch, between the substrate and grown layers, is also a main concern in the epitaxially-grown films. This mismatch produces misfit dislocation networks at or near the interfaces, nucleating new dislocations. This internal-stress produced at the interfaces can be relaxed by diverse mechanisms, such as mechanical twinning. [25]

Discussing the III-V semiconductors, it is necessary to highlight the sub-group of the III-nitrides, highly prized in the fabrication of electronics and optoelectronics devices, for example power and radio frequency (RF) transistors, due to their direct wide bandgaps [29]. As light emitters, these semiconductors cover the whole optical spectrum, going from infrared to deep UV. A peculiar characteristic of the III-nitrides is their piezoelectric response, valuable for the fabrication of acoustic resonators or sensors [29, 30]. Gallium nitride, GaN, is an example of III-nitride, which presents a large bandgap of 3.39 eV and thermal conductivity of 1.3 $W·cm^{-1}·°C^{-1}$. Its piezoelectric coefficients, e_{15}=0.10 C m^{-2}, e_{31}=0.17 C m^{-2}, and e_{33}=0.29 C m^{-2}, and elastic moduli, C_{11}=359.4 GPa, C_{12}=129.2 GPa, C_{13}=92.0 GPa, C_{33}=389.9 GPa and C_{44}=98.0 GPa, predict GaN to be a great candidate for piezo-electric nanogenerators that convert mechanical energy into electricity.[30, 31]

2.4. Two-dimensional materials

Two-dimensional (2D) materials are layered substances, which do not need a substrate to exist, meaning that they can be isolated as freestanding atomically thin films one or few atom-thick. The first material isolated in the 2D structure was graphene, in 2004. [32] Afterwards, many other 2D crystals have been identified and studied.

2.4.1. Graphene

The electronic configuration of carbon allows the possibility of forming different allotropic species (see Fig.2.8), such as diamond, graphite, graphene, nanotubes and fullerene. In particular, graphene, which is probably the most promising allotrope due to its supreme physical properties, structurally forms a two-dimensional crystal with a honeycomb lattice, consequence of the sp2 orbital hybridisation, which forms three bonds in a plane, separated by angles of 120°. [33]

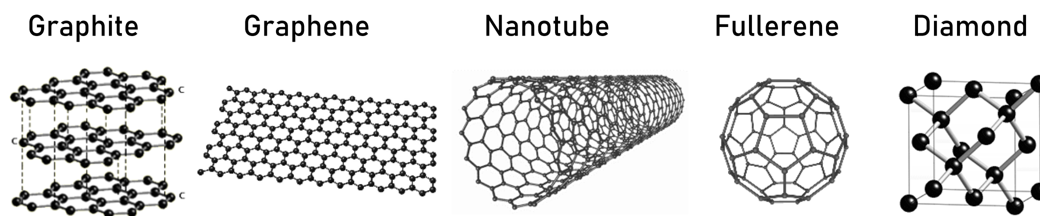

Figure 2.8 The carbon allotropes: graphite, graphene, nanotube, fullerene and diamond. Graphene is a monolayer of graphite and a nanotube is a graphene sheet rolled up.

Graphene has demonstrated an extensive number of outstanding properties, starting with the mechanical ones, mentioned before, where suspended graphene flakes have yielded an in-plane Young's Modulus of 1 TPa with a strength of 130 GPa and a strain break of ~25%. Overall, these values establish graphene as the strongest material ever measured.[9, 34] Nevertheless, the anisotropy in the mechanical properties is a remarkable quality of graphene. For example, its out-of-plane elastic modulus has been reported 0.3–45.4 GPa, few orders of magnitude smaller than the in-plane value. The in-plane graphene thermal conductivity is also higher than in commonly used heat dissipation materials, with a value of 4840–5300 W m^{-1} K^{-1}. [35] In general, 2D materials are considered good candidates for the fabrication of transparent devices - transistors, however, in the case of graphene, the 2.3% of absorption is considerably high for a material that is only one atomic layer thick.

The electrical properties of Graphene have been extensively probed with electron-mobility of up to 230,000$cm^2 \cdot V^{-1} \cdot s^{-1}$ at a carrier density of 2 × 1011 cm^{-3} for suspended and

annealed samples. For samples on a substrate, mobility is typically an order of magnitude lower due to scattering from the substrate phonons. [5]

The main methods for graphene fabrication are mechanical exfoliation and chemical vapour deposition (CVD). The principal advantage of mechanical exfoliation is that it is the cheapest way to obtain high-quality graphene, needing only a graphite piece and Scotch Tape. Moreover, the quality of the crystals is usually high, with a small amount of defects and minimum dopants. However, by this method it is very difficult to obtain big flakes and generally the size is around ~30μm^2. In the case of the CVD, it is possible to obtain big flakes, but their crystal quality is lower. Moreover, due to the etching process for the graphene release from the substrate, the physical properties of the graphene, especially the electrical ones, are affected.

2.4.2. Transition Metal Dichalcogenides

Graphene is an excellent material for multiple applications. However, the absence of a bandgap rules it out for applications in which semiconductor behaviour is required. For this reason, some members of the family of transition metal dichalcogenides (TMDCs) are good alternatives to graphene.

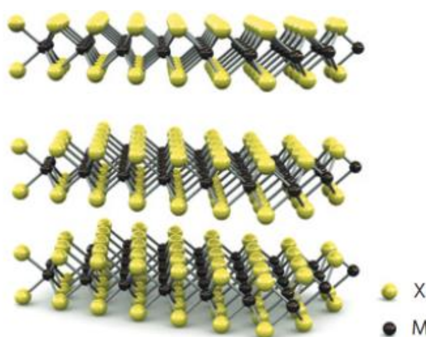

Figure 2.9 General scheme of Transition Metal Dichalcogenides (TMDCs) monolayers.[36]

TMDCs are formed by a sandwich structure composed by X-M-X where M represents the transition metal and X the chalcogen (see Fig.2.9). [6, 26] There are multiple combinations of TMDCs with stable configurations to form materials. However, not all of them can be included in the 2D materials group; for example, all the transition metals from the first row of the periodic table tend to form 3D crystals. Nevertheless, in the case of the heavier elements, van der Waals forces dominate the interaction between the adjacent layers, allowing easy exfoliation of the individual sheets. These can be considered as 2D materials, even if their

hexagonal structures are not atomically flat. Whilst all the TMDCs have a similar configuration, the differences in size and charge of the diverse elements cause considerable changes in the physical properties of the materials. For example, the heavier chalcogens show the higher electrical conductivity, which is an essential requirement for energy storage applications.

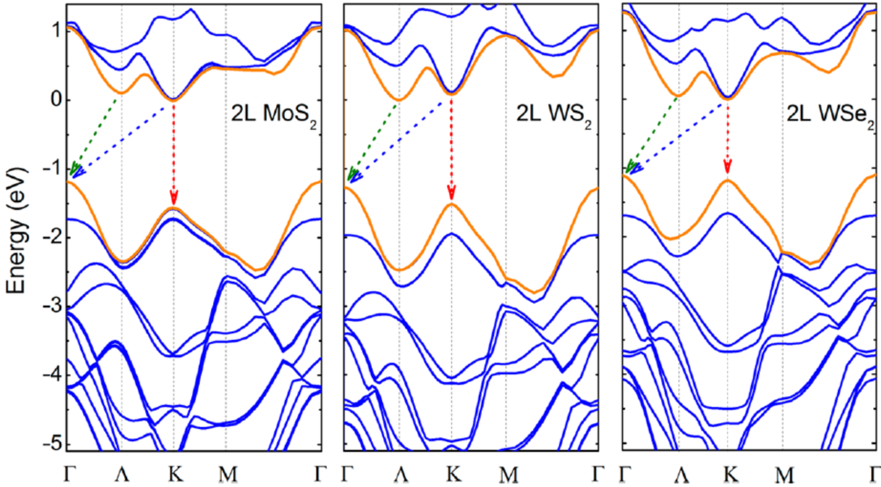

Figure 2.10 Calculated band structure of bilayer MoS_2, WS_2 and WSe_2. The bands forming the conduction band minimum and valence band are indicated in orange.[37]

TMDCs, such as MoS_2, WS_2 and WSe_2, have attracted enormous interest in the last decade for optoelectronic and energy storage applications due to their band structure. The monolayers of these materials are characterised by a direct bandgap, in contrast to the indirect bandgap of the multilayer structure or crystal bulk (see Table 1). Therefore, monolayers present different properties, such as high photoluminescence (PL) intensity and effective excitons.[38, 39] In addition, the presence of defects, such as vacancies or dopants, produce a shift in the PL. [39,40]

Table 1 Bandgap multilayer and bilayer in MoS_2, WS_2 and WSe_2.

Material	*Bandgap monolayer*	*Bandgap bilayer*
MoS_2	1.9 eV	1.2 eV
WS_2	2 eV	1.4 eV
WSe_2	1.6 eV	1.1 eV

Besides their exceptional electric and optical properties, TMDCs have also been reported as exceptional candidates for the fabrication of flexible and stretchable optoelectronic devices due to their mechanical and elastic properties. For example, the 2D elastic modulus of MoS_2, WS_2 and WSe_2 have been found to be approximately 170 Nm^{-1} positioning both among the highest 2D elastic modulus materials, but still far from the graphene record.[41, 42] The most common methods of TMDC monolayer fabrication are the mechanical or liquid exfoliation from the bulk and CVD.[12]

2.5. Nanoscale measurements methodology

2.5.1. Scanning probe microscopy

Scanning probe microscopies (SPM) are a family of microscopies where images are obtained by recording the sample probe interactions when the probe is scanning the surface. This group of microscopies started in 1982 with the invention of the scanning tunneling microscope (STM), followed by the development of the atomic force microscope (AFM) in 1986.

At very short distances, the tip-sample interaction is mainly dominated by the Coulomb and van der Waals forces. The Coulombic interactions are strong, short-range repulsive forces which result from the electrostatic repulsion between the tip and sample electron clouds, being inversely proportional to the tip-sample distance. At the same time, the van der Waals interactions are weak and long-range attractive forces. Nevertheless, they are strong enough to affect the motion of the probe in the vicinity of the surface.

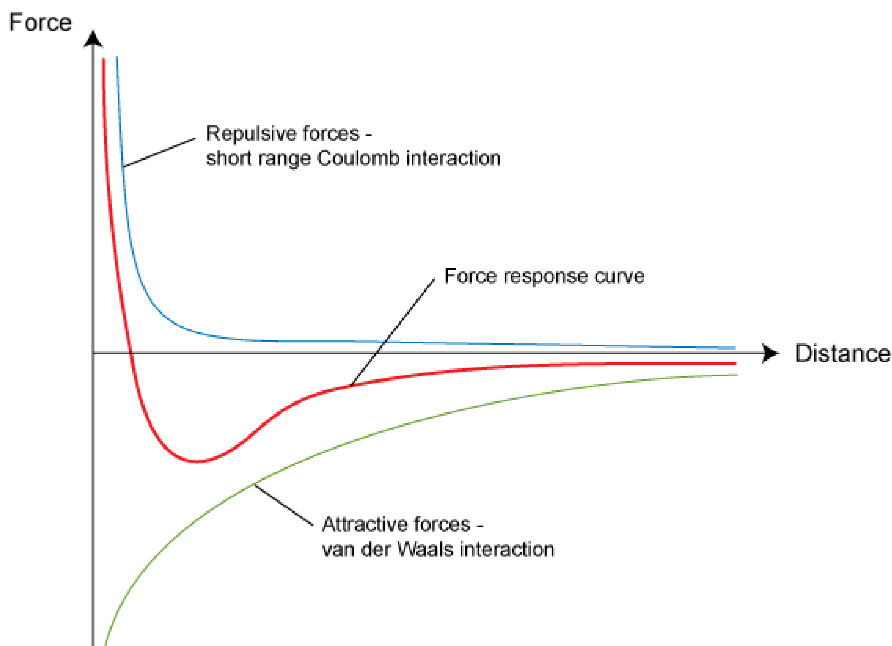

Figure 2.11 Force vs distance plot.
(https://www.doitpoms.ac.uk/tlplib/afm/tip_surface_interaction.php)

In a normal environment, such as in air, the surface of the sample is commonly covered by a thin water layer, which tends to create a water meniscus with the probe by capillary forces. This water layer affects the cantilever dynamics when it is pulling away from the surface, causing the probe to stick to the sample for longer.

As the tip-surface distance increases, long-range forces begin to dominate the interaction, such as magnetic ones, and the electrostatic forces resulting from the cantilever-sample interaction. The exploration of these other interactions has resulted in the development of new techniques.

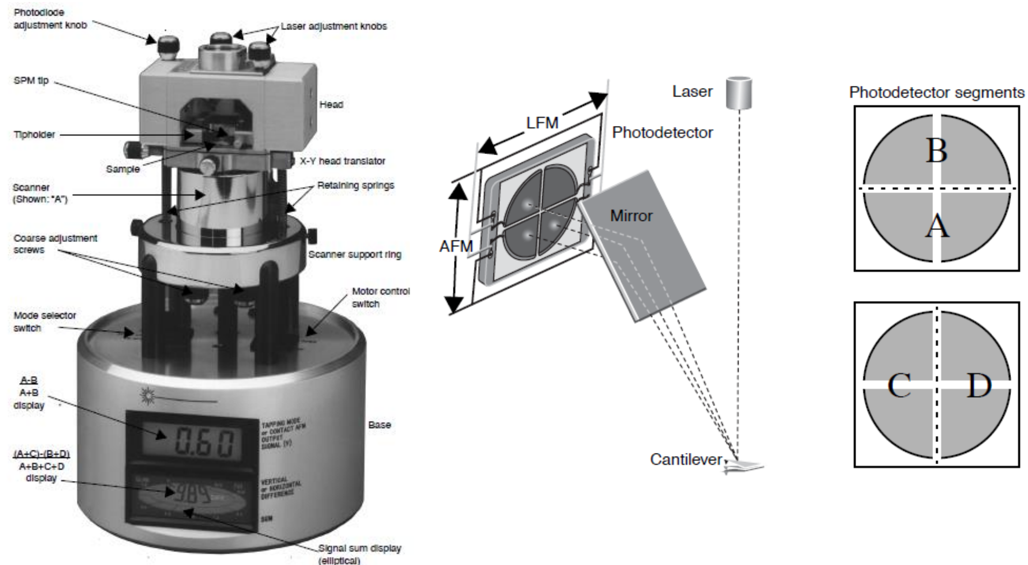

Figure 2.12 a) MultiMode SPM. b) Quad photodetector arrangement. [43]

The basic operation modes for the AFM are contact, tapping and non-contact. The contact is a static mode in which the tip has permanent contact with the sample and the cantilever deflection is monitored to keep constant the setpoint tip-sample force in the repulsive regime. The sample is raised or lowered to compensate for the variations in the deflection from the setpoint value, providing the measure of the surface topography. A friction micrograph can also be generated by monitoring the torsional motion of the probe during the scanning. The tapping (TM-AFM) and the non-contact techniques are dynamic modes in which the cantilever vibrates and the amplitude, frequency and phase of the oscillation are monitored. The cantilever oscillation is driven near to its free resonance by a piezoelectric element. In tapping mode, the signal monitoring in the feedback loop is the amplitude of the oscillation, which decreases with contact, rather than deflection, as in the case of contact mode. Additional information can be also extracted by recording the phase lag, which is also affected by different material properties, such as elasticity, friction and adhesion. The non-contact mode can be operated at frequency or amplitude modulation mode, in which frequency shift or amplitude changes are monitored respectively.

For the monitoring of the deflection and tapping signals, necessary during the performance of sub-methods, one can use a “signal access” box, which allows us to monitor the signals via standard bayonet Neill–Concelman (BNC) connectors.

2.5.2. Nano-mechanical measurements in SPM.

Force Modulation Microscopy and Contact Resonance AFM

Force modulation microscopy (FMM) is a non-destructive method for probing local stiffness in the sample surface and subsurface. It is based on contact AFM, vibrating the sample vertically at low frequency, *i.e.* a frequency below the free resonance of the cantilever (~2-5kHz). The cantilever’s deflection depends on the tip-sample interaction, which is influenced by the sample deformation. Stiffer samples deform less, therefore the deflection response is more greatly affected. By recording the variation in the cantilever deflection it is possible to map the sample elasticity, k_s. [44, 45]

Considering the sample and the cantilever’s behaviour like two springs, k_s can be quantitatively modelled by the relation between the force applied, ΔF, and the cantilever displacement as

$$k_s = \frac{\Delta F}{(\Delta z_m - \Delta z_d)}, \quad (8)$$

where Δz_m is the sample motion, and Δz_d is the cantilever’s deflection. [46, 47]

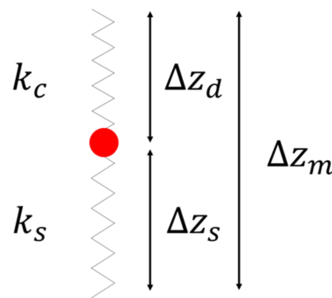

Figure 2.13 Scheme of the springs model for the sample cantilever interaction.

In this methodology, there are different parameters, which can be optimised to map the sample features. For example, increasing the excitation frequency up to the contact resonance of the cantilever allows for the evaluation of the near-surface mechanical properties at the nanoscale, via contact resonance atomic force microscopy (CR-AFM).[48, 49] Working at the resonance modes of the cantilever offers high sensitivity to the changes in the mechanical properties of the different structures. [50, 39, 51]

Ultrasonic Force Microscopy

FMM offers good results in a wide variety of samples. However, this method is inadequate for the mechanical mapping of very stiff samples as it is sensitive in a range close to the cantilever's spring constant value [46]. These difficulties can be solved by inserting a piezotransducer under the sample to oscillate it vertically at high ultrasonic frequencies (>2 MHz) that are amplitude modulated at a few kHz (2-3 kHz). This method is called ultrasonic force microscopy (UFM) and was invented by Kolosov and Yamanaka.[52] They evaluated the AFM cantilever response at low and high excitation frequencies of the sample vibrations and showed that, at low frequency, soft cantilevers cannot probe the elasticity of stiff samples. [53] However, in the case of high-frequency excitation (well above of the resonance of the cantilever), the cantilever response becomes negligible, inertially increasing its spring constant and allowing the cyclical indentation of the tip into the sample.[54] Whilst the tip is indenting into the sample, there is a damage reduction due to the tip-sample contact being broken during part of the cycle, removing the torsional forces on the cantilever and creating a lubricant effect between the tip and the surface. Nevertheless, the high speed hitting of the surface with the sample can also produce light sample wearing. [55, 56]

The normal force experienced by the cantilever in its interaction with the sample in UFM measurements can be defined as a function of the ultrasonic amplitude, a, and the initial indentation, h,

$$F_m(h,a) = \frac{1}{T_{ult}} \int_0^{T_{ult}} F(h - a\cos 2\pi f_{ult}\, t)dt, \qquad (9)$$

where $F(z)$ is the original force dependence of the indentation without ultrasonic vibration and f_{ult} is the ultrasonic frequency; the integral is taken over a period $T_{ult} = 1/f_{ult}$. [57]

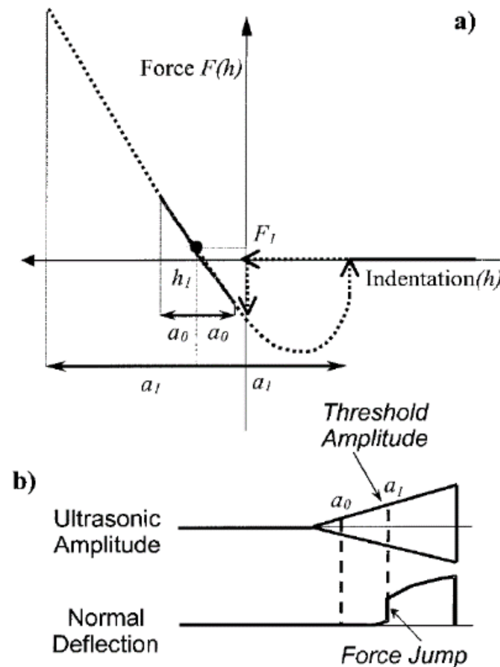

Figure 2.14 (a) For small ultrasonic amplitudes such as a_0, the normal force averaged in time over one ultrasonic period is equal to the initial value F_1 as the force curve is linear in the first approximation. For the threshold amplitude a_1, the average normal force (averaged over the broken line) has a discontinuity that depends on the adhesion hysteresis. The contact is broken for part of the ultrasonic cycle. (b) Schematic normal deflection response induced by an out-of-plane ultrasonic vibration of the sample. There is a variation of the normal deflection only for ultrasonic amplitudes higher than the threshold amplitude a_1. At this amplitude value, a discontinuity in normal force and normal deflection occurs (force jump). [55]

When the amplitude of the vibration is modulated at low frequency, the cantilever experiences a characteristic ultrasonic force at the modulation frequency, which produces the UFM response. Ideally, this ultrasonic response is only dependent on mechanical properties, making UFM a material-sensitive method. Unfortunately, some other factors such as high frequency excitations in the cantilever or piezotransducer resonances make it difficult to universally distinguish between different materials. Nevertheless, Bosse *et al*. demonstrated that in a confined region, typically less than 10 x 10 μm^2 for a 4 MHz piezotransducer, UFM allows for quantitative analysis with the ability to differentiate mechanical properties, between soft and stiff materials [58].

A variant mode of UFM with reported analogous results in the probing of the elastic and viscoelastic properties is waveguide UFM (W-UFM), where the ultrasonic excitation is applied from the tip by the insertion of a piezotransducer in the base of the cantilever.[59, 60]

Heterodyne Force Microscopy

Another methodology to explore nanomechanical properties using nonlinear detection of ultrasonic vibrations is heterodyne force microscopy (HFM). In this mode, analogously to UFM, ultrasonic sample vibrations are excited with a piezotransducer inserted under the sample and, in addition to that, tip vibrations are excited with another piezotransducer inserted in the base of the cantilever. Both piezotransducers are driven at adjacent ultrasonic frequencies. Since the sample is vibrating at a frequency ω_s and the tip at ω_t, the maximum tip-surface distance is modulated at the beat frequency $\omega_{diff} = \omega_t - \omega_s$. Therefore, the tip-sample interaction force can be written, in the second-order approximation as

$$F_{t-s} = k(z_t - z_s) - \chi(z_t - z_s)^2, \quad (10)$$

where $z_t(t) = A_t \sin(\omega_t t)$ and $z_s(t) = A_s \sin(\omega_s t + \omega_s \tau)$ are the distances to the tip and the sample, respectively. The $\omega_s \tau$ term denotes the phase attributed to the dynamic mechanical phenomena on the sample surface, with τ being the characteristic timescale of the phenomena such as the stress relaxation in a viscoelastic material. By doing corresponding algebraic manipulations and considering only the low-frequency terms acting on the cantilever's response, the force experienced by the cantilever can be approximated as

$$F = \chi \left[\frac{1}{2}(A_t^2 + A_s^2) - A_s A_t \, cos\left(\omega_{diff} t - \omega_s \tau\right) \right]. \quad (11)$$

This equation preserves the phase-dependence to the dynamic mechanical phenomena at high frequency, $\omega_s \tau$. Therefore, the monitoring of the amplitude and the phase of the signal can be performed by a lock-in amplifier at the beat frequency, ω_{diff}. The amplitude of the signal provides the elastic and/or adhesive properties of the sample, same as the UFM. The phase output stores the dynamic relaxation information of the sample with high time-sensitivity (nanosecond scale). [61]

2.5.3. Electrical measurements in SPM.

Electrostatic Force Microscopy

The electrostatic force microscopies (EFM) are the SPM methods used to study the electrical properties, such as charge density, work function and surface potential benefiting of AFM nanoscale resolution.

The principle of the EFM is monitoring tip-sample electrostatic interaction that can be explained by the general form of the electrostatic force *F* dependent on the potential *V*, given as

$$F = \frac{1}{2}\frac{\partial C}{\partial z} V^2, \tag{12}$$

where *C* is the capacitance, partially differentiated in the vertical direction *z.* [62]

For EFM measurements, the total voltage term, *V*, is composed of four different components, two of them intrinsic to the materials of the sample and the tip, namely the contact potential difference V_{CPD} and the potential correspondence to the surface charges, V_{SC}.[63] The other two components correspond to the external driving signal for the electrical excitation of the tip-sample system, being the DC component V_{DC} and the sinusoidal one V_{AC} *sin(ωt).* Therefore, the total force can be written as

$$F = \frac{1}{2}\frac{\partial C}{\partial z} \left(V_{CPD} + V_{SC} + V_{DC} + V_{AC}\, sin(\omega t)\right)^2 \tag{13}$$

and can be decomposed into three different terms depending on the frequency dependence, *i.e*. zero frequency, *ω* and *2ω* terms:

$$F_{DC} = \frac{1}{2}\frac{\partial C}{\partial z}\left[(V_{CPD} + V_{SC} + V_{DC})^2 + \frac{1}{2}V_{AC}^2\right], \tag{14}$$

$$F_{\omega} = \frac{\partial C}{\partial z}(V_{CPD} + V_{SC} + V_{DC})V_{AC}\, sin(\omega t), \tag{15}$$

and

$$F_{2\omega} = -\frac{1}{4}\frac{\partial C}{\partial z}V_{AC}^2\, cos(2\omega t). \tag{16}$$

Kelvin Probe Force Microscopy

Kelvin probe force microscopy (KPFM) is a variation of EFM. This technique allows for the study of diverse material properties depending on the nature of the sample. For example, in the case of the metallic samples, the KPFM response is linked with the work function of the material surface. In the case of semiconductors, the band structure including the doping can be obtained from the KPFM response. [64]

The parameter measured by the KPFM is the contact potential difference (V_{CPD}) between the tip and the sample, that is defined as:

$$V_{CPD} = \frac{\phi_{tip} - \phi_{sample}}{-e}, \tag{17}$$

where the ϕ_{tip} and the ϕ_{sample} are the work functions of the tip and the sample, respectively, and e is the electronic charge. [65]

Therefore, the potential term of the electrostatic force of equation *13* can be expressed as

$$V = V_{DC} - V_{CPD} + V_{AC} sin(\omega t), \tag{18}$$

where V_{DC} and $V_{AC}\sin(\omega t)$ are the DC and AC components of the potential applied to the sample, respectively. Hence, the force experienced by the cantilever at the frequency ω is equal to:

$$F_{\omega} = \frac{dC}{dz}[V_{DC} - V_{CPD}]V_{AC}\, sin(\omega t). \tag{19}$$

Therefore, if V_{DC} is equal to V_{CPD}, the component of the force on the cantilever, F_{ω}, is nullified. Then the V_{CPD} can be measured when a feedback loop is used to minimise the cantilever's response at ω.

KPFM simultaneously records V_{CPD} and the topography. There are two different operating modes of KPFM: frequency modulation (FM) mode, which works in semi-contact mode, and amplitude modulation (AM) mode, which works in non-contact mode and in ultra high vacuum (UHV) for high-resolution imaging. In both modes, the cantilever oscillates at or close to its resonance frequency. The changes in the distance between the tip and the sample alter the tip-sample interaction, creating changes in the amplitude and the resonance frequency, which are used as feedback signals to acquire the topography of the sample surface. [66, 67]

The AM-KPFM mode uses the changes in the amplitude of the cantilever's oscillation, which are directly dependent on the forces of the tip-sample interaction, as feedback. Thus, the direct force between the tip and the sample is represented in the AM measurements. In FM-KPFM mode, the feedback signal is the frequency shift produced by the electrostatic tip-sample interaction. FM mode senses the force gradient between the tip and the sample rather than the force itself. The fact that the FM mode is sensitive to the electrical field gradient rather than the force results in the higher spatial resolution of FM, as the detection range of the gradient is short, sensitive mainly to the interaction of the very end of the tip with the sample. In the case of AM, the electrostatic force is influenced by the tip and the cantilever's interaction with the sample, therefore the spatial resolution is reduced by an averaging effect of the tip and the cantilever.[65]

Dielectric Electrostatic Force Microscopy

Useful information can be also obtained by the measurement of the second harmonic term of the tip-sample electrostatic force, which is directly linked with the dielectric constant of the material under examination. This methodology is known as dielectric force microscopy (D-EFM) and allows for intrinsically mapping the electrical permittivity in a quasi-static regime, for low-frequency AC voltage V_{AC} measurements. [68, 69] The interacting force between the sample and the cantilever can be modelled as a two-parallel-plates capacitor, with the interaction between the two plates described as [70]

$$F_{cap} = -\frac{1}{2}V^2\frac{C}{z}. \tag{20}$$

Looking for the analogous term in the sample-cantilever interaction forces in the EFM measurements, it is possible to identify the terms dependent on V_{AC}^2 for the frequency independent F_{DC} (Eq. *14*) and the term dependent of the 2nd harmonic $F_{2\omega}$ (Eq. *16*). For the normal setup implemented in the EFM measurements it is necessary to find a term frequency-dependent for the lock-in detection. Therefore, the dielectric properties of the material can be mapped by monitoring the signal in the 2nd harmonic according to

$$\frac{dC}{dz} = -\frac{4|F_{2\omega}|}{V_{AC}^2}, \tag{21}$$

where

$$C = \varepsilon_r\frac{A}{z}. \tag{22}$$

Piezoelectric Force Microscopy

As mentioned above, some dielectric materials under an applied electric field will provide additional mechanical deformation for piezoelectric samples. This electromechanical response can be mapped by the method called piezoelectric force microscopy (PFM), where the local piezoelectric response is recorded due to a potential difference being created between the sample and the conductive probe.[71]

Due to the nature of the setup, the total amplitude of the cantilever's response in contact with the piezoelectric materials is formed by

$$A = A_{piezo} + A_{cap} + A_{nl}, \tag{23}$$

where A_{piezo} represents the electromechanical response due to converse piezoelectric effect, A_{cap} is the contribution due to the electrostatic force between the tip and the sample, and A_{nl} is the contribution due to non-local electrostatic force between the cantilever and the sample.

The total capacitive force created by the cantilever-sample system is described by

$$F_{cap} = \frac{dW_{cap}}{dz} = \frac{1}{2}V^2\frac{dC}{dz}, \tag{24}$$

where W_{cap} is the total energy stored in the capacitor formed by the tip in the contact with the dielectric surface, V is the potential and z is the vertical distance. The total capacitance C can be written as the sum of the capacitance of the tip (C_{tip}) and the capacitance of the cantilever (C_{cant}). However, in many practical cases, the cantilever term can be considered negligible due to its small contribution, as it is described in the literature.[72]

Piezoelectric materials will present an additional response to an applied AC electric field due to the converse piezoelectric effect. The vertical displacement (in the z-direction) of a homogeneously polarized material can be expressed as follows:

$$\Delta z = d_{33}V + \frac{M_{333}}{t}V^2, \tag{25}$$

where V is the applied voltage, t is the sample thickness and d_{33} and M_{333} are the piezoelectric and electrostrictive constants. The electrostrictive term is usually much smaller than the first one in a polarized state. Applying an external voltage $V = V_{DC} + V_{\omega}\cos(\omega t)$ the surface displacement will have a DC component, which is not detectable by the lock-in amplifier, and the signal is in the first and second harmonics:

$$\Delta z_{\omega} = d_{33}V_{\omega} + 2\frac{M_{333}}{t}V_{DC}V_{\omega}, \tag{26}$$

$$\Delta z_{2\omega} = \frac{1}{2}V_{\omega}^{2}\frac{M_{333}}{t}. \tag{27}$$

The electrostrictive effect does not depend on the polarization direction: it only causes a constant background, but does not influence the detection of the polarisation orientation.

2.6. Optical characterisation methods

The study of ultrasonic vibration is a topic which has been intensively investigated for many years with different methodologies because of the importance of these vibrations in many industrial applications and biomedical diagnosis. The possibility of the study of ultrasonic vibrations with non-destructive measurements, such as optical methods, has attracted special interest in the fabrication of MEMS/NEMS for multiple applications.

There are different modes for optical characterisation of ultrasonic vibrations and these methods can be split into two different groups: interferometric and non-interferometric techniques. Some examples of non-interferometric methods are the knife-edge and the surface-grating techniques, both limited by the finish of the sample surface, being only suitable for low roughness samples. The group of interferometric methods can be split into another three sub-groups; a) optical heterodyne, which uses the scattered wave of the surface interfering with a reference signal; b) differential interferometry, which creates an interference of two waves on the surface; and c) velocity or time-delay interferometry, which consists of the beating of the wave issued from the surface with the same wave delayed in time. [73, 74]

Here, we focus on the optical heterodyne method called laser Doppler vibrometry, which is based on the Michelson interferometer.

2.6.1. Interferometric methods: laser Doppler vibrometry

Laser Doppler vibrometry (LDV) is based on the analysis of the Doppler effect on a reflected laser beam from a solid moving surface. The laser is focused onto the vibrating sample surface, which reflects the beam with a frequency shift Δf_D proportional to the velocity of oscillation of the sample into the parallel axis of the laser, according to the equation

$$\Delta f_D = \frac{2v}{\lambda}, \qquad (28)$$

where v is the velocity of the sample and λ is the laser wavelength.

The interferometric configuration implemented in the LDV is the Mach-Zehnder (see Fig 2.15), in which the laser beam is split in two. One of them is focused on the vibrating surface (measuring beam), carrying the frequency shift information, and the other one is acting as reference (reference beam). Finally, both beams are combined on photodiodes detecting the interference between the beams.

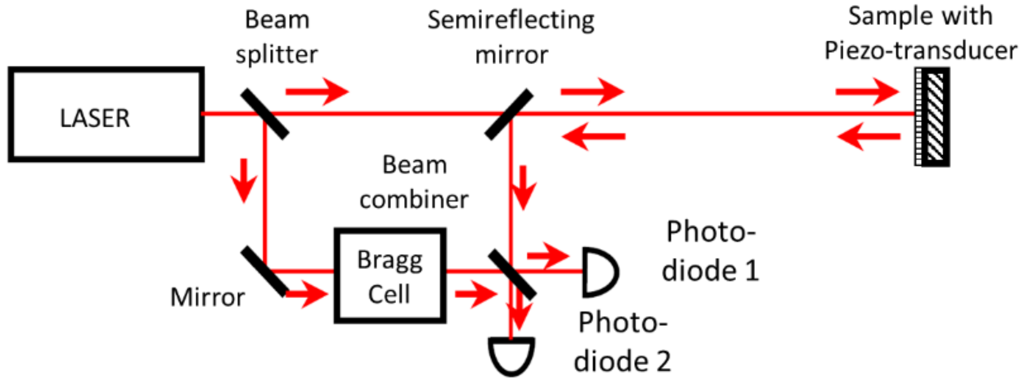

Figure 2.15 Optical schematic of typical components of a single-point vibrometer (Mach-Zehnder). A laser beam is produced by the LDV is focused on a vibrating surface and reflected from there. The Doppler shift in frequency of the reflected beam is used to find out frequency and amplitude of the vibrating target. [74]

The acquired signal will depend on the optical configuration - heterodyne or homodyne, depending if the Bragg cell is in the beam path or not. Moreover, the signal can be treated in a diverse manner depending on the information required. The frequency demodulation of the signal provides the instantaneous velocity and the displacement can be acquired by counting the number of fringes.

The frequency demodulation of the signal in the heterodyne mode is realised by mixing the reference signal from the Bragg cell with the interference one. The Bragg cell is an acousto-optic device employed to fix a frequency shift Δf_{BC} in the reference beam, which is also a method for distinguishing the direction in the velocity measurements. The total frequency shift in the beating of the two waves will be

$$\Delta f_{Total} = \Delta f_D + \Delta f_{BC}, \qquad (29)$$

giving the possibility of eliminating the ambiguity of the velocity direction.

In the measurement of the direct displacement, when the target surface moves a distance *d*, the variation of the interferometer path length is 2*d,* and the signal presents a phase shift directly proportional to the number of fringes *N*, given by

$$\Delta\phi = \frac{4\pi \cdot d}{\lambda} = 2\pi \cdot N. \qquad (30)$$

Each fringe corresponds to a displacement of half of the wavelength λ.[74]

2.6.2. Raman spectroscopy and photoluminescence

The method known as Raman spectroscopy is an optical technique for the identification of molecules and solids by their unique vibrational modes as a consequence of their excitation with a laser beam. When a monochromatic light source, usually a laser, is focused on the sample, the light interacts with the sample's electron cloud, exciting molecular vibrations, phonons or other excitations in the system, and resulting in a frequency shift due to the inelastic scattering of the photons. This is known as Raman scattering and is unique for each species, like a fingerprint. In Raman spectroscopy, the laser does not excite electronic transitions in the sample, therefore Raman scattering is not an emission phenomenon.

Conversely, photoluminescence (PL) is an emission phenomenon. During this process, electrons from the electron cloud are photoexcited to higher energy levels, and in the relaxation process the sample re-emits the photons with a particular energy. In the case of semiconductors, the emitted photons typically have energy similar to the energy bandgap.

2.7. 3D Sectioning and sample preparation for SPM

SPM are high-resolution techniques. However, due to their nature, they can only image features on or immediately near to the surface. Consequently, sample preparation methods are required to access subsurface features. Historically, sample cleaving has been the methodology implemented for sectioning samples. However, this is very imprecise, especially when sectioning samples with a high density of defects, which will lead to material cleavage. Cross-sectional methods such as slow cut diamond saws have been also implemented in the sample preparation. An alternative and more precise method to diamond saws are focused ion beams (FIB), where ion beams are normally focused on the sample surface milling a small cavity. Alternatively, in Ar-ion cross-sectioning, part of the sample is covered with a mask and the un-protected area is milled by the focused beams. Both methods produce cuts that are difficult to access with the SPM probes, due to the geometry and dimensions of the resulting surface. FIB is also widely used in the preparation of samples for transmission electron microscopy (TEM), where accelerated gallium ions are focussed onto the sample surface, milling it until it reaches the area of interest. The main disadvantages of this methodology are the gallium ion implantation, modifying the chemical properties, and the surface damage produced during the milling process.

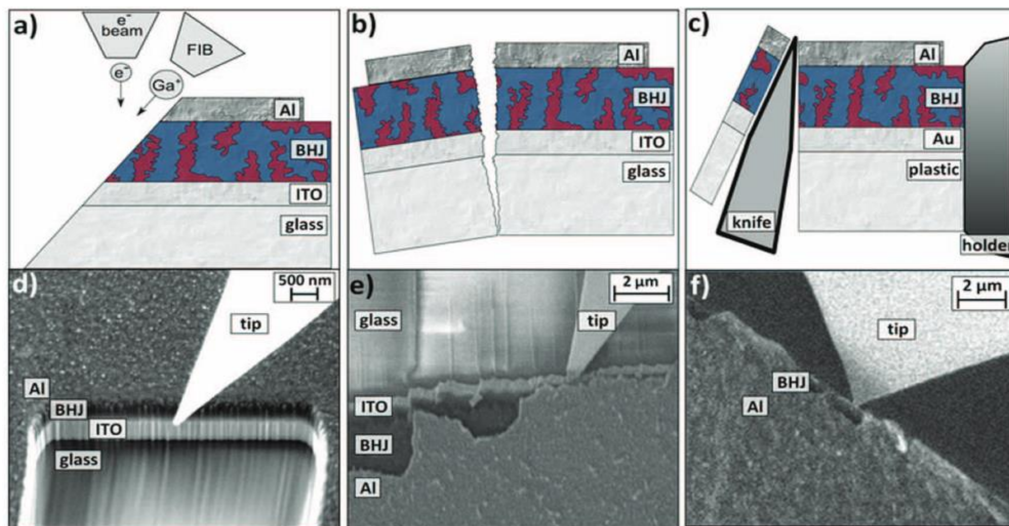

Figure 2.16 Preparation of organic solar cells cross sections by (a) FIB milling, (b) cleavage and (c) microtome cutting is depicted (view perpendicular to the exposed cross-section); SEM images of (d) FIB milled, (e) cleaved and (f) microtome cut cross-sections. [75]

2.8. Micro and nanoscale MEMS and NEMS

Micro- and nano-electromechanical systems (MEMS/NEMS) are new structures that result from the miniaturisation of devices to satisfy the needs of new advances in technology, which demand reduced size and weight, low power dissipation, improved speed and precision when compared with macroscopic counterparts. [76] These "micro- and nano-machines" play an important role in transportation, communication, environment monitoring, automated manufacturing, health care and development of future intelligent systems, to mention some applications.

2.8.1. Mechanical resonators

Nanomechanical resonators, one of the major practical implementations of MEMS and NEMS devices, can be modelled as harmonic oscillators. In the simplest example, a mass m is attached to a spring with spring constant k. Displacing the mass from its equilibrium position, the spring is exerting the restoring force $F = -kx$ proportional to the displacement x and the spring constant k. The periodical oscillating motion of the mass around the equilibrium position can be mathematically modelled by the one-dimensional simple harmonic oscillator equation

$$m\frac{d^2x(t)}{dt^2} + x(t) = 0. \tag{31}$$

However, this model does not represent a realistic situation due to it not considering any damping mechanism, which means the oscillation will continue forever. A more representative model of the motion of a mechanical resonator is the driven damped harmonic oscillator; its equation is given by

$$\frac{d^2x(t)}{dt^2} + \gamma\frac{dx(t)}{dt} + \omega_0^2x(t) = \frac{F_d e^{i\omega_d t}}{m}, \tag{32}$$

where γ is the damping coefficient, F_d is the amplitude of the driving force and ω_d is its angular frequency.

2.8.2. Beams and tuning forks – fundamental principles

In the particular case of AFM cantilevers or tuning forks, they dynamically behave as single-end clamped single or double beams (the tuning fork). They can be modelled by the Euler-Bernoulli equation (Eq. 33) describing the flexural motion of a beam with constant cross-section $A = bh$, moment of inertia $I = bh^3/12$, Young's modulus E and density ρ:

$$EI\frac{\partial^4 y}{\partial x^4} + \rho A\frac{\partial^2 y}{\partial t^2} = 0. \tag{33}$$

The coordinate x is the longitudinal direction of the beam and y is the deflection from the rest position of the length element at x. Both coordinates are represented in Fig. 2.17.

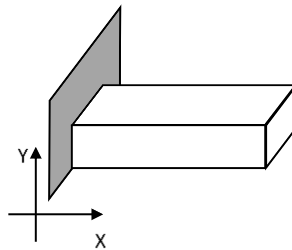

Figure 2.17 Scheme of the single-end clamped beam.

The flexural motion equation has a general solution of

$$y(x,t) = \left(a_1 e^{kx} + a_2 e^{-kx} + a_3 e^{ikx} + a_4 e^{-ikx}\right)e^{-i\omega t}, \tag{34}$$

where $k = 2\pi/\lambda$ is the wavenumber and $\omega = 2\pi f$ is the angular frequency. Both values are obtained from the dispersion relation

$$EIk^4 - \rho A\omega^2 = 0, \tag{35}$$

obtained by combining equations 34 and 33.

Applying the corresponding boundary conditions (Eq. 36), for a beam of total length L and clamped at $x = 0$, the deflection and the slope vanish at the clamped end and the terms of the moment and the shear force disappear in the free end $x = L$.

$$\left[y(x,t) = \frac{\partial y(x,t)}{\partial x}\right]_{x=0} = \left[\frac{\partial^2 y(x,t)}{\partial x^2} = \frac{\partial^3 y(x,t)}{\partial x^3}\right]_{x=L} = 0 \tag{36}$$

By inserting the general equation 34 and its derivatives into equation 36 of the boundary conditions, the resulting four equations can be solved for the coefficients a_i if the characteristic equation *37* is fulfilled. [77]

$$cos\, k_n L\, cosh\, k_n L + 1 = 0 \tag{37}$$

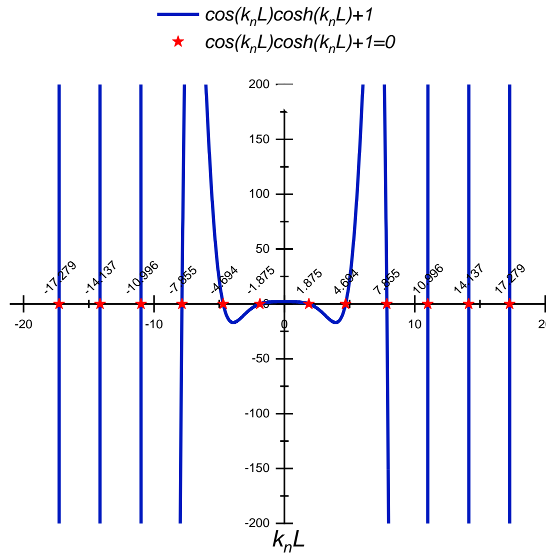

Figure 2.18 Plot of $f(k_n L) = \cos(k_n L)\cosh(k_n L) + 1$, with the numerical solution superposition for $f(k_n L) = 0$.

The solutions for this equation give the wave number k_n of an infinite set of flexural vibration modes where n is the mode number. With the help of the dispersion equation 35, the flexural resonance frequency of the beam can be calculated by

$$\omega_n = 2\pi f_n = k_n^2 \sqrt{\frac{EI}{\rho A}} \qquad n = 1, 2, \ldots, \tag{38}$$

with $k_n L$ = {±1.875, ±4.694, ±7.855, ±10.996,… } the numerical solutions of the equation *37*. [78]

2.8.3. Membranes

Membranes are another type of mechanical resonators. The motion of a rectangular pre-tensioned membrane can be modelled by [79]

$$\frac{\partial^2 z}{\partial t^2} = \frac{T}{\sigma}\left(\frac{\partial^2 z}{\partial x^2} + \frac{\partial^2 z}{\partial y^2}\right), \tag{39}$$

and

$$f_{mn} = \frac{1}{2}\sqrt{\frac{T}{\sigma}}\sqrt{\frac{m^2}{L_x^2} + \frac{n^2}{L_y^2}} \qquad m, n = 1, 2, \ldots, \tag{40}$$

where T is the tension of the membrane, σ is the area density, x and y are the in-plane membrane coordinates and z the out-of-plane one. Solving this equation with corresponding boundary conditions, it is possible to determine the frequency for the different vibrational modes for a rectangular membrane of size L_x by L_y.

2.8.4. 2D materials drums

The implementation of 2D materials in the fabrication of MEMS and NEMS is a new alternative to the Si and Si_3N_4. The main advantages of these materials are their small thickness, low mass and low mechanical losses.[80] An example of a mechanical resonator made by 2D materials is the graphene drum. [81]

The dynamics of these resonators can be modelled as membranes, plates or a combination of both, depending on the relation of their bending rigidity and the pre-tension. In the limit of very thin layers (membranes), the bending rigidity is considered negligible in comparison with the pre-tension, and the resonance frequency is given by

$$f_{membrane} = \frac{2.4048}{2\pi\, R}\sqrt{\frac{T}{\rho t}}, \tag{41}$$

where R is the radius, T is the pre-tension, ρ is the 3D mass density and t is the thickness of the flake.

In the extreme case when the bending rigidity dominates the resonator dynamics, the system is modelled as a plate. The resonance frequency of the plate is given as

$$f_{plate} = \frac{10.21}{4\pi}\sqrt{\frac{E}{\cdot\rho\,(1-\nu^2)}\frac{t}{R^2}}, \tag{42}$$

where E is the Young's Modulus and ν is the Poisson's Ratio.

For intermediate thicknesses, the mechanical resonator dynamics are governed by both membrane and plate regimes with the effect of bending rigidity and the initial pre-tension being comparable. In this case, the resonance frequency can be approximated as

$$f \approx \sqrt{{f_{membrane}}^2 + {f_{plate}}^2}, \quad (43)$$

where the $f_{membrane}$ and f_{plate} are the given equations 41 and 42, respectively.[82]

2.9. Summary.

This chapter provides the background information of physical properties of solids, and we focused on the properties of bulk semiconductors, piezoelectric solids and two-dimensional materials. Furthermore, we reviewed various existing scanning probe methods and optical techniques, as well as sample preparation methods commonly used in the nanoscale characterisation of the mentioned materials. Finally, theoretical concepts of mechanical resonators, MEMS and NEMS have been introduced. All these concepts make a solid foundation for the study of the materials and samples discussed in the following chapter and they will serve as a reference to the newly developed methods.

3. Target materials and sample preparation

In the previous chapter, we presented the theoretical foundations of the most relevant concepts needed in this work. To continue, this chapter presents a condensed description of the materials, structures and fabrication methods implemented throughout the whole study. Preparation of substrates and the following graphene transfer were carried out at Lancaster University by the NowNANO PhD candidates, J. Wengraf, R. McNair, S. Shao and A. Peasey, and myself. The TMDCs heterostructures were grown at the University of Wisconsin-Madison by Prof. S. Jin and Y. Zhao. The III-V semiconductor samples were grown in three different locations, MQW at University College London, by Prof. H. Liu, Dr M. Tang and Dr Y. Gong; VCSELs were fabricated at Cardiff University by Prof. P. Smowton and Dr S. Shutts.

3.1. 2D materials – exfoliation, lifting and transfer

In this work we used diverse 2D materials, synthesised in two different manners. This section details the synthesis processes and fabrication of the thin sheets, including chemical vapour deposition and mechanical exfoliation or etching etc. for each material.

3.1.1. Graphene flakes

Graphene flakes have been obtained by mechanical exfoliation and lifting of a chemical vapour deposited film onto a substrate.

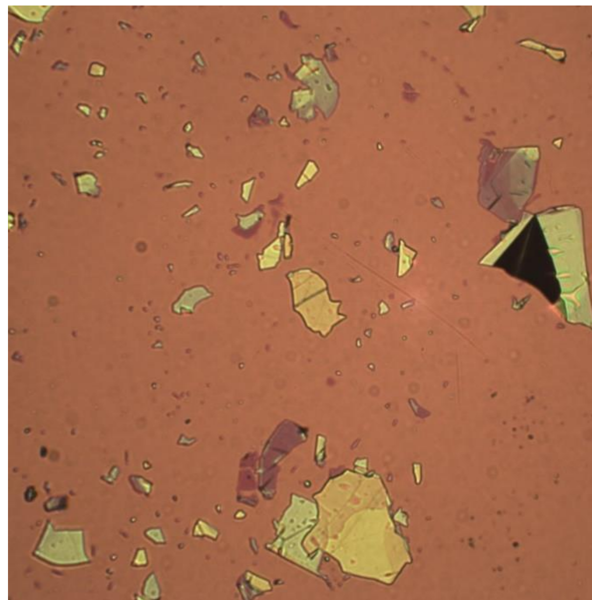

Figure 3.1 Exfoliated graphene transferred onto a Si substrate with top 290 nm SiO_2 layer. Magnification x20. Thin multilayer graphene flakes present pink-like color. Thick flakes are displayed in yellow tones.

In the simplest case, graphene was obtained from the highly oriented pyrolytic graphite (HOPG) bulk by mechanical exfoliation. This process has been carried out following the methods explained in literature[83]. Gel-Pak® tapes with different stickiness values have been tested, establishing Gel-Pak® 4 as the optimum tape. The tape has two polymeric layers protecting the sticky part. Once the soft protecting plastic sheet is removed, the tape is pressed onto the HOPG surface then peeled off in order to obtain some exfoliated graphite from the bulk. In order to obtain thin graphite or even graphene flakes, the peeling process has to be repeated 10 times, always exfoliating the latest peeled area with a fresh area of Gel-Pak® tape in order to not contaminate the newly exfoliated sample. The transfer of the flakes can be made using different methods; the simplest way is to directly press the tape onto the substrate or structure for 1 minute. This method is not very accurate for transferring flakes to a specific region of the sample. The second methodology requires a transfer station for the flake transfer. The transfer station consists of a system made by an optical microscope and two stages, one to control the sample position and orientation and another for a glass slide with the tape and attached exfoliated material (See Figure 3.2).

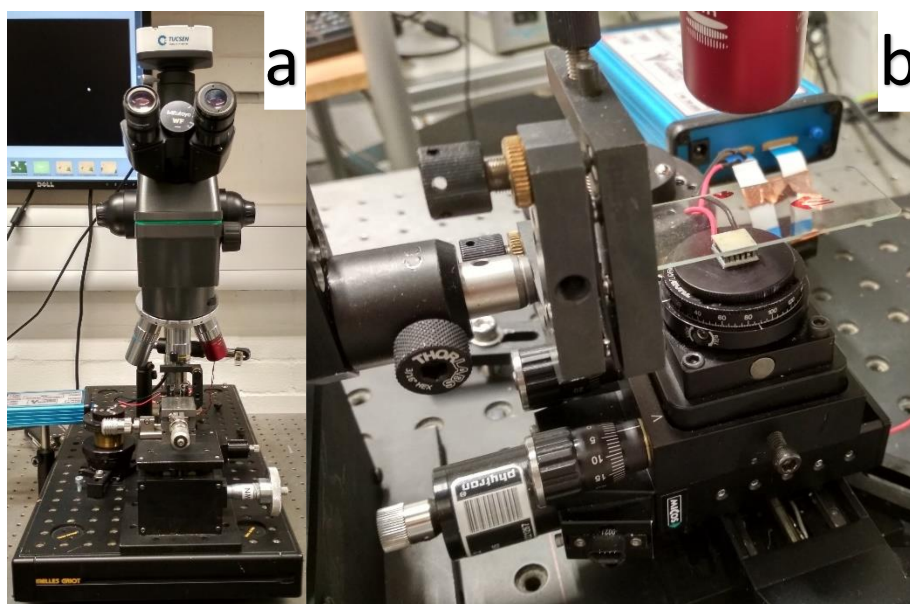

Figure 3.2 2D materials transfer station. a) Front view of the transfer station, showing the setup with the optical microscope and the micro-positioners. b) Lateral view of the stage with a glass slide, where is placed the tape with 2D materials. In addition, the sample stage and its micro-positioners, which allow the tilt and position control, are also shown. There is a Peltier stage on top of the sample stage, to heat up or cool down the sample, to easy the 2D-materials transfer.

This procedure consists of glueing the tape to the glass slide and observing it in the optical microscope where the thin flakes are located. Another option is to glue it to the

substrate with wax. The substrates are first cleaned via sonication with different solvents, firstly with acetone to remove organic material from the surface and then with isopropyl alcohol (IPA). The sample has to be dried with nitrogen to remove the solvent. Then, the sample is cleaned in Ar/O_2 (2%) plasma process to remove any remaining contamination and to activate the surface to facilitate the flake transfer.

For the optimal flake transfer, the sample surface and glass slide with flake attached have to be perfectly parallel. This alignment procedure involves illuminating the sample with a laser through the glass slide, analysing the reflected beam with two laser spots. In case the surfaces are not parallel, the substrate and flake stages allow the tilt manipulation to coincide the spots. The flake transfer can be also made with dissimilar 2D materials.

Whilst the mechanical exfoliation is a simple and cheap method to obtain high-quality graphene, the difficulty of fabricating large flakes is the foremost disadvantage of this methodology. An alternative method is to grow large films of graphene via chemical vapour deposition (CVD) onto SiO_2/Si substrates and then releasing the film by etching the substrate. In this work, we used thin films of graphene grown onto SiO_2/Si substrates with a Ni interlayer, which is easy to etch with a $FeCl_3$ solution, to release the graphene sheet (GRENADA project material). Prior to the etching, the process requires deposition of a layer of poly(methyl methacrylate) (PMMA) with a thickness of 800 nm. The PMMA (950k) is spun in two steps at 1000 rpm, followed by 3 min of annealing at 180 °C. For the etching, the sample is dipped into the $FeCl_3$ (27% w/v) solution for 2 or 3 hours, until the PMMA/graphene film floats in the solution. To remove the remaining etchant from the film, the PMMA/graphene sheet is transferred 5 times into clean glassware with fresh deionized (DI) water, until the $FeCl_3$ is fully rinsed. Then, the graphene sheet can be transferred to the target sample by “fishing” the film. Subsequently, the graphene film is softly blown against the substrate with N_2 to ensure the film is attached to the sample. Afterwards, the sample is heated up for 30 minutes at 180 °C to remove any remaining water and enhance the adhesion between the graphene and the substrate. Finally, the PMMA is removed from the graphene, immersing the sample in pure acetone at 60 °C for 30 minutes and then drying with N_2 to eliminate the solvent.

3.1.2. Multilayer structures of transition metal dichalcogenides

The supported 2D materials' structures of transition metal dichalcogenides (TMDCs) have been directly grown via CVD onto Si substrates with native oxide. During the CVD process, precursors decompose/react and deposit on the exposed substrate at a relatively high temperature. The synthesis of mono- or few layers of TMDCs can be done via different routes; the samples studied in this thesis have been grown via inserting the precursor powder into an alumina boat in the centre of a quartz tube. The substrate is placed with the polished side facing down on top of the boat. The tube is purged with Ar and pressurised. The furnace is maintained at a high temperature (see Fig. 3.3) with constant Ar flow during the deposition process. Controlling the temperature of the synthesis allows the growth of different structures, such as "wedding cake" or "spiral" shape, and using diverse precursors and playing with their activation temperature, it is possible to co-grow different materials in multi-step processes. [84]

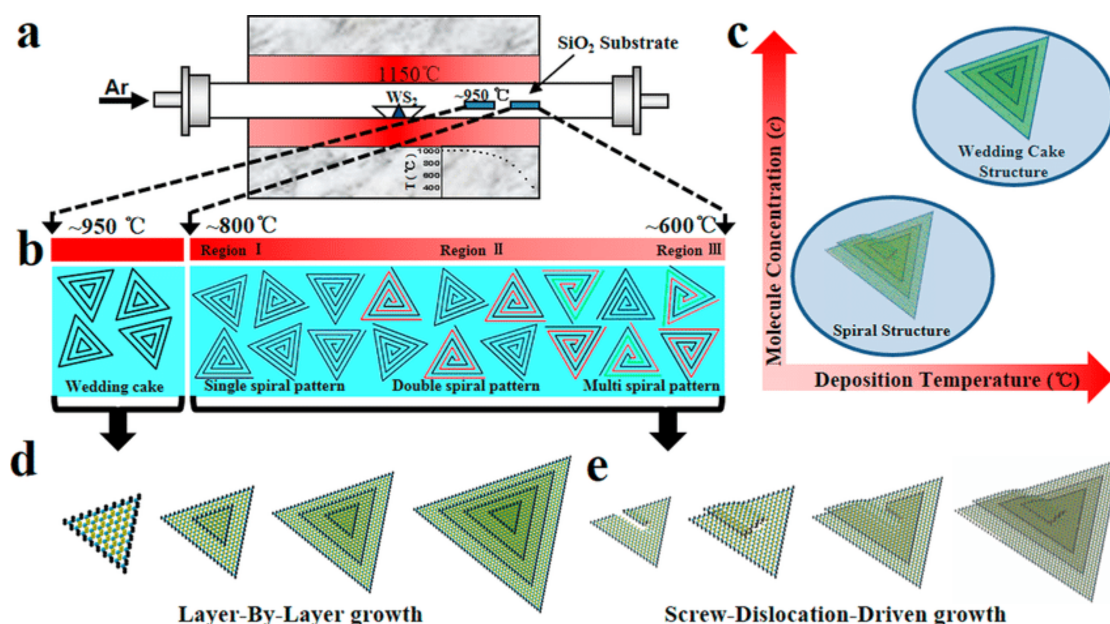

Figure 3.3 Controllable growth of "wedding cake" structure and spiral structure of WS_2. (a) Illustration of the CVD experiment setup for TMDCs synthesis. (b) A schematic of nanoplates illustrate the distribution of wedding cake structures and spiral structures in different deposition regions. (c) Trends in the synthesis conditions for forming the wedding cake structures versus the spiral structures. Schematic illustrations of layer-by-layer (LBL) growth mechanism and (e) screw-dislocation-driven (SDD) growth mechanism. [84]

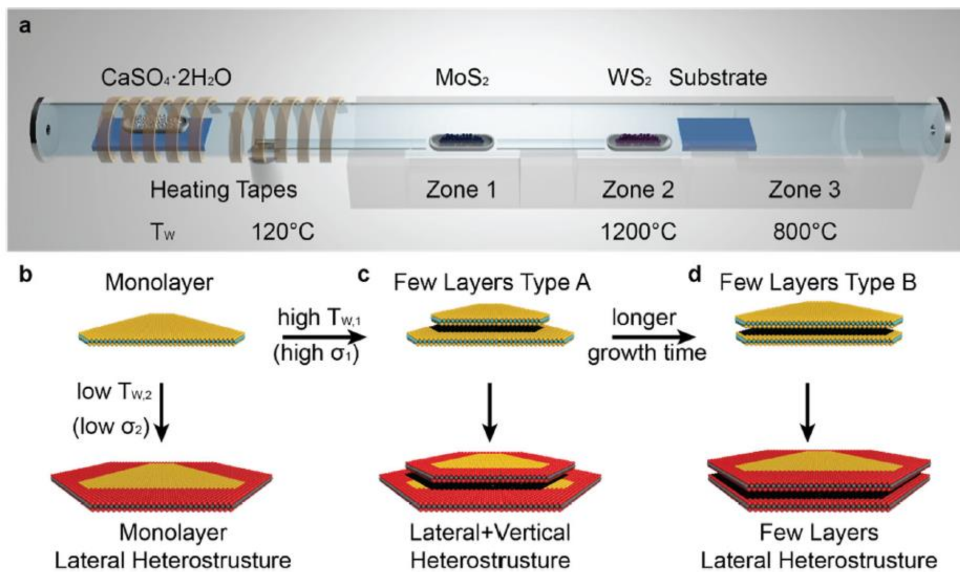

Figure 3.4 (a) Schematic illustration of the experimental setup for WS_2-MoS_2 heterostructure growth by water-assisted chemical vapour transport. The MoS_2 precursor was placed upstream of the WS_2 precursor. When MoS_2 precursor was pushed into Zone 2, WS_2 precursor would simultaneously be pushed into Zone 3, which is downstream of the substrate. (b-d) The growth pathways of WS_2 and WS_2-MoS_2 heterostructures via lateral epitaxy leading to three common types of heterostructures. [85]

The WS_2+MoS_2 lateral heterostructures are synthesised in a two-step process. Firstly, the WS_2 plate is grown and, in the second step, the MoS_2 precursor is activated to grow laterally-epitaxy surrounding the WS_2 layer (See Fig. 3.4).[85]

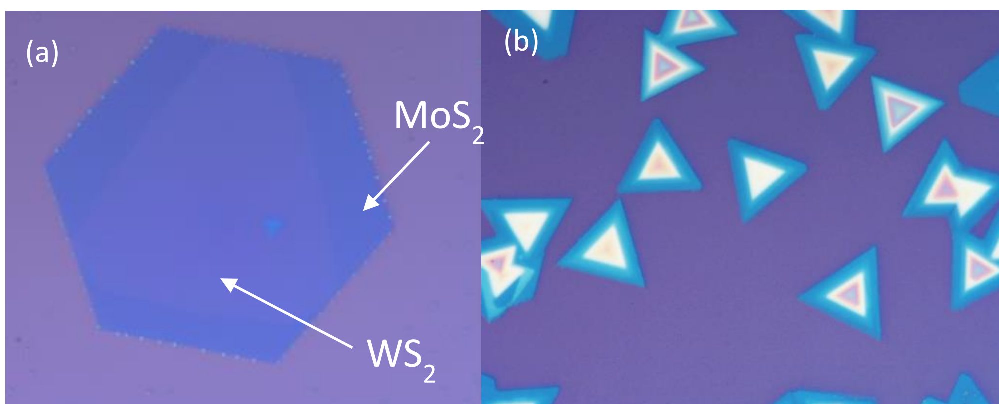

Figure 3.5 Optical images of (a) lateral heterostructure of MoS_2 and WS_2; (b) WS_2 vertical heterostructures.

3.2. Semiconductor nanostructures

Quantum structures are structures of a size comparable with the de Broglie electron wavelength, which restricts the movement of the charge carriers, resulting in quantum confinement. These structures can be categorised by their dimensions, as 0D, 1D or 2D, corresponding to quantum dots (QD), quantum wires (QWi) and quantum wells (QW), respectively. The fabrication of these structures can be made by the combination of different compound semiconductors (CS), which are semiconductors composed by two or more elements, typical groups from the periodic table which form the CS are II-VI and III-V.

3.2.1. III-V materials – growth

The CS samples studied in this work have been grown by molecular beam epitaxy (MBE), which is a technique to obtain high-quality semiconductor crystals. Some of the structures have also been grown by molecular organic chemical vapour deposition (MOCVD). The description of both methods is detailed below.

Molecular beam epitaxy (MBE)

Molecular beam epitaxy (MBE) is an ultra-high vacuum (UHV) technique for producing high-quality semiconductor crystals. The growth process comprises of the sublimation or evaporation of materials in a Knudsen-cell, from solid or liquid sources, respectively, and their condensation on a heated crystalline substrate, which directs the thin film growth and determines the structure. Due to the UHV in the chamber (typically 10^{-10} mbar), the beams of molecules oncoming from different Knudsen-cell have long mean-free-paths (of the order of tens of metres) avoiding their interaction until they reach the sample.

Metal-organic chemical vapour deposition (MOCVD)

Metal-organic chemical vapour deposition (MOCVD) differs from the MBE growth in that MOCVD is not a physical deposition and requires the chemical reaction of the precursors. The basic principle consists of the injection of gaseous reagents into the reactor chamber. These precursors are organic molecules, carrying the required elements (*e.g.* trimethylgallium), which chemically react between each other on the substrate, forming the epitaxial crystals. The thickness and the composition of the epitaxial layers can be precisely controlled by controlling reagent types and flow rates, reactor chamber pressure and substrate temperatures.

3.2.2. Heterostructures – MQW, QD and VCSEL

Both methodologies, MBE and MOCVD, permit control of the thickness and composition of the growth, allowing for the growth of very complex structures. In this section, we detail the studied heterostructures formed by the stack of multiple layers, such as multiple quantum wells (MQWs) and VCSELs.

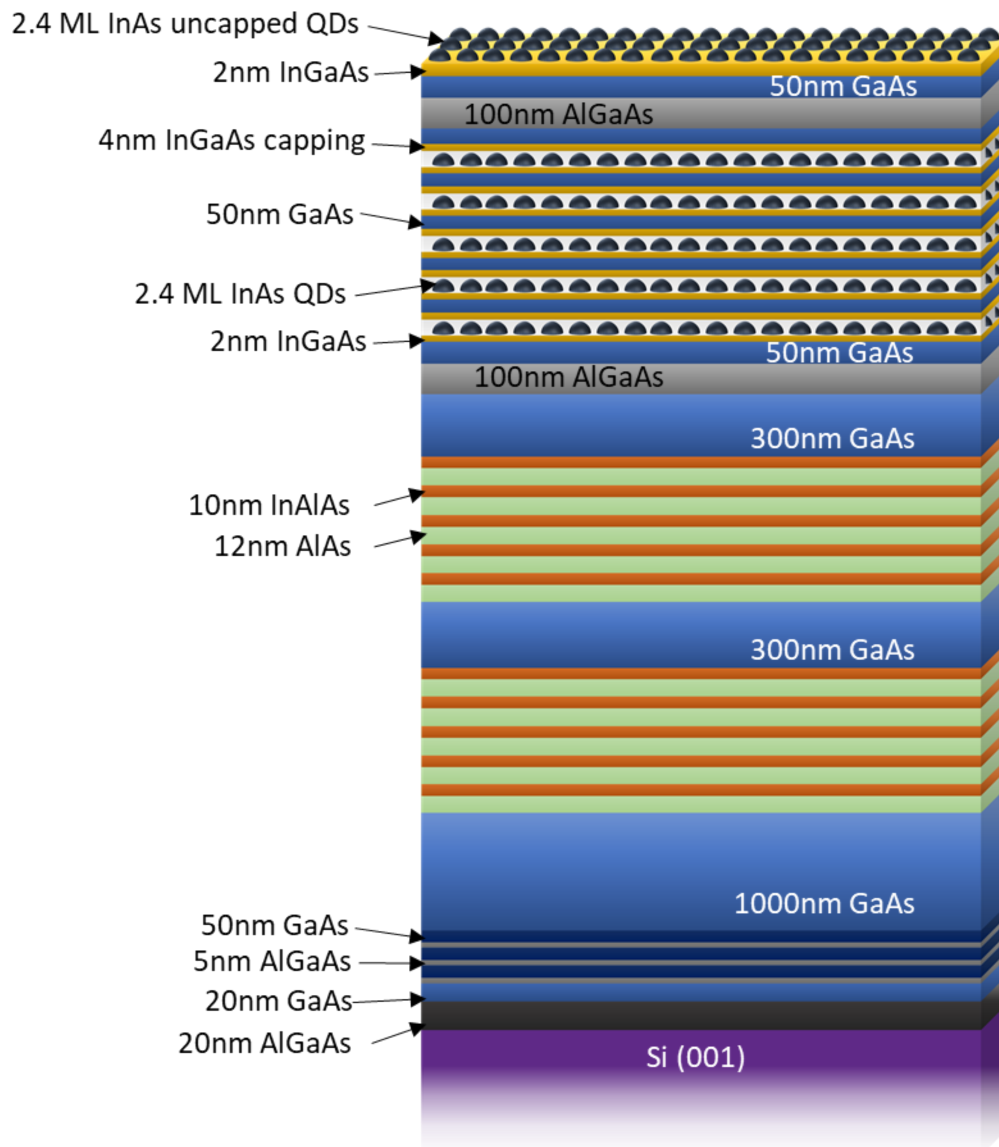

Figure 3.6 Schematic diagram of MQW structure scheme grown on Si substrate with the top layer of uncapped InAs QDs, followed: by 2 nm InGaAs, 50 nm GaAs, 100 nm AlGaAs, 5 periods of GaAs/InGaAs/InAs QDs/ InGaAs, 50 nm GaAs, 100 nm AlGaAs, 300 nm, 2 sets of 5 periods of InAlAs/AlAs separated by 300 nm GaAs, 1000 nm GaAs and 4 periods of GaAs/AlgaAs.

Multiple quantum wells

The QWs are formed by growing different materials on top of each other, embedding thin layers with narrow bandgaps between areas of wider bandgap material. When the narrow bandgap material layer is sufficiently thin then the charge carriers will be confined in this region and the areas with wide bandgap material act as barriers to charge carriers. The stack of several QWs is known as a MQW. Additional to the quantum confinement, MQWs may also suffer from the strain effect in the thin lattice-mismatched layers.

Quantum dots

QD are typically grown by the Stranski-Krastanov method, in which the strain is released by the island formation above the critical thickness of the layer. Due to the small size of the islands, the charge carriers are confined in all three dimensions.

The structures of the samples studied in this work, see Fig. 3.6, were grown on silicon substrates (001), alternating layers of AlGaAs/GaAs, with different thicknesses. Then, there is a layer of GaAs of 1 μm thick, followed by two sets of defect filter layers (DFL) of 5 periods of InAlAs/AlAs (10 and 12 nm thick, respectively) separated by 300 nm GaAs. Afterwards, 100 nm of AlGaAs and 50 nm of GaAs were grown, sandwiching five layers of InAs/GaAs dot-in-the-well (DWELL). Each layer of DWELL has three monolayers of InAs deposited on 2 nm of $In_{0.15}Ga_{0.85}As$ and capped with 6 nm of $In_{0.15}Ga_{0.85}As$. The DWELL structure is sandwiched between a 50 nm GaAs and 100 nm $Al_{0.4}Ga_{0.6}As$ layer. InAs QD layers were also grown in the top surface.

Vertical cavity surface emitting lasers

Semiconductor lasers can be categorised into two groups: conventional edge-emitting where the light is emitted from the cleaved facets of the semiconductor; and surface-emitting lasers, which emit from the top of the structure.

The surface-emitting structures known as vertical-cavity surface-emitting lasers (VCSELs) contain an active region sandwiched between two distributed Bragg reflector (DBR) mirrors. The wavelength of the laser is determined by the thickness of the cavity within with the MQW or QD of the active region located. The DBR mirrors comprise of a large number of pairs of layers of two different semiconductors with different refractive indices, with a period corresponding to a quarter-wavelength for the constructive interference, to maximise the reflectivity.

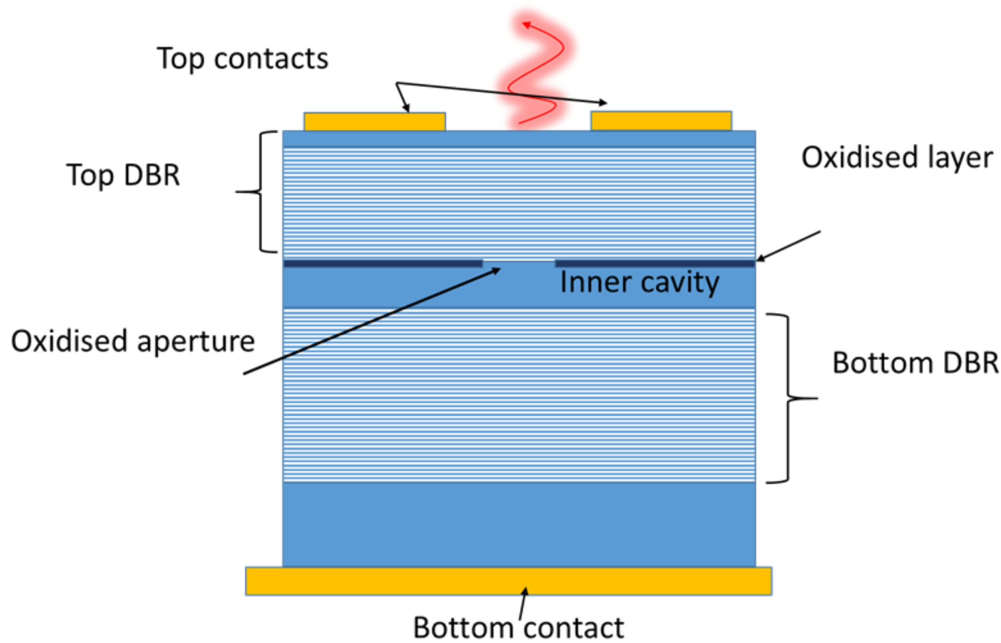

Figure 3.7 Scheme of a lateral view of a VCSEL device.

VCSEL structures have a diverse range of applications, including optical fibre data transmission, display and illumination purposes, biological tissue analysis and sensing applications.

The two VCSEL samples studied in this work comprise of a triple GaAs or InGaAs QW in the active region. In both cases, the top DBR mirror had 20 periods of AlGaAs layers with alternating composition and the bottom mirror was formed by 34 periods of the same structure as the top one. [14, 86]

3.2.3. III-nitrides - GaN nanowires

III-nitrides are excellent candidates for optoelectronic applications, such as solid-state lighting, full-colour displays, laser printers and high-density information storage, due to their wide variable bandgaps which cover a wide range of the spectrum, from the deep UV to the infrared. In the particular case of GaN, it shows a bandgap value of 3.39 eV, 1245 $cm^2 V^{-1} s^{-1}$ in electron mobility and 1.3 W cm^{-1} $°C^{-1}$ in thermal conductivity.

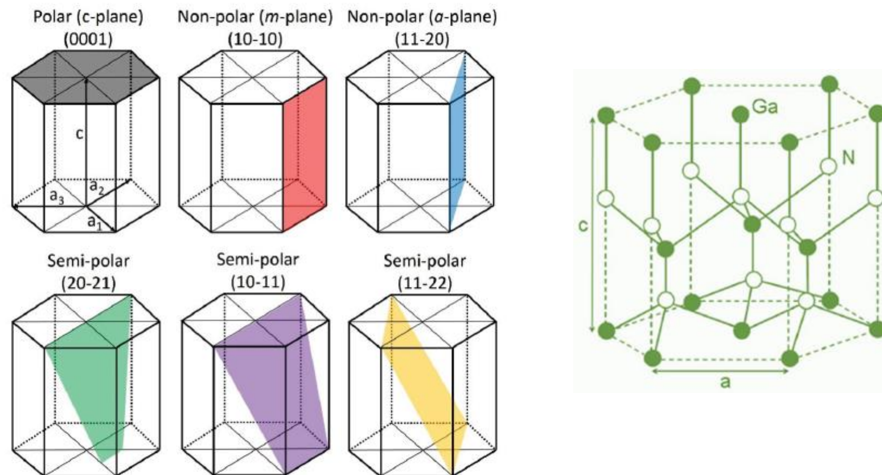

Figure 3.8 (a) Crystallography and c-axis orientation for the growth of GaN layers. Grey scheme shows polar growth with c-axis normal to the layer surface; the growth plane is the (00-01). Red and blue schemes show non-polar growth with c-axis parallel to the layer surface; the growth planes are m-plane (10-10) and a-plane (11-20) respectively. Green, purple and yellow schemes show semi-polar growth with the c-axis inclined with respect to the layer surface; these present the growth planes: (20-11), (10-11) and (11-22), respectively. (b) Wurtzite structure of GaN. [87]

Two different crystal structures are possible in the III-nitrides, named wurtzite and zinc-blende. The GaN samples studied in this work show the wurtzite structure, which is the most thermodynamically stable. The GaN wurtzite cell structure has each nitrogen atom connected to four Ga atoms, forming a hexagonal close-packed configuration, see Fig. 3.8b. This unit cell is characterised by the in-plane a=3.19 Å and out-of-plane c=5.189 Å lattice parameters. The GaN wurtzite crystals are non-centrosymmetric structures, having two possible polar orientations, denoted by Bravais-Miller indices [0001] and [000-1]. The [0001] direction represents the Ga-face plane, meaning the surface is terminated by Ga atoms, while the N-face is labelled by [000-1]. The polarity plays an important role in the epitaxial growth, which usually determines its direction, as well as in the material properties, such as thermal and chemical stability, doping ability, crystalline quality and piezoelectricity. [88]

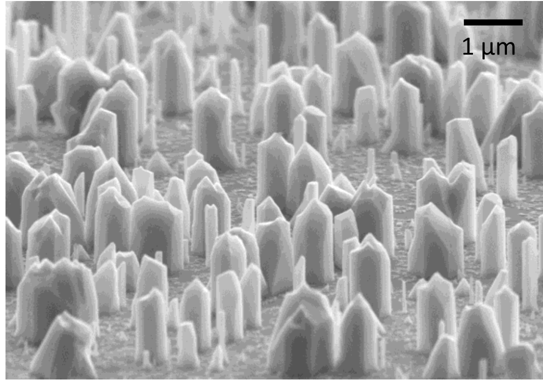

Figure 3.9 SEM image of GaN NWs onto Si substrate.

The samples studied in this work were GaN nanowires grown on (111) Si substrates employing the Thomas Swan close-coupled showerhead reactor using MOCVD. Trimethylaluminum (TMAl), trimethylgallium (TMGa), and ammonia (NH_3) were employed as precursors with H_2 used as the carrier gas for each. Initially, the Si substrate was annealed in an H_2 ambient at 1110 °C for 600 s to remove the natural oxide layer on the surface. Then, 2.7 µmol/min of TMAl was flowed at 1145 °C for 72 s. Preflowing TMAl on the Si substrate generated Al or Al−Si alloy nanodots, which served as nucleation sites for subsequent GaN nanowire growth performed at 866 °C with 6.2 µmol/min of TMGa and 20 mmol/min of NH_3 for 3800 s. The pressures used during the flow of TMAl and the GaN nanowire growth were 65 and 300 Torr, respectively. [89]

3.3. MEMS devices - mechanical resonators

Microelectromechanical systems and their scaled-down siblings, nanomechanical systems, MEMS and NEMS respectively, are micro- or nano-scale vibrating structures, which can take different shapes as cantilevers, double clamped beams, plates, membranes and tuning forks, to mention some of them. The scaling of these structures to the micro or nano size allows for the tuning of their properties due to their low size, including high frequency and fast time response, and lower power dissipation.

Here we present three types of MEMS and NEMS structures, which have been studied and implemented during the course of this thesis.

3.3.1. Silicon nitride membranes

Commercial silicon nitride (Si_3N_4) membranes, Agar scientific S171-6 with a square window of 500x500µm^2 and thickness of 200nm, have been used as a test sample for the study of the distribution of the vibrational mode via laser Doppler vibrometry (LDV) and scanning probe microscopy (SPM).

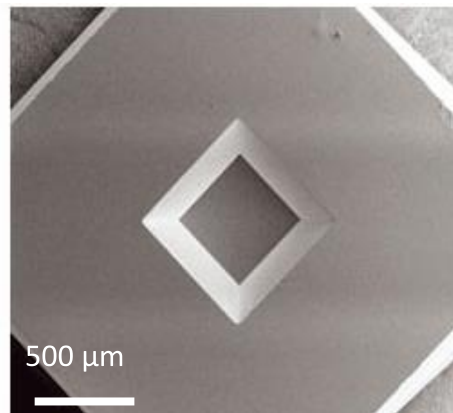

Figure 3.10 SEM image of the silicon nitride membrane. (Agar Scientific)

3.3.2. Tuning forks and cantilevers

Important devices for this work have been tuning forks and AFM cantilevers, which have been treated both as samples and measurements tools. Therefore, they have been extensively studied, theoretically and experimentally, to understand their response during the measurements.

Tuning forks

Tuning forks (TF) are MEMS widely implemented in a different kind of microscopy, such as scanning near-field acoustic microscopy (SNAM), scanning near-field optical microscopy (SNOM) and non-contact AFM (nc-AFM), in particular with the TF derived qPlus sensor. [90] Moreover, due to the high precision that these devices offer, they have also been used as a time reference, viscosity sensors and detectors of quantum vortexes in superfluids. [91, 92] The materials used in the fabrication of the tuning forks have to be piezoelectric, providing the electrical detection of the mechanical displacement or response to an electrical excitation. In this work, two different types of TF have been used, with different geometry and materials, namely, quartz and $LiNbO_3$.

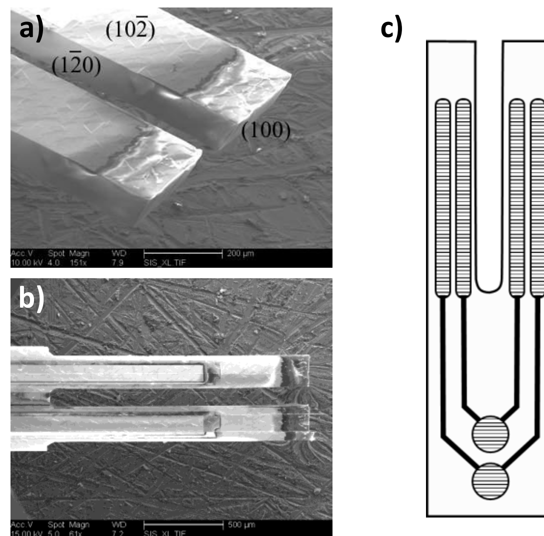

Figure 3.11 (a) and (b) SEM images of a 76 kHz, 393 kHz, multimode quartz TF, showing the two tines in detail. (c) $LiNbO_3$ TF scheme, showing the electrodes shape and location in detail. [93]

The quartz tuning forks used in this work were manufactured by Micro Crystal AG. The TF prongs were designed to have a width of $T = 2.23 \times 10^{-4}\ m$, a thickness of $W = 1.43 \times 10^{-4}\ m$ and a length of $L = 1.61 \times 10^{-3}\ m$. This characteristic geometry and the quartz intrinsic properties, *i.e.* density $\rho = 2659\ kg\ m^{-3}\ m$ and Young's modulus $E = 78.7\ GPa$ [94],

precisely define the resonance frequency of the system. The fundamental resonance frequency of the flexural mode $f_{flex-Quartz} = 75kHz$ was calculated by the following formula:

$$f_0 = \frac{1}{2\pi}\sqrt{\frac{k}{m_{eff}}}, \qquad (44)$$

where

$$k = E\ W\ T^3/4L^3 \qquad (45)$$

is the spring constant of the system[95], and m_{eff} is the effective mass defined by

$$m_{eff} = C_O \rho LTW, \qquad (46)$$

with $C_0 = 0.25$ as the constant determined by the Bradley *et al.* [96] model, ρ is the density, and L, T and W are the length, thickness and width, respectively.

Equally, the resonance frequency $f_{flex-LiNbO_3} = 25.26kHz$ of the $LiNbO_3$ TF was determined, using the measured geometrical parameters: $W = 1.12 \times 10^{-3}\ m$, $T = 9.6 \times 10^{-4}\ m$ and $L = 6.05 \times 10^{-3}\ m$; and the density and Young's Modulus[99] from the literature $\rho = 4643\ kg\ m^{-3}$ and $E = 170\ GPa$. [97]

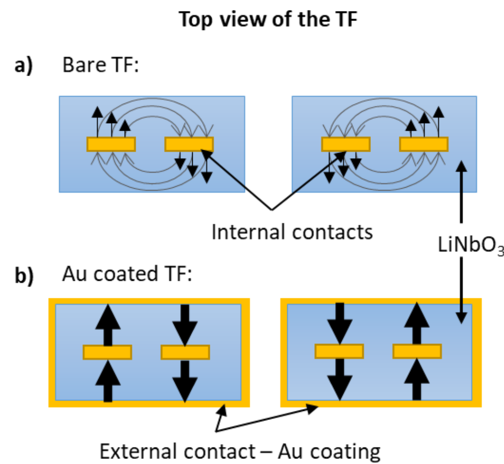

Figure 3.12 Schemes of the top view of the TF with the representation of the electric field in the $LiNbO_3$ TF (a) bare and (b) with Au coating, respectively.

The $LiNbO_3$ TF, contrary to the quartz ones, have electrodes sandwiched between two plates of $LiNbO_3$ [98]. This allows the devices to normally operate in different environmental conditions, such as immersed in a conductive fluid, without shorting the circuit. In addition, the $LiNbO_3$ TF were coated with Au to create the third electrode for the ground. In this way,

the electrical response of the TF is much higher than the uncoated quartz TF because the "orthogonal" component of the electric field is considerably increased due to the third electrode (See Fig. 3.12).

Cantilevers

An AFM cantilever's behaviour is determined by the geometry and the material used. The length and thickness of the beam are the most relevant terms to determine the resonance frequency of the cantilever. Depending on the physical properties to be probed, such as mechanical, electrical, piezoelectric or thermal ones, the cantilever has to be made of a different material or with a different coating.

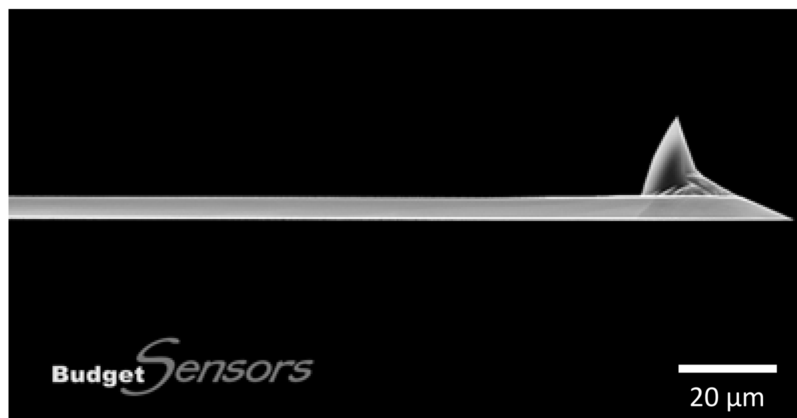

Figure 3.13 SEM image of a typical contact mode cantilever from Budget Sensors (ContAl-G 13kHz).

In this work, we have used silicon cantilevers for the study of the sample morphology and mechanical sensing of the samples. The aluminium coating on the backside of the cantilever increases the reflection of the laser, for a better sensitivity. The cantilevers we used have three different lengths and therefore different resonance frequencies: low frequency - 13kHz (ContAl-G, Budget Sensors) for contact mode and soft samples, 75kHz (Multi75, Budget Sensors) for contact mode and stiff samples or soft tapping and 300kHz (*Tap300Al*-G, Budget Sensors) for the true tapping mode.

For the electrical or piezoelectrical measurements, we have used Si cantilevers with PtSi or doped-diamond coating. In the case of non-contact electrical measurements such as KPFM, the ideal cantilever was 75kHz with PtSi coating, which can work in tapping or contact mode providing good conductivity and reasonable sharpness of the tip to allow for high-resolution

imaging. For the piezoelectric probing, a softer conductive probe was needed, and 15kHz diamond-coated cantilever was used, which was more robust coating than PtSi.

3.4. Sample preparation

Some of the samples required prior sample processing to allow the probing method to access to the area of interest. In particular, in the 3D study of complex structures, the samples were sectioned with the novel methodology developed and patented by Kolosov and Grishin at Lancaster, beam exit cross-sectional polishing (BEXP).[99] For the sectioning of geometrically complex samples, such as with nanowires, this also required additional steps, such as coating with spin-on glass (SOG), which is detailed below. In this section, we also describe the fabrication of graphene nanodrums on silicon patterned substrates, including an explanation of the processing used in the fabrication of cavities.

3.4.1. Beam exit cross-sectional polishing (BEXP)

BEXP consists of a methodology for the sectioning of the samples with a small angle from the top surface via argon ion (Ar+) beams. BEXP uses a modified Leica Microsystems EM-TIC020 or EM-TIC 3X, with three independently controlled Ar+ guns with accelerating voltage between 1 – 8 kV. Each ion gun is composed of a front and a rear cathode assembled with two Wehnelt cylinders, which are isolated from the central anode by ceramic cylinders, see Fig. 3.15.

Figure 3.14 Images of the EM-TIC020 or EM-TIC 3X. https://www.leica-microsystems.com/products/sample-preparation-for-electron-microscopy/p/leica-em-tic-3x/)

Plasma ignition is produced via Ar ionisation from an electric field between the cathode and the anode. The argon gas is pressurised to the gun at 500 mbar, the Ar cations are accelerated towards the cathodes, generating electrons. The electrons will be accelerated

towards the anode, generating new ions due to the collisions with Ar atoms on their way. One of the beams is blocked by the (blind) rear side cathode, and the other beam is lead through the beam exit at front side cathode.

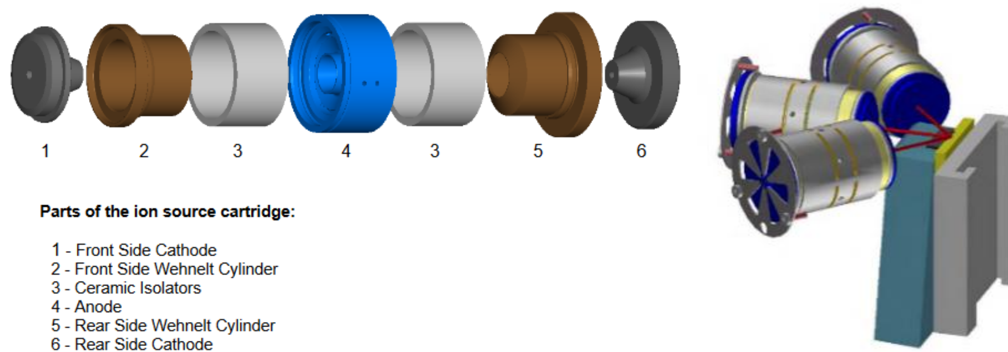

Figure 3.15. Parts of the ion source cartridge. Scheme of the three guns with the focused beams onto the sample. (http://smif.pratt.duke.edu/sites/smif.pratt.duke.edu/files/operating/EMTIC3X_16771403_OM_EN_07_17.pdf) (http://www.semat.lab.uminho.pt/Documentos/TIC%203X%20-Ion%20Beam%20Milling.pdf)

In a conventional cross-sectioning system, the sample is mounted in a holder perpendicular to the ion beams. Inside the system, the sample is mainly covered by a mask, which is protecting most of the surface from the beams and only exposing the interesting area to be milled. In the BEXP configuration, the sample holder has been modified to insert an angled stage. The tilt of the stage is between 0.5 and 30 degrees. The sample is glued to the stage with wax (see Fig. 3.16). Before ion polishing, the sample is mechanically polished with diamond lapping papers of decreasing roughness, to modify its geometry to ensure a perfect perpendicular surface to the beams and parallel to the mask. The sample is placed in the Leica system and aligned to expose 20 – 40 µm of the material above the mask. Once the system is closed, the pump evacuates the chamber. When the vacuum reaches approximately $2{\cdot}10^{-5}$ mbar, the Argon lines are purged 3 times to ensure a clean environment. In the EM-TIC020 system, the warm-up process has to be manually operated, starting with a warm-up process for 10 min at 3kV, before being increased to 5-7 kV. In the EM-TIC 3X, the warm-up process is automatically done by the system. The majority of sample cuts were done at 7 kV. The system is left until beam-exit occurs and the milled area is as wide as approximately a few hundreds of um, which is detected using the stereo microscope mounted on top of the system. Then the accelerating voltage is reduced to 1 kV for 10 min to gently polish the surface at a low energy and reduce the surface roughness.

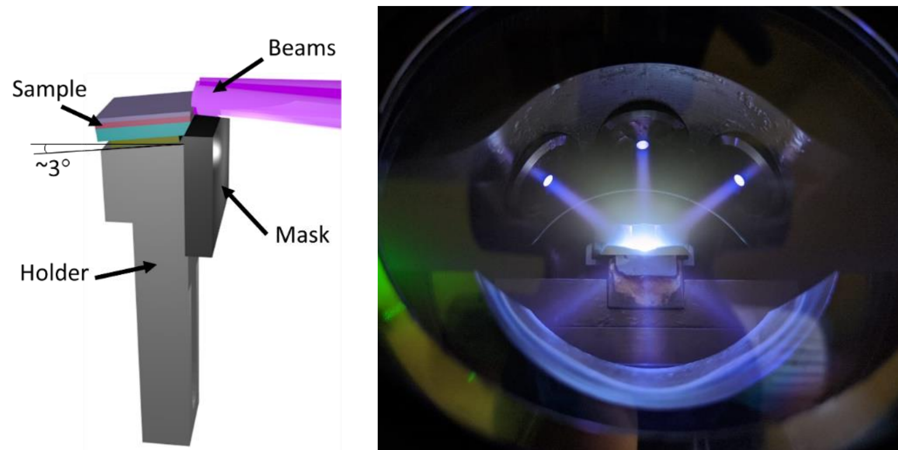

Figure 3.16 Scheme of the sample mounted on the holder in the mask-beam configuration. Real image of the three beams focused on the sample.

As the beam-exit has to be observed by the eye, it can be difficult to precisely determine when the cut is finished. It the cut is not finished a “tooth” of material can be left behind, making the study of the near-surface layers difficult or even impossible.

3.4.2. Nanowires processing with spin-on glass (SOG)

Non-uniform 3D structures, such as nanowires on the surface difficult the cross-section to good-quality. This type of sample was embedded in spin-on glass (SOG) to create a “uniform bulk” sample. SOG is a silicate-based solution with organic solvents commonly used in the semiconductor industry. The low viscosity of this substance allows for coating the samples with a thin film which becomes solid after the evaporation of the solvents. The processing requires the deposition of a drop of SOG on the sample and spinning it at 4000 rpm for 20 seconds to obtain a uniform film with adequate thickness (around 700nm). Afterwards, the sample has to be baked at 150°C for 10 minutes to solidify the SOG. Slow cool down of the sample is required to avoid cracks in the film.

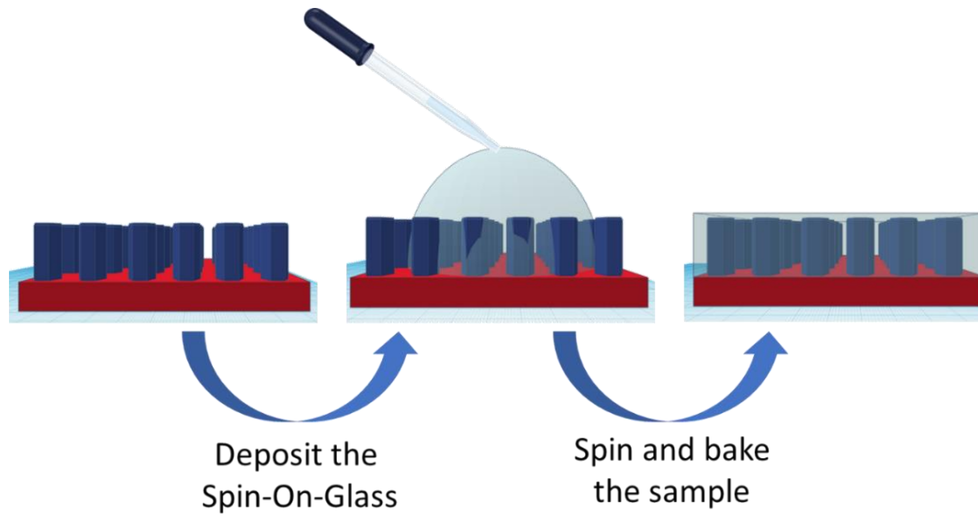

Figure 3.17 Spin-on-glass (SOG) processing. A drop of SOG is deposited using a pipet. Then, the sample is spun to create a uniform thin film. Finally, the sample is baked to remove the solvent and solidify the SOG.

3.5. Fabrication of graphene nanodrums on patterned Si substrates

In the quest to prove the predicted high performance of 2D materials in the fabrication of mechanical resonators, graphene nanodrums were fabricated on patterned silicon substrates.

The silicon substrate patterning was carried out in the Lancaster Quantum Technology Centre (QTC) facilities at Lancaster University. The processing procedure is explained below. The graphene exfoliation and subsequent transfer was performed following the protocol detailed in section 3.1. HOPG graphite was exfoliated with Gel-Pak® 4 and directly transferred onto the patterned substrate.

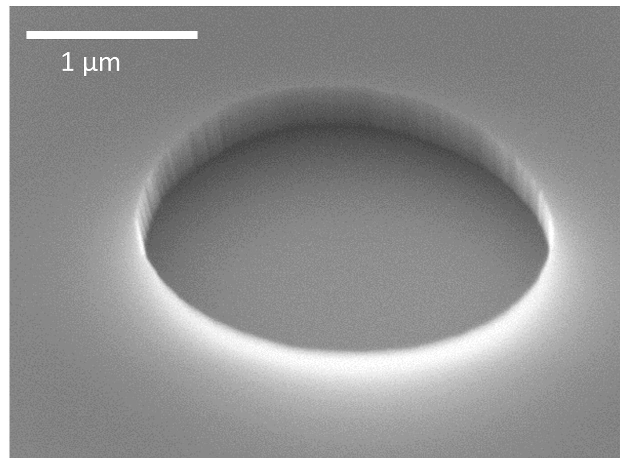

Figure 3.18 SEM image of a hole patterned in the SiO_2/Si substrate by photolithography.

During substrate preparation, holes of 1.5 µm diameter were etched in the silicon wafers in a layer of 300 nm of silicon oxide. The processing used for the hole fabrication is commonly known as photolithography. The silicon wafer was cut in squares of 1x1 inch, cleaned in an ultrasonic bath with acetone and IPA, respectively, for 10 minutes, and dried with nitrogen. Oxygen plasma cleaning for 3 minutes was also performed to remove any remaining organic residue. The sample was spin-coated with resist S1813 and baked for 1 minute at 115°C. The UV exposure of the sample was made using hard contact for 20 seconds in the SUSS MicroTec MJB4 Mask Aligner system. A new bake step was performed, for 1 minute at 115°C. The resist developer used was MF319 for 90 seconds. The etching process in the Oxford Instruments reactive ion etcher (RIE) system requires cleaning and pre-conditioning of the chamber prior to inserting the sample: cleaning with 2 minutes of O_2 and pre-conditioning with CHF_3+Ar for 3 min. The etching recipe was 7 minutes 30 seconds, CHF_3 25 sccm and Ar

sccm, 30 mTorr and 150 W in the chamber. For the last sample cleaning, 2 minutes of oxygen plasma in RIE and then acetone and IPA to remove the remaining resist, and drying with N_2.

3.6. Summary

This chapter reviews the materials, the preparation of the samples and the devices investigated throughout this thesis. First, we explained 2D material sample preparation including exfoliation, lifting and transfer of the flakes, as well as chemical vapour deposited plates and heterostructures. Then, we reviewed the methods for the synthesis of compound semiconductor samples, including MBE and MOCVD, and the different types of compound semiconductor structures, including the multiple quantum wells, the VECSELs and the GaN nanowires, which are studied in the final experimental chapter. We also introduced the sample preparation methodology using the BEXP. Furthermore, in this section we first reported the processing used for the embedding of 3D structures, such as nanowires, using spin-on-glass. Finally, we reviewed the mechanical resonating devices examined in the next experimental chapter, including AFM cantilevers, tuning forks, Si_3N_4 membranes and graphene drums.

4. Nanoscale physical property measurements – methods development

4.1. Introduction

Since the invention of scanning probe microscopy (SPM), it has become a fundamental tool in the investigation of nanoscience and nanotechnology, thanks to its atomic-scale spatial resolution and sensitivity to a wide diversity of physical properties. In particular, atomic force microscopy (AFM) and all its derived methods for the mapping of mechanical, electrical and thermal properties have enabled measurements of stiffness, electrical and heat transport, respectively.

Historically, the study of vibrational modes in mechanical resonators has been performed by diverse optical methodologies, such as the knife-edge method, interferometric systems, etc. However, the down-scaling of devices, such as micro/nano-electromechanical systems MEMS/NEMS, requires characterisation methods with nanoscale spatial resolution, and while optical methods can be very sensitive to vertical displacement, they are limited in spatial resolution by the light wavelength.

4.2. AFM as a platform for nanoscale properties mapping

Throughout this research, all SPM measurements were carried out using a Bruker MultiMode AFM (MM-SPM) with NanoScope controllers IV and V. The MM-SPM comprises of the base unit, the scanner tube and the SPM head. The base unit contains the SPM electronics, the signal displays and the switches for the mode selection (STM, AFM & LFM and TM-AFM) and the motor control for the motion in the z-direction. A support ring holds the scanner tube and the retaining springs to hold the head in place. The scanner tubes are interchangeable and the longer scanner allows for a large scan size. However, shorter scanners are less sensitive to noise for small scan sizes than longer ones, being more appropriate for atomic-scale imaging. The SPM heads contain the optical setup, including the laser, mirror and photodiode array, and the corresponding screws for the laser alignment and cantilever positioning. The photodiode array is divided into four elements and the combination of the information of the four sections provides different information depending on the operating mode. Inside the head, there is also a mounting in which to place the tip holder and clamp it. The sample and mode of SPM to be performed dictate the choice of tip and tip holder.

4.3. SPM - Electrical measurements

For SPM measurements sensitive to the electrostatic probe-sample interaction, it is necessary to electrically contact the sample, to excite or ground it. The contact with the sample can be made by a conductive epoxy or paint, such as silver paint. The standard experimental setup requires a signal generator to apply the AC+DC bias, a lock-in amplifier (Stanford Research System SR830) for the signal monitoring, a conductive probe and a special probe holder adequately modified for the electrical driving or readout (See Fig. 4.1).

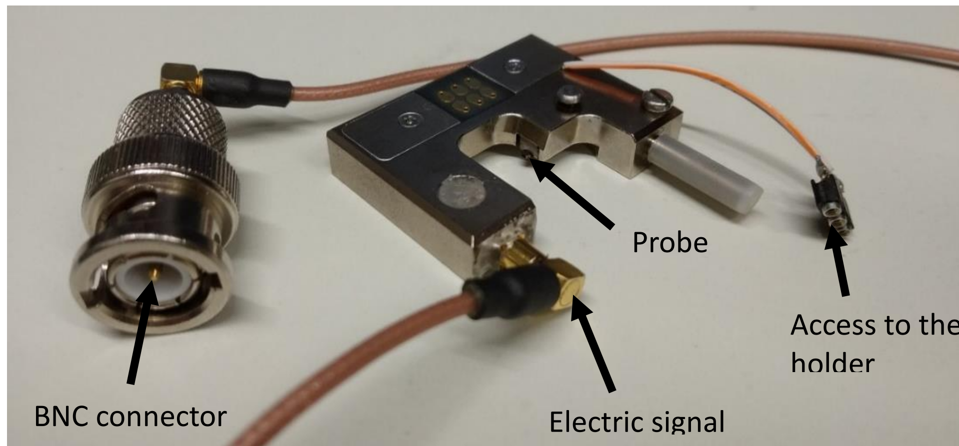

Figure 4.1 Probe-holder for electric measurements. With BNC cable for the active drive or detection. An additional connection to the ground.

However, in some cases, electrical driving is through the sample, and the tip has to be conductive and grounded. In this case, a normal cantilever holder is suitable for the measurements because all the standard holders generally ground the connection with the tip. In any case, a ground connection has to be extracted from the holder to ground the whole system at the same potential. This connection can be seen in Fig. 4.1.

4.3.1. Kelvin probe force microscopy

The Kelvin probe force microscopy (KPFM) mode implemented in the measurements of this thesis is the FM-KPFM. In this case, the magnitude used in the detection is the force gradient between the tip and sample, which affects the effective spring constant of the cantilever. The total effective constant can be modelled as two springs in parallel, being the sum of the natural spring constant k_c of the cantilever and the electric field gradient $\partial F_{el}/\partial z$

$$k_{eff} = k_c - \frac{\partial F_{el}}{\partial z}. \tag{47}$$

Therefore, the resonance frequency will change, being approximately

$$\Delta\omega \approx -\frac{\omega}{2k_c}\left(\frac{\partial F_{el}}{\partial z}\right). \quad (48)$$

Hence, modulating the gradient force via an AC bias, the resonance frequency of the cantilever will be also modulated. The cantilever oscillation will have a component corresponding to the mechanical oscillation of the tapping $f = \omega/2\pi$, with the two sidebands of the AC modulation of the electric field $\pm f_m = \pm 1\ kHz$. The amplitude of the sidebands is used in the KPFM feedback, as this amplitude measures the resonance frequency modulation amplitude. Adjusting the DC bias such that the sidebands disappear leads to the point $V_{DC} = V_{CPD}$. [100]

The FM-KPFM measurements are made in tapping mode. The tapping signal is picked through the break-out box to trigger the excitation signal of the signal generator. The excitation and detection are made by the zi-HF2LI lock-in amplifier (Zurich Instruments, Switzerland). The driving signal is a mixture of AC+DC. The AC signal is made by a sine wave with the frequency of the tapping signal frequency, modulated at 1kHz to create the sidebands for the measurement. The sidebands are close to the resonance frequency to provide a high cantilever response and enhance the cantilever sensitivity. Nevertheless, they have to be far enough to not create crosstalk between the mechanical and the electrical response. The DC component is controlled by the proportional, integral and derivative (PID) feedback, trying to nullify the electrostatic force between tip and sample, this magnitude is directly linked with the surface potential. The potential difference between the tip and the sample is nullified when the surface potential of the tip is equal to the sample one. Therefore, the sample work function is estimated by the potential applied to the sample/tip to compensate for the difference between their surface potentials. The tip work function has to be determined in a calibration sample, where the work function is known, such as a platinum or gold film.

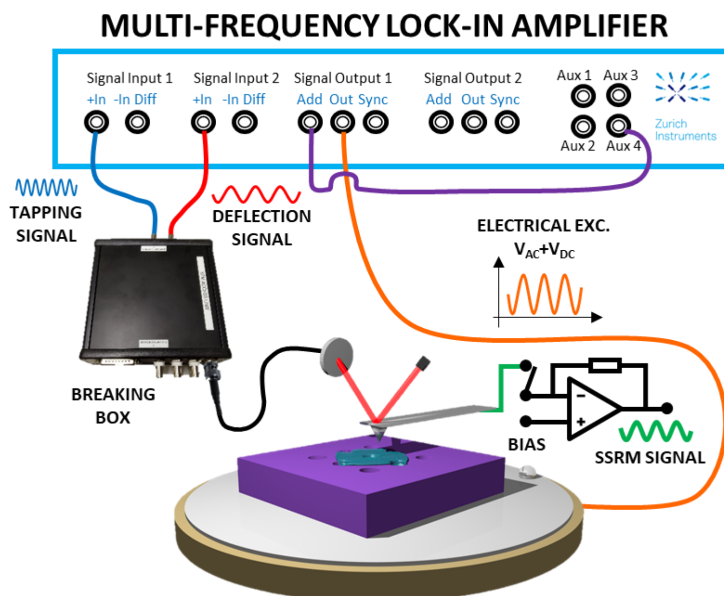

Figure 4.2 General setup for electrostatic SPM measurements. KPFM, D-EFM and SSRM setups are included in the scheme. The electrical excitation applied to the sample is represented by an orange cable, which connect the lock-in output to the sample. This is used all the setups. KPFM and D-EFM setups use the tapping (blue cable) and deflection (red cable) outputs from the breaking box, to trigger the signal and monitoring of the cantilever response, respectively. In addition, KPFM uses the purple cable connecting an auxiliary output of the lock-in, which provides the DC voltage to nullify the tip-sample electrostatic force, to the add input of the driving output. SSRM setup is represented with the green cable, which connects the cantilever (by the electric holder) with the I-V converter scheme.

In order to determine the CPD with accurate precision, closed loop KPFM measurements were performed using the following protocol. Firstly, it is necessary to synchronise the oscillation of the probe with the signal monitoring in the lock-in amplifier (LIA). This is done by tracking the phase of the tapping signal with the phase lock loop (PLL) in the LIA. The tapping signal is directly extracted from the breaking-box and fed into the LIA, being monitored at the tapping frequency by one of the demodulators. The resonance frequencies for the tapping mode of soft-tapping / force modulation cantilevers are usually around 70 kHz. Once the tip is approached, it is necessary to lift it by 50 nm above the surface so it is only sensitive to electrostatic interactions. The CPD is manually determined by shifting the DC bias voltage applied to the sample using one of the auxiliary channels as a “manual” offset until the electrostatic force is nullified. This minimum value will be used as a reference in the following steps. In order to be more sensitive to the electrostatic forces, initially, the bias offset is selected far from the CPD value. To follow, an AC modulation is added to the bias voltage. This modulation results with two sideband peaks on each side of the resonance (see Fig. 4.3). Since the X-component of the sidebands (*i.e*. the X-component of the measured signal that is

in phase with the reference signal) is the magnitude of interest, it is necessary to minimise the Y-component to optimise the phase of the signal (obtaining maximum X-component with 180° difference between the sidebands). To perform the close loop measurements, the DC component of the bias is monitored in the PID feedback loop. It is recommended to start with a moderate value for the Integral-gain (I), such as 10kV/Vrms, and gradually increase the Proportional-gain (P) until reaching the desired noise level, but below feedback oscillation.

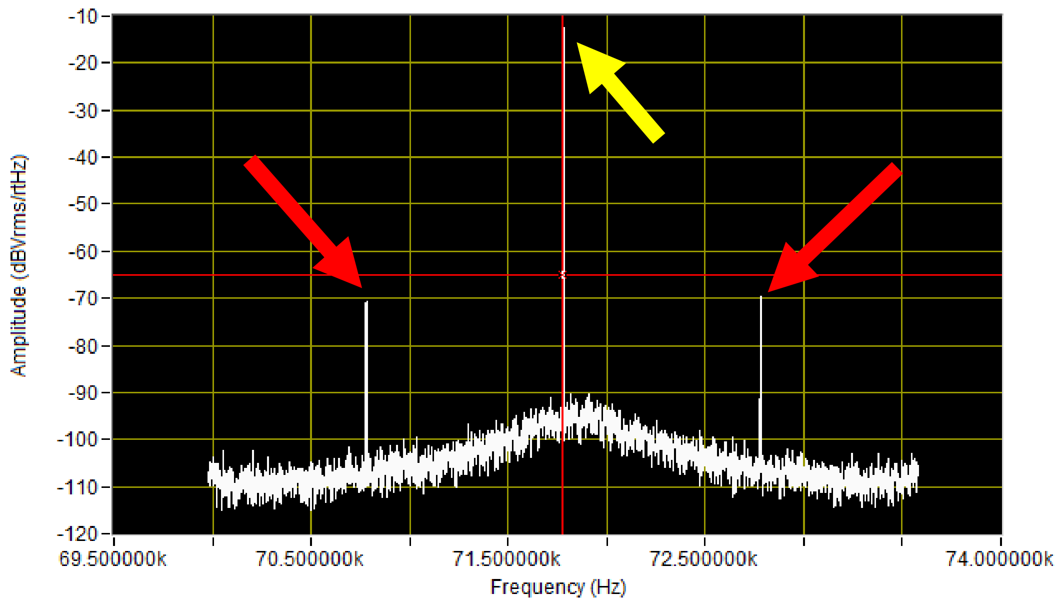

Figure 4.3 Frequency spectrum from a fast Furier transform (FFT). The central peak (indicated by the yellow arrow) displays the tapping frequency. The red arrows point to the sidebands' peaks of the modulation frequency.

4.3.2. Dielectric electrostatic force microscopy

Dielectric electrostatic force microscopy (D-EFM) requires the standard setup for EFM measurements. In the measurements carried out in this thesis, the signal generation and monitoring were made by the zi-HF2LI as in the KPFM setup. In the D-EFM the AFM system works in tapping mode, using as tapping frequency the free resonance frequency of the cantilever. For the electrical excitation, the frequency selected corresponds to 1/2 of the first overtone of flexural free resonance frequency, which is approximately 6.25 times higher than the free resonance. The value of the force depending on the dielectric properties corresponds with the second harmonic. Therefore, to have D-EFM detection, the driving frequency is selected at half of the contact resonance frequency, in order to monitor the signal in the 2nd harmonic and benefit on resonance enhancement.[68-70, 101]

4.4. Nanomechanical measurements

In addition to electrical properties, the study of sample morphology and mechanical properties has also been critical in the development and optimisation of novel materials and structures. Since the AFM's invention, many dynamic AFM modes have been developed, exciting cantilever or sample vibrations to probe the sample mechanical properties with nanoscale resolution.

4.4.1. Ultrasonic excitation

The experimental setups for the nanomechanical mapping with the techniques used in this thesis require high-frequency piezotransducers to excite the mechanical vibrations either in the sample, in the cantilever, or in both (See Fig. 4.4).

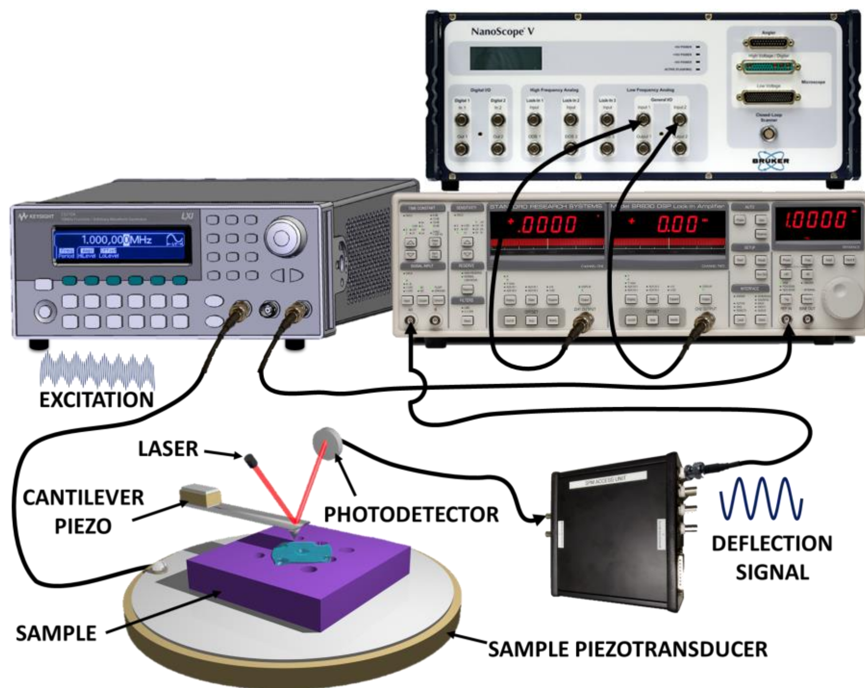

Figure 4.4 Scheme of the AFM setup with the additional piezotransducer under the sample for the excitation of ultrasonic vertical vibrations. The ultrasonic excitation applied to the piezotransducer is driven by a wave generator, which is also triggering the lock-in amplifier for the deflection signal monitoring. The lock-in is fed by the cantilever deflection signal, extracted using a breaking box. The outputs of the lock-in are recorded using two of the auxiliary inputs of the AFM controller.

For sample vibration, we used modified lead zirconate titanate (PZT) piezotransducer discs, with wrap-around electrodes from PI Ceramic (PIC 151 Material). The resonance frequencies of the implemented actuators are 2, 4 and 6-8 MHz. The piezo-stages were built with a standard sample AFM metal disc, with a ceramic piece glued on top to electrically insulate the piezotransducer from the microscope. The piezo transducer is mounted on the

stage with the grounded electrode facing the sample, to avoid the crosstalk in case of electrical excitation of the sample. In some cases, an additional cover-slip is glued between the piezo and the sample to ensure the electrical insulation. However, this additional interface can make the ultrasonic propagation from the piezo to the sample difficult (See Fig. 4.5).

The excitation of the cantilever vibrations for the HF measurements, such in w-UFM or HFM, requires a special probe holder as the resonance frequency of the piezo of the standard tapping holder is not high enough. This non-conventional holder has additional space to insert an HF piezotransducer. Fig. 4.5 shows the home-made probe holder with cantilever attached to the piezotransducer with salol.

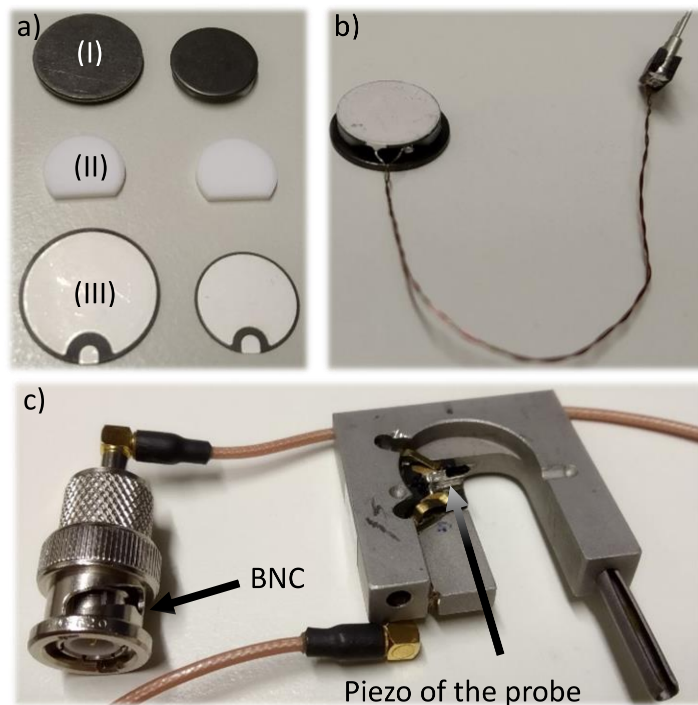

Figure 4.5 a) Metal discs (I), ceramic pieces (II) and piezotransducers (III). b) Piezo-stage for ultrasonic excitation – 4 MHz. c) Home-made heterodyne force microscopy (HFM) probe holder with BNC connector.

4.4.2. Force modulation microscopy and contact resonance AFM

Force modulation microscopy (FMM) uses the standard AFM setup, with a piezo transducer inserted under the sample to create a vertical displacement of the sample at low frequency. It operates below the resonance frequency of the cantilever and the piezotransducer, we generally used a sinusoidal wave at 2.7 kHz. The amplitude of the vertical displacement of the piezo is significantly smaller at low-frequency driving, compared with the amplitude experienced at the resonance frequency of the piezotransducers.

Furthermore, the driving frequency is below the cantilever resonance. Therefore, the cantilever can react to the extra vertical movement of the piezo and keep contact with the sample. Consequently, the tip-sample interaction is produced in the linear regime of the contact. The cantilever deflection is sensitive to the sample's stiffness: soft materials produce low amplitude in the deflection, which corresponds with dark contrast in the FMM images. An important factor for the nanomechanical maps is the ratio between the cantilever's and sample's stiffness. If the sample's stiffness is much greater than the cantilever's, the cantilever will not be sensitive to the sample's elastic moduli.

An alternative to FMM is contact resonance AFM (CR-AFM), which differs in the frequency of the excitation of the piezotransducer. In this case, the frequency selected for the driving of the piezo is equal to the contact resonance of the cantilever. This frequency is known as the first overtone of the fundamental frequency and it is around 6.5 times higher than the cantilever's free resonance. The main benefit of this method is that it can be more sensitive to materials' features due to the high sensitivity of the cantilever at resonance and higher dynamic stiffness at high frequency[102]. However, small changes in the tip, such as material adhesion, can significantly change the resonance frequency and the phase, creating artefacts in the image.

To experimentally determine the contact resonance of the cantilever, frequency sweeps were performed. Once the tip is in contact and the scan size is reduced to 0 nm, the piezo's driving frequency is shifted to obtain the maximum cantilever response.

4.4.3. Ultrasonic force microscopy and waveguide-UFM

An alternative technique to FMM or CR-AFM for the nanomechanical probing of stiff samples is ultrasonic force microscopy (UFM). This method is a quasi-contact technique in which the sample or the cantilever, for the waveguide UFM (w-UFM) mode, vibrates at ultrasonic frequencies (4-10 MHz) with low-frequency amplitude modulation (2.7kHz).

As with previous methods, the experimental setup requires a wave generator for the piezoelectric excitation. Unlike FMM or CR-AFM, in UFM, the high-frequency sinusoidal signal is amplitude modulated with an arbitrary function with a characteristic diamond shape to enhance the ultrasonic response. The deflection signal is extracted from the breakout box and monitored by a lock-in amplifier, this last one triggered by the low-frequency signal. The amplitude of the low-frequency ultrasonic force signal is measured by the LIA and is recorded by one of the auxiliary inputs of the AFM controller. The cantilever's free resonance frequency is important in the ultrasonic response, with contact cantilever or soft tapping ones (13 and 75 kHz free resonance, respectively) being the optimal probes.

4.4.4. Heterodyne force microscopy

Another dynamic AFM mode for the study of mechanical properties is the heterodyne force microscopy (HFM). In HFM, both UFM and w-UFM are combined to provide information about the viscoelastic properties of the sample's surface. This method requires the ultrasonic excitation of the tip and the sample at adjacent frequencies, $f_t=\omega_t/2\pi$ and $f_s=\omega_s/2\pi$, respectively.

In HFM, the sample and the tip are excited at two ultrasonic frequencies (4-5MHz) with a small difference between them of a few kHz. This frequency difference is Δf and is the beating frequency used for nonlinear signal detection of the ultrasonic vibrations.

The experimental setup requires a function generator with two outputs or two generators with trigger input to sync the signals. The amplitude and the phase of the signal offer relevant information about the nanomechanics of the sample: the amplitude shows the adhesion and deformation and the phase shows information about the dynamic relaxation of the material (time resolve).

4.4.5. Modulation ultrasonic force microscopy

The vibrational modes' local probing of MEMS/NEMS at the nanoscale is a problem that is not yet solved. In this thesis, we propose a new methodology for simultaneous sample excitation and probing of the vibrations. Using SPM methods as instrumentation, the methodology benefits from the high spatial resolution.

This methodology requires prior knowledge of the natural resonance frequency of the MEMS/NEMS to be studied. In addition, it is also necessary to know the contact resonance of the probe to discard these resonances in the results and to avoid crosstalk.

The experimental setup is similar to the UFM one, using the MultiMode microscope in contact mode. The ultrasonic excitation of the sample is induced by a piezotransducer inserted under the sample. The driving signal and its detection can be carried out with two different setups. The simplest one is performed by the Zurich Instruments lock-in amplifier (zi-HFLIA2), which allows the driving and demodulation of up to 6 different frequencies. In the M-UFM measurements, 3 demodulators are required, with two of them used in the signal generation for the driving of the piezo and the third one used for the detection at the difference in frequency between the other two. In the other possible setup, one can use a signal mixer, a double-channel wave generator for driving, another wave generator for the synchronisation of the lock-in and a high-frequency lock-in. Both setup schematics can be found in Fig. 4.6

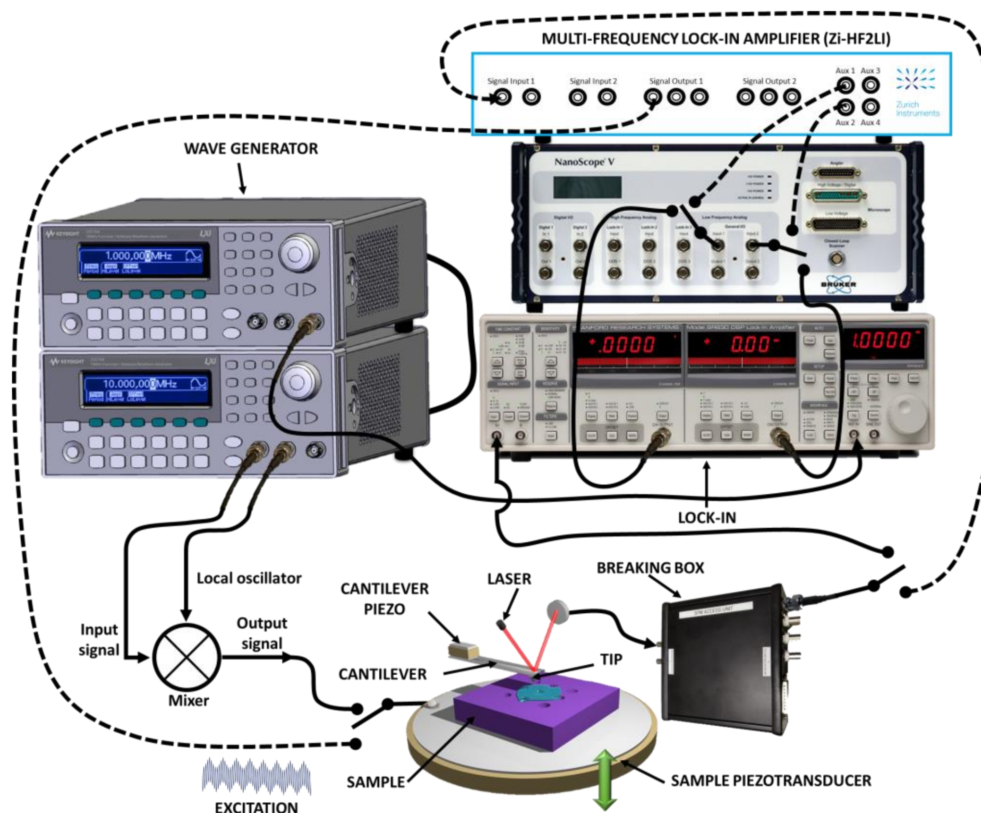

Figure 4.6 Experimental setups of M-UFM. The simplest setup, using the zi-HF2LI is represented with the wires with dashed lines. The setup with the wave generators, the mixer and lock-in are wired with the continuous lines.

4.4.6. Piezoelectric properties measurements – piezoelectric force microscopy

Piezoelectric force microscopy (PFM) is a contact method in which the sample is electrically excited with an AC voltage. Via the scanning of the tip, which is grounded, the sample experiences mechanical expansion or contraction, depending on the crystallographic domain, see Fig. 4.7 . The sample's expansion (contraction) is detected via the cantilever's deflection. Working at the resonance frequency of the cantilever greatly increases the sensitivity. However, piezoelectric maps can be convoluted with the mechanical resonance of the cantilever.

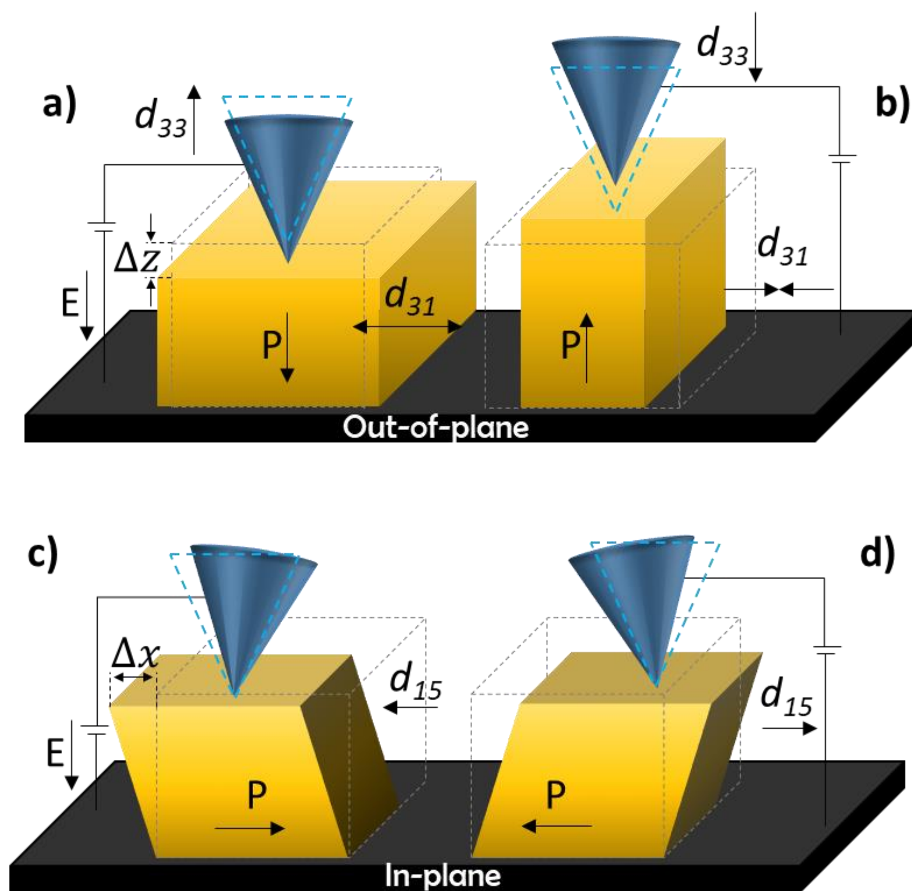

Figure 4.7 Principle of piezoelectric force microscopy (PFM). a) Electric field aligned parallel to the spontaneous polarisation leads to a lifting of the cantilever due to the d_{33} effect (out-of-plane signal). It causes additional lateral contraction of the ferroelectric via the d_{31} piezoelectric coefficient. b) The antiparallel alignment of the electric field and the spontaneous polarisation leads to a vertical contraction and a horizontal expansion of the ferroelectric. c) and d) Electric field applied orthogonal to the polarisation results in a shear movement due to the d_{15} coefficient. This movement causes a torsional deformation of the cantilever forcing the laser spot to move horizontally (in-plane signal).

PFM images are obtained by monitoring the cantilever's deflection signal in contact mode, which exhibits the additional cantilever displacement $d = d_0 + A\cos(\omega t + \varphi)$ resulting from the piezoelectric response of the tested material. Information on the polarisation direction of the sample is yielded from the phase φ of the signal. [103]

The vertical response is obtained by monitoring the deflection signal at the contact resonance frequency of the cantilever; this mode is called vertical piezoelectric force microscopy (VPFM). The vertical displacement will respond to the following equation:

$$\Delta Z = \Delta Z_0 co\, s(\omega t + \varphi), \qquad (49)$$

where $\Delta Z_0 = d_v V_0$ is the vibration amplitude, d_v is the effective piezoelectric constant, V_0 is the applied potential and φ is the phase. This phase term is the phase difference between the imaging voltage and the piezoresponse, containing information on the polarization direction. The domains will vibrate in-phase $\varphi(+) = 0°$ or anti-phase $\varphi(-) = 180°$ depending on the orientation of the domains with respect to the normal of the tip [104].

In the lateral piezoelectric force microscopy (LPFM), the signal monitored corresponds with the lateral deflection or friction. Modulating the voltage at the resonance frequency of the torsional mode across the sample, surface lateral vibration is detectable, being translated via frictional forces to the torsional movements of the cantilever.

In the simplest case of vertical displacement, the effective piezoelectric constant can be assumed as $d_v \approx d_{33}$ for a uniform electric field. However, for the LPFM measurements of lateral domains, this assumption is not as straightforward as with VPFM, due to the sensitivity of the system being dependent onthe domain's orientation with respect to the scan direction. Nevertheless, for a simple approximation, we can consider that the in-plane piezoelectric response is proportional to the piezoelectric constant d_{34} and d_{35}.[105, 106]

Resonance frequency determination for PFM measurements

In order to benefit of the enhancement produced in the cantilever response while working at its resonance frequencies, we used the following procedure to determine the flexural and torsional contact resonances of the cantilevers used in PFM measurements.

Firstly, we bring the tip to contact in the desired area and reduce the scan size to 0 nm to obtain a more smooth resonance curve. Then, the sample is electrically excited, while sweeping the frequency. For the signal monitoring with the zi-HFLIA, we use the vertical and lateral deflection outputs of the AFM microscope, obtained through a home-made "black box".

When the conductive probe is grounded and contacts the electrically excited sample, it produces a local potential difference which results in a mechanical contraction or expansion at the probed point of the piezoelectric sample. The mechanical response depends on the orientation of the piezoelectric domain. To quantify the angle of the orientation of the domains, we investigated the sample, simultaneously monitoring the vertical and lateral piezoelectric response.

4.5. Optical methods

4.5.1. Laser Doppler vibrometry

Laser Doppler vibrometry (LDV) is an interferometric technique, which uses the physical principle of the Doppler Effect for the sensing of small amplitude mechanical vibrations. The laser beam is focussed onto the oscillating sample and, by comparing the frequency shift between the reference and the reflected beams, it is possible to infer the velocity of the vibrations and the displacement.

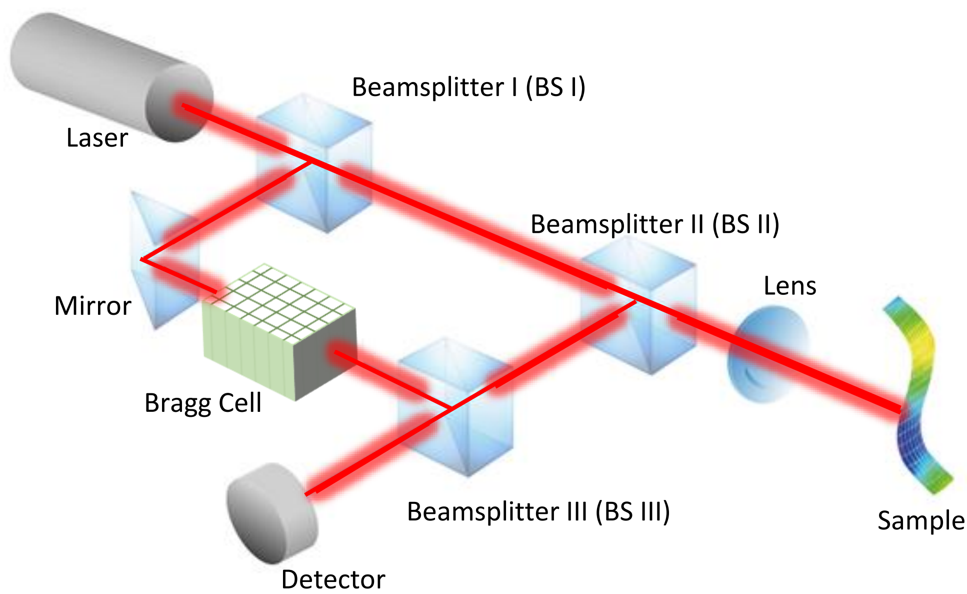

Figure 4.8 Schematic Polytec Laser Doppler Vibrometer.

As can be observed in the scheme in Fig. 2.15, in this heterodyne method the incident beam, with frequency f_0, is divided with a beamsplitter (BS I) into a reference beam and a measurement beam. After passing through a second beam splitter (BS II) the measurement beam is directed to the oscillating target, which reflects it. As a consequence of the sample vibrations, the reflected beam has been frequency modulated with a Doppler shift equal to

$$f_d = 2v(t) \cos \alpha / \lambda, \quad (50)$$

where $v(t)$ is the time-dependent velocity of the sample, α is the angle between the laser beam and the velocity vector, and λ is the wavelength of the laser. Then, the backscattered beam is deflected downwards by the BS II and is then merged with the reference beam onto the detector.

The sample moving away from the interferometer generates the same modulation frequencies as a sample moving towards the interferometer. This set-up alone cannot unambiguously determine the direction the object is moving in. For this and for comparison purposes, the reference beam is passed through a Bragg cell to shift the light frequency ($f_0 \approx 10^{14}\ Hz$) by typically $f_b = 4 \cdot 10^7\ Hz$. This generates an interference pattern modulation frequency of 40 MHz when the sample is at a standstill. If the object then moves towards the interferometer, this modulation frequency is increased, and if it moves away from the interferometer, the detector receives a frequency less than 40 MHz. This means that it is now possible to not only clearly detect the path length but also the direction of movement too.

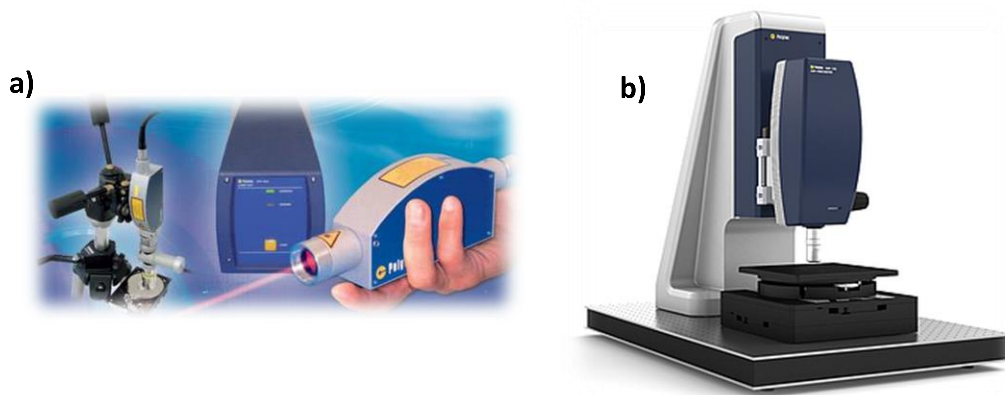

Figure 4.9 Laser Doppler vibrometer images a) Setup for OFV-2500 and OFV-2750 controllers. b) Setup of UHF-120. (Polytec, Germany)

During this work, we used three different LDV systems. For the low and medium frequency detection, we used the Polytec OFV-534 head with OFV-2500 and OFV-2570 controllers, respectively. The OFV-2500 works in the frequency range 0 - 350 kHz and the OFV-2570 is capable of working from 10 kHz to 10 MHz. The last, very powerful system, the UHF-120, also from Polytec, allows works in a bigger range, from 0 to 1.2 GHz.

4.5.2. Raman spectroscopy and photoluminescence

The Raman spectroscopy and photoluminescence measurements were carried out on a Horiba Lab Raman Spectrometer with an electron-multiplying (EM) cooled Synapse camera (Horiba, Japan). For taking spectra, a 100x, 0.90 numerical aperture (NA) microscope objective was used. The system is equipped with red (633 nm) and green (532 nm) lasers.

4.6. Summary

This chapter has reviewed the experimental techniques used throughout the work covered in this thesis. The covered techniques are the functional scanning probe methods used for nanoscale characterisation of mechanical, electric and piezoelectric properties. They have been summarised in Table 2. Furthermore, optical methods, including laser Doppler vibrometry, Raman spectroscopy and photoluminescence, have been also reviewed.

Table 2 Scanning probe methods summary.

Method	Contact	Excitation	Modulation	Frequency	Detection	Detection freq.
AFM	Yes	No			Deflection	
Tapping	Semi	Mechanical	No		Deflection	Free res.
EFM	No	Electrical	No		Deflection	AC freq.
D-EFM	Semi	Electrical	No		Deflection	2nd harm CR/2
KPFM	Semi	Electrical/ mechanical	Yes	1 kHz + tapping freq.	Deflection + CPD	1 kHz
PFM	Yes	Electrical	No	CR cantilever	Deflection	CR
FMM	Yes	Mechanical	No	2.7 kHz	Deflection	2.7 kHz
UFM	Yes	Mechanical	2.7kHz	4-5 MHz	Deflection	2.7 kHz
HFM	Yes	Mechanical	No	4-5 MHz & 4-5 MHz + Δf	Deflection	Δf
M-UFM	Yes	Mechanical	Δf (0-1MHz)	4-5 MHz	Deflection	Δf (0-1MHz)

5. Free oscillating structures MEMS/NEMS

The mapping of the vibrational modes of micro- and nano-electromechanical systems (MEMS and NEMS) with nano-scale resolution is a significant problem, which needs to be addressed for the development of new resonating devices technologies. Here, we present the study of the vibrational modes of four different free oscillating structures, which can be categorised as MEMS or NEMS.

The first part of this chapter is dedicated to one-dimensional (1D) resonating systems, such as the AFM cantilevers, which have been characterised and studied to understand their interaction with the sample during SPM measurements. Here, we should note that 1D refers to the geometry of the resonator, while it does move in three-dimensions (3D) with some modes (*e.g.* pure flexural modes), two-dimensional (2D) movement analysis is sufficient. The second variety of vibrating 1D structures studied here are piezoelectric tuning forks (TF). These kind of devices have been historically implemented in many scientific investigations of different physical phenomena, such as quantum turbulence and acoustic sound emission probing in superfluid ^{4}He. Moreover, owing to their high sensitivity to liquid viscosity, TF have demonstrated their potential in industrial applications, especially in fluid engineering. Throughout this work, we used two different types of TF made of different materials, quartz and lithium niobate ($LiNbO_3$), and with different designs.

The last part of this experimental chapter is devoted to 2D resonating systems. Firstly, a commercial Si_3N_4 membrane is used as a test sample for proving the novel ultrasonic SPM method, called Modulation-UFM (M-UFM), used for the local probing of vibrational modes in high-frequency 2D resonating structures. Then we present the experimental results and the modelling to understand the changes in the stiffness distribution of a suspended few-layer graphene (FLG) flake, using different ultrasonic SPM methods.

5.1. AFM cantilevers: analytical model and optical characterization

AFM cantilevers have been intensely studied since the invention of the AFM, being one of the fundamental pieces of the AFM system. Many dynamic SPM modes use cantilevers as the resonating system to enhance the system sensitivity by the excitation or detection of different vibrational modes of the cantilever. In this section, we initially present a common model for describing the AFM flexural bending and then some of the experimental results of the study of cantilevers.

5.1.1. AFM cantilever modelling

Using the cantilever's theory described in the literature review of this thesis, section 2.8.2, we calculated the free resonances and different overtones of contact mode and force modulation AFM cantilevers. The geometric values of the cantilevers used for the calculations were obtained from the manufacturing supplier datasheet, information also detailed in Table 3. Due to these standard cantilever are made of Si, we used density $\rho = 2330\ kg\ m^{-3}$ and Young's Modulus of Si in the <110> direction $E = 1.69 \cdot 10^{11}\ N\ m^{2}$, as values of the material properties for the calculations. The values obtained of the fundamental resonance frequencies of these cantilevers match with the provided for the manufacturer.

Table 3 Cantilever data used in the SPM measurements

	Contact mode	Force modulation
Resonance frequency	13 kHz	75 kHz
Force Constant	0.2 N m^{-1}	3 N m^{-1}
Cantilever length	450 µm	225 µm
Mean width	50 µm	28 µm
Thickness	2 µm	3 µm
Tip height	17 µm	17 µm
Tip set back	15 µm	15 µm
Tip radius	<10 nm	<10 nm
Coating	none	none
Half cone angle	20° - 25° along cantilever axis 25° - 30° from side 10° at the apex	20° - 25° along cantilever axis 25° - 30° from side 10° at the apex

5.1.2. Optical characterization of AFM cantilevers

The resonance frequency values obtained in the previous section 5.1.1 were experimentally validated by laser Doppler vibrometry (LDV) measurements. This

interferometric method allowed us to record the cantilever displacement distribution for the different frequencies and under diverse conditions. In a preliminary study, ContAl-G and Multi75 (Budget Sensors, Bulgaria) cantilevers were measured by the LDV OFV-2500 (Polytec, Germany). Discrete point measurements were recorded in three different points along the cantilevers to see the maximum and minimum displacement values for the fundamental mode (f_1) and the first overtone (f_2), as they are represented in Fig. 5.1.

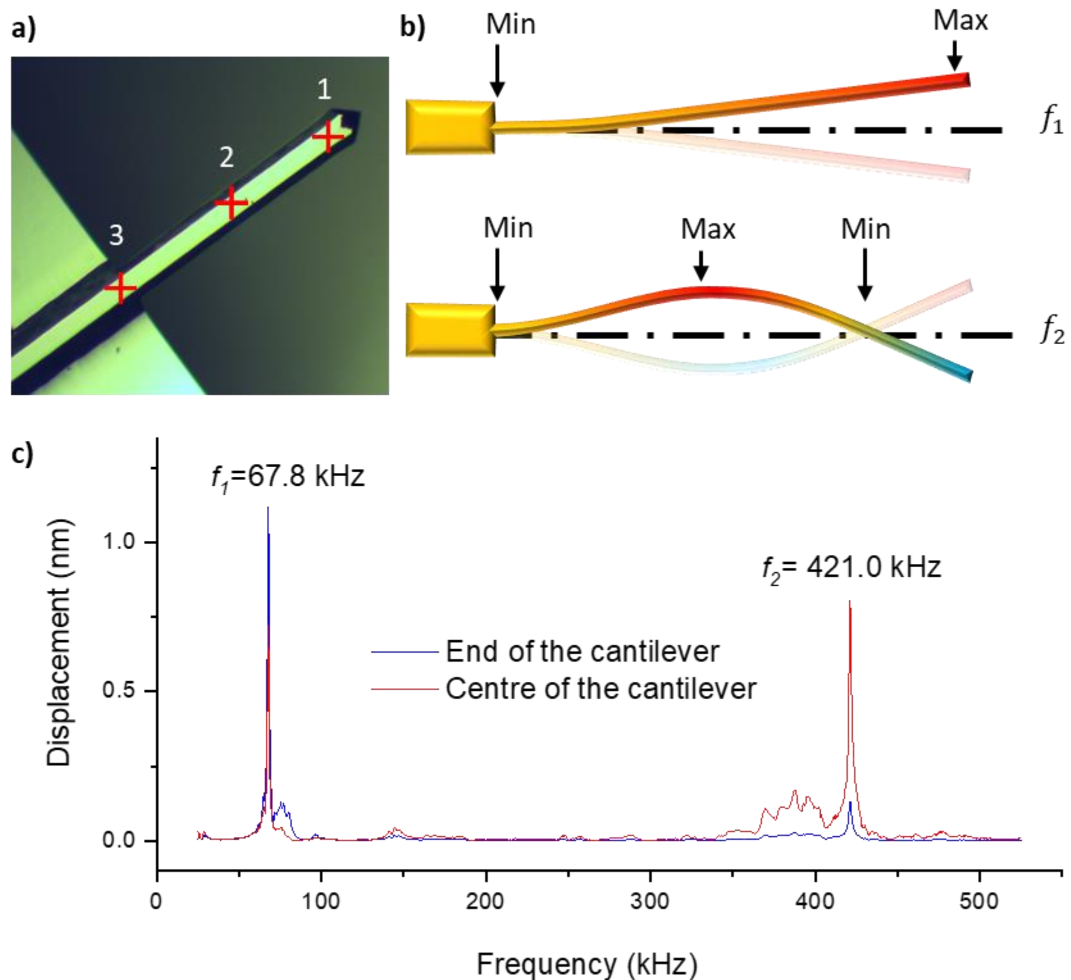

Figure 5.1 a) Optical image of a force modulation cantilever (Multi75, Budget Sensors) with the point measurements superposed. Magnification x20. b) Schematic of the free resonance (f_1) and the first overtone (f_2) of a cantilever. c) Plot of the displacement of the cantilever in the centre and at the end, while sweeping in frequency the driving of a piezotransducer inserted under the cantilevers.

The high sensitivity of the LDV allowed us to study the free vibration of the cantilever as a consequence of thermal excitation. The experimental setup requires use of a spectrum analyser for signal monitoring or, in the absence of this system, signal monitoring can be performed by a lock-in amplifier detecting in "noise" mode, controlled by adequate software.

An example of the LabVIEW software for the data acquisition using a SR830 lock-in amplifier can be found in Annex I. Furthermore, the cantilever can be studied under external ultrasonic excitation, inserting a piezotransducer under the cantilever and sweeping the frequency of the driving signal to find the maximum response for the different vibrational modes. An example of the cantilever displacement measurements while driving the piezo can be found in Fig. 5.1.c. The plot shows the displacement with the laser spot localised in the centre of the cantilever and at the end.

Complementary to the single spot measurements, the cantilevers were studied by the LDV Polytec UHF-120. With this system, it is possible to define a mesh with an arbitrary shape and automatically map the area. The sensitivity in the displacement of this system is in the range of 10 femtometre, potentially offering a wide range of possibilities to characterise quantum electromechanical devices. In the presented cases in Fig. 5.2, standard rectangular shapes were used. The images of the fundamental overtone show the maximum displacement at the free end of the cantilever. Conversely, the 1st overtone images shows higher amplitude closer to the fixed end to the chip.

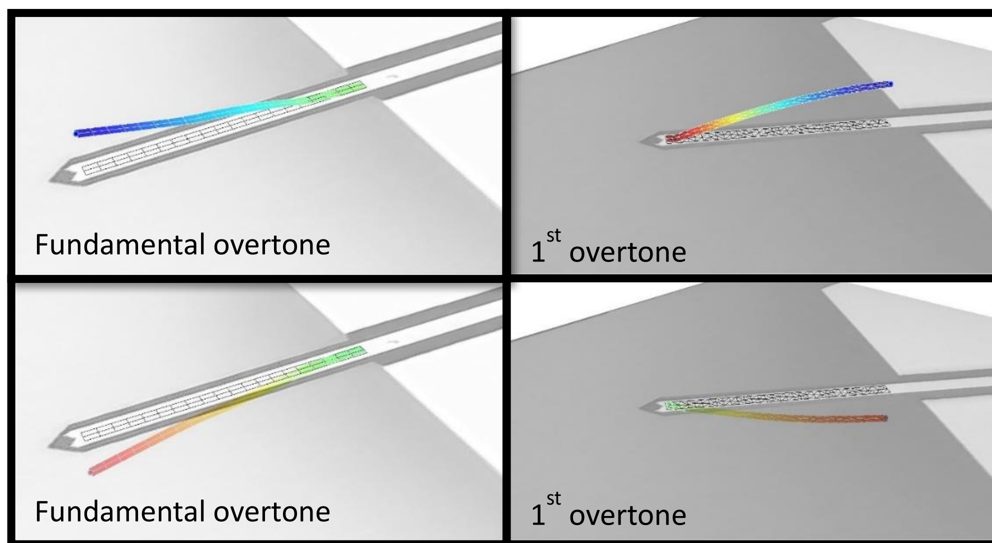

Figure 5.2 LDV displacement maps of a Multi75 cantilever at the fundamental (*f_0=84 kHz*) and first overtone (*f_1=425 kHz*) frequencies. Vibrations excited via an externally driven piezotransducer, inserted under the cantilever chip. Colour scale indicate maximum positive desplacement in the out-of-plane direction with dark blue and maximum in the negative direction with dark red.

These measurements were fundamental to understanding the cantilever's behaviour while scanning in the non-contact SPM modes used throughout this thesis.

5.2. Tuning forks

In addition to the AFM cantilevers, we also investigated the tuning forks (TF) as alternative resonating systems/probes often used in SPM. The high stiffness of TF makes them stable, avoiding jump into contact, and capable of oscillating with small amplitudes, allowing for very accurate control of the oscillation frequency. TF have the advantage of being self-actuating and self-sensing devices, *i.e.*, external detection systems are not necessary for their operation [107, 108].

5.2.1. Quartz tuning forks

The quartz TF used in this work were described in the Materials chapter 3. These devices were used extensively in the flexural mode in low-temperature experiments with quantum fluids, using the antiphase inward and outward movement of the tines in the turbulence generation [95, 109]. The TF flexural motion displaces the surrounding fluid generating normal and shear stress in the medium. In this work, we investigated for the first time the torsional mode of the TF operation in quantum fluid, when the TF tines twist in the opposite direction, creating mainly shear stress at the moving interface.

A clear advantage of these kinds of resonators is that an individual device can simultaneously perform as actuator and detector of quantum turbulence. This fact offers the possibility of measuring the vortices in the same location, where they have been created, without needing to study their propagation. The main disadvantage presented by this methodology is that the measurement is a convolution of the generation and detection phenomena. Reference vacuum measurements are also generally required to deconvolute the results of the interaction with the media from other effects.

In this work, the possibility of creating turbulences in ^{4}He by a flexural mode of the TF and detecting the fluid turbulences in the torsional mode has been proposed. This method does not require vacuum calibration because it directly measures the absolute damping due to the turbulence. These measurements were performed in an immersion cryostat. The TF is driven using an AC voltage supplied by the output of two network analysers (NA). The output current of the TF is passed through an I-V converter with 10^3 V A^{-1} gain and then monitored for turbulence detection. This current can be linked with the mechanical actuation of the TF by the calibration method presented in this work. This methodology employs the interferometric method laser Doppler vibrometry (LDV) for the study of the mechanical

displacement or velocity of the TF tines in the flexural and torsional vibration and is directly linked with the electrical response of the tuning fork.

First, the resonance frequencies of the flexural and torsional modes of the TF were estimated. For the flexural frequency, the same Euler-Bernouilli formulation was used, as previously explained for the cantilevers. For the calculation of the torsional resonance, the model for torsional modes found elsewhere was used [105, 110, 111], in which the fundamental frequency of the torsional motion is determined by

$$f_0 = \frac{1}{2L}\sqrt{\frac{3G}{\rho}\frac{\beta W^2}{T^2+W^2}}, \qquad (51)$$

where $L = 1.61 \times 10^{-3}\, m$, $T = 2.23 \times 10^{-4}\, m$ and $W = 1.43 \times 10^{-4}\, m$ are the beam dimensions: length, thickness and width; $G = 3.11 \times 10^{10}\, N\, m^{-2}$ and $\rho = 2650\, kg\, m^{-3}$ are the shear modulus and the density of the quartz, respectively; β is the dimensionless coefficient dependent on the ratio of *w/h*, which can be found in Table 4.

Table 4 ß coefficients for various values of the ratio w/h.

w/h	1	1.5	2	2.5	3	4	5	6	10	∞
β	0.141	0.196	0.229	0.249	0.263	0.281	0.291	0.299	0.312	0.333

Electromechanical characterisation of vibrational modes quartz TF via laser Doppler vibrometry and electrical readout

The characterisation of the tine displacement and velocity were performed with the high-frequency laser Doppler vibrometer (LDV), with the Polytec Vibrometer Controller OFV-2570. This system works in the range from 10 kHz to 10 MHz. The experimental setup is detailed in the scheme in Fig. 5.3. The TF are driven by the output channel of the Network Analyser (NA) (4395A, Agilent Technologies, USA). This instrument allows for driving the excitation and for detection of the response at the same frequency. The NA covers the range from 0 to 500 MHz. An amplifier was inserted between the NA and the TF for the high-power driving of the TF. Furthermore, for monitoring the electrical TF response, the current output from the TF was transformed with an I-V converter before being fed into the NA. The second channel of the NA was recorded the LDV output, therefore allowing one to record both the mechanical displacement and the electrical signal simultaneously.

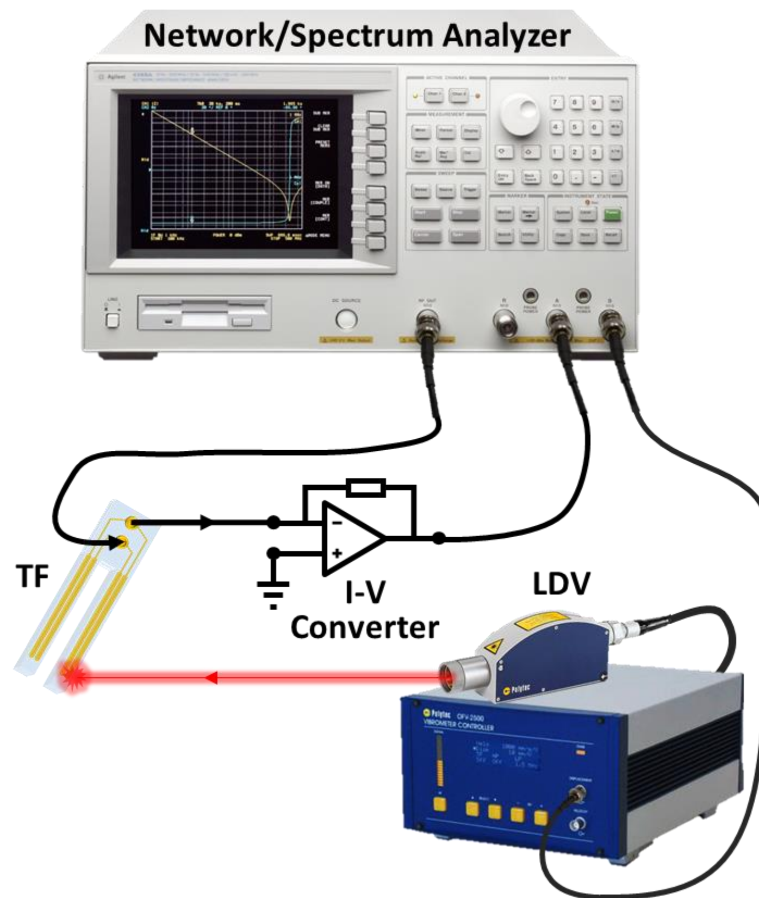

Figure 5.3 Experimental setup of the LDV for TF characterisation.

To achieve a good signal in the optical measurements, the TF were measured focusing the laser spot on the gold-coated area to benefit from the high reflectivity of gold compared with the weak one of quartz. As can be seen in the SEM images of the TF presented in the Materials Chapter 3, the gold coating does not cover the whole side of the tuning fork. We then determined, using an optical microscope image, the position of the coated region of the TF, where we measured the velocity, to a total length of the fork, obtaining a ratio of $\delta = 9.5/5.5 = 1.73$. This value was used as a correction factor for the calculation of the velocity of the tuning fork tip during oscillations. Due to the geometry of the electrodes with respect to the orientation of the quartz crystal, the TF used in these experiments were able to perform in either bending, torsional, or simultaneously in both, modes. During the measurements in torsional mode, the location of the laser spot on the cantilever required critical attention, because to record the maximum displacement of the tine, the laser beam had to be focussed at the very end of the gold-coated section of the region and very close to one of the lateral edges of the tine as the displacement in the normal direction of the central part of the tine vanishes in torsional mode.

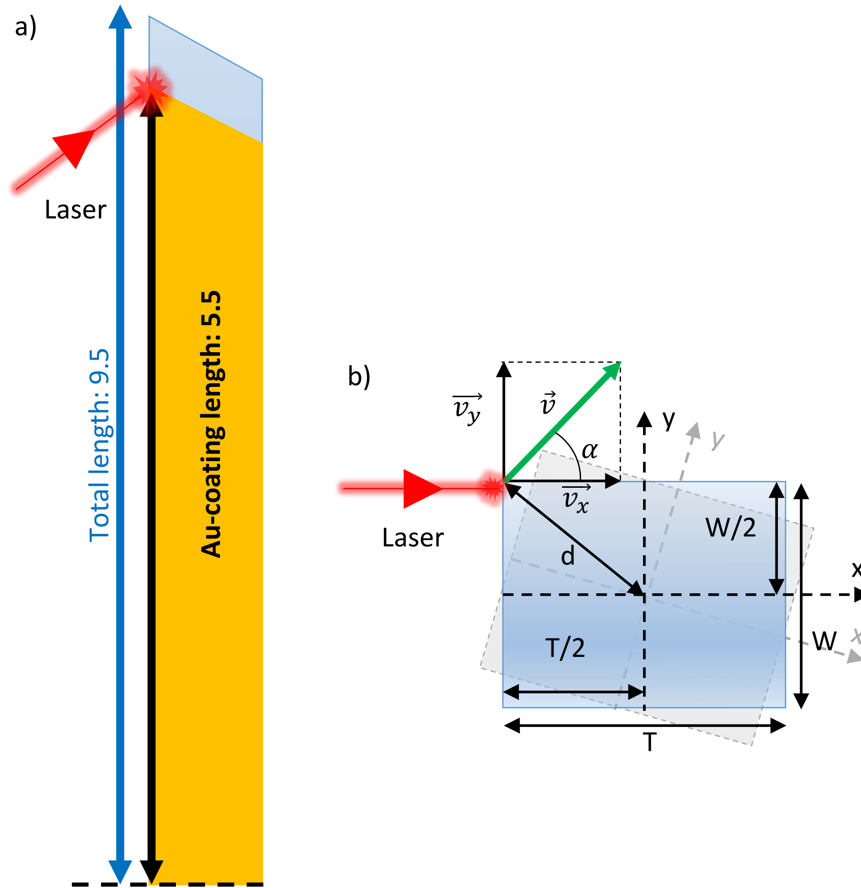

Figure 5.4 a) Schematic of a quart TF side view. The laser spot indicates the place where the LDV laser was focused on the measurements. b) Top view of the TF tine with the velocity vectors of the rotational modes displayed.

The angular velocity of the torsional mode was inferred from the LDV measurements, which are sensitive to the normal component velocity (v_x) in respect to the TF surface. The total velocity, including the geometrical factor and corresponding with the effective radius (*d*), was calculated by the following expression

$$v = \frac{v_x}{cos(\alpha)} = v_x \frac{d}{T/2} = v_x \frac{\sqrt{\left(\frac{W}{2}\right)^2 + \left(\frac{T}{2}\right)^2}}{T/2} = v_x \frac{\sqrt{W^2 + T^2}}{T}. \qquad (52)$$

Table 5 Voltage and current outputs for flexural and torsional modes of TF.

Frequency (kHz)	Power input (dBm)	V_{pp} output (mV)	Current (μA)
76	0	670	1.75
393	0	688	1.80

The electrical response was calibrated by substituting the TF by a 38.2k Ω reference resistor, which has an approximately similar resistance value to the intrinsic TF resistance. We established the reference “zero value” by driving the resistor with 0 dBm (0 dBm corresponds to a power of 1 mW at 50 Ω lead) power output from the NA. Using an oscilloscope to probe the output value of the calibration setup, we recorded the voltage output for the bending and torsional resonance frequencies. The obtained calibration values can be found in Table 5.

In Fig. 5.5 we present the velocity/current output vs driving voltage for the flexural (76 kHz) and torsional (393 kHz) modes. This data was used to correlate the electrical and the mechanical response, to be applied to the experimental results of using the TF in the probing of turbulences in ^{4}He. The low-temperature experiments were carried out by our collaborators from the Ultra-Low Temperatures group at Lancaster University [92]. In these experiments, the TF is used simultaneously as a sensor and turbulence generator. This research demonstrated the possibility of exciting turbulence in the ^{4}He with the flexural mode and detecting the damping produced by the turbulence in the torsional mode of the tuning fork. Also noted was the difficulty to excite turbulences via the torsional mode as these phenomena start to occur after a determined critical velocity, and the higher acoustic damping of the torsional mode combined with the high critical velocity made it difficult to create turbulences.

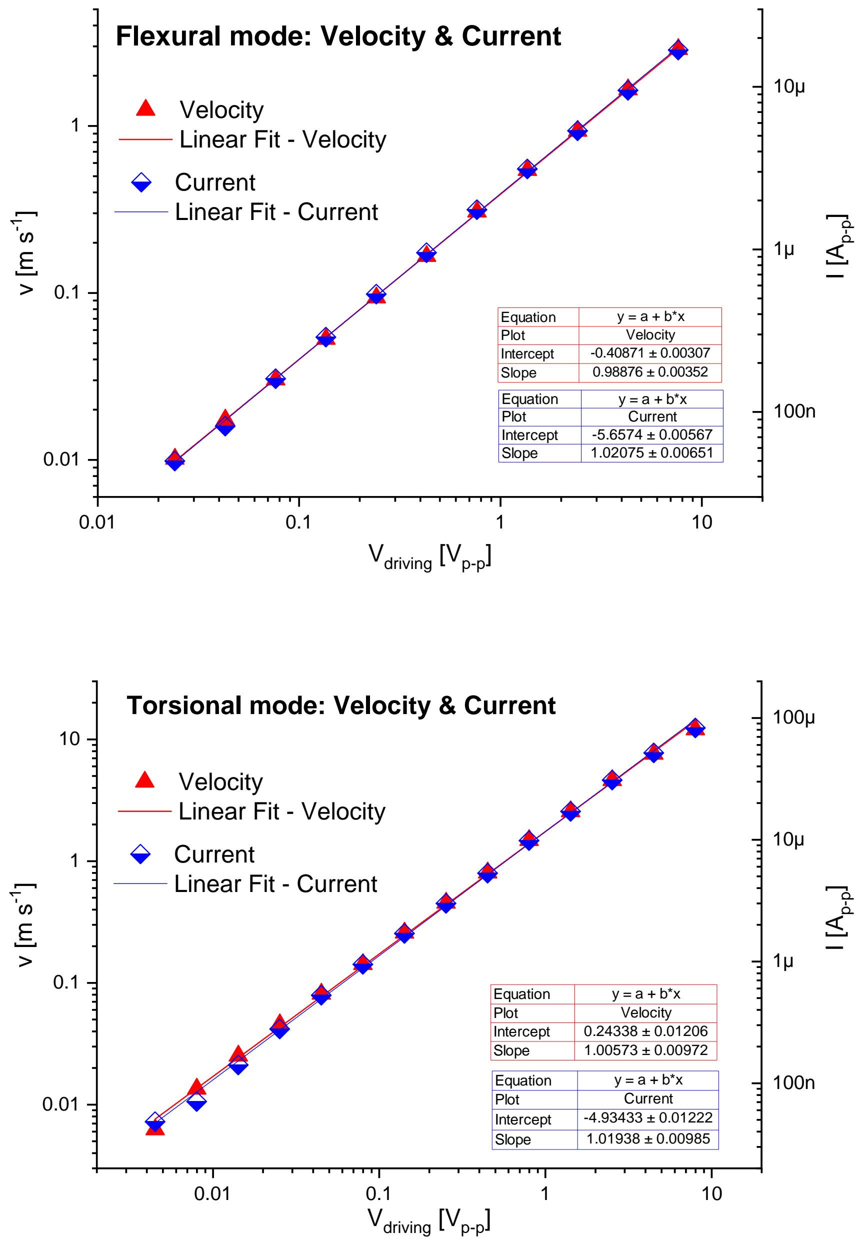

Figure 5.5 Velocity and current plots as a function of the driving voltage. The linear dependence of both vibrational modes, flexural and torsional, allowed us to establish the calibration for the ULT measurements.

5.2.2. Lithium niobate tuning forks

The physical properties of lithium niobate ($LiNbO_3$), such as piezoelectricity and high electromechanical coupling, make $LiNbO_3$ an exceptional candidate for the fabrication of tuning forks with extraordinary sensitivity to the viscosity changes in media.

The TF used in this work were fabricated using two $LiNbO_3$ wafers with the antiparallel domains. One of the particular characteristics of this kind of TF is that electrodes are sandwiched between the two $LiNbO_3$ wafers. This specific morphology makes these TF perfect devices for liquid immersed investigations [98]. Moreover, as was explained in the Materials Chapter 3, some of the $LiNbo_3$ TF used in this research were additionally coated with a gold film, creating an external third electrode and allowing us to ground the system to avoid electrostatic crosstalk between the TF and the environment. In the experiments performed with the coated TF, it was demonstrated how the third electrode produces a significant enhancement of the electrical response and, therefore, a considerable improvement of the system sensitivity. In Fig. 5.6, the resonance curves of a coated and a bare $LiNbO_3$ TFs are plotted, presenting evident differences in the size of the resonance peak. It is also necessary to note that, due to the extra mass added to the TF due to the Au coating, there is a down frequency shift, compared with the bare TF.

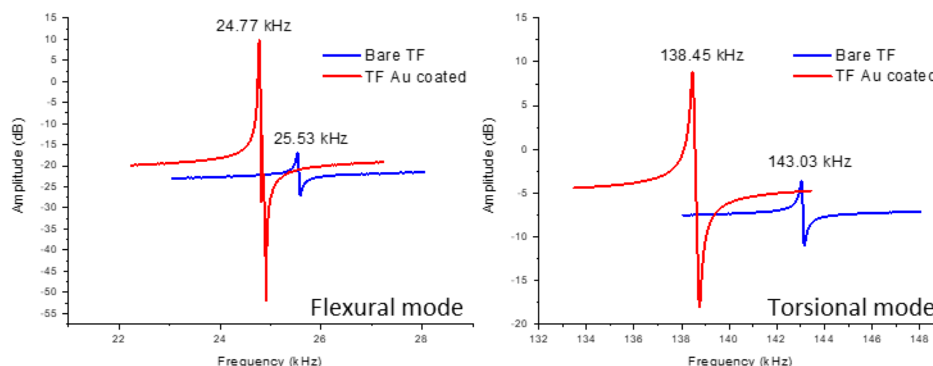

Figure 5.6 Electrical response of the flexural and torsional modes. Comparison between the response of the bare TF and the Au-coated ones.

The gold coated $LiNbO_3$ TF have been used to measure samples in an aqueous environment, in a like qPlus setup, demonstrating high sensitivity as SPM probe. Initially, the TF were characterised in the same way to quartz TF via LDV and electrical response measurements to understand the electromechanical coupling. The characterisation of the displacement and electrical response allowed us to establish the sensitivity of these resonating systems. The setup used for the electrical characterisation is slightly different from the one

used with the quartz TF, due to the fact we did not use the Network Analyser (NA) for the signal driving and detection. The NA was substituted by the HF2LI Zurich Instruments, which allowed us to drive the sample and detect simultaneously. The I-V converter was also used for the current conversion. The amplifier was not necessary for the explained research. The performed frequency sweeps were used to identify the resonances of the TF. Furthermore, amplitude sweeps at the resonance frequency were also made to see the linear dependence between the electrical response and the displacement, such as in the plotted graph in Fig. 5.7.

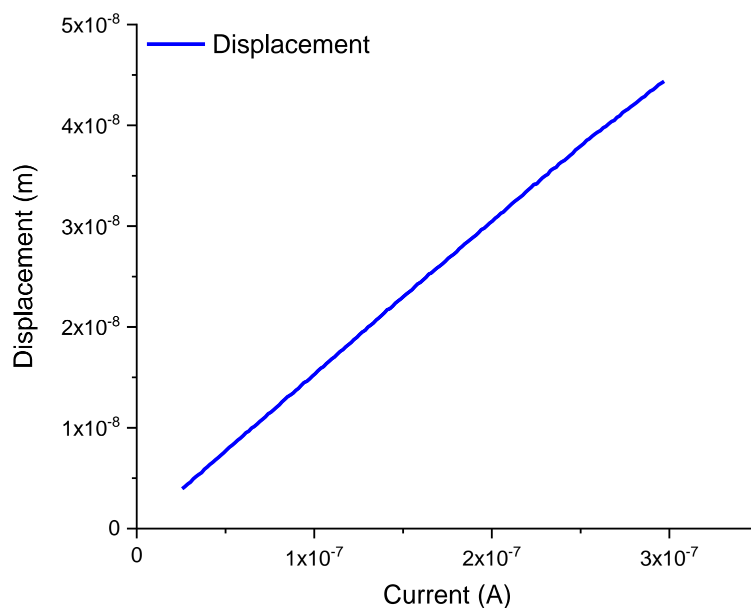

Figure 5.7 Plot of the TF displacement vs current. The plot indicates an almost perfect linear dependence.

To create the SPM images with the TF, a small Au wire (diameter 0.025mm and length: 0.5 mm) was attached to the very end of the TF to act as a tip. The wire was glued with a conductive epoxy to provide electrical contact to the external TF electrode. The additional mass resulting from the glued wire to the fork produces a frequency shift of the system resonance as well as a substantial decrease of the amplitude of the response. The plot from Fig. 5.8 shows both effects; it is important to highlight the different vertical scales for both data lines, presenting a difference of two orders of magnitude between the two responses. This drop in the response is attributed to the unbalance produced in the TF tine resonances when the tip is attached to the prong [112].

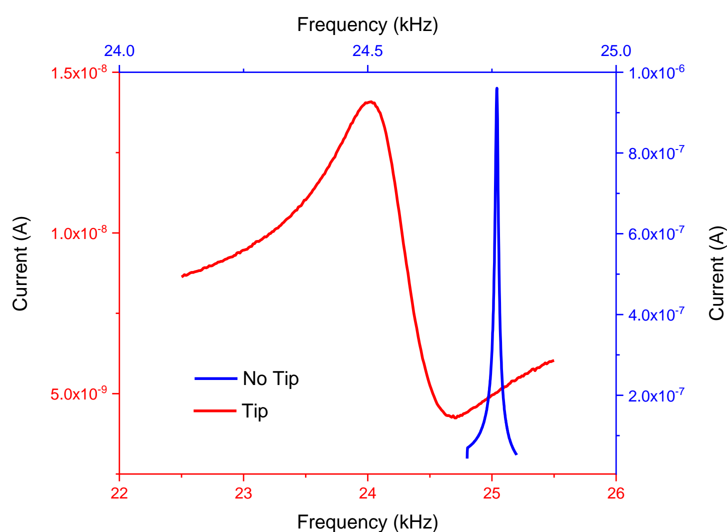

Figure 5.8 A comparison of the resonance curves from the TF response, with and without the tip attached to the end of the TF. The results show the shift in frequency and the significant drop in the amplitude of the response, around two orders of magnitude.

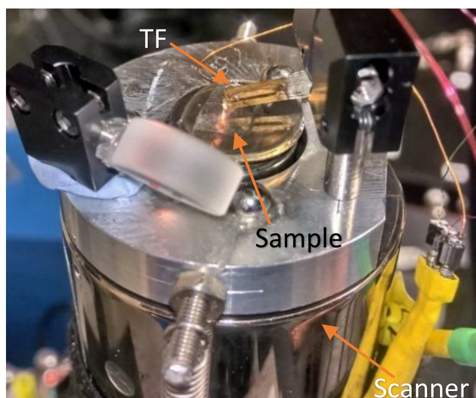

Figure 5.9 Experimental setup for the immersed measurements using the MultiMode scanner and the $LiNbO_3$ TF as a piezoelectric probe.

The experimental setup for the SPM imaging is shown in Fig. 5.9. It was composed by a Bruker scanner from the MultiMode IV and the head of the microscope was removed to allow for placement of the TF holder. The feedback for the measurements was made by the PID of the HF2LI, using the deflection from the breaking box as the signal for the feedback loop. The custom-made signal access box allowed us to feed the TF response and record using the microscope.

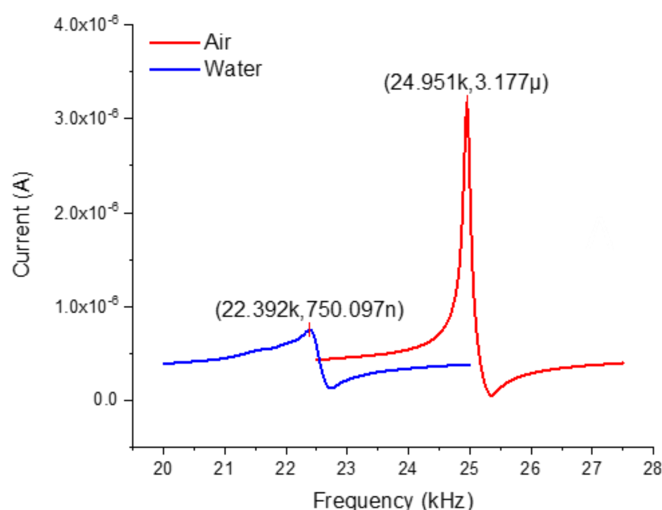

Figure 5.10 Electrical response of the $LiNbO_3$ TF in air (red) and water (blue).

The method used for detection consisted of driving the bending mode of the TF to work in semi-contact mode. The electrical response of the TF was monitored to control the feedback. It was necessary to make a frequency sweep before the measurements to identify the resonance frequency and the phase offset of the TF resonance. The PLL was used to track the phase of the signal. In the PID, the magnitude input is the amplitude of the signal; the setpoint value selected was close to the value of the resonance. The PID values were adjusted to obtain the best resolution. The images recorded by the methodology described above are shown in Fig. 5.11. Both topography images, either in air or in water, show fine structure with topography features below 12 nm, corresponding with the standard roughness from commercial indium tin oxide (ITO) samples [113]. The drive amplitude images present a contrast corresponding with the topographical features. Conversely, the images showing the shift in the frequency (δf) do not show any contrast, as the feedback was well adjusted to reduce the error to the minimum.

These results have demonstrated the feasibility of this methodology to study samples either in air or in water, without crosstalk between the electric driving of the probe and the environment. This methodology has enormous potential for the investigation of the morphology of samples which require liquid environment, like biological materials or living cells [114]. Moreover, it is a promising technique for the investigation of samples immersed in high conductive liquids, such as the liquid electrolytes present in some batteries. [115] For high-resolution imaging, it will be necessary to optimize the shape and size of the Au wire.

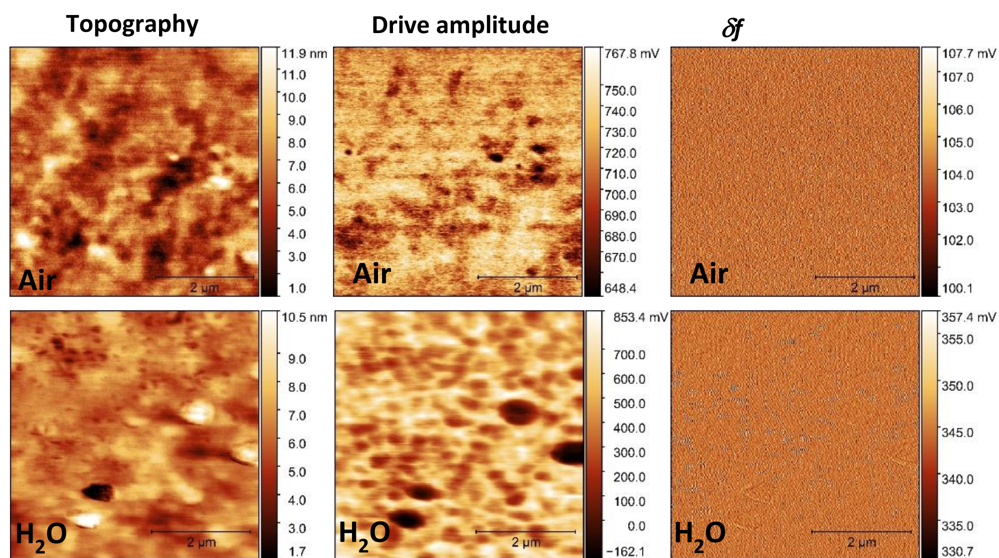

Figure 5.11 Topography, PID drive voltage and δf maps of an ITO sample made the TF probe method. Images of the top row were made in air and the images of the bottom were made in water. Imaging parameters: TF drive V_{AC}=10mV and phase offset φ=-130°.

5.3. Silicon nitride membranes

In addition to the one-dimensional resonating systems, we also studied 2D vibrating structures. Initially, we performed some investigations in commercial silicon nitride (Si_3N_4) membranes. These samples were measured with Laser Doppler vibrometry to identify the free vibrational modes. To follow, they were also investigated via diverse dynamic AFM methods, such as FMM, UFM and Modulation-UFM, comparing the experimental results with theoretical modellings of these systems.

The main motivation was to locally study the distribution of the vibrational modes in MEMS and NEMS with nanoscale resolution. Optical methods have demonstrated themselves to be very efficient for measuring the vibrating devices, reaching picometer resolution for vertical displacement. However, due to the laser wavelength, they are limited in spatial resolution to um length scale. To address this problem, we developed a new methodology based on the AFM. This novel method is called modulation ultrasonic force microscopy (M-UFM) and allows for the mapping of vibrational modes with frequencies much higher than is typically achievable via function generator AM modulation and the required nanoscale spatial resolution. The principles of this method are based in UFM theory, using non-linear interaction of the tip with the sample for detection. M-UFM requires a high-frequency detection setup for the study of high-frequency resonating systems. Prior to the experiments, we had to estimate the resonance frequencies of the sample, providing a more accurate study.

To approach the M-UFM development, we performed separate modelling of the cantilever and membrane dynamics. As it was explained in literature review, the contact resonance of the cantilever can be theoretically determined by the geometry and the material parameters. Likewise, the resonance of a rectangular membrane can be calculated using the expression

$$f_{ij} = \frac{1}{2}\sqrt{\frac{\zeta}{\sigma}}\sqrt{\frac{i^2}{L_x^2} + \frac{j^2}{L_y^2}}, \tag{53}$$

where ζ is the pre-tension of the membrane, σ is the 2D membrane density, i and j are the indexes of the vibrational modes, and L_x and L_y are the length of the membrane for the x and y axis, respectively. In the case of our study, the membrane had a square window, therefore, $L_x = L_y = 500\ \mu m$. The value of the pre-tension of the membrane was calculated from the value of the residual stress found in literature[116] and determined for the particular case of the 200 nm thickness Si_3N_4 membrane (S171-6, Agar scientific), obtaining, $\zeta = 24\ kg \cdot s^{-2}$. The

2D-density is also inferred by the 3D value found in literature and multiplied by the thickness, $\sigma = 6.34 \cdot 10^{-4}\ kg \cdot m^{-2}$. Therefore, the first resonance frequency of the membrane was found to be equal to $f_{11} = 275\ kHz$.

This membrane was first examined with the LDV (Polytec UHF-120, Germany). The vibrations were mechanically excited using a piezotransducer inserted under the membrane. Fig. 5.12 shows the spectrum of resonances obtained from the measurements. We can identify the fundamental resonance frequency in $f_{11} = 315\ kHz$, with additional peaks appearing at $f_{22} = 630\ kHz$, corresponding to the second harmonic of the fundamental frequency that we treated as spurious LDV signal. The maps of the vibration's amplitude obtained via UHF LDV for each of the mentioned overtones are superposed to the corresponding resonance peaks in the spectrum in Fig. 5.12.

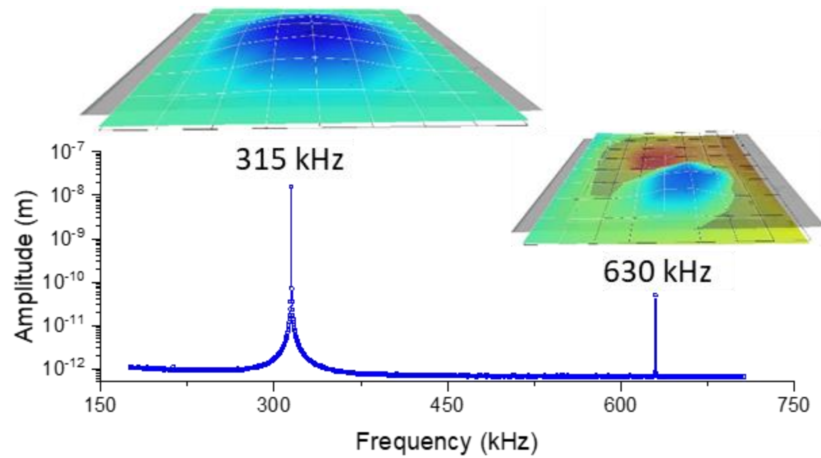

Figure 5.12 Plot of two resonance peaks of the Si_3N_4 membrane measured via LDV. The peak at 315 kHz correspond with the fundamental mode of the membrane shown in the inset above the peak. The peak at 630 kHz correspond with the second harmonic also shown in the inset above the peak.

In the first attempt at the nanoscale mapping of the vibrational modes via SPM modes, we created UFM images in the corner of the membrane, recording the topography and the nanomechanical images simultaneously. These results are displayed in Fig. 5.13., where we see that the topography shows negligible contrast between the suspended and supported areas, suggesting membrane under high tension. Nonetheless, in the UFM image the suspended area is clearly visible, presenting dark contrast. This dark contrast represents the low UFM response, corresponding to the low mechanical stiffness in the suspended areas. One can observe that both images present triangles on the membrane inhomogeneities. During

the experiments in the Si_3N_4 membranes, we realised that the tips were degrading very quickly during the scanning of these particular samples.

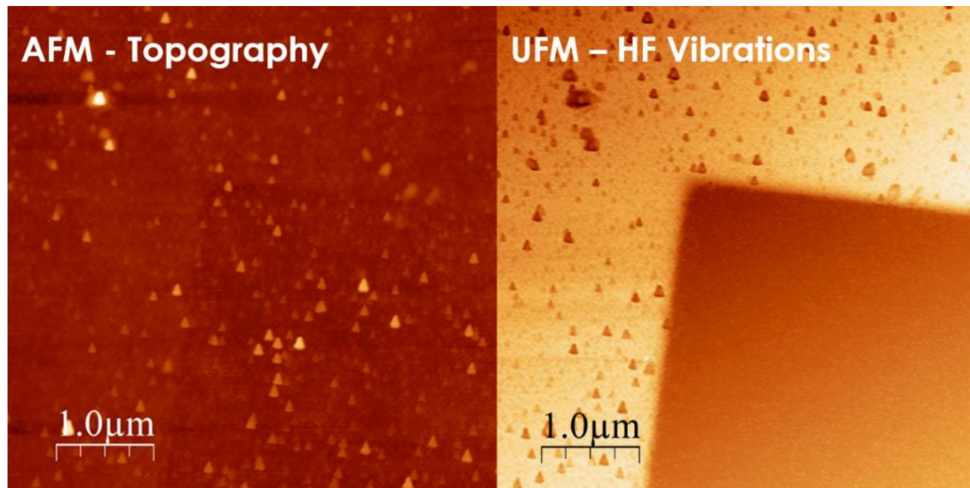

Figure 5.13 Topography and UFM images of a corner of a Si_3N_4 membrane. The topography image shows neglegible contrast between the suspended and the suported regions of the membrane. Conversely, the UFM image presents clean contrast between the two areas. The dark contrast indicates low UFM response, due to the poor propagation of ultrasounds, and corresponds with the suspended region.

In order to establish a comparison between the diverse ultrasonic existing methods and the novel technique, the same region of the Si_3N_4 membrane was examined using FMM, UFM and M-UFM modes. The images created using the three different methods are presented in Fig. 5.14. Across the three images of the panel, the suspended and supported areas are delimited with a dashed white line. Meanwhile, the UFM shows valuable information to accurately localise the boundary between the supported and suspended regions of the membrane; this method does not offer much information about the distribution of the vibrational modes. This is a consequence of the ultrasonic excitation used, which is in the range of 4-5 MHz, being at least one order of magnitude higher than the free resonance frequency of the membrane.

The FMM image in Fig. 5.14 was measured using 350 kHz as the excitation frequency, which is close to the free resonance of the membrane. In this image, we can identify an area with a higher response located in the suspended region. Conversely to the UFM, the FMM image does not show the contrast between the suspended and supported areas in the vicinity of the membrane edge. The third map, presented in Fig. 5.14, corresponds to the M-UFM method, which allows non-linear excitation and probing of the sample vibrational modes simultaneously. This image was made using 340 kHz as the modulation frequency for 4.41 MHz

of the carrier signal. The M-UFM image shows a different contrast between the suspended and supported area, as in the UFM, and it also shows that the high-response in the suspended region is corresponding with the excitation of the vibration of the membrane. Furthermore, M-UFM benefits from being a method in which the force at the modulation frequency is only produced at the probing point, allowing for local excitation of vibrations.

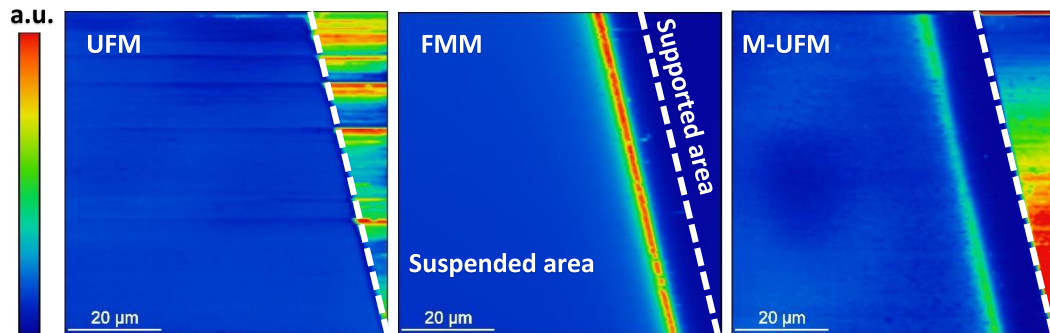

Figure 5.14 Comparison of UFM, FMM and M-UFM results for the same area. The dashed lines represent the boundary between the supported and the suspended areas.

The image a) in Fig. 5.15. shows the reconstruction of one-dimensional scans across the membrane boundary whilst changing the frequency from 280 to 380 kHz, displaying the map of the vibrational mode distribution near the edge. Correspondingly, Fig. 5.15.b shows an M-UFM scan made using 330, 340, 350 and 360 kHz at the modulation frequency (from top to bottom). Both FMM and M-UFM images show that the local maximum in the response of the suspended area shifts in distance from the membrane boundary for different frequency values. Therefore, we are simultaneously exciting and mapping the vibrational modes of the membrane in contact. In the case of the excitation of the fundamental mode, the maximum displacement (and response) should be placed in the centre of the membrane. Nevertheless, in the presented case, the probing of the vibrational modes is made in contact, making it necessary to consider the ratio between the effective mass of the cantilever and the membrane. When the effective mass of the cantilever is dominant in the interaction, the excitation of the resonance becomes extremely difficult, losing sensitivity in the probing.

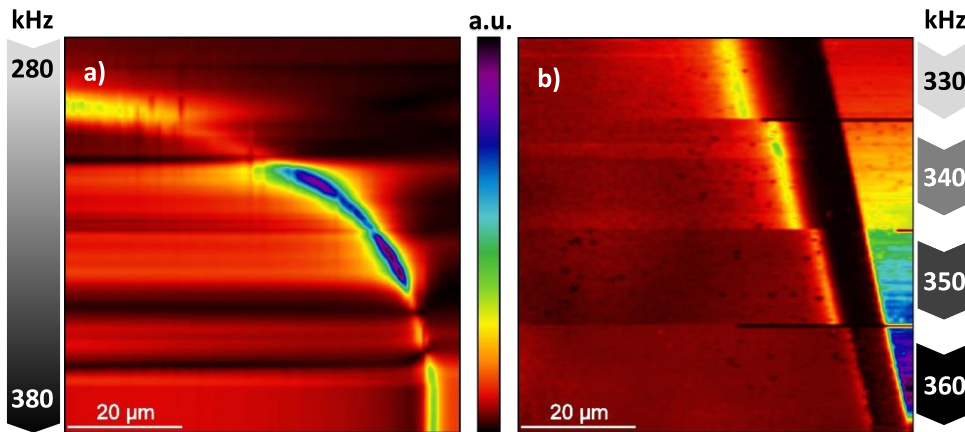

Figure 5.15 a) Image of 1D scans across the membrane while sweeping frequency, from 280 to 380 kHz using FMM setup. b) Image of M-UFM scans using 330, 340, 350 and 360 kHz at the modulation frequency.

For a better understanding of these SPM experimental results, the cantilever-membrane system was theoretically modelled. We have approximated the cantilever and the membrane as massless springs individually attached to a mass. This mass represents the cantilever and membrane's masses, being denoted by m_c^* and m_m^*, respectively. By effective mass, we refer to the fraction of mass, which is contributing to the motion under the experimented forces. The dynamics of the membrane under the cantilever probe was modelled as a rod with negligible mass and length *L*, which has attached to one of its ends the membrane mass point, and to another point has the cantilever mass point. This last position is not fixed, due to it representing the position (*l*) of the cantilever during the scan. The rod is supported to a pivoting point, which allows it to hinge when the cantilever is moving along the rod.

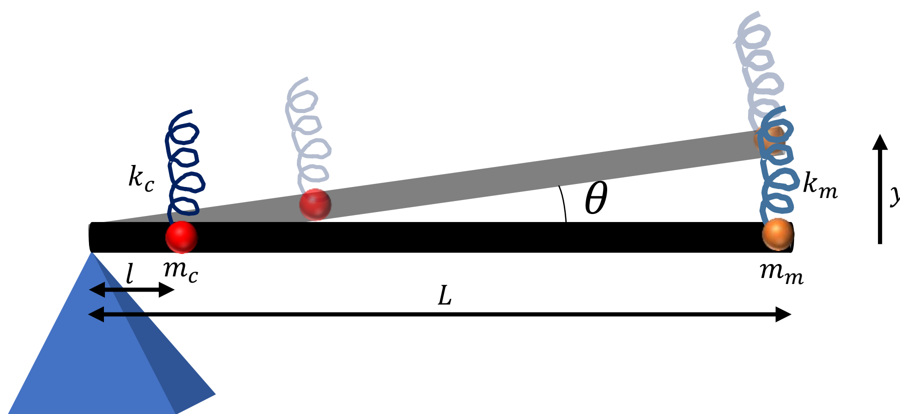

Figure 5.16 Schematics of the probing of the cantilever across the membrane. The cantilever behaviour is approximated to a spring attached to a mass point. The membrane dynamics are represented as a lever with a mass point at the free end attached to spring.

The moment of inertia (I) of the system is described by

$$I = m_c^* l^2 + m_m^* L^2. \tag{54}$$

Considering the small angle (θ) approximation $\tan\theta \approx \theta$, the torque created in the pivoting rod is equal to

$$\tau = -k_c l\theta L - k_m L\,\theta. \tag{55}$$

The angular acceleration of the system, $= \frac{d^2\theta}{dt^2}$, links both magnitudes, moment of inertia and torque, as is described by

$$I\alpha = \tau. \tag{56}$$

Therefore, we can write the motion equation dependent on the time as

$$I\frac{d^2\theta}{dt^2} = -k_c lL\theta - k_m L^2\,\theta. \tag{57}$$

Transforming the above equation from the angular to the vertical coordinate, with the expression $y = \theta L,$ we obtain

$$(m_c^* l^2 + m_m^* L^2)\frac{d^2 y}{dt^2}\frac{1}{L} + (k_c l + k_m L)y = 0. \tag{58}$$

Therefore, the natural frequency of the system is described by

$$\omega = \sqrt{\frac{k_c \frac{l}{L} + k_m}{m_c^* \left(\frac{l}{L}\right)^2 + m_m^*}}. \tag{59}$$

With MATLAB simulations made using the above described model, we calculated a resonance frequency distribution that is dependent on the change of the cantilever position along the membrane. For both systems, cantilever and membrane, we assumed in the calculations that their effective mass was a quarter of the total mass, for the natural frequency oscillation of the systems. The shape of the membrane was approximated to a circular membrane in order to simplify the calculations of its resonance frequency. The value of the membrane stiffness $k_m = 121.83\ N \cdot m^{-1}$ was inferred from the LDV experimental values of its resonance frequency $f_m = 315\ kHz$ and the effective mass $m_m^* = 3.11 \cdot 10^{-11} kg$. The stiffness of the cantilever was taken from the values offered by the cantilever manufacturer $k_c = 3\ N \cdot m^{-1}$ and the effective mass of the cantilever $m_c^* = 1.10 \cdot 10^{-11} kg$ was determined by its geometry and its density. The plot of the total system's resonance frequency

for the different cantilever position along the membrane shows that the maximum resonance frequency value is near to the edge of the membrane, at $l = 8.75 \cdot 10^{-6} m$.

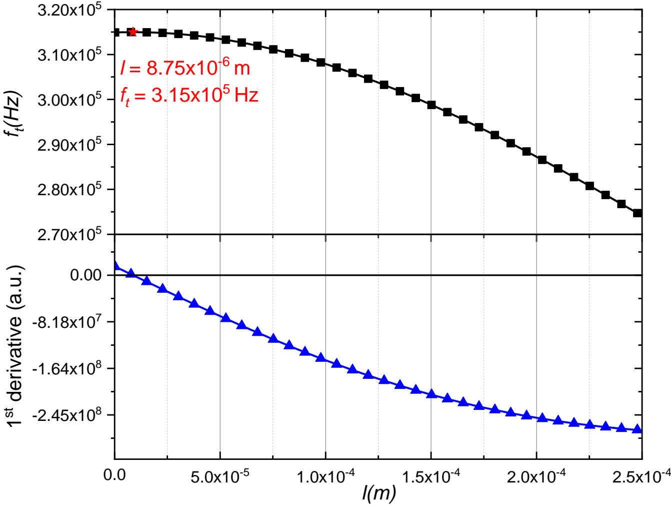

Figure 5.17 Plot of the resonance frequency as a function of the distance from the edge. The plot of the bottom is the first derivative of the top plot.

The MATLAB programme can be found in Annex II. The results obtained from this model are a simple first approximation to explain the experimental results. More accurate results, considering the real geometry of the membrane for example, requires FEA calculations, such as COMSOL.

5.4. Graphene nanodrums

5.4.1. Experimental measurements.

Upon studying the dynamics of commercial Si_3N_4 membrane, we decided to fabricate and characterise other mechanical resonators that could potentially have very high resonance frequencies. The reasonable approach would be to use 2D materials, such as graphene, which has high stiffness and lower area mass to achieve very high frequency resonating devices. In this section, I describe the study of a mechanical resonator made by a suspended graphene flake on top of a hole, as it is shown in optical images in Fig. 5.18. The fabrication of the graphene drum was carried out following the procedure detailed in the Materials Chapter 3, including the substrate patterning, graphene exfoliation and transfer. The resonator was characterised using various ultrasonic SPM methods, including UFM and contact resonance AFM (CR-AFM). We also elaborated on the complementary modelling of the systems, for a better understanding and interpretation of the experimental results.

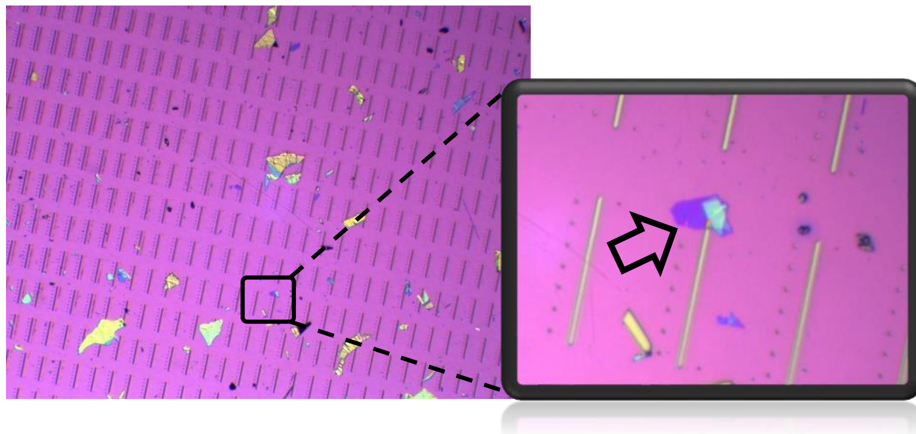

Figure 5.18 Optical images of the patterned substrate with the transfer of multiple multi-layer graphene (MLG) flakes.

It has been demonstrated that the combination of AFM with higher excitation frequencies increases the sensitivity in probing of the mechanical properties and realises nanoscale spatial resolution in a non-destructive approach. These dynamic AFM modes include the detection of the cantilever displacement at the probing point, whereas the sample oscillates vertically with the corresponding excitation waveform. In the case of low frequency excitation, in the range of the contact resonance frequency of the cantilever, the method is called CR-AFM as described in Chapter 4. CR-AFM benefits from the high sensitivity of the cantilever at the resonance frequency for the nanomechanical probing. Using higher excitation frequencies and detecting the tip-sample interaction in the non-linear regime, UFM and M-UFM can be used.

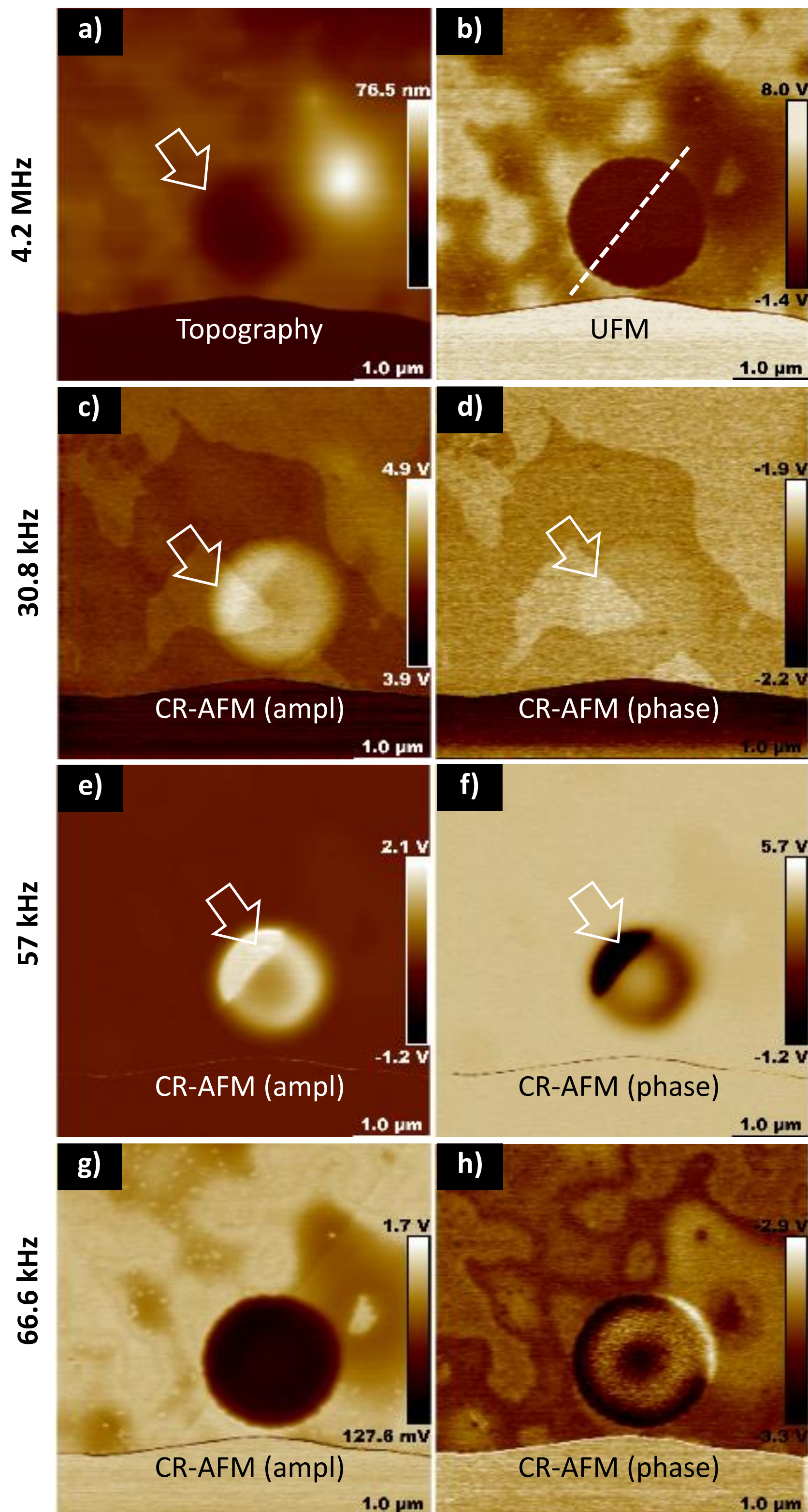

Figure 5.19 a) AFM topography. b) UFM. c) and d) CR-AFM amplitude and phase respectively at 30.8 kHz. e) and f) CR-AFM amplitude and phase respectively at 57 kHz. g) and h) CR-AFM amplitude and phase respectively at 66.6 kHz.

In Fig.5.19.a-b, we can see, respectively, the topography and the UFM images simultaneously recorded a few-layer graphene (FLG) flake covering one of the patterned holes in the substrate. The topography image allows us to precisely determine the thickness of the flake (*t*=12nm). Nevertheless, in this image, a smooth depression is barely observed in the area of the hole (arrow on the image). At the same time, the UFM image presents a clear contrast between the suspended and supported regions of the flake, allowing us to determine the exact radius of the hole, *R*=940± 5 nm. In the vicinity of the hole, this nanomechanical map also shows dark contrast, revealing weak interaction of the FLG flake with the substrate and interfacial defects. Whereas the UFM results are very sensitive to the subsurface defects in the supported region of the FLG flake, the UFM contrast in the suspended regions shows poor sensitivity to the subsurface features [117].

Fig. 5.19 c-h shows amplitude and phase images of the CR-AFM images at different sample excitation frequencies. We can see that, depending on the frequency used, there are considerable variations in the contrast, shape and dimensions of the drum. Comparing panels c and d from Fig. 5.19, both made at f_{dr}=30.8 kHz, a frequency that is considerably lower than the resonance frequency of the cantilever in contact, $f_{\mathrm{CR\text{-}R}}$=64.6 kHz, the amplitude image shows the hole as a bright halo. Whereas, the phase poorly present contrast in the hole. Nevertheless, both images reveal the internal structure of the membrane not visualised in the topography, UFM or CR-AFM at other frequencies. This particular contrast is interpreted as an internal crack in the FLG flake, which induces a change in the stiffness without altering the topography. Conversely to the f_{dr}=30.8 kHz images, both amplitude and phase CR-AFM maps made at f_{CR}=57.0 kHz, from Fig. 5.19 e-f, show a donut-shaped hole with a smaller diameter. Furthermore, an additional subsurface feature is revealed in both images (bright in the amplitude and dark in the phase image) is presented as a contrast segment at 45° across the hole. Ultimately, CR-AFM images made at f_{CR}=66.6 kHz are shown at the bottom of the panel. The amplitude image shows a consistently dark contrast in the hole whilst the phase map shows a bright halo surrounding the darker hole.

Therefore, CR-AFM demonstrates the ability to reveal the material defects hidden under the surface of the suspended material. Nevertheless, the strong frequency dependence of the contrast demanded comprehensive theoretical and experimental studies. In the quest for understanding the frequency-dependent response of CR-AFM, we carried out one-dimensional scans across the hole, whilst changing the frequency in 1kHz from 50 to 69 kHz and simultaneously recording amplitude and phase. The collected data is shown in Fig. 5.20, displayed as 2D maps of amplitude or phase, where the vertical axis is the driving frequency

f_{dr} and the horizontal axis is the position of the probe across the hole, *r*. The resulting images show the apparent variation of the hole diameter, from the smaller diameter at lower driving frequencies to the largest at the contact resonance $f_{dr} = f_{CR-R}$. Furthermore, in the central region of the hole, at driving frequencies lower than the contact resonance, a second maximum appears (indicated by the arrow in Fig. 5.20.a). This phenomenon is attributed to the change in the contact stiffness of the tip-membrane, being lower in the centre of the membrane and increasing when approaching the supported region, where the stiffness can be considered "infinite". It is known that the resonance frequency of the cantilever-tip in contact with the membrane decreases as its stiffness also decreases. Therefore, the condition for the resonance for the decreased driving frequency f_{CR} is satisfied in the more central area of the membrane away from its border, resulting in the smaller diameter of the membrane creating a bright ring at the position where the resonance occurs.

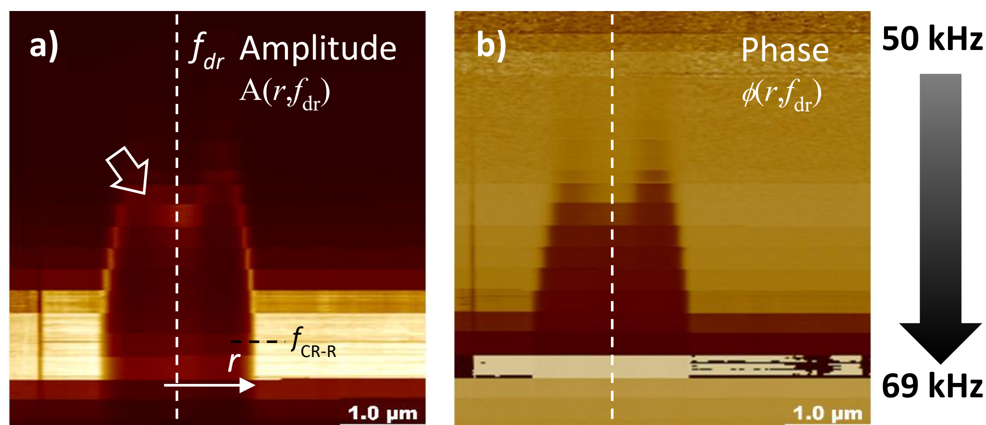

Figure 5.20 Plot of the CR-AFM response as the function of the position *r* across the hole (horizontal axis, *r*) and frequency (vertical axis, f_{dr}) with (a) amplitude A as the function of A(r,f_{dr}) and (b) $\phi(r,f_{dr})$ phase profile at driving frequency f_{dr} changing from 50 to 69 kHz in 1 kHz steps.

To fully understand these observed phenomena, we analytically and numerically modelled the tip-membrane dynamics as described below.

5.4.2. Analytical modelling for the cantilever behaviour in a FLG drum

As was previously explained, in general the resonance frequency of mechanical resonators is mainly dependent on the physical properties and geometry of the system. For the particular cases of 2D resonators made by 2D materials, the initial condition of the pre-tension (ζ) and the thickness of the film play fundamental roles in the resonance frequency. For example, in the ideal case of a mechanical resonator made by a tensioned monolayer of graphene, the dynamic behaviour of such a system is described as membrane, where the bending rigidity is negligible compared with the pre-tension term. Nevertheless, for non-ideal resonators, such as the free suspended FLG flake studied in this work, its dynamics are dominated by a circular-plate-like behaviour. The resonance frequency of the plate can be calculated with the equation *42* from the literature review (chapter 2).

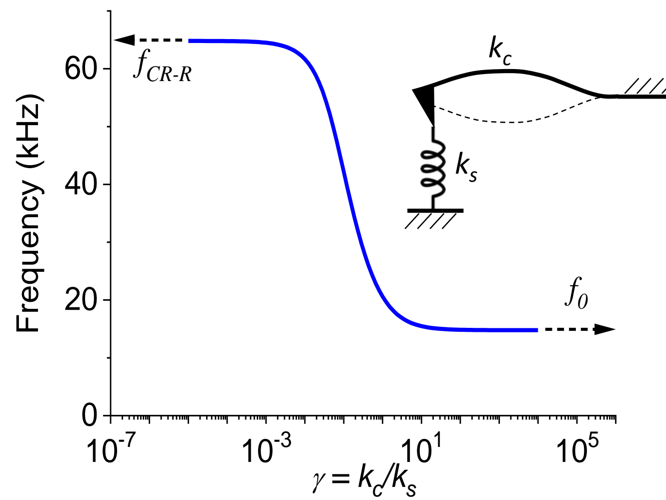

Figure 5.21 Resonant frequencies of the cantilever for the first contact resonance mode (n=1) for the different values of the sample stiffness.

For the FLG flake with the dimensions previously presented, the fundamental resonance frequency is f_{plate} = 138.34MHz. Due to f_{plate} being several orders of magnitude higher than the driving frequencies used in UFM and CR-AFM experiments, we cannot excite the vibrational modes of the plate itself. This condition allowed us to use the point-mass model reported elsewhere [118] to describe the dynamics of the tip-membrane system. This approximation considers the GR membrane as a negligible mass-spring with k_s stiffness, attached at the free end of the cantilever (see the schematic of the inset in Fig. 5.21). The flexural motion of the

cantilever was modelled as was previously detailed in the literature review chapter, section 2.8.2, using Eq.*33*. We used the silicon density and Young's modulus values found in the literature. The length and width of the cantilever can be easily determined by an optical microscope image. However, with this method, the thickness can not be determined with accurate precision. We used the "Sader" model to find the experimental cantilever stiffness [119], $k_c = 0.184 \pm 0.008$ N m^{-1}. That allowed us to estimated the thickness of the cantilever $h = 5.86\ 10^{-7}$ m.

To study the higher-order modes of cantilever resonances, we used the theoretical model developed by Yamanaka K. et al. [120], where they assumed that the solution of the equation of 2D deflection vibrations (Eq. *33*) takes the form of

$$z = C\, sin(\omega t + \delta)\Phi(x), \tag{60}$$

with

$$\begin{aligned}\Phi(x) = (sin\, \alpha + sinh\, \alpha)\left(cos\frac{\alpha}{L}x - cosh\frac{\alpha}{L}x\right) \\ + (cos\, \alpha + cosh\, \alpha)\left(sin\frac{\alpha}{L}x - sinh\frac{\alpha}{L}x\right),\end{aligned} \tag{61}$$

where ω is the angular frequency, L is the length of the cantilever and the constant

$$\alpha = \left(\frac{12\rho\omega^2 L^4}{Eh^2}\right)^{\frac{1}{4}} \tag{62}$$

relates the cantilever parameters with the resonance frequency. This constant was obtained from the boundary conditions. Furthermore, considering that the sample behaves like a linear spring and making the corresponding analytical changes described in the paper, the motion equation can be written as

$$\frac{k_c}{3k_s}\alpha^3 P(\alpha) = Q(\alpha), \tag{63}$$

where *P(α)* and *Q(α)* are defined as

$$P(\alpha) = 1 + cos\, \alpha\, cosh\, \alpha, \tag{64}$$

and

$$Q(\alpha) = cos\, \alpha\, sinh\, \alpha - sin\, \alpha\, cosh\, \alpha. \tag{65}$$

Solving numerically equations *64* and *65*, for the boundary conditions below of the relation between the stiffness of the sample and the cantilever, we calculated the value of $\alpha = 3.92$.

$$k_s \ll k_c \Rightarrow P(\alpha) \to 0 \tag{66}$$
$$k_c \ll k_s \Rightarrow Q(\alpha) \to 0 \tag{67}$$

In the first case, the ratio between the stiffness of the sample and the cantilever corresponds experimentally with free cantilever, $k_s \rightarrow 0$, with resonance frequency: $f_{free\text{-}cantilever}$ = 13.8kHz. And the second one corresponds with the probing point in the supported FLG $k_s \rightarrow \infty$, $f_{substrate}$ = 64.6kHz. By these equations, we obtained the resonant frequency curve, plotted in Fig. 5.21, which relates the resonant frequency of the cantilever with the stiffness of the sample for the first overtone of the cantilever in contact.

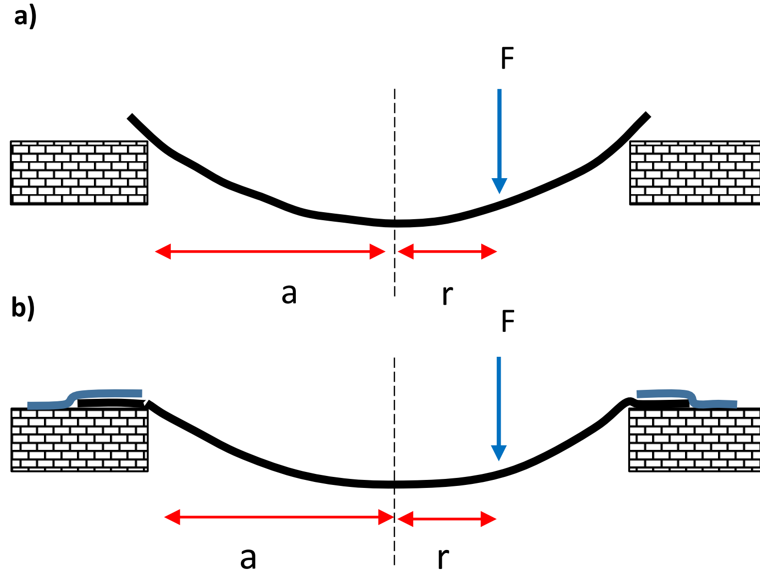

Figure 5.22 Two typical boundary conditions for the plate suspended over a circular hole. (a) simply supported edges and (b) clamped edges.

In the case of a sample such as FLG drum, the stiffness of the sample is dependent on the probing distance from the centre of the drum. This stiffness distribution can be modelled considering different boundary conditions of the supported flake. For example, it can be assumed that the FLG flake is a plate supported on top of the substrate and clamped in the edges, see Fig. 5.22.b. In this case, the stiffness distribution, as a function of the probing point from the centre of the drum r, is given by

$$k_s(r) = \frac{16\pi D {R_s}^2}{\left({R_s}^2 - r^2\right)^2}, \tag{68}$$

where R_s is the total radius of the drum and D is the bending rigidity term given by

$$D = \frac{E_s t_s^3}{12(1 - \nu_s^2)}, \tag{69}$$

where E_s is the Young's modulus, v_s is the Poisson's ration and t_s is the thickness of the sample. Thus

$$k_s(r=0)=\frac{16\pi D}{{R_s}^2}. \tag{70}$$

By substituting the parameters of the flake into Eq. *70* and using the in-plane Young's modulus of graphene of 1 TPa [121], we obtain the calculated value of the stiffness in the centre of the plate of k_s = 5.94 N m^{-1}, which is more than twice the experimental one, k_s = 2.15±0.008 N m^{-1}. By changing the assumption of the clamped edges of the plate to the FLG flake simply supported onto the substrate with non-clamped edges, see Fig. 5.22.a, the distribution of the drum stiffness is given by

$$k_s(r)=\frac{1}{H(r)c_0{R_s}^3}, \tag{71}$$

where R_s is the total radius of the drum, and $H(r)$, b_0 and c_0 are expressed as

$$H(r)=\frac{1}{\pi D{R_s}^4}\frac{2(1+\nu_s)}{9(5+\nu_s)}\left(r^3-b_0R_sr^2+c_0{R_s}^3\right), \tag{72}$$

$$b_0=\frac{3(2+\nu_s)}{2(1+\nu_s)}, \tag{73}$$

$$c_0=\frac{4+\nu_s}{2(1+\nu_s)}. \tag{74}$$

Simplifying these equations to obtain the stiffness in the centre of the plate, they can be expressed as

$$k_s(r=0)=\frac{1}{H_0c_0{R_s}^3}, \tag{75}$$

with

$$H_0\equiv H(r=0)=\frac{c_0}{\pi DR_s}\frac{2(1+\nu_s)}{9(5+\nu_s)}. \tag{76}$$

Once again, comparing the experimental value of the stiffness in the centre of the drum k_s = 2.15±0.008 N m^{-1}, with the calculated $k_s(r=0)$ = 2.35 N m^{-1} via the latest formulation, we can confirm that the simply supported model better predicts the experimental results.

We then can use the equations for stiffness distribution in a simply supported plate together with the cantilever-sample relation obtained in Fig. 5.21 to calculate the location of the maximum amplitude with respect to the edge of the membrane. We further extended the analysis by considering the amplitude and phase of a cantilever as a driven damped simple harmonic oscillator. In this case, the amplitude *A* and phase φ of the cantilever's response are expressed as

$$A = \frac{A_0[\omega_{CR}(r)]^2}{\sqrt{([\omega_{CR}(r)]^2 - \omega_{dr}^2)^2 + \frac{\omega_{dr}^2}{[\omega_{CR}(r)]^2 Q}}} \quad (77)$$

and

$$\varphi = tan^{-1}\left(\frac{[\omega_{CR}(r)]^2 \omega_{dr}}{Q([\omega_{CR}(r)]^2 - \omega_{dr}^2)}\right), \quad (78)$$

where A_0 is the maxima amplitude, $\omega_{CR}(r)=2\pi f_{CR}(r)$ is the resonance frequency of the cantilever in contact that depends on the position *r*, $\omega_{dr}=2\pi f_{dr}$ is the driven frequency and *Q* is the quality factor of the cantilever in contact.

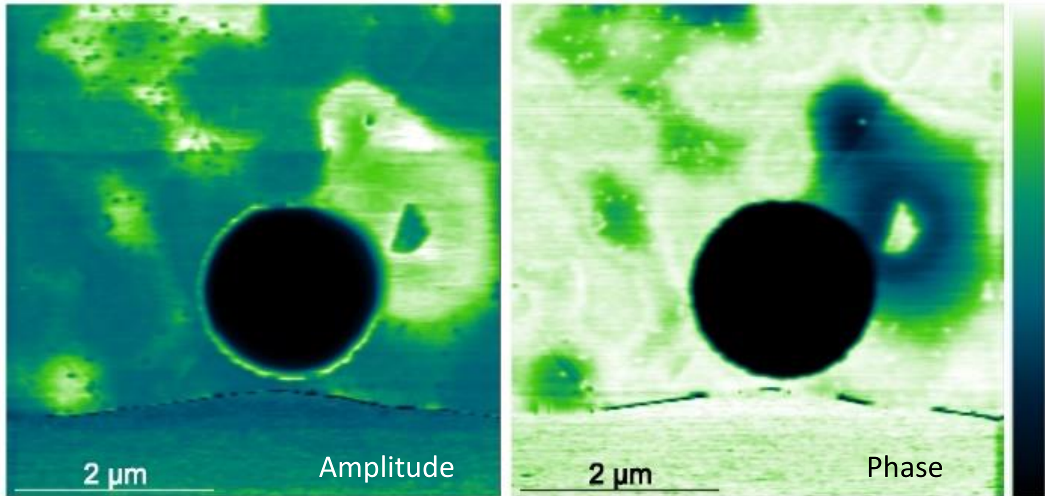

Figure 5.23 CR-AFM at 62 kHz, amplitude and phase, respectively.

Using this formalism, we simulated the amplitude dependence of the CR-AFM A(r,fdr) displayed in Fig. 5.20.a. The simulation and experimental results are presented in Fig. 5.24(a-b), showing an exceptional agreement. In Fig. 5.24.c, we have the superposition of the experimental and simulated profiles of the amplitude at f_{dr}=62 kHz, below the resonance of

the cantilever in the supported region f_{CR-R}= 64.4 kHz. In this image, we can see the low response in the suspended region, whereas close to the edge we can observe the higher response corresponding with the bright ring shown in Fig.5.23. We observe that a positive correlation between the model and the experiment is also shown in the comparison of the profiles at f_{dr}= 65kHz, close to the contact resonance of the supported flake. Finally, the plot in Fig. 5.24.e shows the experimental measurement of CR-AFM response in the centre of the drum vs the supported FLG plate; the frequency shift allows for precise determination of the stiffness of the GR membrane.

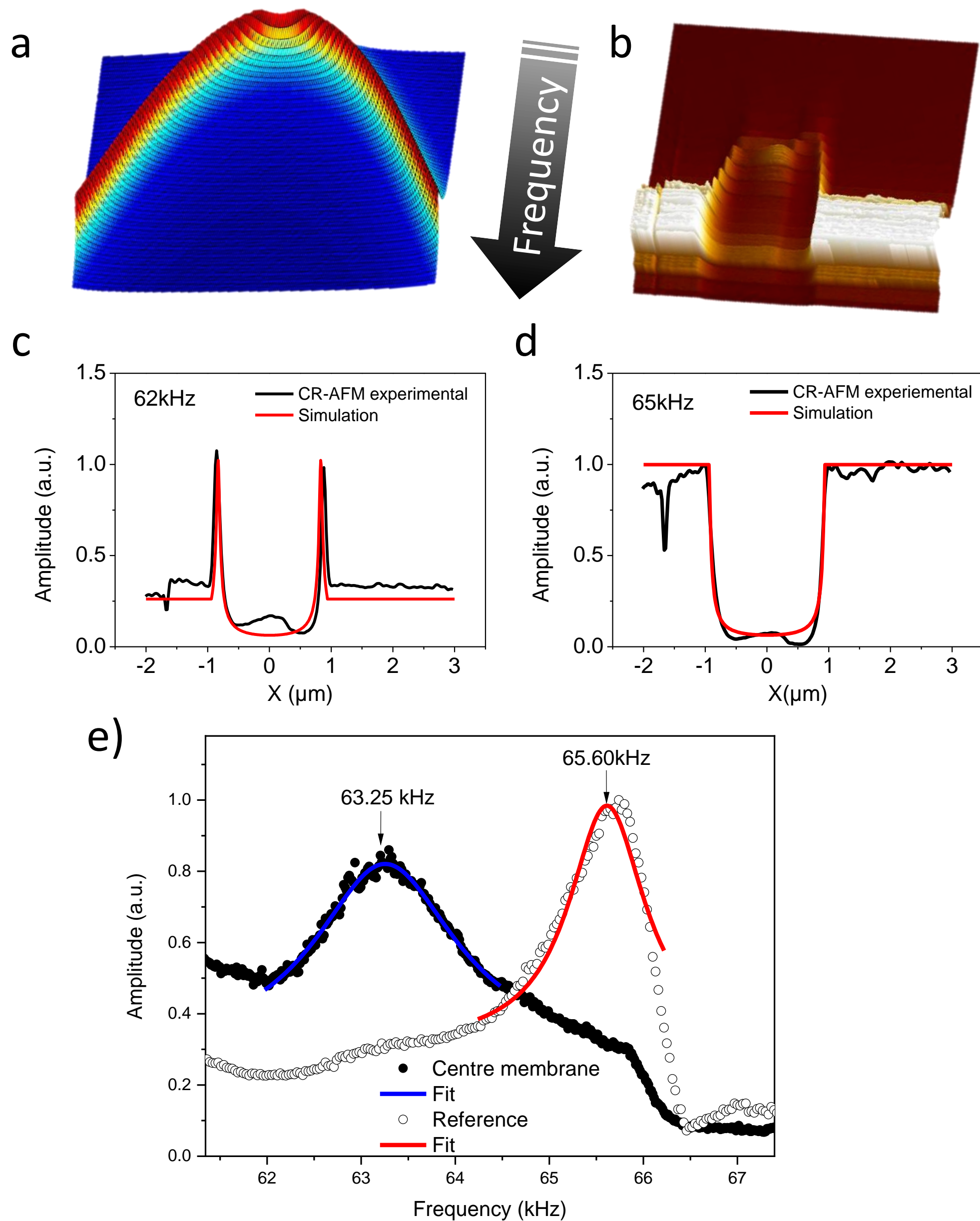

Figure 5.24 (a) Matlab modelling of the amplitude response A(r,f_{dr}) of the CR-AFM as the function of the radius from the centre of the plate and the driving frequency f_{dr} for the 50 to 69 kHz frequency range, (b) experimental CR-AFM data of the A(r,f_{dr}) response for the same frequency range. (c, d) comparison of the simulated and measured one-dimensional profiles *A(r)* at the frequencies below and above contact resonance frequency for the solid contact. (e) Experimentally measured CR-AFM response in the centre of the MLG plate vs supported graphene, the frequency shift allows for precise determination of the stiffness of the GR membrane.

It is interesting to apply the interpretation of the sample stiffness in a simple, suspended graphene layer on a round shape hole to a more complex system of a quasi-suspended structure produced in a lateral heterostructure of MoS_2 and WS_2, which was qualitatively described in Chapter 3 in (Fig. 3.4). The suspended region here is the result of the ripples formed to release the strain cause because the lattices mismatch between the two materials. The results of the one-dimensional scan while changing the frequency from 60 to 68 kHz across the ripples are displayed in Fig. 5.25. The figure shows topography and the CR-AFM amplitude and phase maps. In the CR-AFM images, the response observed in the ripples is analogous to that experienced in the graphene drum, where the apparent variation of the ripple diameter is dependent on the frequency of the excitation. More details about these structures can be found in the next experimental chapter dedicated to the supported structures of 2D materials. However, the nanomechanical analysis of these complex structures forms part of a future work.

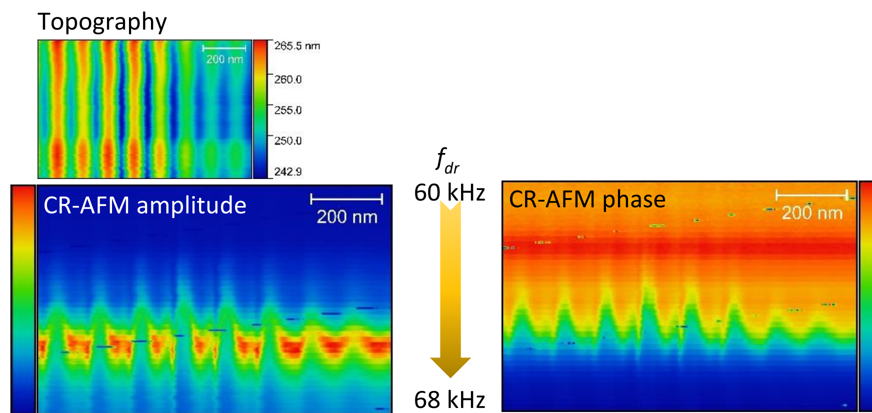

Figure 5.25 One-dimensional scans across the ripples while sweeping frequency from 60 to 68 kHz.

5.5. Summary

To address the necessity of new technique for the exploration of vibrational modes with nanoscale resolution in MEMS and NEMS, in this chapter, we presented the study of the mechanics of four different resonating devices.

Initially, we optically investigated AFM cantilevers, which are the already existing resonating devices implemented in the state-of-the-art SPM. The laser Doppler vibrometry (LDV) measurements of the AFM cantilevers allowed us to identify the free vibrational modes of such systems, being an essential result for the understanding of the cantilever's behaviour in the non-contact SPM modes.

To follow with the 1D- resonators, the LDV and electrical readout results obtained on the quartz and $LiNbO_3$ tuning fork characterisation allowed us to elaborate the calibration of the mechanical and electrical response of such devices and confirmed the possibility of simultaneous excitation and detection of quantum turbulence in ^4He using flexural and torsional vibrational modes of quartz TF at the same time. Moreover, we also proved which $LiNbO_3$ TF can be used as piezoelectric sensors for measurements in a liquid environment. The absence of electric crosstalk shown between the electric driving of the probe and the environment make these devices promising probes for the biological investigations as well as for battery technologies studies.

For the investigation of the local distribution of vibrational modes in 2D-resonators, we developed the novel method called modulation ultrasonic force microscopy (M-UFM). It is worth noting that our study of the vibrational modes in Si_3N_4 verified that the M-UFM allows local excitation and simultaneous mapping of vibrational modes in 2D resonators.

Finally, pushing the limit of 2D-resonators using 2D materials, we established that high-frequency UFM mapping allows for precise determination of the geometry of the suspended region, even for the relatively thick plate, as well as observation of the faults at the FLG-substrate interface. Furthermore, the excellent agreement between the modelling and CR-AFM experimental data revealed the possibility of performing absolute measurements of the mechanical stiffness of 2D material nanostructures, opening many opportunities to investigate multilayer heterostructures of 2D materials and the 2D material –substrate interface.

6. Supported Layered Structures

Two-dimensional (2D) material nanostructures exhibit interesting behaviour as a consequence of their low dimensionality. The understanding of nanoscale physical properties in such systems is fundamental for their application, requiring nanoscale measurement capabilities. In this chapter, we used ultrasonic, electrostatic and thermal scanning probe microscopies to map such properties of 2D supported heterostructures. Part of this chapter is dedicated to the results of transition metal dichalcogenides (TMDCs) heterostructures grown by our collaborators Dr Melinda Shearer, Yuzhou Zhao and Prof. Jin Song from Wisconsin-Madison University. Firstly, we report the results of non-destructive measurements of inhomogeneities in the material stiffness of vertical chemically vapour deposited heterostructures of WS_2 in the presence of buried defects. Then, we present the nanomechanical measurements of BEXP sectioned structures of WS_2. In this section, the nanomechanical and thermal measurements of WS_2 and MoS_2 lateral heterostructures are also reported. The final section of the chapter is dedicated to the nanomechanical characterisation of natural heterostructure Franckeite. This latest sample was prepared by Dr Aday Molina-Mendoza and Assoc. Prof. Thomas Mueller from the Institute of Photonics, TU Wien.

6.1. Synthetic structures – introduction

Heterostructures of various low-dimensional materials, in particular layered species with van der Waals (vdW) interlayer bonding forces, have been observed to exhibit novel properties compared to the bulk. For example, encapsulated MoS_2 among BN dielectric layers increases electron mobility. [122] The stacking of different materials permits the engineering of new materials, whereas control of the layers makes the tuning of the physical properties possible. In the quest for the tailoring of physical properties, different methodologies have been developed for the sample fabrication. For example, "scotch-tape" mechanical exfoliation and transfer. This procedure is a cheap method commonly used in the preparation of vertical heterostructures and has been fundamental in proving multiple new physical phenomena. However, this technique presents some disadvantages, such as polymeric residues stuck to the interfaces and the difficulty of mass-production of heterostructures. Alternatively, a potential route for the fabrication of van der Waals heterostructures is chemical vapour deposition (CVD) growth, which allows for the synthesis of structures in an ultra-clean environment, guaranteeing no-glue residuals at the interfaces with the prospect of scalability for mass-production. Nevertheless, the mechanisms inducing the nucleation of CVD multi-

layers stacks are still not fully understood. The possibility of solving this enigma for the precise control of synthesis of these structures was very motivating in our research. We decided to study CVD grown multi-layered plates of WS_2 (see Fig. 6.1), using diverse methods sensitive to surface and subsurface defects. These heterostructures have demonstrated themselves to be excellent candidates for flexible optoelectronic device fabrication thanks to the photosensitivity of WS_2 and the exhibited flexibility of thin films.[12]

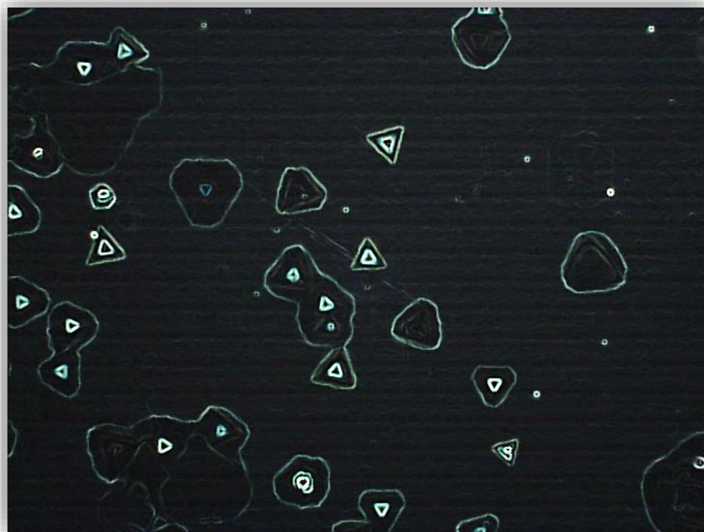

Figure 6.1 Triangular islands of WS_2. Magnification x20. (False colour scale)

6.1.1. Nanomechanical probing of subsurface defects in synthetic layered vertical heterostructures

The ability of ultrasonic force microscopy (UFM) to detect subsurface structures under a few-layer graphene flake was demonstrated in the previous chapter. This is of major importance as many devices fabricated from 2D materials consist of many layers and one would like to be able to test the mechanical integrity of such devices. In this section, we are particularly interested in observing beneath defects in CVD grown WS_2 vertical heterostructures. While topography and friction of WS_2 nanosheets and structures have been investigated [123, 124], nanomechanical maps of such structures have not been reported in the literature. To get a first impression of the possible mechanical inhomogeneities in the WS_2 pyramids, we first produced UFM and HFM maps. These images show essentially qualitative information, but allow one to discern between different regions of mechanical stiffness and adhesion.

We used UFM and HFM methods, described in Chapter 4, operating with a 75 kHz Si cantilever, to map the sample stiffness (see Fig. 6.2). The mapped area evidences, as observed in the optical images (see Fig. 6.1), the presence of a continuous layer all over the substrate and pyramidal heterostructures with a relative thickness of ~22 nm, which are non-uniformly distributed. As the UFM and HFM amplitudes increase with the local sample stiffness, we conclude that the sample stiffness can be seen decreasing as the pyramid thickness increases. However, this behaviour is not consistent throughout the map. Such response is expected in the presence of sub-surface defects, which disrupts the homogeneous layers. Additionally, both HFM images, amplitude and phase (Fig. 6.2.c-d), show similar information as the UFM map, being consistent the thicker part of the structure presenting lower stiffness.

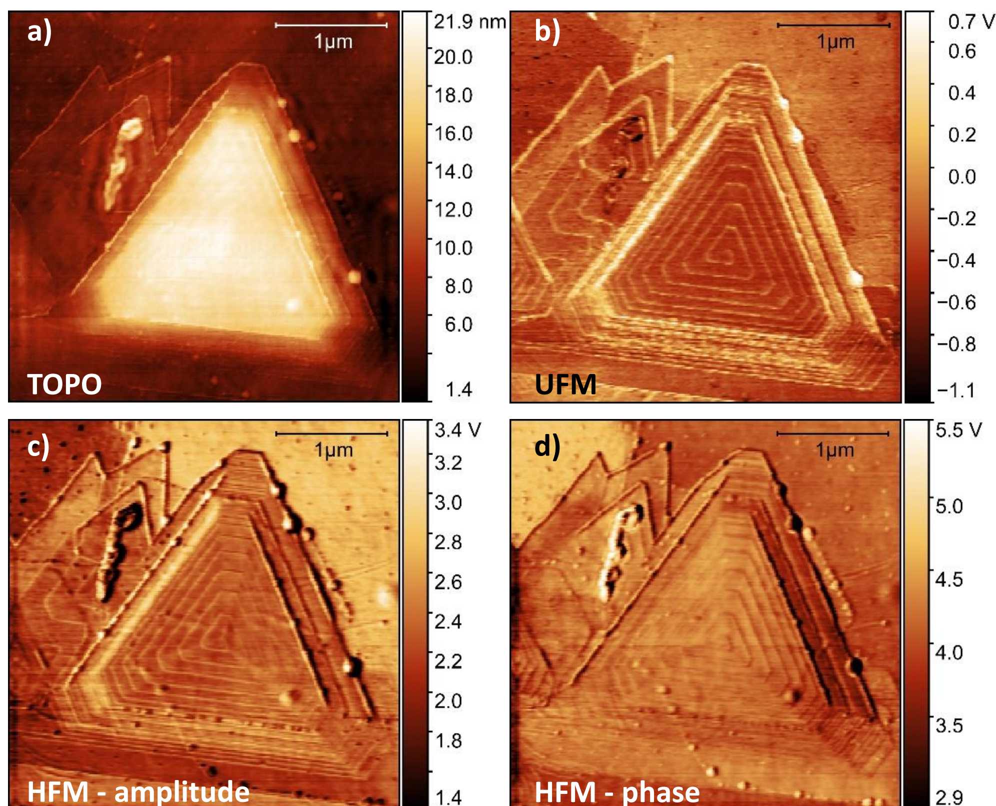

Figure 6.2 Image in a) shows the topography of a WS_2 pyramidal heterostructure over a continuous layer of the same material. Image b) shows the UFM image of the region in a) clearly displaying low stiffness (dark contrast) in the centre of the structure. Image c) and d) are the amplitude and phase of HFM images of the same region, respectively.

In order to obtain a qualitative analysis of the mechanical inhomogeneities in the sample, we performed traces in the topography and UFM images in the equivalent areas. Fig. 6.3 compares three possible different scenarios of topography vs UFM profiles. Firstly, the mechanical stiffness is dependent of the topography. It is shown that the thicker layer stacks

exhibit higher stiffness. This result is displayed in graph 1. The second observation illustrated in Fig. 6.2 was the unexpected variation of the local stiffness in the absence of any topography feature; this could be attributed to a missing interlayer within the stack. The missing plane produces negligible variation in the surface topography if it happens deep enough. However, the UFM measurements are sensitive to this singularity due to the disruption of the ultrasound propagation in a non-compact material. The third illustration, Fig. 6.3.e, was also dedicated to the case where the material stiffness changed without full topography correlation. A possible interpretation of this result is that the changes in the mechanical stiffness could be a consequence of misorientation of the crystallographic axis of the layers stacking. Twisted stacked layers should not create changes in the surface morphology, whereas they produce transversal strain due to the lattice mismatch.

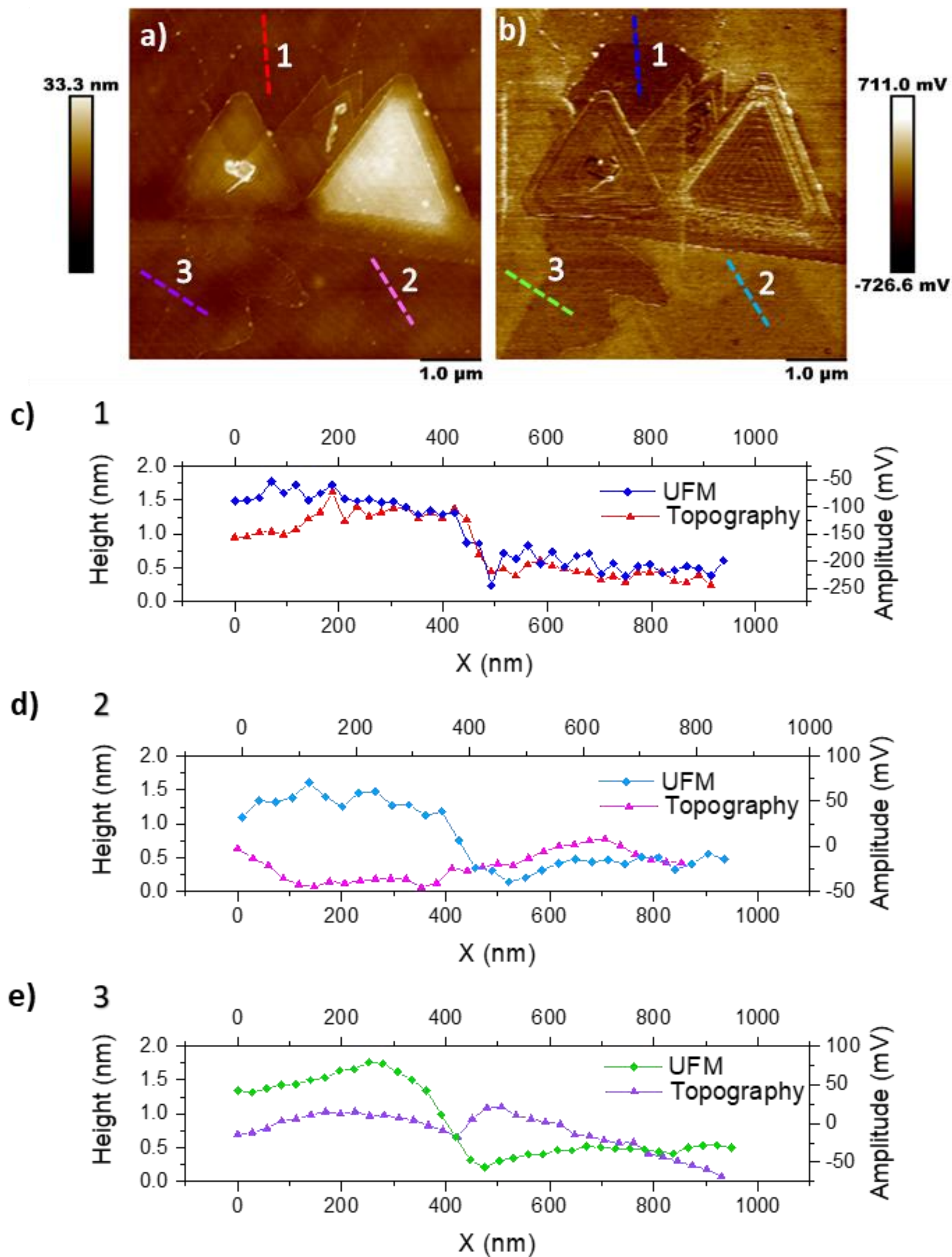

Figure 6.3 Image a) shows the topography of multiple WS_2 vertical heterostructures where the whole region of the map is fully covered by a continuous layer of the same material. Image b) shows the nanomechanical map made by UFM of the same region shown in a). In images a) and b) the dashed lines are superposed, where the profiles show in the plots c), d) and d) were extracted. Plot c) presents profile #1, where the step in the topography corresponds with the change in contrast. Plot d) shows profile #2 where UFM contrast is produced without apparent topographical feature. Plot e) displays profile #3 where mechanical change is produced with no direct topography link, presenting a possible change in the crystallographic orientation.

6.1.2. 3D nanomechanical mapping of synthetic WS_2 heterostructures

In this section, we report the first beam exit cross-sectional polishing (BEXP) of 3D van der Waals structures of 2D materials. We demonstrate that the combination of the unique BEXP tool and functional SPM analysis provides many advantages for the investigation of buried defects in TMDCs vertical heterostructures with nanoscale resolution.

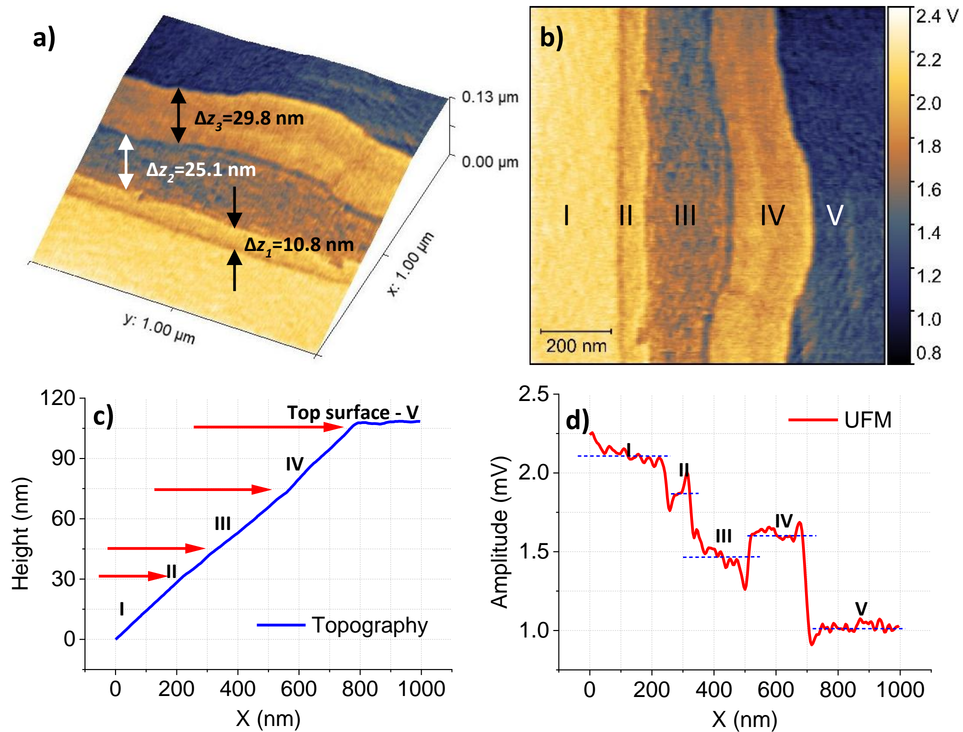

Figure 6.4 Image a) is a 3D render of the topography with superposed UFM contrast of the sectionioned WS_2 heterostructure. The thickness of the layers with different UFM contrast are also superposed on the map. Image b) shows the UFM image of the sectioned WS_2 vertical heterostructure. The image has superposed the labels, I, II, III, IV and V, which are used to identify the areas with different UFM response. Plot c) and d) present the profiles of the topography and UFM response, respectively, extracted in the same region.

In the quest for accessing sub-surface defects with SPM probes, adequate conditions have to be considered to dive into the area of interest, with an easily accessible surface being recommended. We cut the sample at a shallow angle using the BEXP method described in Chapter 4, using an in-house modified cross-section polisher (Leica EM TIC 3X, Germany), which provides optimal geometry for the SPM studies of the cross-section. To achieve a final polished angle of approximately 8° from the surface normal, the surface of each sample was mechanically lapped to ensure adequate contact with the mask. The ion-polisher cutting voltage was set to 7 kV until the cross-section was completed. The cutting voltage was then

lowered to 1 kV for 10 minutes to finely polish the section. As seen below, this method is suitable for studies of van der Waals heterostructures in UFM that, when the Si probe scan across the sectioned heterostructure is vertically ultrasonic excited, the cantilever deflection is affected by the non-linear interaction of the tip-sample, providing mapping of local mechanical moduli of the 3D structure of 2D material samples.

In Fig. 6.4.c-d, one can see the profiles of the topography and the UFM responses of a cross-sectioned WS_2 heterostructure. In the nanomechanical map (Fig. 6.4.a-b) and the corresponding extracted profile (Fig. 6.4.d), the five regions with different contrast are clearly evident. The substrate region (I) with a higher stiffness, is followed by the native SiO_2 layer (II) of approximately 10 nm thick. The next region, correspond to the first layer of WS_2 (III), which shows low contact stiffness, and a fine structure corresponding to possible inhomogeneities in the material. Finally, the topmost part of the slope (IV) corresponds to another phase of WS_2. We believe that the III-phase is less stiff as this region is more amorphous, being formed at the beginning of the growth, covering the most of the substrate surface. Then, over this semi-amorphous layer (III), the phase (IV), presents higher crystallinity, exhibiting higher stiffness. It is also worth pointing out the contrast of the top surface (V), which is significantly darker, representing substantially less stiffness. This behaviour is a predictable consequence of the strong anisotropy presented by WS_2. The elastic modulus in the c-axis is one order of magnitude smaller than in the a-axis for this material. In addition, a fine structure is also observed on the top surface as an effect of a possible minor re-deposition of material produced during the BEXP nano-sectioning process.

In order to perform more accurate and quantitative analysis of the morphology and relative stiffness of the substrate and WS_2 heterostructure, the RMS variation of the UFM signal was normalised and presented in Fig. 6.5. According to the ultrasonic response, the Si substrate was found to be the strongest, followed by the SiO_2, and then the diverse phases of WS_2. This is consistent with the ranking shown in Table 6 of the calculated local effective Young's moduli in contact with the tip by the expression

$$\frac{1}{E^*} = \frac{1 - \nu_{tip}^2}{E_{tip}} + \frac{1 - \nu_{sample}^2}{E_{sample}}, \qquad (79)$$

where E_{tip}=169 GPa and ν_{tip}=0.17 are respectively the Young's Modulus and Poisson Ratio of Si used in the calculations. The values of Young's Moduli of the sample materials, E_{sample}, were obtained from the moduli values found in the literature for each material [25, 125, 126] and the

corresponding corrections considering the angle of the slope, extracted from the topography profiles.

Table 6 Values of the angle formed between the sectioned area and the top surface, Young's Modulus with the angle correction and effective Young's Modulus of Si, SiO_2 and WS_2 in phases I, II and III.

	Angle (°)	E_{sample} (GPa)	E* (GPa)
Si	8.06	186.55	192.10
SiO_2	7.05	157.83	162.52
WS_2 - phase (III)	7.13	91.06	94.08
WS_2 - phase (IV)	8.63	97.86	101.10
WS_2 - phase (V)	0	58.00	59.92

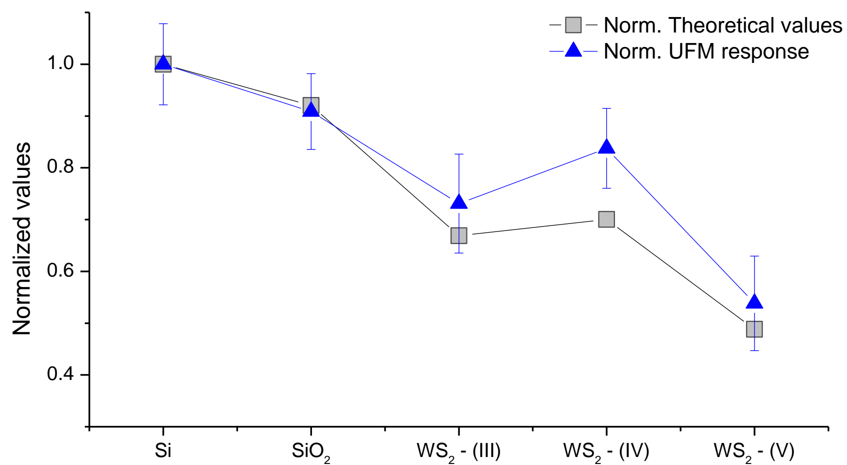

Figure 6.5 Plot of the normalised values of Young's Modulus to the Si for the UFM response and the theoretical values inferred from the material Young's Modulus and experimental conditions.

6.1.3. 3D dielectric mapping of vertical WS_2 heterostructures

In an attempt to understand the nature of the difference between layers of 2DM's we studied the electrical properties of the sectioned structures using the method sensitive to the dielectric properties, namely, dielectric electrostatic force microscopy (D-EFM) [101]. We used the experimental setup described in Chapter 4, which allowed us to simultaneously record the topography, as well as the amplitude and phase of the D-EFM response. The obtained experimental results are displayed in Fig. 6.6.a-c. The topography shows the intact morphology of the TMDCs heterostructure of a low angle triangular pyramid and the clear BEXP section. The topography of the sectioned part does not show morphological features as can be observed in the profile displayed in the plot in Fig. 6.6.d. Conversely, the dielectric maps present an abrupt change, corresponding with the boundary between the substrate and the WS_2 heterostructure. Both amplitude and phase signals were sensitive to the dielectric change. In the profiles extracted from the maps and plotted in Fig. 6.6.d, one can observe a rapid change in dielectric properties in the absence of any particular morphological feature of the sectioned area. It is worth noting that, conversely to the UFM maps, there is no contrast change in the sectioned region of the pyramid, which could indicate the presence of another material in the heterostructure. Therefore, the D-EFM results support the explanation presented in the analysis of the UFM maps, where we have hypothesized that the UFM contrast may be attributed to a change in the crystallinity of the WS_2 layers.

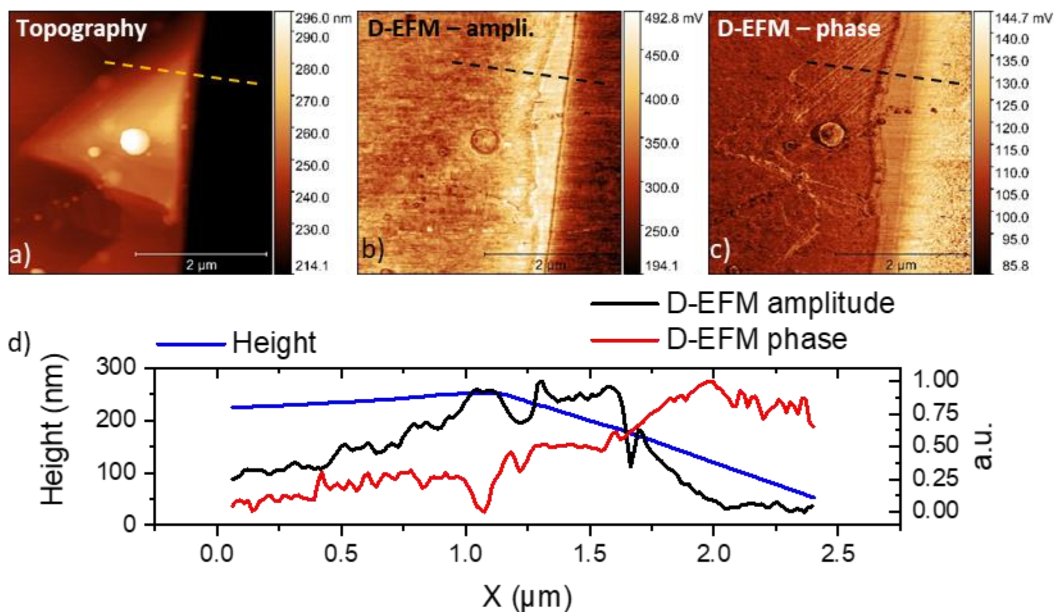

Figure 6.6 Images a), b) and c) show the topography, D-EFM amplitude and phase maps, respectively. Plot d) shows the profiles extracted from the images a), b) and c).

6.2. Synthetic lateral heterostructures of MoS_2 and WS_2

Van der Waals vertical heterostructures have demonstrated the possibility of tailoring their physical properties by interlaying the 2D materials. However, it is essential to consider the anisotropy in their physical properties. For the out-of-plane direction, in the direction of the stacking by the weak van der Waals forces, the materials present very different properties when compared with the in-plane properties. The anisotropy does not need to be a disadvantage, because, for certain applications different properties are required, for example electric and thermal transport, in selected directions. Similarly, the lateral structures of 2D materials are of interest due to the linear interfaces between dissimilar 2D materials. Here, we present an example of a lateral heterostructure between MoS_2 and WS_2 (see Fig. 6.7), where the interface junction is formed by covalent bonds between the atoms of the two different species. The structure was CVD grown, firstly the WS_2, followed the MoS_2.

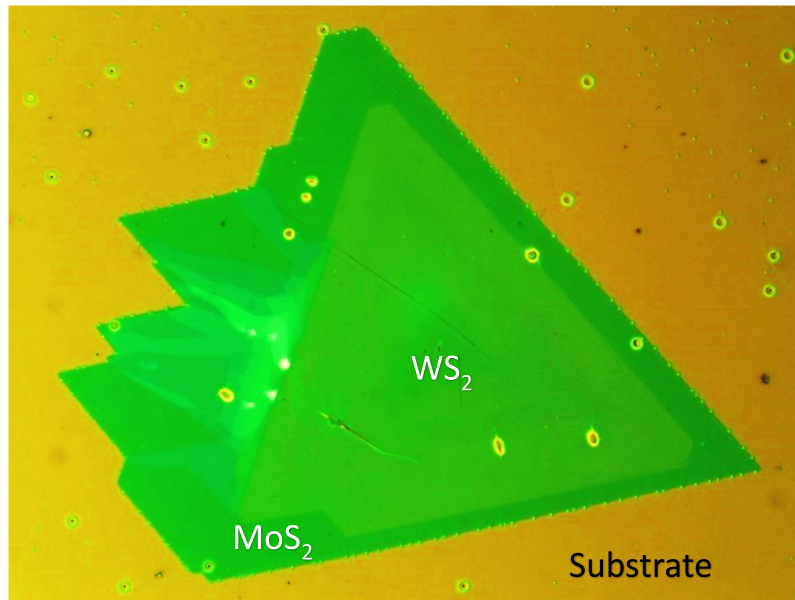

Figure 6.7 Optical microscope image of the WS_2-MoS_2 lateral heterostructure. Magnification x40.

This section focuses on the nanomechanics as well as the thermal transport of these WS_2-MoS_2 lateral heterostructures. Using our UFM, HFM setups, we could map the contact stiffness of these structures supported on a Si with native oxide substrate. With SThM, we could also measure the changes in the thermal conductivity of MoS_2 for various interfacial scenarios.

Morphology and nanomechanics of the lateral heterostructures

The investigation of the morphology and nanomechanics of such WS_2-MoS_2 lateral heterostructures is essential for understanding the interfacial interaction between the layered materials and the substrate, as well as the strain produced at the epitaxial interface between the TMDCs materials. These WS_2-MoS_2 heterostructures can be considered as atomical superlattices, in which metal dichalcogenides monolayers are laterally integrated with less likely defects in the plane despite the lattice mismatch [127]. It has been reported in the literature that the physical properties of similar heterostructures by the control of the interfacial strain were produced as a consequence of the difference between the lattice parameter of the structure materials.

During the nanomechanical mapping of these structures, some rippled regions were found. The undulated areas extend for a few microns from the possible interface between the WS_2 and MoS_2 following the growth direction. We observed that the topography images show reasonable periodicity in the ripples, suggesting more detailed analysis for understanding the wrinkling phenomena. We extracted a profile across the ripples (Fig. 6.8.a-b) and then performed a fast Fourier transform (FFT) of the obtained profile (Fig. 6.8.e), using the predefined function in Origin^{TM}. From the FFT, we selected the four most intense peaks at n_1= 8.07x10^{-6} m^{-1}, n_2= 8.85x10^{-6} m^{-1}, n_3= 9.83x10^{-6} m^{-1} and n_4= 1.10x10^{-7} m^{-1}. These peaks correspond to the wavelength values of λ_1=124 nm, λ_2=113 nm, λ_3=102 nm and λ_4=91 nm. Using these values, we tried to schematically present the undulated surface as the sum of four Fourier Transform components. The result is plotted in Fig. 6.8.b and shows reasonable correlation with the experimental profile. It is important to notice the uniform periodicity in the ripples, making it complicated to produce an accurate simulation using only four peaks of the FFT analysis.

The nanomechanics of the same region was simultaneously mapped using the heterodyne force microscopy (HFM) technique, where the amplitude and phase images show the information related to the viscoelastic properties and the dynamic relaxation processes, respectively. In the HFM images presented in Fig. 6.8, one can see that the mechanical response in the region on the left (A), in both amplitude and phase HFM images, presents a stronger contrast than on the right side (B). Unexpectedly, this intense change in the mechanical response is not significantly evidenced in the topography image as a morphology change, whereas the boundary between areas A and B is well defined in the topography. The change in the mechanical stiffness arises from the frontier between the WS_2 and MoS_2. In this case, the area corresponding with the WS_2 would be displayed brighter than the MoS_2 region,

due to WS_2 having higher elastic modulus than MoS_2. In addition, the difference in the lattice parameter between both materials would create a compressive strain released by the rippling of the MoS_2 layer. Assuming that this experimental case is analogous to the example presented in the literature by Xie et al. [127], only the material, which presents lower stiffness and a larger lattice parameter, should present the undulated morphology. It is also worth noting that, because the WS_2 and MoS_2 lattice parameters are closer than the WS_2 and WSe_2 of the experiment of Xie, one could think that, in our case, both materials could present the undulated pattern. In order to thoroughly confirm this hypothesis, the area should be mapped with a chemically sensitive technique to identify the species, like KPFM.

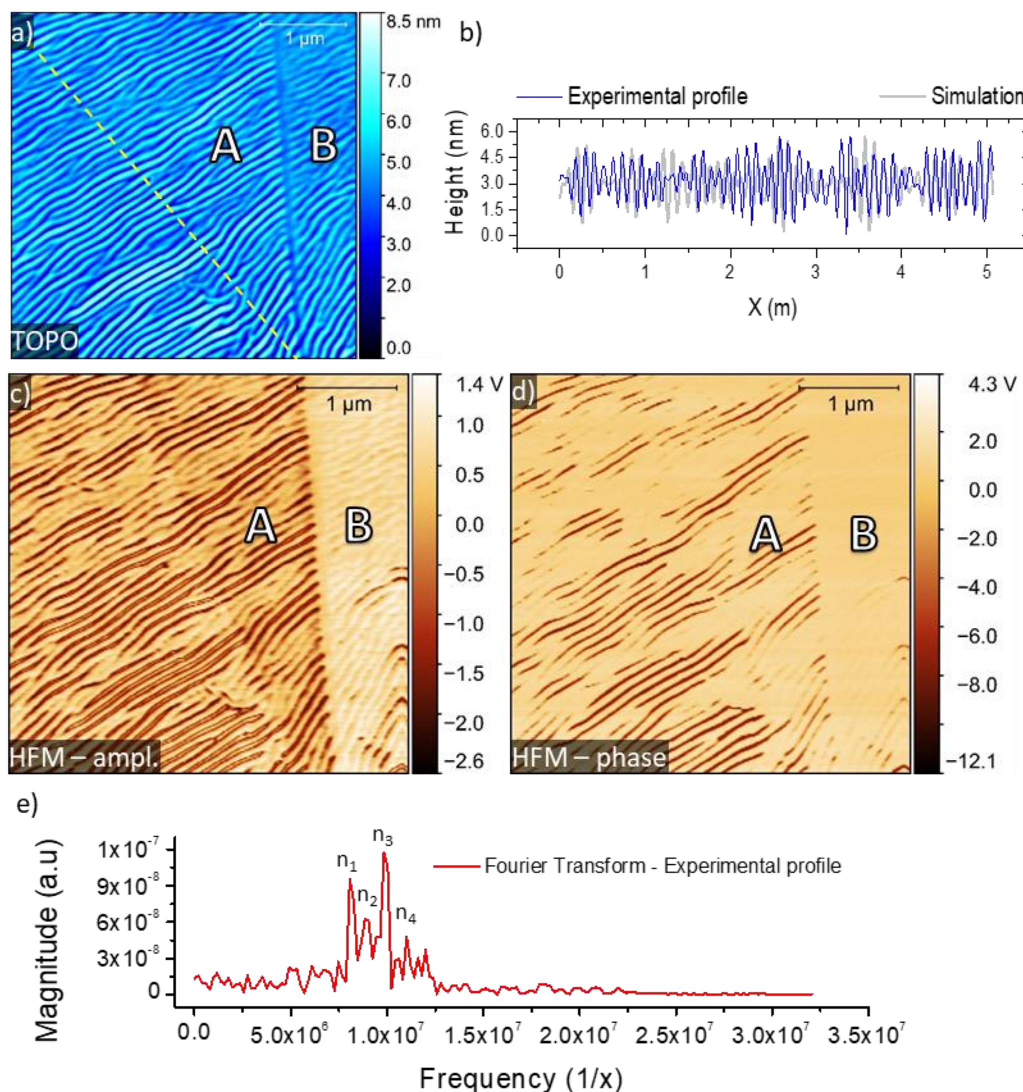

Figure 6.8 Image a) topography of the rippled area. Image b) shows the of the profile extracted from a) in the area highlighted with the yellow dashed line. In the same plot the simulation of the surface undulation is also superposed. Images c) and d) show the HFM amplitude and phase, respectively. e) shows the plot of the FFT of the profile extracted from a) in the area highlighted with the yellow dashed line.

In addition to the HFM, we also performed nanomechanical maps via UFM, which are displayed in Fig.6.9, in another region of the heterostructure, close to the edge with the substrate. In the topography, the silicon region (#1) presents some contamination in the surface, which meant it was not straightforward to establish the substrate as the completely zero value in the extracted profiles and to refer the thicknesses of the layers to that level. The height of the substrate is very similar to area #4. Therefore, we had assumed that region #4 corresponded with a monolayer of MoS_2. Interestingly, it was found that region #3, corresponding with a bilayer of MoS_2, presents higher contact stiffness than the monolayer, represented with brighter UFM contrast. We have to keep in mind that the increase in stiffness is not linearly dependent on the thickness, as is shown in the plot in Fig. 6.9.d. The thickest region shows the least stiffness in the map and this can be attributed to the fact that the thickest region appears to be overgrown from the edge of the bilayer, being weakly interacting with the underneath material for both substrate and MoS_2 bilayer, resulting in a sponge-like behaviour.

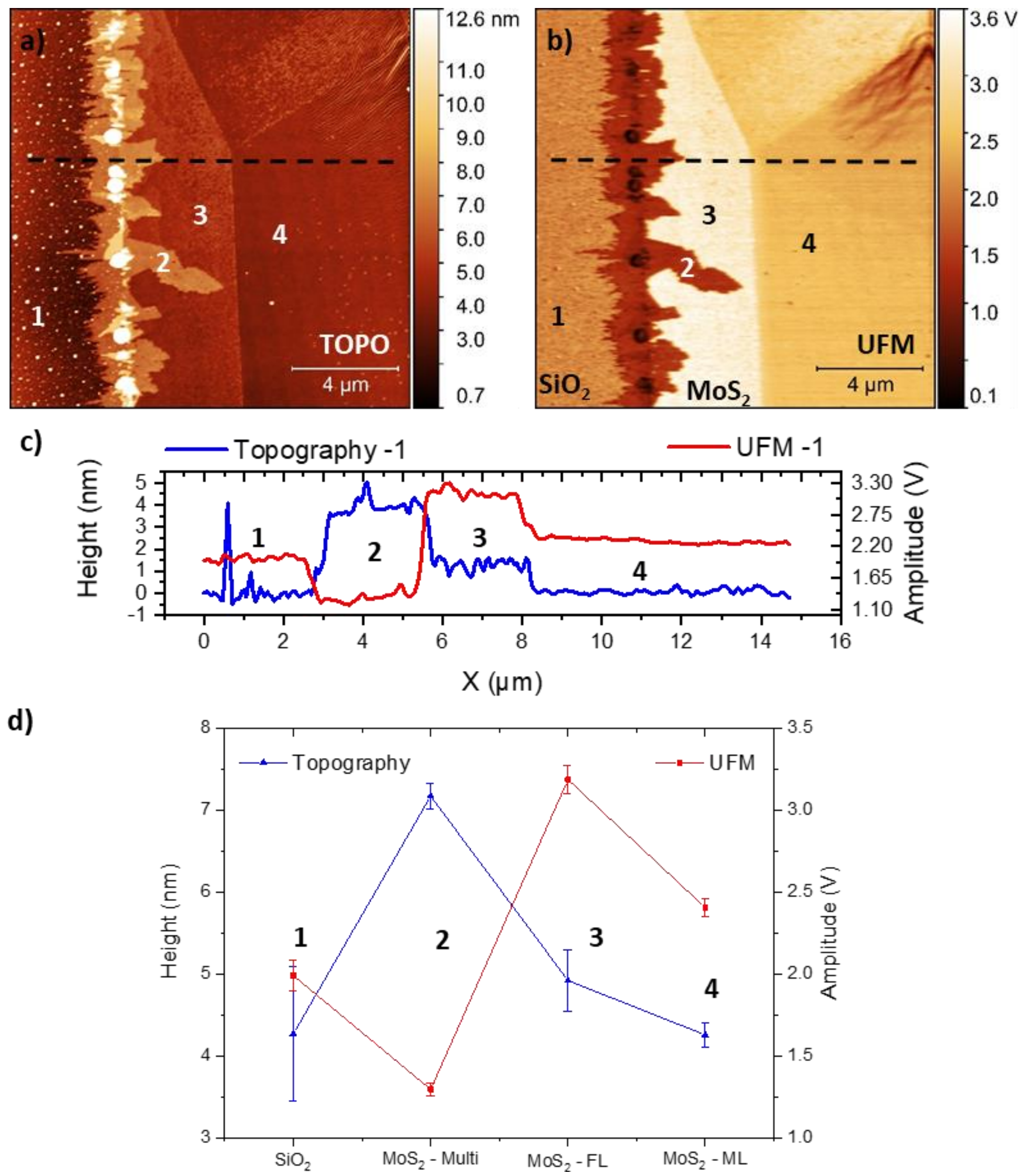

Figure 6.9 a) and b) are the topography and UFM maps of the MoS_2 region of the lateral heterostructure. Plot c) shows the profiles extracted from topography and UFM response in the region displayed with the dashed black lines in images a) and b). Plot d) shows the correlation between the thickness of the layers and the UFM nanomechanical response.

Heat transport in lateral heterostructures of two-dimensional materials

In the previous section, we reported the nanomechanical study of a WS_2-MoS_2 lateral heterostructure and, although the study of the thermal properties are not a main matter of this thesis, we have investigated the heat transport in such nanostructure, providing additional information.

The experimental values of the thermal conductivity of monolayers of MoS_2 and WS_2 have been reported as 34.5 W m^{-1} K^{-1} and 32 W m^{-1} K^{-1}, respectively, far from the graphene value ~50005 W m^{-1} K^{-1}. [128, 129] Therefore, these low values make MoS_2 and WS_2 interesting materials for the fabrication of devices that require poor heat dissipation. Due to the length scale of the TMDCs studied in this section, standard measurement techniques cannot be easily applied to measure nanoscale thermal properties of WS_2-MoS_2 heterostructures. Here, we use state of the art SThM, for qualitative identification of the different materials as well as changes in the thermal transport due to the underlying layers.

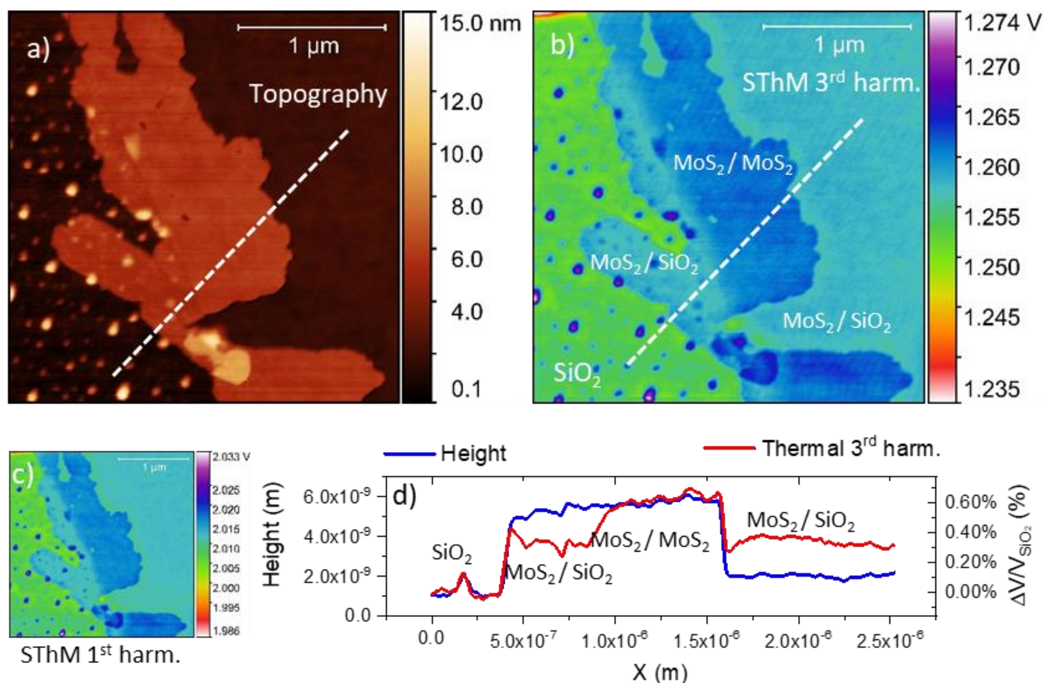

Figure 6.10 a) Topography and b) SThM response in the 3rd harmonic maps of the boundary of the structure. c) SThM image in the 1st harmonic response. d) plots of the topography and SThM profiles extracted from the images a) and b) in the area presented with the white dashed line.

SThM measurement can be operated using DC and AC modes. AC mode is generally more sensitive, with lower drift and less noise [130, 131]. In addition, AC measurements allow one to use the *3ω* method, tracking the third harmonic of the Wheatstone bridge output, which shows the direct relation of the probe self-heating and therefore the heat losses [12]. Here, we

report the first simultaneous recording of the first and third harmonics of the signal for a comparative study.

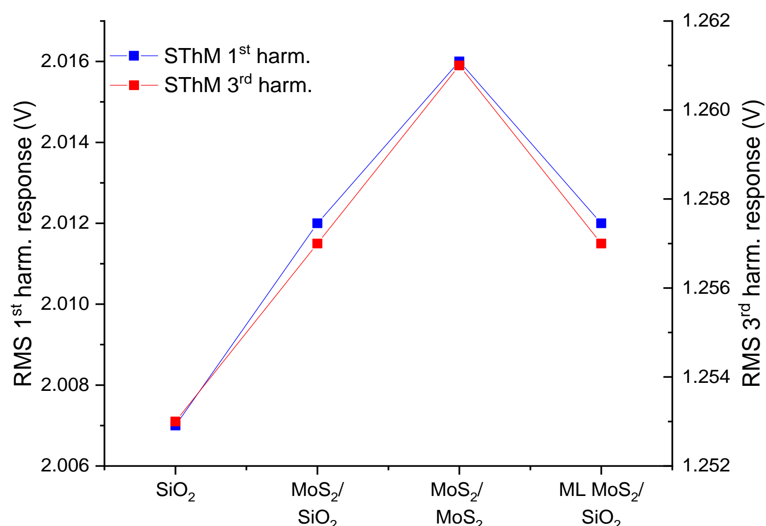

Figure 6.11 Plot of the RMS response of the SThM measurements in the 1st and 3rd harmonic for the different materials and interfaces.

An example of topography and SThM image is shown in Fig. 6.10. The image shows areas of SiO_2, MoS_2 on SiO_2 and MoS_2 on MoS_2. The SThM image (Fig. 6.10.b) shows the thermal conductivity response of each area. As expected, SiO_2 shows the lowest thermal conductivity in the SThM map, followed by the MoS_2 monolayer directly supported on the SiO_2. The contrast displayed in the overgrown layer is very interesting, showing the same response in the area directly supported in the SiO_2, whereas the region covering the homogeneous MoS_2 monolayer presents higher thermal conductivity. This effect can be explained as the overgrown MoS_2 layer is less affected by the poor thermal conductivity of the SiO_2 substrate due to the intermediate MoS_2 monolayer. These results are also shown in the plot in Fig. 6.10.d, which are the extracted profiles of the topography and SThM response images in the regions indicated with the dashed white lines. The profiles have been extracted from the measurements in the third harmonic because the amplitude of the voltage measured in the third harmonic $V_{3\omega}$ is directly proportional to the increase of temperature due to Joule heating. [131] However, the response in the first harmonic includes the sum of the thermal and electric contributions [132]. Consistent results were equally obtained in the SThM map, tracking the first harmonic in the response. In order to show that both methods present the same qualitative response, the RMS values of the SThM response in the analogous areas for both of the harmonics have been plotted in Fig. 6.11, where one can see the coherence in both measurements.

6.3. Natural occurring heterostructures

After the outstanding success of graphene, many studies have targeted the expansion of the family of 2D materials, investigating other layered materials in the search for interesting novel properties. During this, naturally occurring heterostructures have been found to be very fascinating, as they are layered materials whose atomic structure changes at each layer up to form a unit cell of several layers. These heterostructures could potentially solve the long and costly fabrication process of synthetic heterostructures and significantly decrease the problems of the randomness and cleanness produced in the fabrication of artificial heterostructures.

6.3.1. Franckeite

In this section, we report the first UFM measurements of the naturally occurring and air-stable heterostructure franckeite, which is a layered mineral with a structure composed of alternating stacks of SnS_2-like and PbS-like layers. Franckeite has a narrow bandgap and p-type conductivity, which makes it an excellent candidate for the fabrication of optoelectronic devices. It has already demonstrated its potential technological application as a photodetector [133, 134].

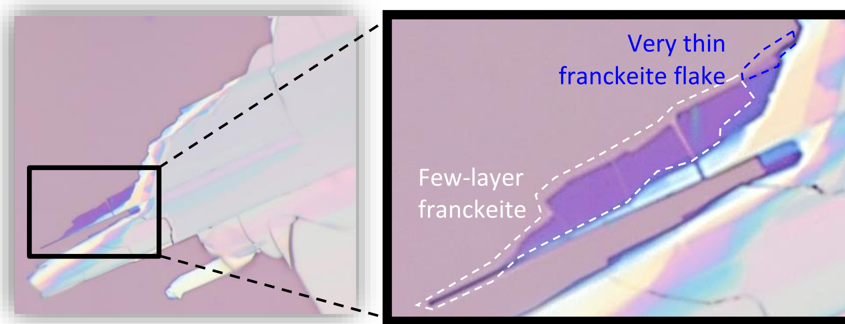

Figure 6.12 Optical image of the franckeite flake and a zoomed-in section of the area with the thinnest region.

Whilst electrical, optical and thermal properties of franckeite have been reported, no records of the nanomechanical properties have been found in the literature. Therefore, using UFM, we first mapped the franckeite's mechanical response. Fig. 6.12 shows the optical image of the area identified with the presence of various and selected thicknesses for the UFM measurements. In Fig. 6.13, one can see the topography and the UFM response of the franckeite flake in a bulk-like region and a very thin film. As the UFM amplitude decreases with the contact stiffness, comparing the profiles extracted from the topography and UFM maps

displayed in Fig. 6.13.c-d, one can observe that the contact stiffness decreases with the franckeite thickness. Such behaviour has also been reported in the literature of other 2D materials [135]. As UFM has demonstrated to be sensitive to the features beneath 2D materials [136], this phenomena can be attributed to the probing of non-uniform adhesion between the franckeite film and the substrate as a consequence of the corrugations present on the susbtrate surface, which might make the uniformly adhesion of the flake difficult. The thick part of the franckeite presents a stiffness comparable with the substrate value. In this case, the flake is excessively thick for the UFM sensing to the features of the substrate-flake interface. Therefore, the contact stiffness is determined by the bulk stiffness of franckeite.

We hope that these first nanomechanical measurements of a franckeite bulk and thin layers will provide insights for the future development of franckeite devices.

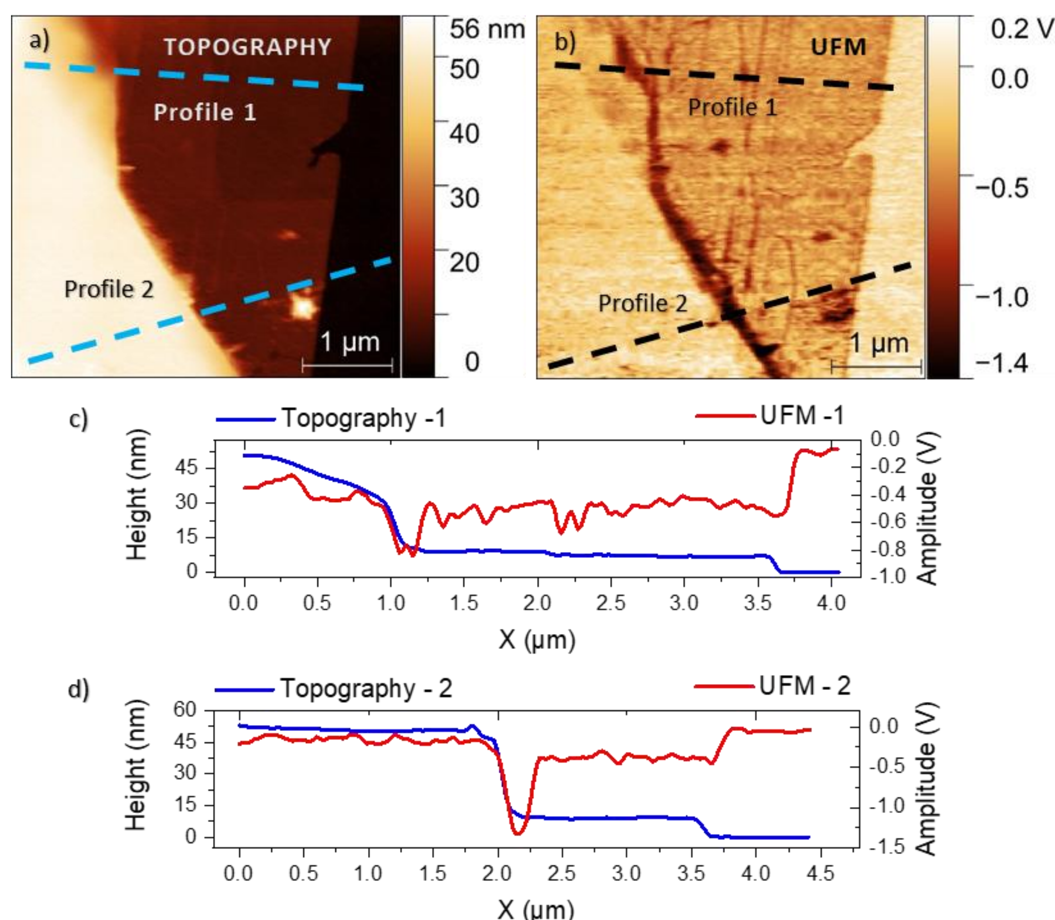

Figure 6.13 Images a) topography and b) UFM maps of an exfoliated franckeite flake. Several thicknesses can be observed with different mechanical responses. As the franckeite thickness increases, its stiffness increases as well. Images c) and d) show the plots of profiles 1 and 2 respectively, where topography vs UFM response are compared.

6.4. Summary

2D material and their heterostructures show exotic behaviour and physical properties compared to their bulk counterparts, making them very attractive for the development of new devices for novel applications. For a full understanding of these new physical phenomena and optimal investigation of materials and structures defects, adequate characterization techniques with nanoscale resolution and material properties sensitive are required.

In this chapter, we have demonstrated the outstanding capabilities of non-destructive ultrasonic AFM methods, such as UFM and HFM, for the mapping of buried defects in vertical van der Waal heterostructures of WS_2. Then, based on the evidence of the presence of sub-surface defects in such structures, we nano-sectioned the 3D pyramidal stacks of this TMDC using the BEXP method, allowing for direct access to the internal 3D properties of the nanostructure. Combining this with functional SPM techniques, UFM and D-EFM, we were able to identify two phases of $WS_{2,}$ suggesting a difference in the material crystallinity inside individual structures. Furthermore, we resolve the substrate-heterostructure interface, not observable in topographical images, and confirmed that two layers of TMDC have similar material composition, using local probing of the dielectric properties in D-EFM mode.

The lateral heterostructures of MoS_2 and WS_2 investigated via UFM, HFM and SThM provided information of the morphology, local stress and contact stiffness, as well as heat transport of these structures by using the substrate as a reference. These measurements have confirmed the superior sensitivity of these functional SPM methods to the thickness of the layers and the interface between the layers, as well as with the substrate.

Finally, using UFM, we reported the nanomechanics of the naturally occurring heterostructure franckeite, observing remarkable softness of this material for very thin layers compared to the significant stiffness of the franckeite bulk.

7. 3D structures of Compound Semiconductors

In this chapter, we demonstrate that the combination of the BEXP and materials-sensitive SPM analysis is a very powerful tool for the 3D exploration of subsurface defects in compound semiconductor (CS) quantum nanostructures, namely quantum dots, multilayer structures and nanowires. We use nanomechanical properties, electrical potential distribution and piezoelectric response mapping to analyse the 3D structures of these complex materials. These structures were produced by the Compound Semiconductor Manufacturing Hub UK (CSHub) in collaboration with University College London, and Cardiff and Sheffield Universities.

7.1. Introduction

Nowadays, silicon (Si) dominates the market of semiconductor devices with manufacturing pathways well established. At the same time, 3D nanostructures made of other semiconductors and their compounds can offer better physical properties than Si, improving the performance of electronic devices for multiple applications. However, the manufacturing of high-quality CS nanostructures presents a big challenge for the engineering and manufacturing of materials. Growing CS on silicon wafers seems to combine the established manufacturing processes and the performance of CS devices. Nevertheless, the lattice mismatch between CS and Si, and dissimilar growth conditions, create multiple defects at the interface, which propagate throughout the structures, affecting the quality of the structure and the performance of the final device.

In order to develop successful CS – Si devices, suitable characterisation methods are required. Standard methods of materials property characterisation are limited to either surface or bulk probing and are not able to be evaluated, *e.g.* the electrical transport or charges distribution in the inner regions of the structures. Furthermore, the conventional methods for the study of the morphology or the composition of these nanostructures, including their internal structure, such as transmission electron microscopy (TEM), are not sensitive to their local physical properties that are key to device performance.

Various SPM techniques, such as Kelvin probe force microscopy (KPFM), scanning spreading resistant microscopy (SSRM) and piezoelectric force microscopy (PFM) allow the studies of local charges distribution, electrical transport and piezoelectric response with nanoscale resolution, but, unfortunately, they cannot assess subsurface properties. Mechanical cleaving of the samples is a possible solution to access their inner structures. However, it is only suitable for limited applications because it is affected by the local stresses.

It also produces a very sharp edge which hinders access with the SPM probes. Traditionally, focused ion beam (FIB) methods allow for sample sectioning; nonetheless, the nature of the ions implemented in the process, generally gallium ions (Ga^+), are not best suited for exploring material properties. The high reactivity of the ions alters the sample physical properties and allows the ion implantation into the material. In addition, the big size of the Ga^+ produces surface damage [137]. Also, FIB produces cuts only a few µm wide, which is generally insufficient for using AFM probes.

To tackle the problem, we employed Ar-ion beam exit cross-sectional polishing (BEXP), described in Chapter 4, to produce high-quality sections of the samples. By measuring via Kelvin force probe microscopy (KPFM) the wedge-shaped section of multiple-quantum well (MQW) structured samples, both with and without anti-phase domains (APD), we were able to map the surface contact potential difference (CPD) linked to the local work function (electron affinity) of the material. These allowed us to highlight the presence of APD-linked material defects that affect the potential distribution. Furthermore, we investigated the doping concentration in VCSEL structures, mapping the surface potential of the sectioned structures via KPFM. In the application of III-nitride nanowires onto the silicon substrates that we were able to cross-section using embedding of the nanowires with spin-on-glass (SOG), piezoelectric force microscopy (PFM) allowed us to identify the polarity reversal in individual nanowires. Overall, we corroborated the feasibility of the BEXP+SPM methodology to explore buried defects and piezoelectric phenomena in complex CS nanostructures. The simplicity of this methodology and the excellent results settle our approach as a fundamental one in the applied material research and with enormous potential for future investigations.

The nanomechanical analysis of the samples was performed via ultrasonic force microscopy (UFM), which offers very accurate qualitative measurements in the changes in elastic moduli for stiff samples, such as the III-V semiconductors. KPFM was then used for electrical characterisation. Finally, for the investigation of electromechanical coupling in the response of piezoelectric samples, we used PFM, in vertical and lateral modes.

7.2.III-V multiple quantum wells nanostructures on Si

Complex multiple quantum well (MQW) structures grown on silicon substrates were studied to investigate their physical properties, in particular the material defect called anti-phase domains (APD). APD and anti-phase boundaries (APB) are arguably the most critical and detrimental defects in the growth of III-V on Si. These defects are produced due to the monoatomic steps created in the diamond lattice of silicon (one-atomic basis) and the two-atomic basis of the zinc-blende structure of the III-V compound, creating APD at each terrace edge of the mono-atomic steps of the Si surface (see Fig.7.1). To get APD-free layers is needed to precisely double the Si surface steps density and/ or ensure the self-annihilation of all APD. [138, 139]

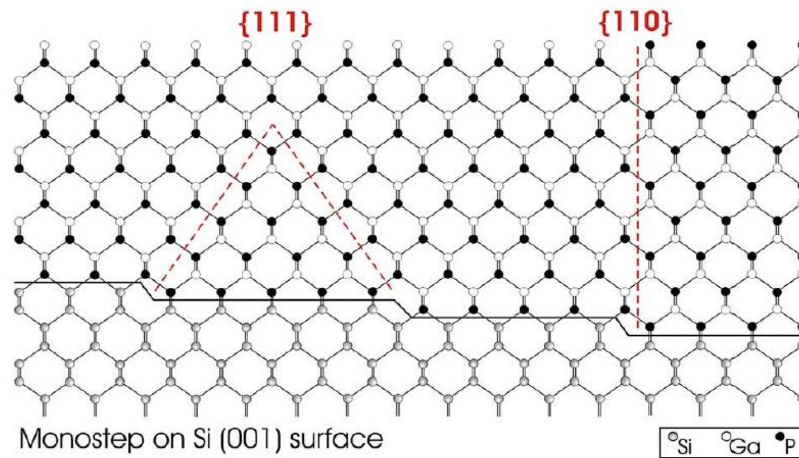

Figure 7.1 Sketch of the APB formation in the [111] and [110] lattice planes of the GaP zinc-blende structure due to the presence of mono-layer steps on the Si surface. [139]

Among the diversity of the samples studied, here we report the most representative two samples, which were grown by molecular beam epitaxy (MBE) in University College London (UCL) by our collaborators Dr Mingchu Tang and Dr Pamela Jurczak from Prof Huiyun Liu's group. Both samples have the same structure and composition, but one of them had developed APD during the growth process. The typical sample structure is shown in Fig. 3.6 in section 3.2.2 of this thesis. The results presented below correspond with the two sets of dislocation filtering layers (DFL) made of 5 periods of 10nm of InAlAs and 12nm of AlAs, spaced by a layer of 300nm of GaAs and sandwiched between GaAs layers.

7.2.1. Study of the 3D morphology and nanomechanical properties of DFL with and without the presence of APD

The quality of the material interfaces is always a challenge for material engineering, especially in the case of manufacturing complex nanostructures, where there could be more than 25 different interfaces. Defect-free morphology at each interface is crucial to guarantee the sample quality. Therefore, a suitable methodology to assess their inner structures will facilitate the progress by early defects detection guiding the process improvement.

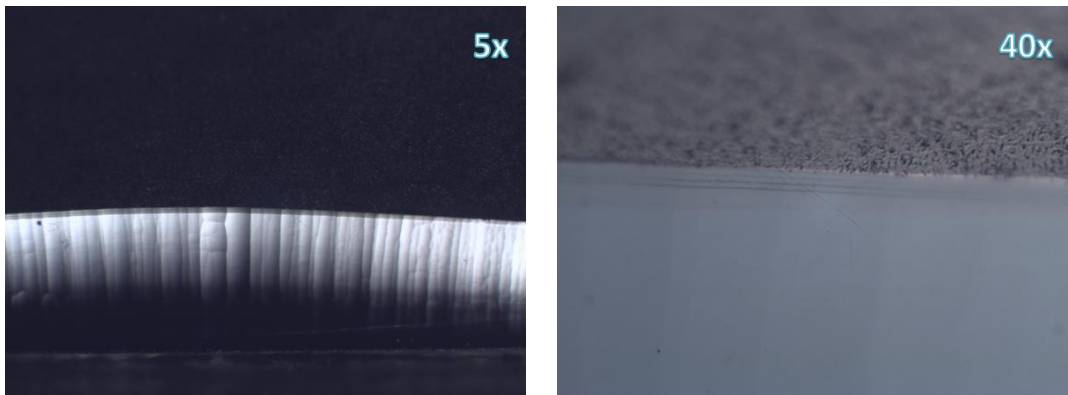

Figure 7.2 Optical images of the BEXP section of the MQW structure sample.

To approach the subsurface interfaces, we nano-sectioned the samples using the BEXP method described in Chapter 4, implementing a sample-stage with a shallow angle of 3°. The process was carried out in two steps: the first one involved removing the main part of the material by high energy beams (7kV) over 7 hours; the second polishing step was made at 1 kV for 10 minutes, to smooth the surface. The sample was then cleaned with acetone and IPA, both for 10 minutes in the ultrasonic bath. The optical images displayed of the sectioned area in Fig.7.2 shows the successful polishing result. The same fact was also confirmed by the AFM images and the corresponding profile (see Fig. 7.3.a), presenting almost negligible roughness in the section of the homogeneous material and a sharp end in the sample top surface. In Fig. 7.3.b, one can see the 3D render of an example of the sample morphology with the presence of APD. In this figure, one can also see the propagation in the z-direction, from the bottom to the top surface of the APDs generated at the interface with the substrate. Fig. 7.3.c-d shows AFM images, comparing the morphology of the MQW area of the sample and presenting evidence of APD in Fig. 7.3c. Conversely, Fig.7.3.d shows largely parallel layers, without the rippled regions.

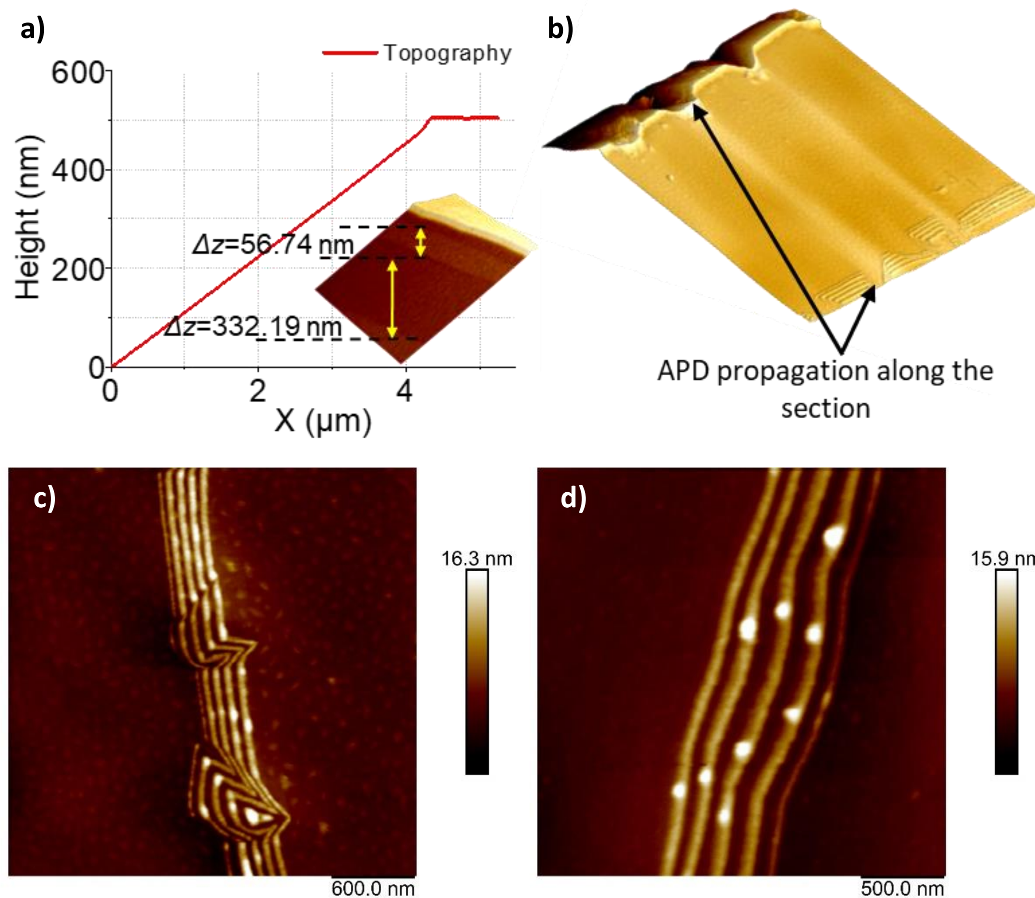

Figure 7.3 a) Profile of the topography of the 3D section. Inset: 3D render of the topography overlaid with KPFM response. b) 3D rendering of the topography, displaying the presence and propagation of APD. c) and d) Topography images of the area of the DFL structure, c) in the presence of APD; d) Sample free of APD.

In Fig. 7.4, simultaneously recorded topography and nanomechanical maps – UFM image – of the InAlAs/AlAs DFL in the BEXP sectioned sample are shown. These DFL stacks of InAlAs/AlAs are also sandwiched between GaAs layers (300nm thick). The topography image shows some topography protrusions in the InAlAs areas of the DFL; these features can be explained as the material releasing the strain in the out-of-plane direction of the section, whereas the local oxidation cannot be completely ruled out. Analogous to the case of MQW of InGaAs/GaAs detailed in literature by Peter S.Z. et al. [140], when a layer of InGaAs is pseudomorphically grown on GaAs, the InGaAs layer will be biaxially strained because the lattice constant of unstrained InGaAs is larger than that of GaAs. Equally, in the present case, the biaxially strained layer of InAlAs by the AlAs could relax in the out-of-plane direction after the BEXP nanosectioning, creating the topography features shown in the AFM images. Conversely, the lattice constant of AlAs and GaAs are comparable; therefore, the strain induced by the GaAs to the AlAs layers is negligible compared with the strain created in the

InAlAs. Complementary, the UFM image shows the sample stiffness. As one can expect, a material with lower elastic moduli presents lower stiffness in the UFM images – represented as a darker contrast. These results agree with the values found in the literature for GaAs, AlAs and InAs, summarised in Table 7. The InAlAs elastic modulus is determined by the concentration of Al. Therefore, this value is found between the moduli values of AlAs and InAs [141]. The profiles of topography and UFM maps, shown in Fig.7.4.c, were taken along the direction of the overlaid dashed line on the images. The profiles were performed strategically across the structure to show a variety of nanomechanical features. One can observe that, generally, the crests in the topography profile (red line) correspond with the valleys in the UFM-line. Moreover, the presence of protuberant regions in the topography is remarkable, displaying very dark contrast in the UFM and denoting extremely little stiffness. We found that these features probably correspond with an initial oxidation stage of the InAlAs layers. One could think that the lesser stiffness denoted in the UFM map could disagree with the fact that the indium or aluminium oxides are very stiff materials, with Young's Modulus equal to 150 and 260 GPa [142, 143], respectively. Nevertheless, it is noticeable that the oxides formed in this case are amorphous phases, presenting a much lesser stiffness than the crystalline values obtained from the literature.

Table 7 Elastic moduli and Young's Modulus of GaAs, AlAs and InAs.

Parameter	GaAs	AlAs	InAs
C_{11} ($\times 10^{10}$ Pa)	11.9	12.0	8.3
C_{12} ($\times 10^{10}$ Pa)	5.4	5.7	4.5
C_{44} ($\times 10^{10}$ Pa)	5.9	5.9	4.0
E ($\times 10^{10}$ Pa)	8.5	5.4	5.1

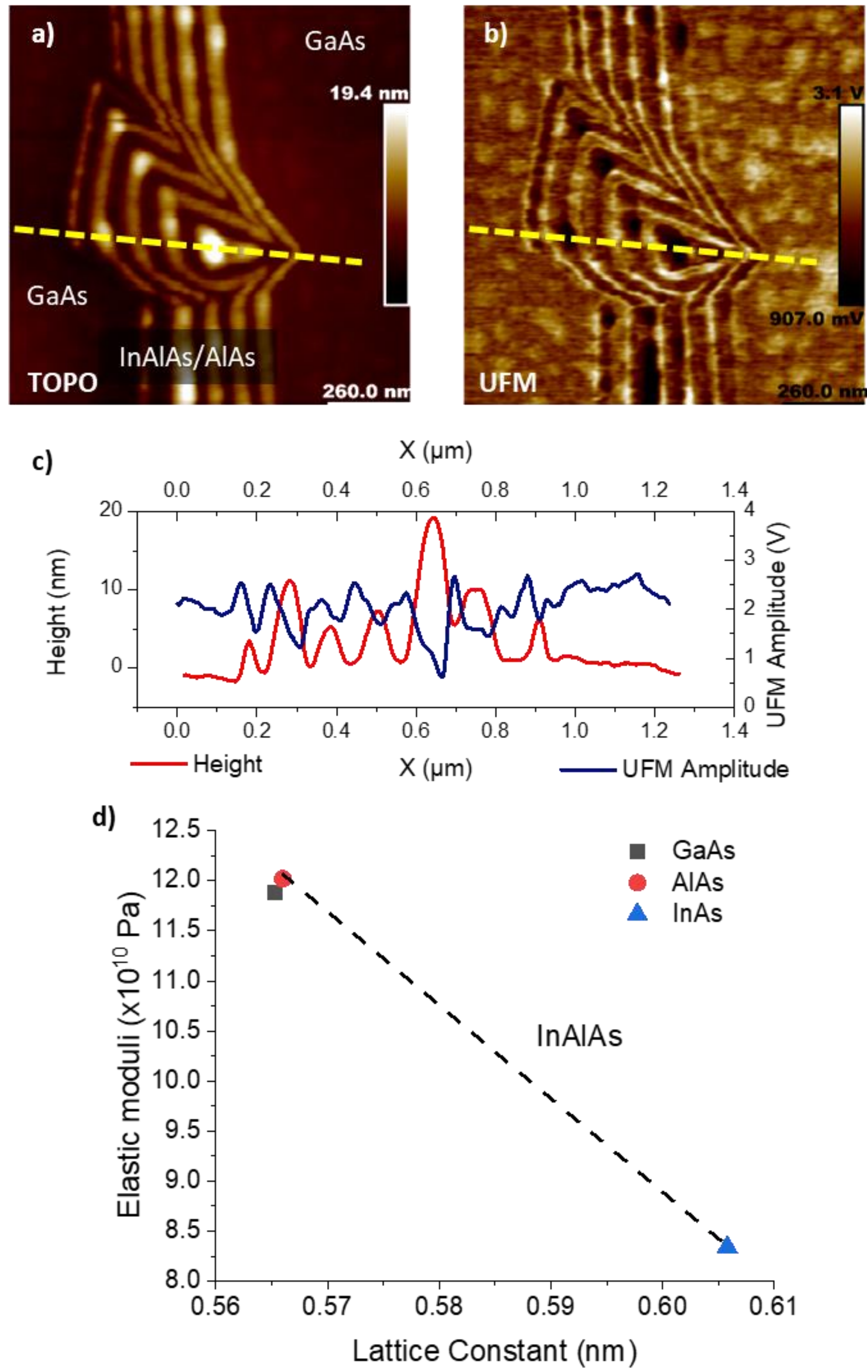

Figure 7.4 a) image of the topography of the rippled InAlAs/AlAs superlattice due to the APD. b) UFM image simultaneously recorded with image a). c) shows the profiles extracted from the images a) and b), the crests in the topography correspond with the InAlAs layers, which show lower UFM amplitude; the AlAs layers present the valleys in topography matching with the higher UFM response. d) shows the comparison of the elastic moduli (C_{11}) of GaAs, AlAs and InAs.

7.2.2. Comparison of contact potential distribution in MQW structures with and without the presence of APD

With confirmed evidence of the presence of APD in this structure via AFM and UFM images, it was decided to investigate the electrical properties of these samples to compare the consequence of the defects. SPM methods, such as KPFM, are potent techniques for the nanoscale mapping of electrical properties. Particularly for the development of semiconductor structures, these methods have demonstrated themselves to be essential tools for the study of doping concentration, band structure studies and charge distribution.

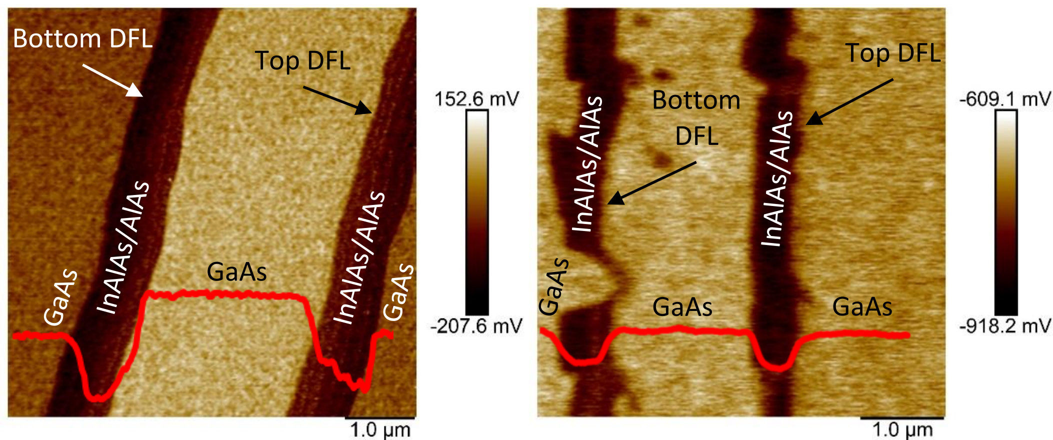

Figure 7.5 KPFM images of the InAlAs/AlAs superlattices separated by the GaAs layer. a) Image of a sample free of APD; the darkest contrast represents the InAlAs/AlAs superlattice, GaAs is displayed by the medium and light contrast. b) Image of a sample with APD; InAlAs/AlAs layers are shown darker than the GaAs areas.

Firstly, we locally mapped the surface potential via KPFM measurements in both samples, with and without APD. The results confirmed the devastating effects in the potential distribution with the presence of APD. Fig. 7.5 shows the comparison of the local contact potential difference (LCPD) maps of the DFL section of the MQW structures. These maps present KPFM images with superposed profiles of the potential distribution. Unexpectedly, the sample free of APD (Fig. 7.5a) shows different contrast between three layers of GaAs, being the same material. These GaAs layers are separated by the InAlAs/AlAs barriers, also very well defined and represented in both images in Fig. 7.5 with the darker contrast. A possible explanation for the unforeseen behaviour of the GaAs layers is that the GaAs layer sandwiched between the InAlAs/AlAs MQW could present different LCPD due to the InAlAs/AlAs layers acting as a charge barrier, confining the GaAs charges. This explanation is supported by the investigation made using a sample with the same structure with APD, which presents a different potential distribution compared with the defective specimen. In this second sample,

the disruption of the MQW that occurs due to the APD creates a more uniform potential distribution in both regions of GaAs. Therefore, we believe that the presence of APD could break the electron confinement effect of the InAlAs/AlAs DFL barriers.

7.3. Charges transfer in complex structures for light-emitting applications – VCSEL

The stimulated emission of radiation was first suggested by Albert Einstein; nevertheless, it was not until 1960 when the first laser was experimentally demonstrated. Since then, different technologies have been developed for the fabrication of lasers. Semiconductors are excellent candidates for solid-state lasers, typically producing light emission from the edge of the device that is cleaved. The vertical cavity lasers, such as the vertical-cavity surface-emitting laser (VCSEL) can have provided a breakthrough for high-speed communication technologies with a much higher surface density of the devices made possible. These devices are more complex and generally require a quantum well or active region sandwiched between upper and lower distributed Bragg reflectors (DBRs). Like in the MQW structure presented above, the VCSEL structure is also a superlattice formed by multiple interfaces, with the quality of the layers determining the performance of the device. In order to understand the potential distribution in the different regions, we nanosectioned the wafers and a final VCSEL device via BEXP followed by the KPFM study.

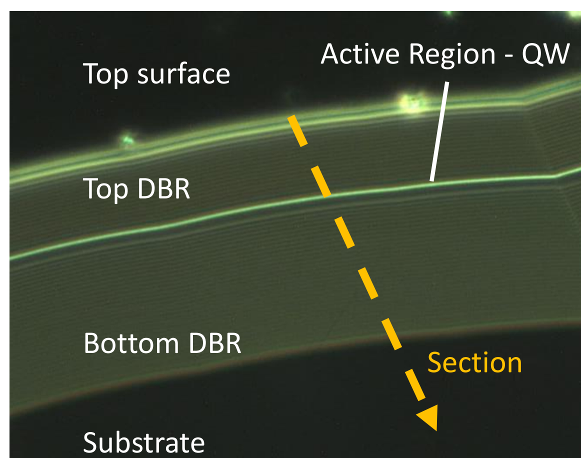

Figure 7.6 Optical image in the dark field of the VCSEL wafer after BEXP sectioning.

Three different samples were sectioned; two of them were the substrates with the grown layers on the top surface. The third sample was a patterned wafer, forming mesa

structures and the gold contacts to contact the devices. The first sample (A) consists of a GaAs substrate with DBR of 34 periods of AlGaAs/GaAs, with the thickness of the layers corresponding to a quarter of the laser wavelength (850 nm) to optimise the reflectance. On top of this bottom DBR, there is the cavity (of approximately 3/2 of the wavelength in thickness) with the active region, in which there are 3 GaAs/AlGaAs QWs. This is followed by a 30 nm thick "oxidation layer" of $Al_{0.98}Ga_{0.02}As$ above. This layer is only oxidised in the final devices, leaving the non-oxidised centre to concentrate the injection current. The wafer is topped with the top DBR, in this case only 20 periods, and the GaAs cap. In the second sample (B – 892nm wavelength), the structure is identical except for the active region, which is made by three $In_{0.06}Ga_{0.94}As$/AlGaAs QWs. The VCSEL sample of the devices studied in this work was processed in a wafer with structure A.

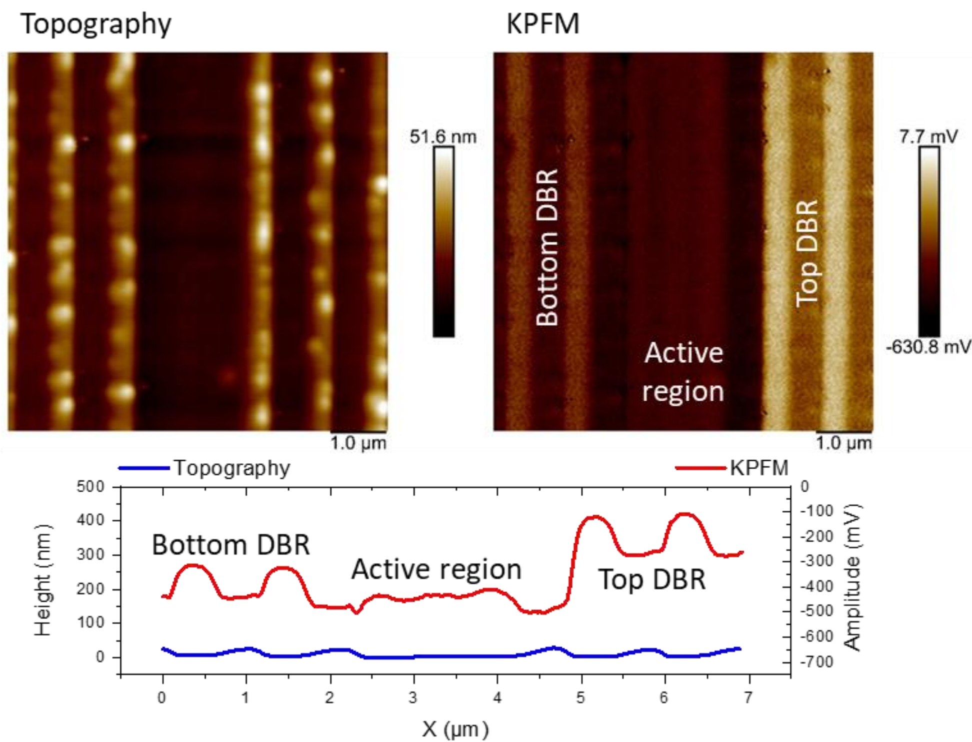

Figure 7.7 Topography and KPFM images of the VCSEL (A) section in the area of the active region. Profiles of both images plotted in the graph.

In the quest to understand the potential distribution of the sample, KPFM measurements were performed on a BEXP sectioned sample. The KPFM maps display the changes in the LCPD for each of the individual layers of the DBR superlattice. Moreover, in Fig.7.7 a step between the level of the LCPD in the top and bottom DBR can be observed, reflecting the difference in the doping concentration between the two sections. Focusing on

the active region and performing high-resolution imaging such as in Fig.7.8 it is just possible to identify the three QWs. As these measurements were made in the wafer and not in the device, the “oxidation layer” is not shown oxidised.

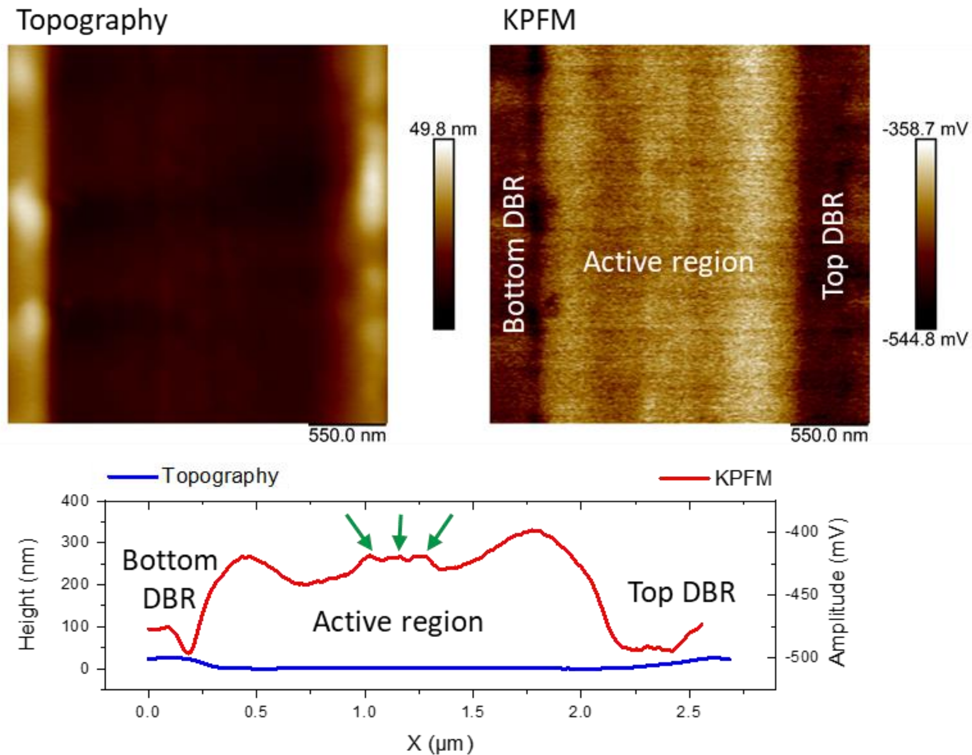

Figure 7.8 High magnification of the topography and KPFM images in the active region area. Plot of the profiles highlighting the 3 QW in the active region with the green arrows. (VCSEL A)

Having demonstrated the feasibility of the combination of the BEXP+SPM, we explored the possibility of observing the sectioned area via optical spectroscopy. Namely, as the BEXP sectioning with a small sectioning angle increases the projection of the thickness of the layers by around ten times, we contemplated that optical methods such Raman spectroscopy or photoluminescence could resolve the sub-micrometre thin layers. We performed Raman spectroscopy maps in the sectioned region, using the experimental setup described in Chapter 4, with the green laser (532nm). In addition, a map of the same region was also obtained for the PL response. Conversely, in the PL measurements, the red laser (633 nm) was implemented. Fig.7.9 shows the Raman spectrum of the VCSEL A obtained in the BEXP sectioned region. Fig.7.9 presents the optical image of the region investigated in the Raman and PL measurements. The Raman and PL maps are also shown in Fig.7.9b-c, respectively. The maps do not resolve the individual layers, but in both cases it was possible to observe some

features which allow one to distinguish between the different parts of the structure, such as substrate, bottom and top DBR, and the active region.

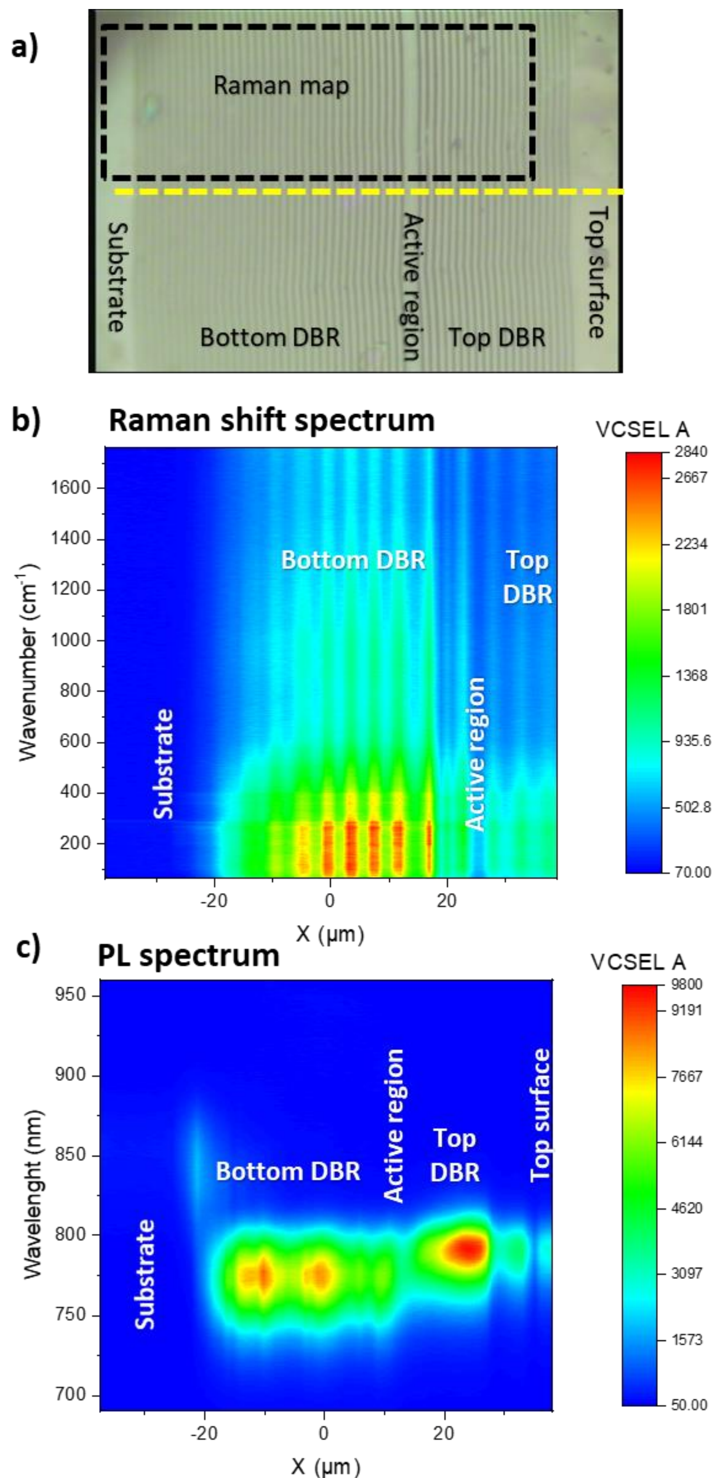

Figure 7.9 a) Optical image of the section area of the VCSEL A, with magnification x100. b) Raman map of the VCSEL A extracted in the area highlighted with the black square in a). c) Map of PL response of VCSEL A, covering the whole structure from the substrate to the top surface. The fringes in b) are due to the interference phenomena, rather than picking up individual DBR layers.

7.4. Metamorphic III-Nitride nanowires on Si

In this section, the mechanical, electrical and piezoelectric behaviour of GaN nanowires (NWs) grown on a silicon substrate is investigated. A novel methodology, never reported prior in literature, was used to embed the NWs in a SiO_2 matrix for the easy BEXP sectioning and further SPM analysis. We, therefore, were able to directly map, using nanoscale resolution, the variations in the contact stiffness and the LCPD at the substrate-NW interface, with this last one showing the depletion region formed between GaN and Si. Finally, via PFM, we observed the orientation variation inside of individual NWs via observing the PFM piezoelectric response.

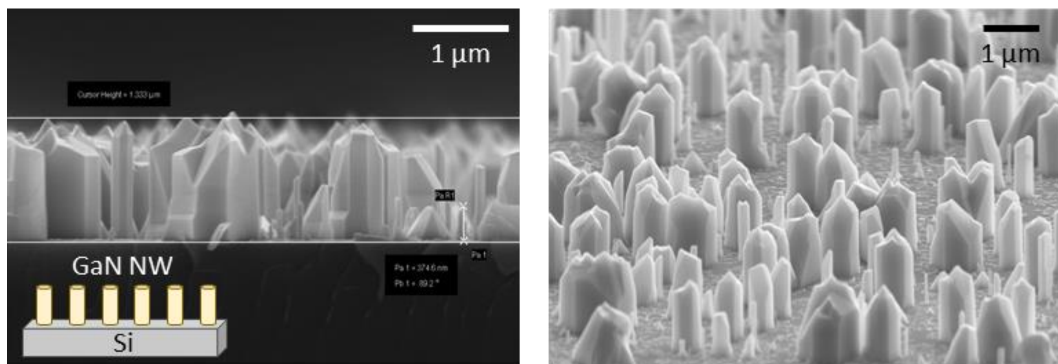

Figure 7.10 SEM images of the GaN nanowires.

In the approach to the inner structure with SPM tips, we used the methodology previously detailed in Chapter 4, which combines BEXP nano-sectioning with the functional SPM analysis of the surface and sub-surface. Samples with irregular surfaces, such as nanowires sticking out of the surface, pre-patterned devices or other complex 3D structures are very challenging for cross-sectioning techniques. This is especially prevalent in the particular case of BEXP, as the discontinuities in the surface can strongly affect the quality of the cut due to the geometry of the sectioning setup. The NWs can create shadows, which will affect the smooth resulting section. For these reasons, the GaN NWs samples were embedded in spin-on-glass (SOG) following the protocol described in Chapter 3: Materials. The SOG coating is a low viscosity liquid, making it adequate for the coating of the whole surface, including the gaps between the individual nanowires, which, after baking, produces a uniform silicon oxide solid layer. This additional step in the sample preparation has enabled marked progress in the study of the internal structure of GaN NWs.

7.4.1. Nanomechanical mapping of GaN nanowires

In the quest to study the mechanical properties of the GaN NWs, we performed nanomechanical mapping of the sectioned region using the standard UFM setup described in Chaper 3: Materials. The results obtained during the scans are displayed in Fig. 7.11, where one can see the simultaneously recorded topography and nanomechanics maps. The Fig. 7.11.a shows the topography image, which was flattened to highlight the morphological features. In Fig.7.11.b, the corresponding UFM image is displayed. In this image, one can identify the area with dark contrast, corresponding to the SOG. However, one can also notice the absence of contrast between the region corresponding with the Si substrate and the GaN nanowires. This effect is attributed to the sensitivity limit of the UFM response, occurring for large values of the effective contact stiffness (E^*) of the sample compared with the tip. In the presented case, we used a standard silicon cantilever, which probably also presented a thin layer of native oxide in the tip surface, which additionally decreased the sensitivity. This interpretation has been supported by Fig.7.12, where theoretical values of the effective contact stiffness whilst increasing the sample stiffness for various tip materials were plotted. In this figure, one can see that all the curves saturate and this effect is occurring earlier for lower tip material stiffness, such as SiO_2. In the figure the grey background indicates the range where the GaN Young's Modulus is found. This area mainly covers the saturated part of the Si and SiO_2 curves. Therefore, we can assume that the UFM response is not fully sensitive to the changes in the stiffness between Si and GaN, due to the GaN value of the stiffness found in the saturated region.

Fig. 7.11.c-d present the profiles extracted from images a) and b) in the areas marked with the dashed lines. The plot corresponding with profile #1 shows part of the substrate and part of one of the nanowires. The topography profile presents a minor change in the slope between the substrate and the NW regions. In the UFM profile, as it was previously detailed, there is no evident change between the substrate and the NW. The plot of profile #2 shows the strong change between the slopes of the substrate and the SOG. Furthermore, the UFM profile also presents a clear decrease in the amplitude signal in the SOG, corresponding with a lower contact stiffness. The values found about the elastic moduli elsewhere [144] confirm that the SOG should present lower stiffness than the silicon substrate.

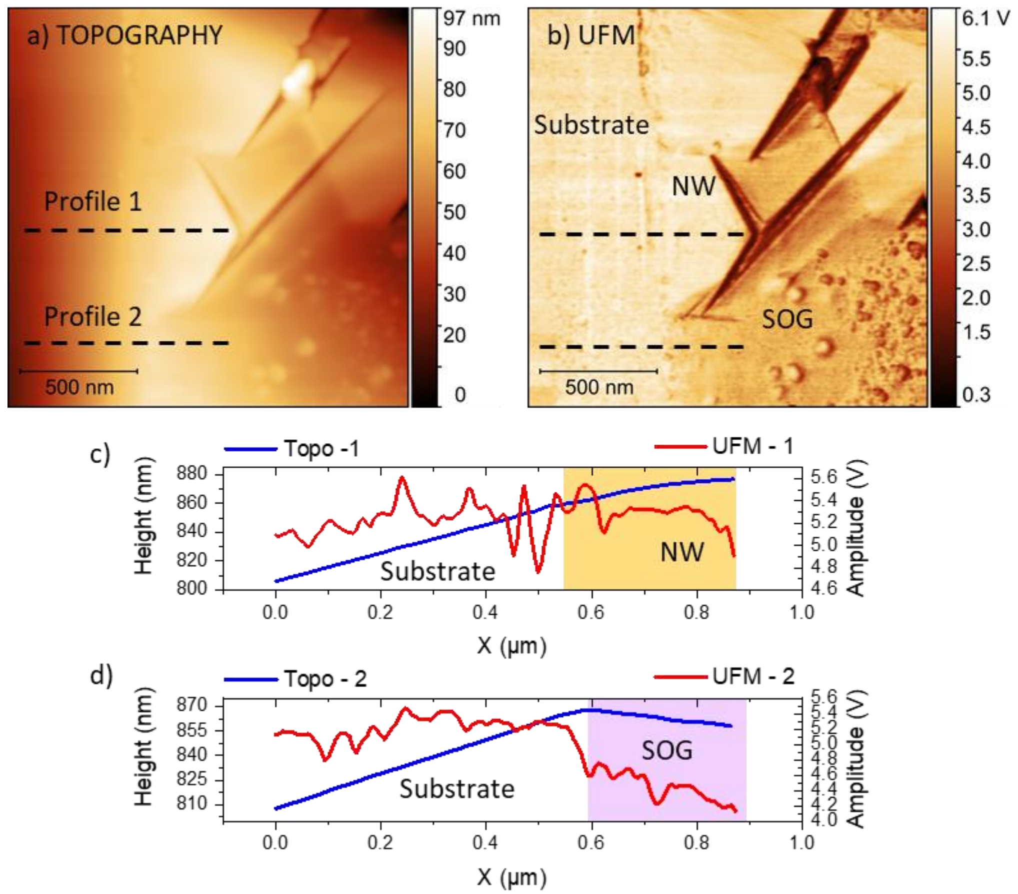

Figure 7.11 a) image of the topography of the substrate-NW boundary (beginning of the growth) of the sectioned area. b) UFM image of the same area as image a). c) and d) are the profiles extracted from images a) and b) in the highlighted regions with the dashed lines.

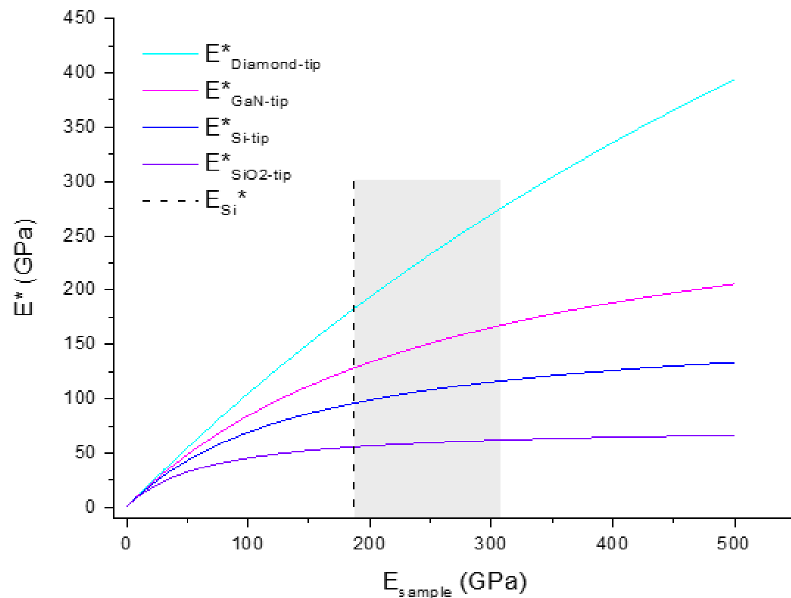

Figure 7.12 Plot of the effective contact stiffness (E^*) whilst increasing the sample stiffness (E_{sample}) for various tip materials; Diamond, GaN, Si and SiO_2.

7.4.2. Surface potential study at the substrate-NW interface

The KPFM characterisation of piezoelectric nanowires has developed great interest due to the ability of these structures to perform as light-emitting diodes, sensors and electromechanical transducers for harvesting ambient mechanical energy. In the case of GaN nanowires, numerous studies of the surface potential using KPFM have been reported in the literature [145-148]. However, these investigations do not report the surface potential at the interface between the substrate and the NW as it is generally not accessible by SPM. In this section, we use BEXP to access this area for the first time and to probe the local contact potential difference at the interface between the substrate and the nanowires.

The results obtained during the KPFM measurements are displayed in Fig.7.13. Fig.7.13.a shows the topography of the sectioned area. The KPFM map is shown in Fig.7.13.b. The contrast of the KPFM allows one to distinguish between the substrate, which shows the brighter contrast, the GaN NWs, which presents the darkest contrast of the map, and the SOG that reveals the intermediate contrast surrounding the NWs. Fig.7.13.d shows a higher magnification of one of the nanowires at the boundary with the substrate. For a better understanding of the potential distribution at the interface with the substrate, we extracted the profiles of the topography and the KPFM images, which are displayed in Fig.7.13.e. It is worth noting that in the boundary between the GaN and the Si substrate there is no sharp interface in the potential (KPFM). The occurring gradient corresponds with the depletion region formed at the junction between the GaN and Si. In the plot of the superposition of the topography and KPFM profiles (Fig. 7.13.e), one can see that the gradient potential starts inside the GaN region and increases until it reaches the Si potential. The width of this depletion region is $\Delta X_{depl.}$= 0.13 µm as directly measured in the potential profile.

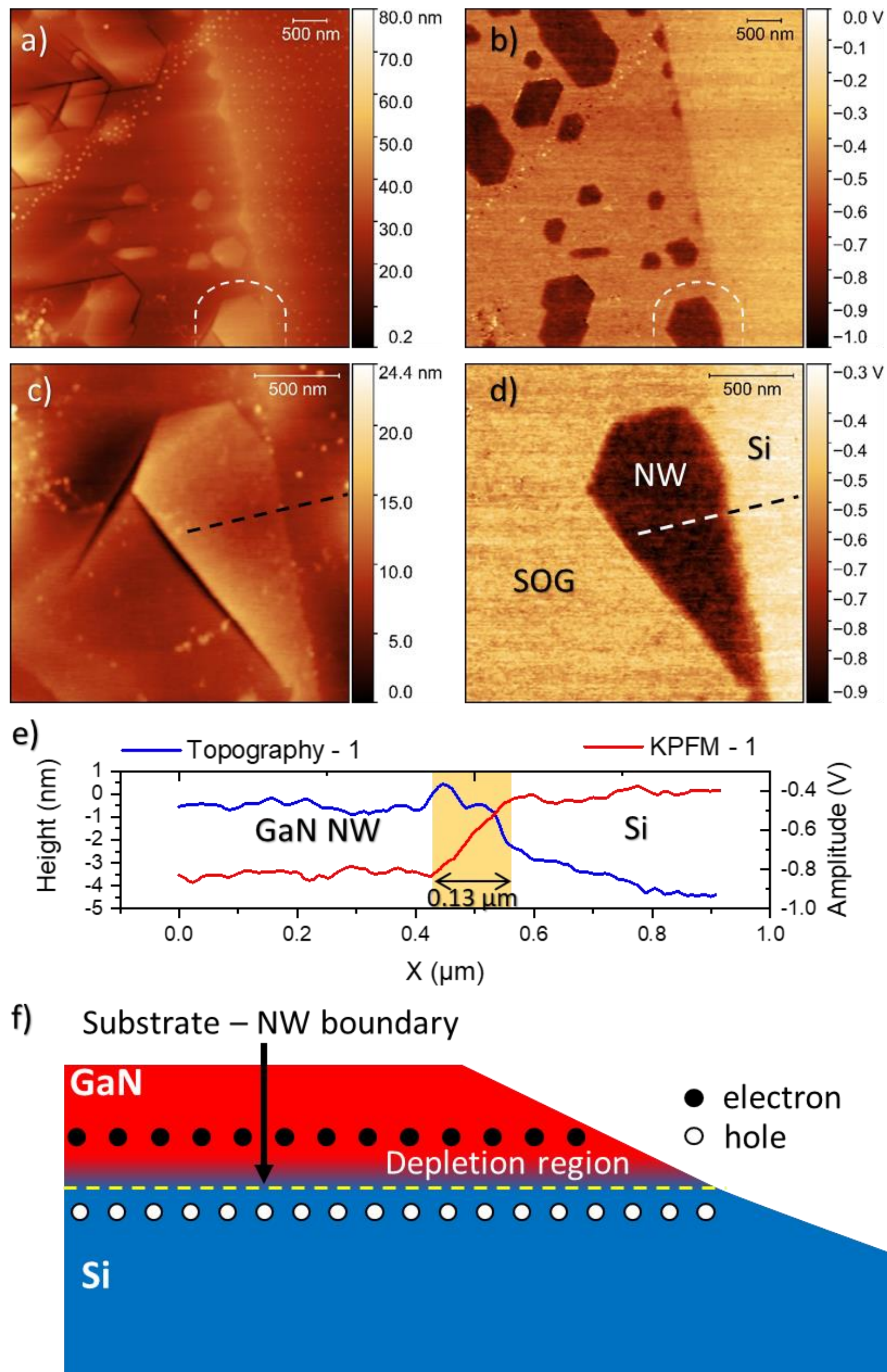

Figure 7.13 a) topography of the NWs forest embedded in SOG and BEXP nanosectioned. b) KPFM map of the same area of image a). c) and d) topography and KPFM images, respectively, of a higher magnification of one of the NWs, sectioned in the initial part of the growth. e) plot of the profiles extracted from images c) and d). f) scheme of the depletion region formed at the interface between the substrate and the NWs.

7.4.3. PFM mapping of polarity reversal in individual NWs

The piezoelectric properties of III-nitrides, and in particular of GaN, have been widely studied over the last decades. It is well known that the piezoelectric response changes with the polarity and the crystallographic orientation [149]. As it can be observed in the diagram in Fig. 7.14, the polarisation is determined by the angle to the c-plane with the piezoelectric response proportional to the piezoelectric polarisation vector (P_{pe}) as described by

$$P_{pe} = e \times S, \qquad (80)$$

where e is the piezoelectric stress constant and S is the mechanical stress. [150]

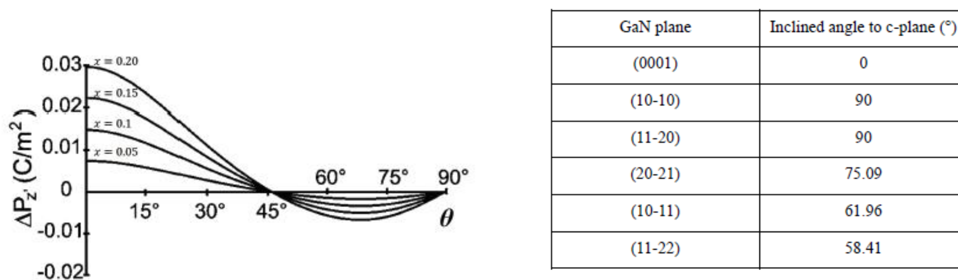

GaN plane	Inclined angle to c-plane (°)
(0001)	0
(10-10)	90
(11-20)	90
(20-21)	75.09
(10-11)	61.96
(11-22)	58.41

Figure 7.14 Total polarisation as a function of the angle in the c-plane. List of polar, non-polar and selected semi-polar planes with inclined angles to the c-plane. [151]

Gallium and nitrogen have different electronegativity, forming a dipole in each Ga-N covalent bond. The absence of a centre of symmetry in the c-plane direction of the GaN structure results in an accumulation of these dipoles, creating macroscopic polarisation along the c-axis. This phenomenon is known as spontaneous polarisation (P_{sp}). In the GaN, the spontaneous polarisation is anti-parallel to the Ga-polar growth direction, as is indicated in the scheme in Fig.7.15. Additionally to the spontaneous polarisation, when the material is mechanically deformed, the phenomena of the piezoelectric polarisation (P_{pz}) appears. This polarisation is proportional to the piezoelectric coefficients (d), to the elastic constants (C) and to the strain produced in the material under an elastic deformation. The piezoelectric polarisation is also induced in the material if it is subjected to a potential difference.

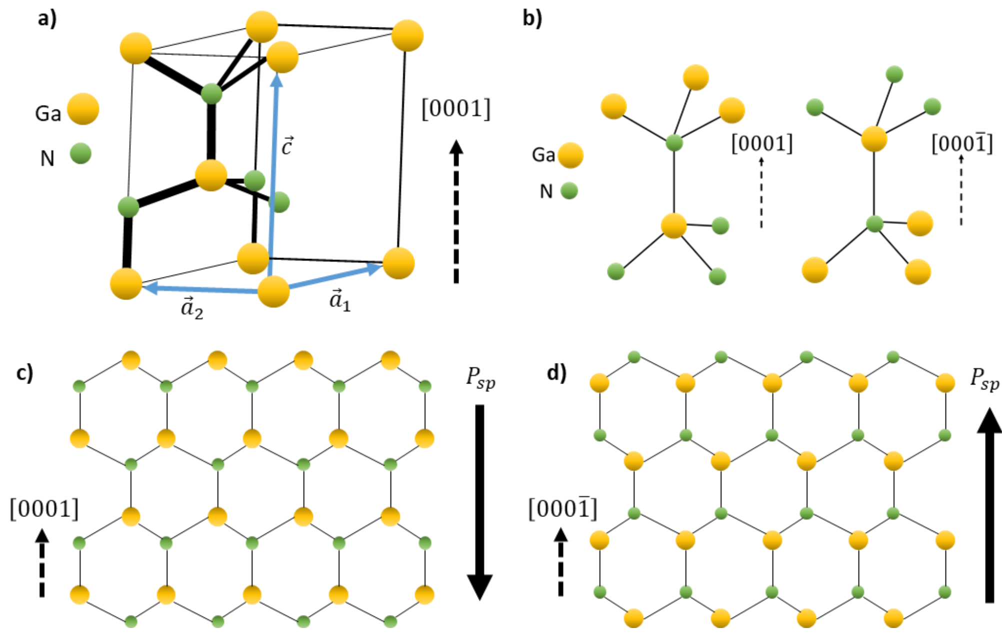

Figure 7.15 a) Schematic of a unit cell of wurtzite GaN. The lattice parameters are indicated as *a* and *c*. Vectors $\vec{a_1}$, $\vec{a_2}$ and $\vec{c}$ are the bases in the hexagonal coordinates. b) Schematic of Ga-polar and N-polar GaN structures. c) and d) schematics of Ga-polar and N-polar atomic layers stacking with spontaneous polarisation (P_{ps}) indicated in each case.

In the quest of the identification of reversal crystallographic domains in individual GaN nanowires with nanoscale resolution, we performed piezoelectric force microscopy (PFM) measurements, simultaneously recording locally the vertical and lateral piezoelectric response. We used the same nanosectioned samples as in the mechanical and electrical studies. The implemented experimental setup was described in Chapter 4. In particular, for the set of measurements presented in Fig. 7.17, we used the lock-in amplifier, zi-HF2LI (Zurich Instruments, *Switzerland*), which allowed for the simultaneous excitation and demodulation of two different frequencies. This allowed us to track one of the frequencies corresponding with the first bending contact resonance of the cantilever, $f_{CR} = 320kHz$ and the other one was the contact resonance of the first torsional mode $f_{Tor} = 817kHz$. The determination of both resonances was experimentally obtained following the procedure also detailed in Chapter 4, selecting the silicon substrate for the resonance frequency probing. The resonance peaks obtained during the sweeps have been plotted in Fig.7.16, presenting the bending and torsional contact resonances in figures a) and b) respectively.

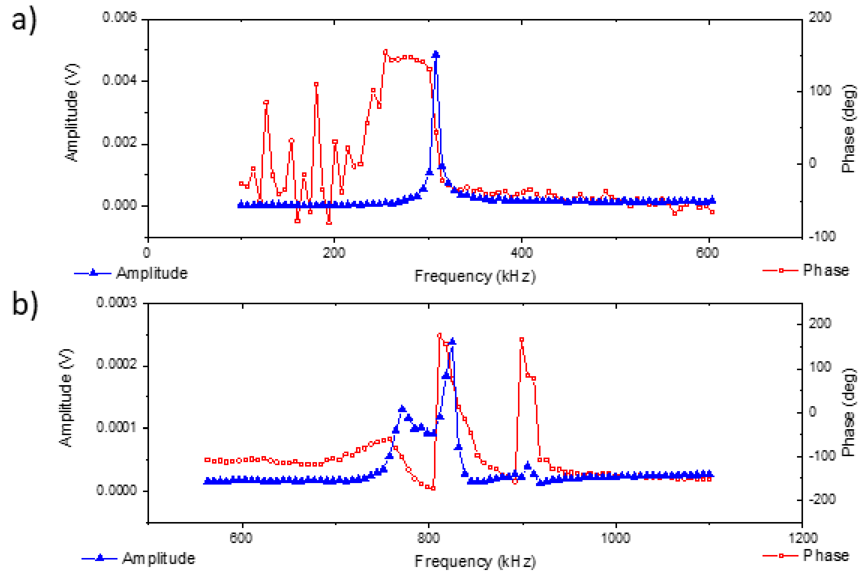

Figure 7.16 Plot of the frequency sweep of the contact flexural and the torsional resonances.

Using these frequencies, we obtained the vertical and lateral PFM (VPFM and LPFM) maps of an individual nanowire shown in Fig. 7.17. Figures a) and b) show the amplitude images of the VPFM and LPFM, respectively. One can see that, in both images, the amplitude response in the SOG region is almost zero, as was expected. Inside the mapped nanowire, we can observe regions with different amplitude response in the VPFM, which do not fully correspond to a contrast in the LPFM. We speculated that this can be attributed to two different facts: one is that the crystallographic domains are not purely vertical, and the other is that they can have a lateral component that is perpendicularly oriented to the scan direction, therefore the cantilever is not very sensitive to the local displacement in that direction. The phase maps shown in Fig. 7.17.c-d present the phase inversion in both cases, VPFM and LPFM. Therefore, we can confirm that the orientation of the domain is not purely vertical, because of the contrast shown in the LPFM phase. However, with these results, it is not straightforward to conclude that the domains are normally oriented to the scan direction. In order to prove it, we should spin the sample exactly at 90° along the axis, normal to its surface, and perform a new LPFM scan. This precise rotation was a challenging movement due to some geometrical limitations in the used experimental setup and we did not succeed in the trial. Hence, this experiment is proposed for a future work, which would allow one to experimentally determine the vector, which fully defines the polarity of the diverse piezoelectric domains.

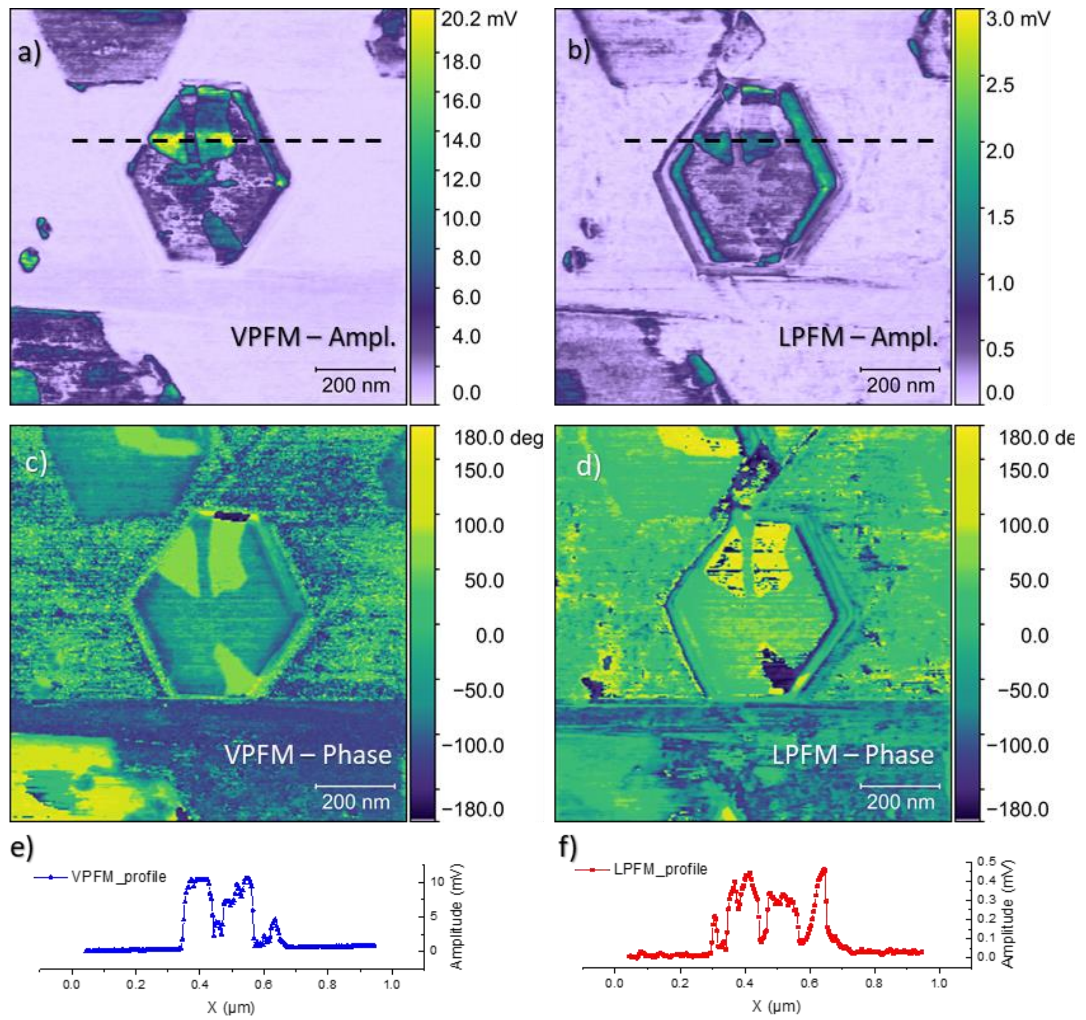

Figure 7.17 Amplitude and phase PFM images of the response of the vertical and lateral PFM modalities, respectively. Profiles of the section presented in the images with the dashed line.

7.4.4. Understanding of the electrostatic contribution in the PFM response

As PFM requires the electrical excitation of the tip or sample, electrostatic attraction of the cantilever to the sample can disguise the piezoelectric response of the material under the tip in the PFM maps. In order to distinguish between the piezoelectric and electrostatic contributions, PFM scans at different offset potential were performed. Fig.7.18 shows the PFM images recorded at different potential offsets (-1 V, 0 V and +1 V). The results obtained agree with the explanations found in literature from *Balke et al.*, which explain the combined piezoelectric and electrostatic signal contributions.[78] As it was explained in the literature review in Chapter 2, the electrostatic force depended on the applied DC offset voltage, whereas the piezoelectric response corresponding to the domain orientation is independent of the DC bias and depends only on the AC component.

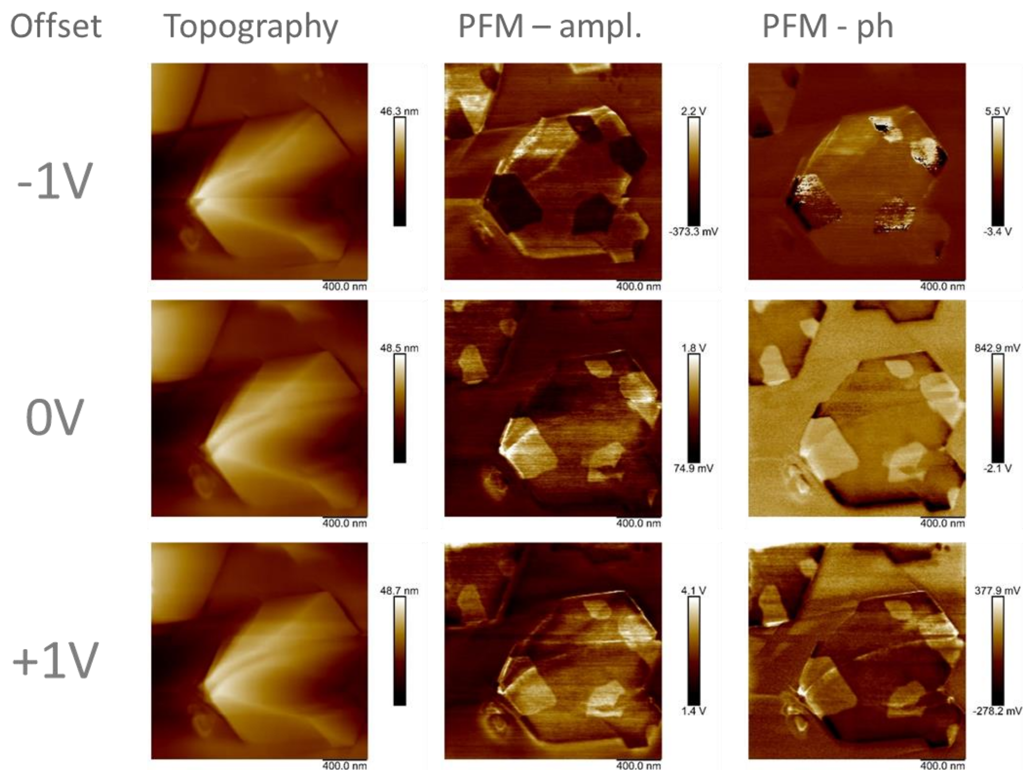

Figure 7.18 PFM images of an individual nanowire for different potential offsets, +1 V, 0V and -1 V.

The changes and the inversion in PFM image contrast, for the various applied biases, can be understood with the help of the schemes shown in Fig. 7.19, with the vector representation of the piezoelectric and electrostatic contribution. The first case corresponds to the minimal electrostatic contribution to the AC signal; then, the vector's moduli are equal for positive and negative piezoresponse. However, the phases are inverted 180°. In the second

cartesian axis, the situation in which there is a positive electrostatic contribution (ES_1) to the PE_1 signal is emphasised. Likewise, in the first case, the absolute values of the amplitude are equal for the positive and negative response, just shifted by the electrostatic vector ES_1. Whereas, the phase difference between positive and negative domains is much smaller, even showing the same orientation (same quadrant)

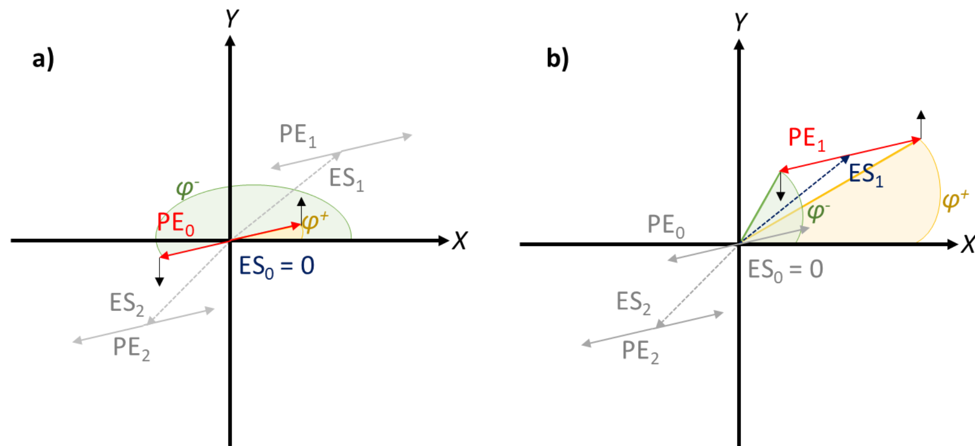

Figure 7.19 Schematic analysis of the piezoelectric and electrostatic signal contributions. PE – Piezoelectric response. ES – Electrostatic contribution. Plot a) represents the piezoresponse vectors PE_0 (with red arrows), in the cartesian coordinates and in absence of electrostatic contribution ($ES_0 = 0$). Also, the representation of the phases of the PE vectors are superposed, represented by yellow and green arcs the positive and the negative responses, respectively. Plot b) shows the PE_1 response with positive electrostatic contribution ES_1. [78]

7.5. Summary

The integration of compound semiconductor (CS) on silicon (Si) wafers combines the established manufacturing processed of Si and the outstanding properties of CS for more efficient devices fabrication. Nonetheless, the dissimilar growing conditions and lattice mismatch between CS and Si, create interfacial defects, which can propagate throughout the structures affecting the crystal quality and diminishing the efficiency of devices. Suitable characterization methods offering nanoscale resolution, material properties sensitivity and allowing the access to the internal structures are required to feedback the CS manufacturers for fast development of the CS-Si hybrid devices.

In this chapter, we have presented the implementation of a unique method for the exploration of materials defects in nanostructures of compound semiconductors, merging the advanced nano-cross-sectional BEXP tool with the functional scanning probe microscopy. This methodology allows the 3D investigation of the defects, providing fundamental information about how the physical properties are affected by the presence of these defects.

We were able to visualise the effects of the propagation of atomic-scale defects, such as antiphase domains (APD) occurring in hybrid structures of III-V and Si, in the morphology of the superlattices and the top surface. Furthermore, we observed the consequences of these defects in the surface potential distribution across the structure. The nanomechanical mapping allowed for the study of strained layers in the superlattice.

In this chapter, we also reported the local changes in the surface potential caused by diverse doping concentration in multi-layered structures such as VCSELs. In addition, we were able to optically investigate the structures, thanks to the increase in the projection of the thickness of thin layers by the BEXP sectioning.

Finally, we reported the feasibility of the sectioning of 3D nanostructures, such as GaN nanowires, using a novel process for the sample preparation. We studied, via KPFM, the surface potential distribution at the interface between the Si substrate and the GaN nanowires, finding the depletion region. Also, we were able to simultaneously map vertical and lateral piezoelectric responses inside of nanowires. By these measurements, we were able to visualise reverse piezoelectric domains inside of individual nanowires.

8. Achievements and perspectives

In conclusion, we have studied the physical properties of diverse low-dimensional structures of advanced materials using a variety of scanning probe methods. Below, we summarise the main outcomes of our work.

8.1. Key achievements of this thesis

- ***Multi-mode excitations in tuning forks for quantum turbulence and in-liquid SPM probing***

We investigated the complex oscillation behaviour of the tuning fork MEMS devices allowing simultaneous excitation and probing of two vibrational modes – torsional and flexural. We demonstrated that the torsional mode can be used for the detection of the damping produced by turbulence, simultaneously excited by the flexural mode. We also revealed that the critical velocity needed for the excitation of the quantum turbulence regime in ^{4}He was not reached by the tines of the TF operating in the torsional mode. Furthermore, we presented a new SPM experimental setup using electrically shielded $LiNbO_3$ tuning forks as piezoelectric probes. We demonstrated that these probes can effectively operate in a liquid environment for nanoscale resolution mapping.

- ***Nonlinear point excitation-probing of resonating structures using modulation ultrasonic force microscopy (M-UFM)***

In order to explore nanoscale resonating systems, and reduce the linear coupling of the SPM probing tip to the nanostructure, we developed the method called modulation ultrasonic force microscopy (M-UFM), for the local excitation and detection of the vibrational modes of a silicon nitride membrane. In this approach, two significantly differing frequencies are applied to the tip (f_t) and the probed MEMS structure (f_s) that are outside of the structure or tip resonance, whereas the difference frequency ($f_s - f_t$) is equal to the resonance of the MEMS device. As a result, both the excitation and detection are performed simultaneously. We demonstrated that this method is sensitive to the vibrational modes and the subsurface features of the MEMS device (e.g. supported or suspended layers).

- ***Study of dynamic and structural properties of graphene drums via nanoscale mapping of coupled vibrational modes of drum-SPM probe system***

In the study of the nanomechanical behaviour of a multilayer graphene drum via CR-AFM mapping, we established the difference in the local stiffness of the drum as a function of the probing position and we found an excellent agreement between the experimental and modelling data. In addition, the modelling allowed us to confirm that the graphene flake behaviour is more comparable to a supported plate than a tensioned membrane. Furthermore, we confirmed that UFM is a very effective method to find the boundaries between the suspended and the supported regions of the graphene plate, allowing precise determination of the drum geometry. We also revealed that CR-AFM can provide misleading information of the diameter of the drum. In addition, we also demonstrated that CR-AFM provides useful information of the internal structure of suspended regions.

- ***Nanoscale physical properties mapping and defect identification in heterostructures of 2D materials***

We studied buried defects in CVD grown vertical heterostructures of WS_2 using UFM, a non-invasive and non-destructive method, able to image sub-surface features with nanoscale resolution. In addition, we performed for the first time the BEXP nano-sectioning of 2D material heterostructures and we demonstrated the possibility of directly mapping the material defects formed in the internal structure. We also confirmed that UFM is sensitive to the nanomechanical inhomogeneities in the internal structure, suggesting the presence of defective layers at the beginning of the grown heterostructure, being features not observable in the dielectric properties maps. Furthermore, we determined the local contact stiffness and heat transport of lateral heterostructures of WS_2 and MoS_2, and we confirmed the outstanding sensitivity of these functional SPM techniques to the interface between the layers. In addition, we revealed the local contact stiffness depending on the thickness of the layers in the natural occurring heterostructure franckeite.

- ***3D Mapping of APD in III-V on Si structures – morphology and effects on the surface potential distribution***

  We used the nanosectioning BEXP method to study the propagation of the APD from the Si substrate interface to the top surface of complex MQW structures. We demonstrated that the combination of BEXP sectioning and the functional SPM analysis creates an excellent methodology for the investigation of the effects caused in physical properties in the presence of APD. Via UFM and KPFM mapping of the sectioned structures, we

confirmed the distortion in the InAlAs/AlAs superlattices morphology and the alteration of the surface potential distribution in the GaAs layers surrounding the superlattices caused by the APD.

- ***Piezoelectric domains diagnosis***

We demonstrated that the embedding of nanowires in spin-on-glass, followed by the BEXP nanosectioning of these structures, is an appropriate sample preparation methodology allowing the direct access to the internal structure and the substrate-nanowires interface via SPM techniques. In addition, we confirmed the presence of reverse piezoelectric domains in individual GaN nanowires and we also verified the presence of diverse polarity orientation of the crystallographic domains by the simultaneous mapping of vertical and lateral piezoelectric response via PFM measurements.

8.2. Perspectives

In order to provide insights into the future direction of the research of micro- and nanostructures of advanced materials using scanning probe methods, I can envisage several directions that may expand the research that was initiated in this thesis. There are a number of different experiments that will follow up in this research group, which could establish the methodologies developed along this thesis, as the state-of-the-art techniques to explore physical properties of advance materials with nanoscale resolution. Below, we summarise the main ideas.

The shielded $LiNbO_3$ tuning forks were found to be useful as piezoelectric probes for the nanoscale mapping in liquid environments. Further research in highly-conductive liquids could be carried out using these probes to study solid-liquid interfaces, such as between the cathode and/or anode in batteries with liquid electrolytes. This could result in a breakthrough in the battery research, allowing the *in-situ* nanoscale investigation of these solid-liquid interfaces. In addition, biological material and living cell, which also require immersive techniques, could be morphologically characterized using shielded $LiNbO_3$ tuning forks as probes.

The potential of the M-UFM technique was demonstrated using a commercial Si_3N_4 membrane. Therefore, the implementation of the M-UFM to explore 2D materials resonating systems, such as the circular graphene drums investigated via CR-AFM and UFM, could be an interesting experiment. This will could establish M-UFM as a revolutionary technique for the local investigation of nanomechanical properties in high-frequency resonating systems.

In addition, other free-oscillating 2D-materials layers, such as the quasi-suspended structures produced in the lateral heterostructures of MoS_2 and WS_2 (explained in section 6.2) could also be investigated using M-UFM.

The VCSEL structures were investigated in passive mode, using electrical SPM methods, such as KPFM. For a better understanding of the potential distribution and charge transfer across the VCSELs *in-operando*, we propose to use a wafer with VCSEL structures and patterned devices, as it is shown in Fig. 8.1. The devices can be sectioned at a steep angle, using a sample stage angled 30° in the BEXP machine. This allows the sectioning of full devices in the centre of the cavity and to keep part of the electrodes for electrical excitation of the structures. Using the sectioned devices, simultaneous KPFM or SSRM mapping of the section could be performed while operating the VCSEL devices. Other functional SPM measurements, such thermal studies using SThM, could provide essential information about heat dissipation, for further development and performance improvement of these devices.

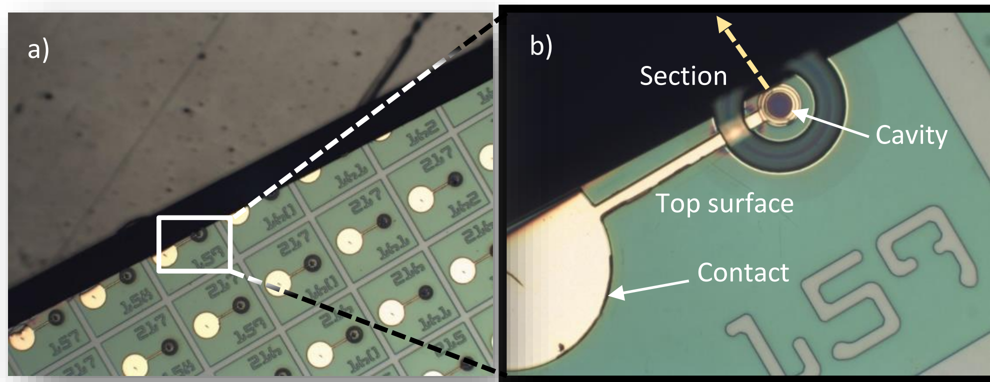

Figure 8.1 Optical images of the VCSEL devices after BEXP sectioning. a) shows the 5x magnification of multiple devices, some of them sectioned in the edge of the sample. b) shows 40x magnification of one of the sectioned devices.

Finally, to provide a full diagnosis of the polarity of the piezoelectric domains in GaN nanowires, we propose to investigate these structures performing scans using two configurations, rotating the sample 90° in the x-y plane. This will allow one to extract the three components of the vector, which defines the direction of the crystallographic domains. In addition, COMSOL modelling of the piezoelectric response and potential distribution of these nanostructures will help in the quantification and full understanding of the experimental results.

References

1. Roduner, E., *Size matters: why nanomaterials are different.* Chemical Society Reviews, 2006. **35**(7): p. 583-592.
2. Drexler, E., *There's Plenty of Room at the Bottom*, in *Richard Feynman, Pasadena*. 2009.
3. Nie, S., et al., *Nanotechnology applications in cancer.* Annu. Rev. Biomed. Eng., 2007. **9**: p. 257-288.
4. Wilson, M., et al., *Nanotechnology: basic science and emerging technologies*. 2002: CRC press.
5. Novoselov, K.S., et al., *Electric field effect in atomically thin carbon films.* Science, 2004. **306**(5696): p. 666-669.
6. Eftekhari, A., *Tungsten dichalcogenides (WS2, WSe2, and WTe2): materials chemistry and applications.* Journal of Materials Chemistry A, 2017. **5**(35): p. 18299-18325.
7. Huang, W., et al., *Generating electricity using graphene nanodrums.* RSC Advances, 2015. **5**(43): p. 34065-34069.
8. Geim, A.K. and I.V. Grigorieva, *Van der Waals heterostructures.* Nature, 2013. **499**(7459): p. 419-425.
9. Lee, C., et al., *Measurement of the elastic properties and intrinsic strength of monolayer graphene.* Science, 2008. **321**(5887): p. 385-388.
10. Nair, R.R., et al., *Fine structure constant defines visual transparency of graphene.* Science, 2008. **320**(5881): p. 1308-1308.
11. Nika, D.L. and A.A. Balandin, *Phonons and thermal transport in graphene and graphene-based materials.* Reports on Progress in Physics, 2017. **80**(3): p. 036502.
12. Wang, Q.H., et al., *Electronics and optoelectronics of two-dimensional transition metal dichalcogenides.* Nat. Nanotechnol., 2012. **7**(11): p. 699.
13. Thakar, K. and S. Lodha, *Optoelectronic and photonic devices based on transition metal dichalcogenides.* Materials Research Express, 2020. **7**(1): p. 014002.
14. Kuech, T., *Handbook of Crystal Growth: Thin Films and Epitaxy*. 2014: Elsevier.
15. Bhattacharya, P., R. Fornari, and H. Kamimura, *Comprehensive Semiconductor Science and Technology: Online Version*. 2011: Newnes.
16. Roelkens, G., et al., *III-V-on-silicon photonic devices for optical communication and sensing.* Photonics, 2015. **2**(3): p. 969-1004.
17. Allhoff, F., P. Lin, and D. Moore, *What is nanotechnology and why does it matter?: from science to ethics*. 2009: John Wiley & Sons.
18. Fan, X., et al., *Band structure engineering of boron–oxygen-based materials for efficient charge separation.* Materials Chemistry Frontiers, 2019. **3**: p. 1440-1448.
19. Fox, M., *Optical properties of solids*. Second ed. 2002: Oxford University Press.
20. Bower, A.F., *Applied mechanics of solids*. 2009: CRC press.
21. Hajgató, B., et al., *Out-of-plane shear and out-of plane Young's modulus of double-layer graphene.* Chemical Physics Letters, 2013. **564**: p. 37-40.
22. Briscoe, J. and S. Dunn, *Nanostructured Piezoelectric Energy Harvesters*. 2014: Springer, Cham.
23. Manbachi, A. and R.S.C. Cobbold, *Development and Application of Piezoelectric Materials for Ultrasound Generation and Detection.* Ultrasound, 2011. **19**(4): p. 187-196.
24. Sirohi, J. and I. Chopra, *Fundamental understanding of piezoelectric strain sensors.* Journal of intelligent material systems and structures, 2000. **11**(4): p. 246-257.
25. Pelleg, J., *Mechanical properties of materials*. Vol. 190. 2012: Springer Science & Business Media.
26. Hopcroft, M.A., W.D. Nix, and T.W. Kenny, *What is the Young's Modulus of Silicon?* Journal of microelectromechanical systems, 2010. **19**(2): p. 229-238.
27. Ogi, H., et al., *Elastic, anelastic, and piezoelectric coefficients of α-quartz determined by resonance ultrasound spectroscopy.* Journal of Applied Physics, 2006. **100**(5): p. 053511.
28. Weis, R.S. and T.K. Gaylord, *Lithium niobate: Summary of physical properties and crystal structure.* Applied Physics A, 1985. **37**(4): p. 191-203.
29. Hangleiter, A., et al., *The role of piezoelectric fields in GaN-based quantum wells.* Materials Research Society Internet Journal of Nitride Semiconductor Research, 1998. **3**.

30. Nakamura, N., H. Ogi, and M. Hirao, *Elastic, anelastic, and piezoelectric coefficients of GaN.* Journal of Applied Physics, 2012. **111**(1): p. 013509.
31. Huang, C.-T., et al., *GaN nanowire arrays for high-output nanogenerators.* Journal of the American Chemical Society, 2010. **132**(13): p. 4766-4771.
32. Geim, A.K., *Graphene: Status and Prospects.* Science, 2009. **324**(5934): p. 1530-1534.
33. Antonietti, M., et al., *Nanocarbon-inorganic hybrids: next generation composites for sustainable energy applications*. 2014: Walter de Gruyter GmbH & Co KG.
34. Liu, K. and J. Wu, *Mechanical properties of two-dimensional materials and heterostructures.* Journal of Materials Research, 2016. **31**(7): p. 832-844.
35. Balandin, A.A., et al., *Superior thermal conductivity of single-layer graphene.* Nano letters, 2008. **8**(3): p. 902-907.
36. Parvez, K., *Two-Dimensional Nanomaterials: Crystal Structure and Synthesis*, in *Biomedical Applications of Graphene and 2D Nanomaterials*. 2019, Elsevier. p. 1-25.
37. Zhao, W., et al., *Origin of Indirect Optical Transitions in Few-Layer MoS2, WS2, and WSe2.* Nano Letters, 2013. **13**(11): p. 5627-5634.
38. Zhao, W.J., et al., *Evolution of Electronic Structure in Atomically Thin Sheets of WS2 and WSe2.* ACS Nano, 2013. **7**(1): p. 791.
39. Zhao, W., et al., *Evolution of Electronic Structure in Atomically Thin Sheets of WS2 and WSe2.* ACS Nano, 2013. **7**(1): p. 791-797.
40. Cong, C., et al., *Synthesis and Optical Properties of Large-Area Single-Crystalline 2D Semiconductor WS2 Monolayer from Chemical Vapor Deposition.* Advanced Optical Materials, 2014. **2**(2): p. 131-136.
41. Liu, K., et al., *Elastic properties of chemical-vapor-deposited monolayer MoS2, WS2, and their bilayer heterostructures.* Nano letters, 2014. **14**(9): p. 5097-5103.
42. Zhang, R., V. Koutsos, and R. Cheung, *Elastic properties of suspended multilayer WSe2.* Applied Physics Letters, 2016. **108**(4): p. 042104.
43. Tompkins, B., *MultiMode™ SPM Instruction Manual*. 1999, Digital Instruments Veeco Metrology Group, Santa Barbara.
44. Maivald, P., et al., *Using force modulation to image surface elasticities with the atomic force microscope.* Nanotechnology, 1991. **2**(2).
45. Mazeran, P.-E. and J.-L. Loubet, *Normal and lateral modulation with a scanning force microscope, an analysis: Implication in quantitative elastic and friction imaging.* Tribology Letters, 1999. **7**(4): p. 199-212.
46. Kay, N.D., *Nanomechanical and Nanoelectromechanical Phenomena in 2D Atomic Crystals: A Scanning Probe Microscopy Approach*. 2017: Springer.
47. Maivald, P., et al., *Using force modulation to image surface elasticities with the atomic force microscope.* Nanotechnology, 1991. **2**(103).
48. Yuya, P.A., D.C. Hurley, and J.A. Turner, *Relationship between Q-factor and sample damping for contact resonance atomic force microscope measurement of viscoelastic properties.* Journal of Applied Physics, 2011. **109**(11): p. 113528.
49. Stan, G. and R.F. Cook, *Mapping the elastic properties of granular Au films by contact resonance atomic force microscopy.* Nanotechnology, 2008. **19**(23): p. 235701.
50. Tu, Q., et al., *Quantitative Subsurface Atomic Structure Fingerprint for 2D Materials and Heterostructures by First-Principles-Calibrated Contact-Resonance Atomic Force Microscopy.* ACS Nano, 2016. **10**(7): p. 6491-6500.
51. Huey, B.D., *AFM and acoustics: Fast, quantitative nanomechanical mapping*, in *Annual Review of Materials Research*. 2007. p. 351-385.
52. Yamanaka, K., H. Ogiso, and O. Kolosov, *Ultrasonic force microscopy for nanometre resolution subsurface imaging.* Applied Physics Letters, 1994. **64**(2): p. 178-180.
53. Kolosov, O. and K. Yamanaka, *Nonlinear detection of ultrasonic vibrations in an atomic-force microscope.* Japanese Journal of Applied Physics Part 2-Letters, 1993. **32**(8A): p. L1095-L1098.
54. Dinelli, F., C. Albonetti, and O.V. Kolosov, *Ultrasonic force microscopy: Detection and imaging of ultra-thin molecular domains.* Ultramicroscopy, 2011. **111**(4): p. 267-272.
55. Dinelli, F., et al., *Mapping surface elastic properties of stiff and compliant materials on the nanoscale using ultrasonic force microscopy.* Philosophical Magazine A, Physics of Condensed Matter Structure Defects and Mechanical Properties, 2000. **80**(10): p. 2299-2323.

56. Dinelli, F., et al., *Ultrasound induced lubricity in microscopic contact.* Applied Physics Letters, 1997. **71**(9): p. 1177-1179.
57. Dinelli, F., et al., *Measurements of stiff-material compliance on the nanoscale using ultrasonic force microscopy.* Physical Review B, 2000. **61**(20): p. 13995-14006.
58. Bosse, J.L., et al., *Physical mechanisms of megahertz vibrations and nonlinear detection in ultrasonic force and related microscopies.* Journal of Applied Physics, 2014. **115**(14): p. 144304.
59. Inagaki, K., et al., *Waveguide ultrasonic force microscopy at 60 MHz.* Applied Physics Letters, 2000. **76**(14): p. 1836-1838.
60. Cuberes, M.T., G.A.D. Briggs, and O. Kolosov, *Nonlinear detection of ultrasonic vibration of AFM cantilevers in and out of contact with the sample.* Nanotechnology, 2001. **12**(1): p. 53-59.
61. Cuberes, M.T., et al., *Heterodyne force microscopy of PMMA/rubber nanocomposites: nanomapping of viscoelastic response at ultrasonic frequencies.* Journal of Physics D-Applied Physics, 2000. **33**(19): p. 2347-2355.
62. Girard, P., *Electrostatic force microscopy: principles and some applications to semiconductors.* Nanotechnology, 2001. **12**(4): p. 485-490.
63. Kay, N.D., et al., *Electromechanical Sensing of Substrate Charge Hidden under Atomic 2D Crystals.* Nano Letters, 2014. **14**(6): p. 3400.
64. Collins, L., et al., *Band excitation Kelvin probe force microscopy utilizing photothermal excitation.* Applied Physics Letters, 2015. **106**(10): p. 104102.
65. Melitz, W., et al., *Kelvin probe force microscopy and its application.* Surface Science Reports, 2011. **66**(1): p. 1-27.
66. Zerweck, U., et al., *Accuracy and resolution limits of Kelvin probe force microscopy.* Physical Review B, 2005. **71**(12): p. 125424.
67. Ding, X.D., et al., *Resonant multi-frequency method for Kelvin probe force microscopy in air.* Measurement Science & Technology, 2012. **23**(10): p. 105402.
68. Collins, L., et al., *Dual harmonic Kelvin probe force microscopy at the graphene–liquid interface.* Applied physics letters, 2014. **104**(13): p. 133103.
69. Fumagalli, L., et al., *Label-free identification of single dielectric nanoparticles and viruses with ultraweak polarization forces.* Nature materials, 2012. **11**(9): p. 808.
70. Martin, Y., D.W. Abraham, and H.K. Wickramasinghe, *High-resolution capacitance measurement and potentiometry by force microscopy.* Applied Physics Letters, 1988. **52**(13): p. 1103-1105.
71. Pan, K., et al., *The electromechanics of piezoresponse force microscopy for a transversely isotropic piezoelectric medium.* Acta Materialia, 2013. **61**(18): p. 7020-7033.
72. Kalinin, S.V. and A. Gruverman, *Scanning probe microscopy: electrical and electromechanical phenomena at the nanoscale*. Vol. 1. 2007: Springer Science & Business Media.
73. Monchalin, J.P., *OPTICAL-DETECTION OF ULTRASOUND.* Ieee Transactions on Ultrasonics Ferroelectrics and Frequency Control, 1986. **33**(5): p. 485-499.
74. Righini, G.C., A. Tajani, and A. Cutolo, *An introduction to optoelectronic sensors*. Vol. 7. 2009: World Scientific.
75. Scherer, M., et al., *Sample preparation for scanning Kelvin probe microscopy studies on cross sections of organic solar cells.* AIP Advances, 2013. **3**(9): p. 092134.
76. Bhushan, B., *Nanotribology and nanomechanics.* Wear, 2005. **259**(7–12): p. 1507-1531.
77. Van Eysden, C.A. and J.E. Sader, *Resonant frequencies of a rectangular cantilever beam immersed in a fluid.* Journal of Applied Physics, 2006. **100**(11): p. 114916.
78. Balke, N., et al., *Quantification of surface displacements and electromechanical phenomena via dynamic atomic force microscopy.* Nanotechnology, 2016. **27**(42): p. 425707.
79. Rossing, T.D. and N.H. Fletcher, *Principles of vibration and sound*. 2004, Acoustical Society of America: New York.
80. Chen, C.Y., et al., *Performance of monolayer graphene nanomechanical resonators with electrical readout.* Nature Nanotechnology, 2009. **4**(12): p. 861-867.
81. Eriksson, A.M., et al., *Frequency tuning, nonlinearities and mode coupling in circular mechanical graphene resonators.* Nanotechnology, 2013. **24**(39): p. 9.
82. Castellanos-Gomez, A., et al., *Mechanics of freely-suspended ultrathin layered materials.* Annalen Der Physik, 2015. **527**(1-2): p. 27-44.
83. Novoselov, K.S. and A.H.C. Neto, *Two-dimensional crystals-based heterostructures: materials with tailored properties.* Physica Scripta, 2012. **2012**.

84. Fan, X., et al., *Controllable Growth and Formation Mechanisms of Dislocated WS2 Spirals.* Nano Letters, 2018. **18**(6): p. 3885-3892.
85. Zhao, Y. and S. Jin, *Controllable Water Vapor Assisted Chemical Vapor Transport Synthesis of WS2-MoS2 Heterostructure.* ACS Materials Letters, 2019. **2**(1): p. 42-48.
86. Liu, Z., et al., *Origin of defect tolerance in InAs/GaAs quantum dot lasers grown on silicon.* Journal of Lightwave Technology, 2019. **28**(2): p. 240-248.
87. Yu, X., 2017, MOCVD Growth of Novel GaN Materials on Silicon Substrates, PhD Thesis, University of Sheffield, Sheffield
88. Cao, Z., *Thin film growth: physics, materials science and applications*. 2011: Elsevier.
89. Gunasekar, N.K., et al., *Determining GaN nanowire polarity and its influence on light emission in the scanning electron microscope.* Nano letters, 2019. **19**(6): p. 3863-3870.
90. Giessibl, F.J., *The qPlus sensor, a powerful core for the atomic force microscope.* Review of Scientific Instruments, 2019. **90**(1): p. 011101.
91. Matsiev, L., et al., *High precision tuning fork sensor for liquid property measurements*, in *2005 IEEE Ultrasonics Symposium, Vols 1-4*. 2005, IEEE: New York. p. 1492-1495.
92. Guthrie, A., et al., *Multimode probing of superfluid 4 He by tuning forks.* Applied Physics Letters, 2019. **115**(11): p. 113103.
93. Bennett, J., O. Kolosov, and L. Matsiev, Flexural resonator sensing device and method, 2009, US 7,562,557
94. Falter, J., et al., *Calibration of quartz tuning fork spring constants for non-contact atomic force microscopy: direct mechanical measurements and simulations.* Beilstein Journal of Nanotechnology, 2014. **5**: p. 507-516.
95. Blaauwgeers, R., et al., *Quartz tuning fork: Thermometer, pressure- and viscometer for helium liquids.* Journal of Low Temperature Physics, 2007. **146**(5-6): p. 537-562.
96. Bradley, D.I., et al., *Crossover from hydrodynamic to acoustic drag on quartz tuning forks in normal and superfluid (4)He.* Physical Review B, 2012. **85**(1): p. 014501.
97. Jazbinšek, M. and M. Zgonik, *Material tensor parameters of LiNbO3 relevant for electro-and elasto-optics.* Applied Physics B, 2002. **74**(4-5): p. 407-414.
98. Ahlstrom, S.L., et al., *Response of a Mechanical Oscillator in Solid 4He.* Journal of Low Temperature Physics, 2014. **175**(1-2): p. 140-146.
99. Kolosov, O. and I. Grishin, Method and apparatus for ion beam polishing, 2011, PCT/GB2011/000169
100. Li, C., et al., *PeakForce Kelvin probe force microscopy.* Bruker Appl. Note, 2013. **140**: p. 1-14.
101. Gramse, G., et al., *Quantitative dielectric constant measurement of thin films by DC electrostatic force microscopy.* Nanotechnology, 2009. **20**(39): p. 395702.
102. Ma, C., et al., *Detection of subsurface cavity structures using contact-resonance atomic force microscopy.* Journal of Applied Physics, 2017. **121**(15): p. 154301.
103. Kalinin, S.V. and D.A. Bonnell, *Imaging mechanism of piezoresponse force microscopy of ferroelectric surfaces.* Physical Review B, 2002. **65**(12): p. 125408.
104. Gruverman, A. and S.V. Kalinin, *Piezoresponse force microscopy and recent advances in nanoscale studies of ferroelectrics.* Journal of materials science, 2006. **41**(1): p. 107-116.
105. Reinstaedtler, M., et al., *Imaging of flexural and torsional resonance modes of atomic force microscopy cantilevers using optical interferometry.* Surface Science, 2003. **532**: p. 1152-1158.
106. Koc, H., E. Deligöz, and A.M. Mamedov, *The elastic, electronic, and optical properties of PtSi and PtGe compounds.* Philosophical Magazine, 2011. **91**(23): p. 3093-3107.
107. Giessibl, F.J., *Atomic resolution on Si (111)-(7× 7) by noncontact atomic force microscopy with a force sensor based on a quartz tuning fork.* Applied Physics Letters, 2000. **76**(11): p. 1470-1472.
108. Akiyama, T., U. Staufer, and N. De Rooij, *Self-sensing and self-actuating probe based on quartz tuning fork combined with microfabricated cantilever for dynamic mode atomic force microscopy.* Applied Surface Science, 2003. **210**(1-2): p. 18-21.
109. Clubb, D.O., et al., *Quartz tuning fork viscometers for helium liquids.* Journal of Low Temperature Physics, 2004. **136**(1-2): p. 1-13.
110. Green, C.P. and J.E. Sader, *Torsional frequency response of cantilever beams immersed in viscous fluids with applications to the atomic force microscope.* Journal of Applied Physics, 2002. **92**(10): p. 6262-6274.

111. Ugural, A.C. and S.K. Fenster, *Advanced strength and applied elasticity*. 2003: Pearson education.
112. Castellanos-Gomez, A., N. Agraït, and G. Rubio-Bollinger, *Force-gradient-induced mechanical dissipation of quartz tuning fork force sensors used in atomic force microscopy.* Ultramicroscopy, 2011. **111**(3): p. 186-190.
113. Esro, M., et al., *Structural and electrical characterization of SiO2 gate dielectrics deposited from solutions at moderate temperatures in air.* ACS applied materials & interfaces, 2017. **9**(1): p. 529-536.
114. Pyne, A.L. and B.W. Hoogenboom, *Imaging DNA structure by atomic force microscopy*, in *Chromosome Architecture*. 2016, Springer. p. 47-60.
115. Etacheri, V., et al., *Challenges in the development of advanced Li-ion batteries: a review.* Energy & Environmental Science, 2011. **4**(9): p. 3243-3262.
116. Edwards, R.L., G. Coles, and W.N. Sharpe, *Comparison of tensile and bulge tests for thin-film silicon nitride.* Experimental Mechanics, 2004. **44**(1): p. 49-54.
117. Robinson, B.J., et al., *Nanomechanical mapping of graphene layers and interfaces in suspended graphene nanostructures grown via carbon diffusion.* Thin Solid Films, 2014. **550**(0): p. 472-479.
118. Rabe, U., K. Janser, and W. Arnold, *Vibrations of free and surface-coupled atomic force microscope cantilevers: Theory and experiment.* Review of Scientific Instruments, 1996. **67**(9): p. 3281-3293.
119. Sader, J.E., et al., *A virtual instrument to standardise the calibration of atomic force microscope cantilevers.* Review of Scientific Instruments, 2016. **87**(9): p. 093711.
120. Yamanaka, K. and S. Nakano, *Ultrasonic atomic force microscope with overtone excitation of cantilever.* Japanese Journal of Applied Physics Part 1-Regular Papers Short Notes & Review Papers, 1996. **35**(6B): p. 3787-3792.
121. Lee, C., et al., *Measurement of the elastic properties and intrinsic strength of monolayer graphene.* Science, 2008. **321**(5887): p. 385-388.
122. Banszerus, L., et al., *Ultrahigh-mobility graphene devices from chemical vapor deposition on reusable copper.* Science Advances, 2015. **1**(6): p. e1500222.
123. Fang, L., et al., *Thickness dependent friction on few-layer MoS2, WS2, and WSe2.* Nanotechnology, 2017. **28**(24): p. 245703.
124. Maharaj, D. and B. Bhushan, *Characterization of nanofriction of MoS2 and WS2 nanotubes.* Materials Letters, 2015. **142**: p. 207-210.
125. Feng, L.-p., Z.-q. Wang, and Z.-t. Liu, *First-principles calculations on mechanical and elastic properties of 2H- and 3R-WS2 under pressure.* Solid State Communications, 2014. **187**: p. 43-47.
126. Wang, J., Q.-A. Huang, and H. Yu, *Effect of native oxides on the elasticity of a silicon nano-scale beam.* Solid state communications, 2008. **145**(7-8): p. 351-354.
127. Xie, S., et al., *Coherent, atomically thin transition-metal dichalcogenide superlattices with engineered strain.* Science, 2018. **359**(6380): p. 1131-1136.
128. Peng, B., et al., *Thermal conductivity of monolayer MoS 2, MoSe 2, and WS 2: interplay of mass effect, interatomic bonding and anharmonicity.* RSC advances, 2016. **6**(7): p. 5767-5773.
129. Peimyoo, N., et al., *Thermal conductivity determination of suspended mono- and bilayer WS2 by Raman spectroscopy.* Nano Research, 2015. **8**(4): p. 1210-1221.
130. Grossel, P., et al., *Multifrequential AC modeling of the SThM probe behavior.* International Journal of Thermal Sciences, 2007. **46**(10): p. 980-988.
131. Gomès, S., A. Assy, and P.-O. Chapuis, *Scanning thermal microscopy: A review.* physica status solidi (a), 2015. **212**(3): p. 477-494.
132. Lefevre, S. and S. Volz, *3 omega-scanning thermal microscope.* Review of Scientific Instruments, 2005. **76**(3): p. 033701
133. Molina-Mendoza, A.J., et al., *Franckeite as a naturally occurring van der Waals heterostructure.* Nature communications, 2017. **8**(1): p. 1-9.
134. Frisenda, R., et al., *Symmetry breakdown in franckeite: spontaneous strain, rippling and interlayer moiré.* Nano Letters, 2020. **20**(2): p. 1141-1147.
135. Robinson, B.J., et al., *Structural, optical and electrostatic properties of single and few-layers MoS2: effect of substrate.* 2D Materials, 2015. **2**(1): p. 15005.

136. Dinelli, F., et al., *Subsurface imaging of two-dimensional materials at the nanoscale.* Nanotechnology, 2017. **28**(8): p. 085706.
137. Pekin, T., F. Allen, and A. Minor, *Evaluation of neon focused ion beam milling for TEM sample preparation.* Journal of microscopy, 2016. **264**(1): p. 59-63.
138. Németh, I., et al., *Heteroepitaxy of GaP on Si: Correlation of morphology, anti-phase-domain structure and MOVPE growth conditions.* Journal of Crystal Growth, 2008. **310**(7): p. 1595-1601.
139. Kunert, B., et al., *Si (001) surface preparation for the antiphase domain free heteroepitaxial growth of GaP on Si substrate.* Thin Solid Films, 2008. **517**(1): p. 140-143.
140. Liao, P.F. and P. Kelley, *Quantum well lasers*. 2012: Elsevier.
141. Adachi, S., *Properties of aluminium gallium arsenide*. 1993, London: Inspec.
142. Jeppesen, M.A., *Some optical, thermo-optical, and piezo-optical properties of synthetic sapphire.* JOSA, 1958. **48**(9): p. 629-632.
143. Bartolomé, J., et al., *In-situ scanning electron microscopy and atomic force microscopy Young's modulus determination of indium oxide microrods for micromechanical resonator applications.* Applied Physics Letters, 2014. **104**(16): p. 161909.
144. Doucet, L. and G. Carlotti, *Elastic Properties of Silicate Glass and Spin-On Glass Thin Films.* MRS Proceedings, 2011. **356**: p. 215.
145. Sun, X., et al., *Identifying a doping type of semiconductor nanowires by photoassisted kelvin probe force microscopy as exemplified for GaN nanowires.* Optical Materials Express, 2017. **7**(3): p. 904-912.
146. Hetzl, M., et al., *Polarity Control of Heteroepitaxial GaN Nanowires on Diamond.* Nano Letters, 2017. **17**(6): p. 3582-3590.
147. Minj, A., et al., *Direct assessment of p–n junctions in single GaN nanowires by Kelvin probe force microscopy.* Nanotechnology, 2016. **27**(38): p. 385202.
148. Parida, S., et al., *Role of the surface density of states in understanding size-dependent surface band bending in GaN nanowires.* Applied Surface Science, 2020. **510**: p. 145502.
149. Minary-Jolandan, M., et al., *Individual GaN Nanowires Exhibit Strong Piezoelectricity in 3D.* Nano Letters, 2012. **12**(2): p. 970-976.
150. Dahiya, R.S. and M. Valle, *Robotic tactile sensing: technologies and system*. 2012: Springer Science & Business Media.
151. Romanov, A., et al., *Strain-induced polarization in wurtzite III-nitride semipolar layers.* Journal of Applied Physics, 2006. **100**(2): p. 023522.

Annexe I

LabVIEW programme

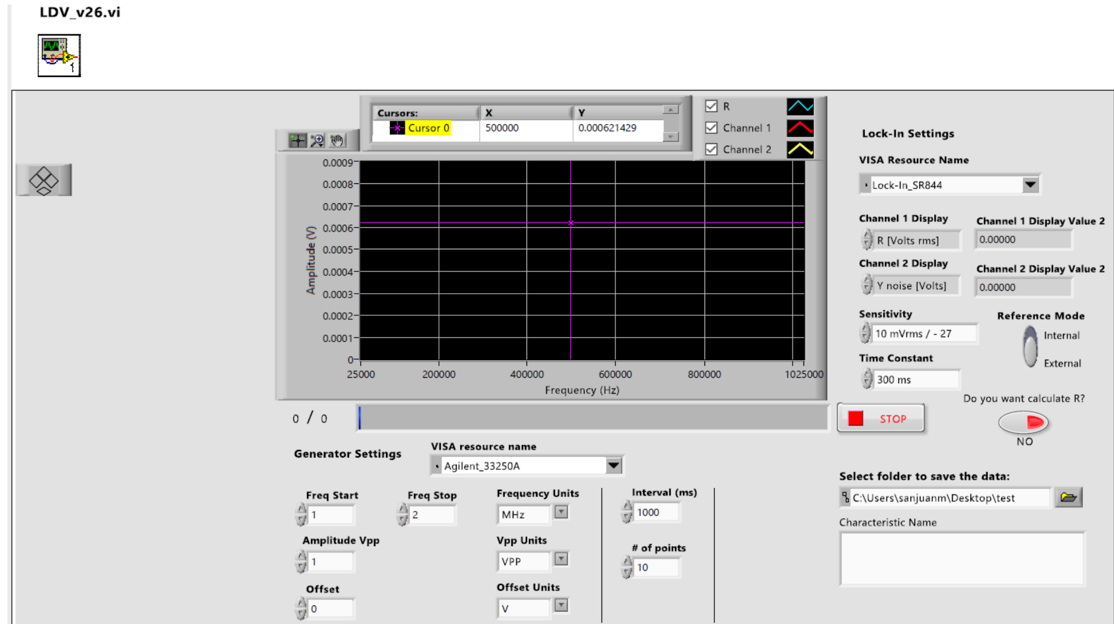

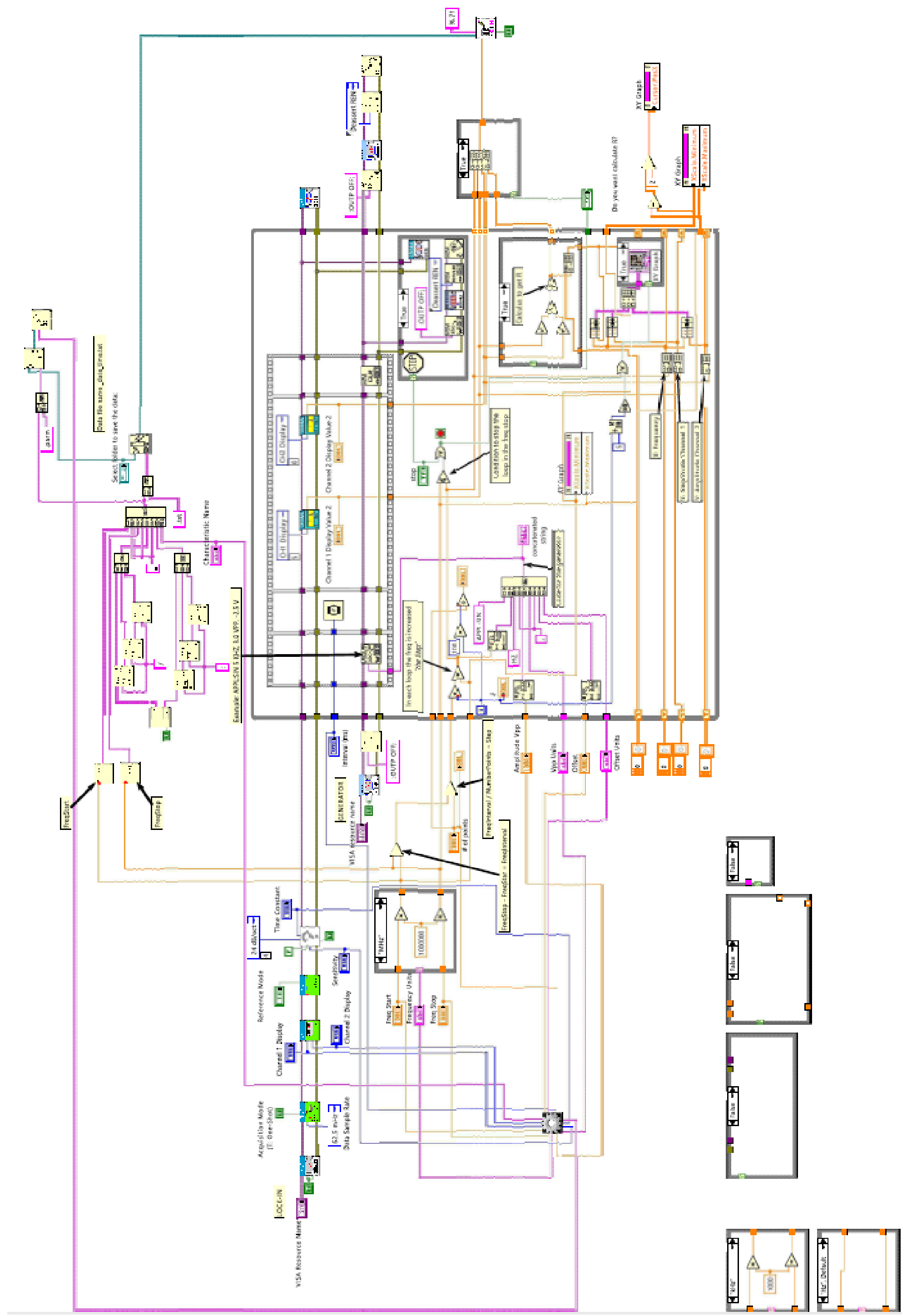

Annexe II

Matlab code for the membrane modelling.

```
function [] = memfmm()
%memfmm(rmax)
;
format COMPACT
%MEMBRANE
dm=500E-6;  %membrane diameter - [m]
tm=200E-9;  %membrane thickness -[m]
em=166E9;   %membrane Young's modulus - [Nm^-2]
ttm=1.2E9;  %membrane tension - [Pa]
rhom=3.17E3;%membrane density - [kgm^-3meff=0.25;  %(TO CALCULATE)
membrane effective mass coeff
mm=meff*rhom*tm*pi*(dm/2)^2; %effective membrane mass - [kg]
km=121.83;       %(TO REPLACE WITH DERIVED) membrane stiffness -
[Nm^-1]
%CANTILEVER
lc=225E-6;  %cantilever length - [m]
wc=28E-6;   %cantilever width - [m]
tc=3E-6;    %cantilever thickness - [m]
rhoc=2.32E3;%cantilever density - [kg m^-3]
ceff=0.25;  %cantilever effective mass coeff (fundamental mode)
mc=ceff*rhoc*lc*wc*tc;  %cantilever effective mass - [kg]
kc=3;     %(TO REPLACE WITH DERIVED) cantilever stiffness, [N/m]
;
nn=1000;
;
mc
fc=1/(2*pi)*sqrt(kc/mc)
mm
fm=1/(2*pi)*sqrt(km/mm)
pause

L = zeros(nn-1,1);
Ft = zeros(nn-1,1);

for n=1:nn
    l(n)=(dm/2)*n/nn;
    ft(n)=1/(2*pi)*sqrt((km+kc*2*l(n)/dm)/(mm+mc*(2*l(n)/dm)^2));
    L(n)=l(n);
    Ft(n)=ft(n);

end
plot(l,ft);

LFt=[L';Ft'];
LFt2=LFt';
fileID = fopen('freq.txt','wt');
fprintf(fileID,'%6s %12s\r\n','l','ft(l)');
fprintf(fileID,'%6.10f  %12.8f\r\n',LFt);
fclose(fileID);
```